UNIVERSITY OF CALIFORNIA, MERCED

Understanding and Tuning Ionic Transport and Electrochemical Reactions on Air Electrodes of Solid Oxide Fuel Cells at the Nanoscale

by
Hung-Sen Kang

A dissertation
submitted in partial satisfaction of the
requirements for the degree of
PhD
in
Mechanical Engineering

Committee in charge:
Professor Min Hwan Lee, Chair
Professor Ashlie Martini
Professor Abel Chuang
Professor Gerardo Diaz

The dissertation of Hung-Sen Kang is approved:

Min Hwan Lee, Chair Date

Ashlie Martini Date

Abel Chuang Date

Gerardo Diaz Date

University of California, Merced

To my girlfriend, friends, family and everyone whoever helped me.
This accomplishment wouldn’t have been possible without their love and support.

ACKNOWLEDGEMENTS

In my acknowledgments I would like to give particular thanks my research advisor, Min Hwan Lee, department of Mechanical Engineering at the University of California, Merced, for his supervision, guidance, and encouragement during my six years of research. I also would also like to thank my colleague Haoyu Li for his invaluable assistance in conducting experiments and collecting experimental data. I wish to express my gratitude to Simi Grewal, Angela Macedo and Ziqi Liu for their helpful comments and assistance in compiling and formatting my thesis document. I would like to acknowledge the NASA-funded Merced nAnomaterials Center for Energy and Sensing (MACES) for financial support of my research and for access to equipment used in collection of experimental data.

LIST OF SYMBOLS

σ_i ..... ionic conductivity
A ..... cross-sectional area
P_{O_2} ..... oxygen partial pressure
R_p ..... polarization resistance
$R_s/R_{ohm}/Z_\Omega$ ..... ohmic resistance
Z ..... impedance
ϕ ..... phase shift
Z_{fA} ..... anodic polarization resistance
Z_{fC} ..... cathodic polarization resistance
F ..... Faraday's constant ($96400\ C/mol$)
R ..... universal gas constant ($8.314\ J/K \cdot mol$)
j ..... current density
j_0 ..... exchange current density
E_a ..... activation energy
α_{anode} ..... anodic charge transfer coefficient
$\alpha_{cathode}$ ..... cathodic charge transfer coefficient
η ..... activation overpotential
P ..... maximum power density
λ ..... wavelength
V_{DC} ..... external bias
V_{CPD} ..... contact potential difference
E_v ..... vacuum energy level
E_{fs} ..... Fermi energy level of sample
E_{fp} ..... Fermi energy level of the AFM probe
f_p ..... pressing force
f_a ..... adhesion force
h ..... Planck's constant ($6.626 \times 10^{-34}\ J/Hz$)
m_0 ..... free-space electron mass
m^* ..... effective mass
ρ ..... charge density
$\tilde{\rho}$ ..... resistivity
σ ..... conductivity
R_{SR} ..... spreading resistance

LIST OF ABBREVIATIONS

SOFC……..…….solid oxide fuel cell
PEMFC……..polymer electrolyte membrane fuel cell
HOPG…….highly oriented pyrolytic graphite
AFM…….atomic force microscopy
CAFM……...conductive atomic force microscopy
KPFM……...…Kelvin probe force microscopy
SEM…..……scanning electron microscope
TEM……transmission electron microscope
MFM……magnetic force microscope
SFA……surface forces apparatus
XRD……..……...X-ray diffraction
EIS…..……electrochemical impedance spectroscopy
RDS……..rate-determining step
STO…..……$SrTiO_3$
YSZ…...……Y_2O_3-stabilized ZrO_2
ScSZ…….scandia-stabilized zirconia
GDC…..……gadolinium-doped ceria
LNF…...…….$LaNi_{0.6}Fe_{0.4}O_{3-\delta}$
LSC……$La_{1-x}Sr_xCoO_{3-\delta}$
LSM……$La_{1-x}Sr_xMnO_{3-\delta}$
LSF……Sr-doped $LaFeO_3$
LSCo……Sr-doped $LaCoO_3$
SDC……..….$Sm_{1-x}Ce_xO_{3-\delta}$
LCF……..Ca-doped $LaFeO_3$
LBF……..Ba-doped $LaFeO_3$
ZTO……..zinc tin oxide
LSCF…….……$La_{1-x}Sr_xCo_{1-y}Fe_yO_{3-\delta}$
LSCM……..……$La_{0.8}Sr_{0.2}Mn_{0.8}Co_{0.2}O_3$
TPB…….……triple phase boundary
ALD…...……atomic layer deposition
MIEC…….……mixed oxygen ionic and electronic conductor
CTE……..……...coefficient of thermal expansion
CPE……...constant phase element
ORR…….…….oxygen reduction reaction
OER……..……oxygen evolution reaction
OCV……..……..open circuit voltage
CVD…..……chemical vapor deposition
PVD……...physical vapor deposition
ASR……..……area specific resistances
CF……..……..conducting filament
EOP……..……electro-chemical oxygen pumps
POM……..partial oxidation of methane
DCP…..……diamond-coated probe

TABLE OF CONTENT

ACKNOWLEDGEMENTS……..……**v**
LIST OF SYMBOLS……..…**vi**
LIST OF ABBREVIATIONS……..……**vii**
LIST OF FIGURES……..……**xi**
LIST OF TABLES……..……...**xxi**
ABSTRACT……..……**xxii**

Chapter

1 Introduction……..……**1**
2 Background……..……**4**

2.1 SOFC overview……..……4

2.1.1 Operation…….....……4
2.1.2 SOFC components……...……5

2.1.2-1 Electrolyte……..…..……5
2.1.2-2 Cathode……..……..……8
2.1.2-3 Anode……....……10

2.2 Fabrication approaches for nanoscale……..……11

2.2.1 Solid Oxide Fuel Cells……..……11

2.2.1-1 SOFC Cathodes……..……13
2.2.1-2 SOFC Anodes……..……..……17

2.2.2 Infiltration……..……17

2.2.2-1 Overview……..……..…17
2.2.2-1 Materials……..……..…18

2.2.3 ALD Method……..……...……40

2.2.3-1 Overview……..……..40
2.2.3-2 Applications……..……41

2.3 Characterization Methods……..……46

2.3.1 Electrochemical Impedance Spectroscopy……...…46
2.3.2 Electrode Performance……48
2.3.3 Rate-determining step……..……..……51

2.4 Microstructure characterization……..……52

2.4.1 Scanning Electron Microscopy……...……52
2.4.2 X-Ray Diffraction……...……53
2.4.3 Atomic Force Microscopy……...……54
2.4.4 Conductive atomic force microscopy……..……62
2.4.5 Kelvin probe force microscopy……...…66

3 Topic I: Nanoscale engineering effects on cathodes for intermediate-temperature SOFCs……**69**

3.1 Introduction……..……69
3.2 Experimental……70

3.2.1 Cell Preparation…….……70
3.2.2 Infiltration solvent preparation…...…….……71
3.2.3 Equivalent circuit ……..71

3.3 Results and Discussion…….……72
3.3.1 Electrochemical and Microstructure Characterization……...……72
3.3.2 Durability…….…...83
3.4 Conclusions……..…86

4 Topic II: Effects of mechanical and electrical applications on AFM……..…**87**

4.1 Introduction……...…87
4.2 Experimental……87

4.2.1 Preliminary Steps ……..……88
4.2.2 Fabrication of Pt-Ir AFM tips ……...…88
4.2.3 CAFM measurement and Microstructure Characterization …….91

4.3 Results and Discussion…….……94
4.4 Conclusions……..……96

5 Topic III: Ionic Transport and Electrochemical Reaction on Air Electrodes of Solid Oxide Fuel Cell Study via AFM ……..……97

5.1 Introduction……..……97
5.2 Experimental……98

5.2.1 Experiment setup and sample preparation ……...……98
5.2.2 Oxygen vacancy generation ……...……99
5.2.3 Removal implementation ……99
5.2.4 Data analysis……...100

5.3 Results and Discussion……..……109

5.3.1 Induced charge on STO/YSZ ……..109
5.3.2 Oxygen vacancy mobility on STO/YSZ surface ……..…109
5.3.3 Oxygen vacancy mobility in the bulk of STO/YSZ ……111
5.3.4 Diffusivity ……...……...112
5.3.5 Activation energy ……113

5.4 Conclusions……..……115

6 Summary……**116**
REFERRENCES……..……..……**118**

LIST OF FIGURES

2.1 A schematic drawing of a SOFC.[9] ……....……..……..……4

2.2 Oxygen vacancies created by doping zirconia with yttria: (a) the un-doped zirconia host and (b) an empty O^{-2} site created by replacing two Zr^{+4} cations with two Y^{+3} cations.[11] ……....…….……7

2.3 (a) Ionic conductivity vs yttria doping concentration for YSZ; (b) ionic conductivity vs temperature for YSZ and GDC.[11] ...…….……...……8

2.4 Phenomenological roles of the electronically conducting (electronic) phase (α), gas phase (β), and ionically conducting (ionic) phase (γ) in accomplishing oxygen reduction.[18]....…….……..…..……8

2.5 Atomic structure and oxygen transport in mixed conducting perovskites $ABO_{3-\delta}$. (a) Basic structural element, consisting of a corner-sharing BO_6 octahedron surrounded by charge-compensating A-site cations. (b) Bulk oxygen transport mechanism, involving random hopping of oxygen ion vacancies on the oxygen sub-lattice.[18] ....…….……..…….....9

2.6 Schematic diagram showing triple phase boundary area for (a) a standard electrode; and (b) a mixed ionic-conducting electrode.[11] ....…….…….....10

2.7 Schematic showing the roles of anode, cathode, and electrolyte in a SOFC.[18] ……....12

2.8 XRD patterns of LNF64 ($T_{calcination}$ = 1000 ℃ for 5 hours) synthesized by four methods: (a) WC, (b) MWC, (c) NC, and (d) MNC.[76] ....…….…….....15

2.9 SEM micrographs of LNF64 ($T_{calcination}$ = 1000 ℃ for 5 hours) synthesized by four methods: (a) WC, (b) MWC, (c) NC, and (d) MNC.[76] ....…….……...16

2.10 Nyquist plots of LNF64 cathodes prepared using four methods at 700 ℃.[76] ….....16

2.11 Infiltration growth mechanism. ....…….…….....17

2.12 Cole-Cole plots for the cells with LNF-YSZ, LSNF-YSZ, and LSF-YSZ cathodes calcined to 1100 ℃. The measurements were performed at open circuit holding the cathodes in air at 700 ℃.[67] ....…….…….....18

2.13 Schematic diagrams showing (a) the location of the three-phase boundary (TPB), i.e., the boundary between the YSZ electrolyte, LSM electro-catalyst and current conductor, and the gas phase, and (b) idealized structure of a cathode.[87] ….....19

2.14 Diagram showing the steps used to fabricate an SOFC in which the electrodes are produced by infiltration of active components into a porous YSZ scaffold. [100,101] ….....20

2.15 Cole-Cole plots of impedance spectra collected at 700 ℃ for a symmetric cell with two LSF-YSZ electrodes fabricated by infiltration as a function of the current density applied to the cell: (◆) OCV, (•) 100 mA cm^{-2}, (△) 200 mA cm^{-2}, (◇) 400 mA cm^{-2} (•) 600 mA cm^{-2}, and (*) OCV immediately after applying 600 mA cm^{-2}. Prior to measuring the impedance spectra the electrodes were aged by annealing in air at 700 ℃ for 2500 hours.[121] ....…….....23

2.16 Schematic diagram of infiltrated LSF-YSZ cathode (a) after calcining in air at 850 ℃ and (b) after calcining at higher temperatures (>1000 ℃) or long term aging.[8] ….....24

2.17 Impedance spectra obtained from fuel cells with infiltrated electrodes as a function of the active component, LSF (■), LBF (•), and LCF (▲), used in the cathode. The composite cathodes in each of, these cells were calcined at 1100 ℃. The filled symbols show data measured at open circuit while the open symbols were obtained at a current density of 100 mA cm^{-2}. Reproduced with permission from reference.[124] ….....25

2.18 Impedance spectra for a SOFC with an LSM-YSZ cathode and Cu-CeO_2-YSZ anode at 700 ℃ in humidified H_2 (3% H_2O). The cathode in this cell was fabricated by co-sintering LSM and YSZ powders. All of the spectra were measured at open circuit immediately after applying a current for 10 min. The current densities were applied in the following order: (◇) after heating at OCV, (△) 60 mA cm^{-2}, (•) 150 mA cm^{-2}, (○) 850 mA cm^{-2} (short circuit). The constant ohmic resistance of the cell has been subtracted from each spectrum.[137] ….....27

2.19 Equilibrium composition of $La_{0.8}Sr_{0.2}MnO_{3+d}$ as a function of $P(O_2)$.[146] ….....27

2.20 Cross-section of three types of cathode near the electrolyte. (a) Cathode with GDC-LNF composite active layer, (b) cathode with $Pr_xCe_{1-x}O_{2-\delta}$ (x = 0.1, 0.3, 1.0)-LNF composite active layer, and (c) cathode with Pr_6O_{11} active layer.[65] ….....30

2.21 AC impedance plots for cathodes with different active layers. The effective area was 0.785 cm^2.[65] ….....31

2.22 Schematic diagram of one side of the symmetric cell structure for cathode A, cathode.[64] ….....31

2.23 X-ray diffraction pattern of the powder of (a) LNF, (b) GDC, (c) 50 wt.% LNF + 50 wt.% GDC at room temperature and (d) 50 wt.% LNF + 50 wt.% GDC calcined at 1100 ℃ for 5 hours.[64] ….....32

2.24 SEM images of (a) composite LNF-based cathode (70 wt.% LNF:30 wt.% GDC) and (b) GDC-impregnated LNF.[64] ….....32

2.25 Electrochemical impedance spectra of LNF-based cathodes measured at different temperatures in air: (a) 650 ℃, (b) 700 ℃, (c) 750 ℃, (d) 800 ℃ and (e) 850 ℃. EIS was measured at open circuit. (f) The equivalent circuit for data fitting. (g) Impedance sketch map on the complex plane.[64] ….....34

2.26 Arrhenius plots of the specific polarization resistance (R_p) for three different configurations of LNF-based cathodes.[64] ….....35

2.27 XRD of LNF powders synthesized by glycine nitrate process and calcined at 1000 ℃ and SDC powders prepared by solid state reaction calcined at 1200 ℃. The index of crystallographic plane was marked.[78] ….....36

2.28 Polarization resistance (R_p) of blank LNF cathode sintered at 1000 ℃, 1100 ℃ and 1200 ℃ for 2 hours in air.[78] ….....37

2.29 Electrochemical impedance spectra of blank LNF and BLF infiltrated with BLF, BSCF, SDC and Pr_6O_{11} nano-catalysts measured at 750 ℃.[78] ….....38

2.30 SEM of LNF electrode infiltrated different promoting agents (a) BSCF infiltrated cathode calcined at 800 ℃, (b) BLF infiltrated cathode calcined at 800 ℃, (c) Pr_6O_{11} infiltrated cathode calcined at 750 ℃ and (d) SDC infiltrated cathode calcined at 750 ℃.[78] ….....39

2.31 Typical atomic layer deposition cycle: (a) Bare functionalized substrate; (b) precursor A attaches to substrate; (c) Inert gas purges chamber and evacuates remaining precursor A; (d) precursor B fills chamber and attaches to precursor A; (e) remaining precursor B is purged from chamber with inert gas; (f) cycle is repeated until desired thickness is reached.[7] ….....41

2.32 Examples of ALD strengths. (a) TEM image of conformal SnS_x ALD film on Au nanoparticles. Scale bar is 100 nm. (b) SEM cross-sectional image of conformal $Ge_2Sb_2Te_5$ ALD film in trenches.[165] (c) $SrTiO_3$ stoichiometry as a function of $SrCO_3$ and TiO_2 ALD super cycle ratio.[161] ….....43

2.33 Top-view SEM images of Pt films (a) without and (b) with a nanoscale YSZ coating before (left) and after an annealing process (right) at 500 °C for 20 hours. Upper schematic diagrams depict conceptual microstructures of each sample. For this characterization, the Pt film was deposited on a Si substrate.[41] ….....45

2.34 Cross-sectional TEM images of a YSZ-coated Pt film (a) before and (b) after an annealing at 600 °C for 10 hours. A thermally induced agglomeration of YSZ coating is observed. (c) An EDS line mapping scanned through the dotted vertical line in the TEM image on the left side.[41] ….....45

2.35 Nyquist plot showing sample SOFC electrochemical impedance spectroscopy data for illustration; Z_{Ω} is the cell ohmic resistance, $Z_{fA}$is the anodic polarization resistance, and Z_{fC} is the cathodic polarization resistance.[11] ….....47

2.36 simplified equivalent circuit for an SOFC. ….....47

2.37 (a) *i*-V polarization curve and (b) Cole-Cole impedance spectrum for a SOFC/SOE operating at 700 ℃ on a fuel consisting of 90% H_2 and 10% H_2O. The cell composition was as follows: 40 wt.% LSF in YSZ/YSZ (65 mm)/0.5 wt.% Pd, 5 wt.% $Ce_{0.48}Zr_{0.48}Y_{0.04}O_2$, and 45 wt.% LSCM in YSZ. More details on the cell fabrication can be found in reference.[177] ……50

2.38 A regular array of scatterers (atoms' electrons) produces a regular array of spherical waves when X-ray waves come from some specific angle. ……....54

2.39 Typical configuration of an AFM. (1): Cantilever, (2): Support for cantilever, (3): Piezoelectric element(to oscillate cantilever at its eigen frequency.), (4): Tip (Fixed to open end of a cantilever, acts as the probe), (5): Detector of deflection and motion of the cantilever, (6): Sample to be measured by AFM, (7): xyz drive, (moves sample (6) and stage (8) in x, y, and z directions with respect to a tip apex (4)), and (8): Stage. …….....55

2.40 Interaction forces (per unit area) for the Hertz, JKR, and DMT models, compared to a realistic interaction. There is no attractive force in the Hertz model, only hard wall repulsion at contact. The JKR model includes short range adhesion which is essentially a delta function with strength γ and thus acts only within the contact zone. The DMT curve shown represents a long-range surface force. A volume integrated force, like the van der Waal's force, can also lead to a DMT dependence, where the contact profile remains Hertzian and the attractive forces act like an additional external load. For an actual interaction force, the integral of the force–distance attractive well corresponds to the work of adhesion, γ.[191] …….....57

2.41 The force-distance relation for the Dugdale model used by Maugis. A constant adhesive stress (force per unit area) σ_0 acts between the surfaces over a range δ_t. At greater separations, the attractive force is zero. The work of adhesion is thus $\gamma = \sigma_0 \times \delta_t$.[191] 58

2.42 The Hertz area-load curve, and the JKR-DMT transition, plotted in Maugis' units (Equation 2.19). Area–load curves for the JKR limit, the DMT limit, and an intermediate case are shown. These approach the Hertz curve in the limit $\gamma \to 0$ (no adhesion). Adhesion increases the contact area from the Hertz case for a given load by an amount dependent upon the range of attractive forces.[191] …….....59

2.43 Plot of α vs λ from Table I (filled circles) and the empirical conversion equation, Equation 2.20 (solid line), fit to the data.[191] ……...…....61

2.44 Non-repeatability of I-V curves measured in the same location of the sample surface.[208] …….....63

2.45 Current fluctuation and degeneracy behaviors in the nano-contact under constant ~5 nN contact load and 10 V bias voltage. The I–t curves after biased 1 min (a), 15 min (b), 30 min (c) and 40 min(d) are shown, respectively.[208] …….....63

2.46 The degenerative behavior of the average current, noting it becomes completely undetectable after biased 45 min.[208] …….…….....64

2.47 AFM impedance measurement. (a) General concept. Impedance is measured between a local probe (the AFM tip) and a bulk electrode. A significant spreading resistance contribution at the AFM tip/sample contact point ensures local characterization. (Shown schematically by the hemi- spherical lines.) (b) Detail of the Pt/Nafion impedance experiment. ORR kinetics at the interface between a Pt-coated AFM tip and a Nafion electrolyte membrane are measured using AFM impedance. Electrochemical bias is applied relative to the bulk bottom electrode (a reversible hydrogen electrode) which is hermetically sealed and supplied with hydrogen gas.[212] …….....……..65

2.48 Simple equivalent circuit model of the tip/sample contact. R_{tip} represents the resistance contribution from the tip, R_{cont} accounts for the tip/sample interfacial resistance, which may include Schottky or Faradaic effects if the contact is non-ohmic. C represents the tip/sample capacitance. R_{SR} accounts for the spreading resistance associated with a small volume of material just beyond the tip/sample contact.[212] ……....66

2.49 Three stages of electronic energy levels of the AFM probe and sample: (a) before contacting the AFM probe with a sample area separated by distance z with no electrical contact; (b) while in contact the AFM probe and samples also conduct electricity; and (c) the external bias (V_{DC}) is applied between AFM probe and sample to nullify the contact potential difference (V_{CPD}). E_v is the vacuum energy level, E_{fs} is the Fermi energy level of sample, and E_{fp} is the Fermi energy level of the AFM probe.) ……..67

2.50 Schematic graph of KPFM system with AM and FM modes. The lower side of the graph is an FM mode AFM system for topography imaging and the upper side is a KPFM system for contact potential difference (V_{CPD}). [213] ……..….……..67

3.1 The configuration of symmetric cathode fuel cell. ……...70

3.2 The equivalent circuit for symmetric cathode fuel cell (half-cell). ...……..……..72

3.3 The EIS performance and SEM images: (a) shows the graph of all LNF-infiltration LNF-based cathodes with different concentrations. The graph on upper right shows the overall of LNF-infiltration LNF-based cathodes, compared to the blank LNF-based cathodes. (b) shows the SEM image of blank LNF backbones of LNF-base cathodes. (c)

and (d) show the SEM images of LNF-infiltration LNF-base cathodes with concentrations of 0.2 M and 0.6 M, respectively. The scale bar indicates 200 nm. …..……..…….72

3.4 The EIS performance and SEM images: (a) shows the graph of all LSCF-infiltration LNF-based cathodes with different concentrations. The graph on upper right shows the overall of LSCF-infiltration LNF-based cathodes, compared to the blank LNF-based cathodes. (b) shows the SEM image of blank LNF backbones of LNF-base cathodes. (c) and (d) show the SEM images of LSCF-infiltration LNF-base cathodes with concentrations of 0.2 M and 0.8 M, respectively. The scale bar indicates 200 nm. …….....……..….73

3.5 The EIS performance and SEM images: (a) shows the graph of all $Pr_6O_{11}(PrO_x)$-infiltration LNF-based cathodes with different concentrations. The graph on upper right shows the overall of $Pr_6O_{11}(PrO_x)$-infiltration LNF-based cathodes, compared to the blank LNF-based cathodes. (b) shows the SEM image of blank LNF backbones of LNF-base cathodes. (c) and (d) show the SEM images of $Pr_6O_{11}(PrO_x)$-infiltration LNF-base cathodes with concentrations of 0.8 M and 1.5 M, respectively. The scale bar indicates 200 nm.. ……74

3.6 The EIS performance and SEM images: (a) shows the graph of all LSM-infiltration LNF-based cathodes with different concentrations. The graph on upper right shows the overall of LSM-infiltration LNF-based cathodes, compared to the blank LNF-based cathodes. (b) shows the SEM image of blank LNF backbones of LNF-base cathodes. (c) and (d) show the SEM images of LSM-infiltration LNF-base cathodes with concentrations of 0.2 M and 0.8 M, respectively. The scale bar indicates 200 nm. …….....75

3.7 The EIS performance and SEM images: (a) shows the graph of all GDC-infiltration LNF-based cathodes with different concentrations. The graph on upper right shows the overall of GDC-infiltration LNF-based cathodes, compared to the blank LNF-based cathodes. (b) shows the SEM image of blank LNF backbones of LNF-base cathodes. (c) and (d) show the SEM images of GDC-infiltration LNF-base cathodes with concentrations of 0.4 M and 1.5 M, respectively. The scale bar indicates 200 nm. ……..……..76

3.8 The EIS performance and SEM images: (a) shows the graph of all PDC ($Pr_{1-x}Ce_xO_{3-\delta}$)-infiltration LNF-based cathodes with different concentrations. The graph on upper right shows the overall of PDC-infiltration LNF-based cathodes, compared to the blank LNF-based cathodes. (b) shows the SEM image of blank LNF backbones of LNF-base cathodes. (c) and (d) show the SEM images of PDC-infiltration LNF-base cathodes with concentrations of 0.2 M and 1.0 M, respectively. The scale bar indicates 200 nm. ……...77

3.9 (a) The equivalent circuit we used for fitting our data, and (b) and (c) show the polarization resistance of infiltrated LNF cathode. . …….....78

3.10 XRD spectra of bare and infiltrated LNF cathode. ……79

3.11 TEM images of (a) bare LNF backbone, (b) Pr_6O_{11}-infiltrated and (c) GDC-infiltrated LNF cathodes. All the scale bars correspond to 20 nm. ……..……79

3.12 Arrhenius plots of R_H and R_L deduced from the EIS measurements of bare and infiltrated LNF cells. ……..……80

3.13 Nyquist plots of (a) bare LNF and (b)-(f) infiltrated LNF obtained under the open circuit condition at 700 °C. The nitrate concentration was optimized for lowest polarization resistances; for LNF and LSM, 0.8 M and for others, 1.0 M. The insets show the (P_{O_2}) dependency of R_H and R_L and the corresponding reaction order (m) values. ….82

3.14 (a)-(c) Nyquist plots of LNF, LSCF and GDC-infiltrated symmetric cells obtained at the open circuit condition as a function of time in Cr-containing environment at 700 °C. 100 sccm of dry O_2 was fed to both electrodes of each cell for the measurement. (d) Evolution of area specific electrode polarization resistances from LNF, LSCF and GDC-infiltrated samples. The durability test of LNF-infiltrated cell was stopped at 65 h due to power outage. ……..……..……84

3.15 SEM images of LNF backbones infiltrated with (a, b) 0.8 M LNF, (c, d) 1.0 M LSCF and (e, f) 1.0 M GDC, before and after exposing the cell under a Cr-containing gas environment at 700 °C (65 h for LNF, 100 h for LSCF and GDC). The red arrow in (b) indicates highly sintered inter-particle necks. The scale bars correspond to 200 nm. …….85

4.1 (a)This illustrates the fabrication process of Pt-Ir AFM. (b) From left to right are continuous steps before, after rough etching and after fine etching and (c)-(e) show the SEM images of Pt-Ir AFM tips we fabricated by different time and voltage on rough etching and rough etching. ….…..…….……..……..…….90

4.2 SEM images of Pt-Ir AFM tips made from different procedures: (a) flame annealing for too long, (b) after low-voltage pulse micro-polishing, (c) after intermedia-voltage pulse micro-polishing, and (d) after high-voltage pulse micro-polishing. ……...90

4.3 (a)-(c) SEM images of mechanically-degraded, Au-coated tips superimposed on another image of an as-cleaned tip. The images were taken after being exposed to a pressing force of 100 nN (a), 150 nN (b), and 440 nN (c) on an HOPG surface. Scale bar: 500 nm. (d) – (g) SEM images of tips after compressed on an HOPG surface with different pressing forces (f_p) at the approaching speed of (d) and (e) 0.2 μm/s and (f) and (g) 2 μm/s. Scale bar: 100 nm. Even with a small intended f_p of < 10 nN, the tips were deformed significantly when engaged at 2 μm/s. Note that the as-purchased tip apex diameter quantified from SEM images is 43 nm on average with a standard deviation of ~ 2 nm; the dimension from TEM images is somewhat different and the reason is yet to be clarified. [238] ……...…...91

4.4 (a) Force-distance graph of the Au-HOPG interface, showing little hysteresis between approaching and retreating processes, and little difference in their trajectories with repeated cycles. (b) and (c) Adhesion forces measured after applying a range of pressing forces

using an as-purchased (b) and an as plasma- cleaned tip (c). For all the measurements, the Au-coated tip was pressed on and detached from an HOPG surface.[238] ……..……..92

4.5 (a) The change of measured resistance with pressing force. The sweeps were quantified by impedance measurement with 2mV of ac bias. [(b) and (c)] TEM images of a new plasma-cleaned tip (b) and another plasma-cleaned tip that experienced an LRS (c). [238]…93

4.6 (a) The change of calculated area and distance with pressing force. (b) A fitting of an f_p–R curve [Sweep 3 shown in Figure 4.5(a)] to an equation of field-assisted tunneling.[238]……95

5.1 The cubic unit cell and schematic diagrams depicting the oxygen vacancy configurations (isolated state) of (a) $SrTiO_{3-\delta}$ and (b) Y_2O_3-stabilized ZrO_2. ……....97

5.2 (a) Experiment setup with conductive atomic force microscopy method (CAFM, path in red) and Kelvin probe force microscopy (KCFM) on the AFM device, (b) AFM sample heating stage setup, and (c) thermal imaging of the heating stage using different voltages. ……..…...98

5.3 The continuous steps of oxygen vacancy generation: (a) provide a positive bias on the AFM probe; (b) vicinity oxygen ions have an oxidation reaction to generate oxygen vacancies and release oxygen; and (c) those oxygen vacancies move through the surface and bulk. ……..…99

5.4 (a)Demonstration of the sample surface removal process with diamond-coated probe on the AFM; and (b)Topography AFM images of before and after the sample surface was removed. There is a square removal area of about 3μm×3μm in the after image. …….....100

5.5 (a) A drawing demonstrating induced charge on the surface and in the bulk after charging ; and (b) the method quantifying the amount of induced charge by integral. ….101

5.6 (a) Graph plotting percentage of induced charge according to temperature; and (b) The percentage of induced charge on STO and YSZ at the temperature of 25 ℃ in an environment of pure oxygen. …….....……..…….……..102

5.7: Extended initial distribution. [281] ……103

5.8: The temperature increase and decrease speed of (a) STO and (b) YSZ on the heating plates from room temperature (25 ℃) to the temperatures we need (100 ℃ and 200 ℃). .104

5.9: The different ratios between temperature and time from different activation energy assumption for (a) STO surface at 100 ℃, (b) STO surface at 200 ℃, (c) YSZ surface at 100 ℃, (d) YSZ surface at 200 ℃, (e) STO bulk at 100 ℃,(f) STO bulk at 200 ℃,(g) YSZ bulk at 100 ℃, and (h) YSZ bulk at 200 ℃. ……..104

5.10: The timeline for oxygen vacancy diffusivity experiment for STO surface, STO was on the heating plate from 25 ℃ to 100 ℃ and dropped back to 25 ℃. ……...105

5.11: The timeline for oxygen vacancy diffusivity experiment for STO surface, STO was on the heating plate from 25 ℃ to 200 ℃ and dropped back to 25 ℃. ……...105

5.12: The timeline for oxygen vacancy diffusivity experiment for STO bulk, STO was on the heating plate from 25 ℃ to 100 ℃ and dropped back to 25 ℃. ……106

5.13: The timeline for oxygen vacancy diffusivity experiment for STO bulk, STO was on the heating plate from 25 ℃ to 200 ℃ and dropped back to 25 ℃. ……106

5.14: The timeline for oxygen vacancy diffusivity experiment for YSZ surface, YSZ was on the heating plate from 25 ℃ to 100 ℃ and dropped back to 25 ℃. ……...107

5.15: The timeline for oxygen vacancy diffusivity experiment for YSZ surface, YSZ was on the heating plate from 25 ℃ to 200 ℃ and dropped back to 25 ℃. ……..107

5.16: The timeline for oxygen vacancy diffusivity experiment for YSZ bulk, YSZ was on the heating plate from 25 ℃ to 100 ℃ and dropped back to 25 ℃. ……108

5.17: The timeline for oxygen vacancy diffusivity experiment for YSZ bulk, YSZ was on the heating plate from 25 ℃ to 200 ℃ and dropped back to 25 ℃. ……108

5.18: (a) Graph plotting percentage of induced charge according to temperature; and (b) The percentage of induced charge on STO and YSZ at the temperature of 25 ℃ in an environment of pure oxygen. ……...109

5.19 KPFM images of an STO surface at 25℃, 100℃, and 200℃ after charging with 10 V for 10 seconds each time. This was conducted and measured under a pure nitrogen environment. ……...110

5.20 KPFM images of a YSZ surface at 25℃, 100℃, and 200℃ after charging with 10 V for 10 seconds each time. This was conducted and measured under a pure nitrogen environment. ……..110

5.21 KPFM images of STO and YSZ surfaces at 25℃ after charging with 10 V for 10 seconds each time. This was conducted and measured under a pure oxygen environment. ……111

5.22 (a) AFM topography images detailing the before and after of removal work (30 times) on an STO surface; and (b) KPFM images of each slice that was removed layer by layer at 25℃, 100℃, and 200℃ after charging with 10V for 10 seconds on an etched STO bulk surface. This was conducted and measured under a pure nitrogen environment. ……....112

5.23 (a) AFM topography images detailing the before and after of removal work (30 times) on a YSZ surface; and (b) KPFM images of each slice that was removed layer by layer at 25℃, 100℃, and 200℃ after charging with 10V for 10 seconds on an etched YSZ bulk surface. This was conducted and measured under a pure nitrogen environment. …...…..112

5.24: Plot of diffusivity (*D*) vs temperature, with activation energy of (a) STO and (b) YSZ surface and bulk. ……114

5.25: (a) The graph shows diffusivity values of STO and YSZ surface at the temperature of 25 ℃ and in the environment of pure oxygen (in orange) and pure nitrogen (blue) and (b) KPFM images. …..…….....……..114

LIST OF TABLES

2.1 The compositions of three cathode samples.[64] ……..…….……..31

2.2 Fitting parameters for ORR on the LNF-based cathodes.[64] ……..33

2.3 The value of the gas phase diffusion resistance (R_2).[64] ……...……..33

2.4 The ohmic resistance (R_s) of blank LNF cathode sintered at 1000, 1100 and 1200 ℃ for 2 hours in air.[78] …….37

2.5 Ohmic resistance R_s and polarization resistance R_p of SOFC cathode materials.[78] ….38

2.6 The most conventional types of ALD-grown materials [165–171] ……...…...44

2.7 The optimized values of α for various values of λ.[191] …….....61

3.1 Different infiltration solvents with different concentration LNF-based cathodes ……78

3.2 ohmic resistance (R_O), polarization resistances from high frequency (R_H) and low frequency (R_L) arcs, and CPE parameters (Q and α) of bare and infiltrated samples obtained at 700 °C (open circuit condition). The equivalent circuit shown in Figure 3.2 was used to fit the data. The capacitance values (C_H) and C_L) were calculated based upon Q and α. …….80

5.1 The diffusivity values of STO and YSZ's surface and bulk that we calculated at different temperatures of 25 ℃, 100 ℃, and 200 ℃ listed in the table. …….113

ABSTRACT

In this dissertation, there are three topics including nanoscale engineering effects on cathodes for intermediate-temperature solid oxide fuel cells, effects of mechanical and electrical application on atomic force microscopy, and ionic diffusivity and mobility study of oxygen reduction/evolution reaction by nanoscale in situ characterization via atomic force microscopy. Their abstracts are listed below.

Topic I: The impact of various infiltrates on the kinetics and rate-limiting step of oxygen reduction reaction (ORR) is examined with $LaNi_{0.6}Fe_{0.4}O_{3-\delta}$ (LNF) as the cathode backbone of solid oxide fuel cells (SOFC). Multiple materials were infiltrated on the backbone. The dependencies of electrode polarization resistance on the precursor concentration, temperature, and oxygen partial pressure are presented, and related discussions are made to interpret the differences in ORR kinetics and the rate-determining step for ORR.

Topic II: Conductive atomic force microscopy (CAFM) has been widely employed to study the localized electrical properties of a wide range of substrates in non-vacuum conditions by the use of noble metal-coated tips. In this topic, the impact of mechanical and electrical stimuli on the apex geometry of gold-coated tips and electrical conduction properties at the tip-substrate contact is discussed by choosing gold and highly-ordered pyrolytic graphite as the representative tip and substrate materials, respectively.

Topic III: The ionic transport in solid oxides after becoming thermally activated is understood as hopping to point defects (i.e. oxygen vacancies), and the kinetics behind it are highly dependent upon the bonding state of the ionic species with their surrounding lattice environment. In this study we report the findings of our recent efforts to directly observe ionic transport in $SrTiO_3$ (STO) and Y_2O_3-stabilized ZrO_2 (YSZ)–the most widely used cathode material in intermediate temperature SOFC–by use of Kelvin probe force microscopy (KPFM) and conductive atomic force microscopy (CAFM).

Chapter 1

Introduction

Our current economy is based on fossil fuels such as crude oil, coal, natural gas, and heavy oils. The intense use of these energy sources resulted in a significant global warming for the last century, causing threats of resource depletion, natural disasters and diseases. Currently, more than 88% of all energy consumed is via the combustion process of fossil fuel. The process generates billions of tons of harmful pollutants and particulates, such as carbon-dioxide and sulfur and nitrogen oxides, into the atmosphere every year.[1,2] This pollution contaminates the air, water, and soil, and causes disease and illness, killing an estimated half a million people every year.[3] Moreover, the emission of carbon-dioxide and methane into the atmosphere directly contributes to an increases in average global temperature. According to a report on climate change published by the United Nations in 2007,[3] the presence of carbon-dioxide in the atmosphere has increased dramatically since the Industrial Revolution, and the concentration of greenhouse gas is the highest in 500,000 years.[3] The long-term effects of continued emission of carbon-dioxide and other greenhouse gasses such as methane and nitrous oxide into the atmosphere are not completely known. However, there is a good possibility that these emissions could eventually result in a dramatic shift in the global climate.[4] A significant global temperature increase could cause the polar ice caps to melt, leading to a sea level increase by which the hundreds of millions of homes in coastal regions would be submerged. In addition, global temperature increase can manifest itself in the form of extreme weather conditions such as detrimental tornadoes and hurricanes.[3] Furthermore, severe drought would lead to a considerable lack of food.

In response to these current and foreseeable challenges, mankind has sought after clean and sustainable energy sources. Renewable energies such as wind and solar photovoltaic energy have found ways of wide commercial successes due to continued research, development and mass production for the last decade. In many countries, these renewable energies recently achieved cost competitiveness against conventional fossil fuel-based energies. However, due to the intermittency of these renewable energies, a massive scale energy storage medium is indispensable. The pumped hydro energy storage has the highest cumulative energy capacity among all electrical energy storage schemes. However, their total energy capacity worldwide is less than 0.01% of total annual electricity demand. While pumped hydro systems can serve GW-range energy conversion and storage per plant, their expandability is highly limited due to multi-faceted geographical requirements and environmental concerns. Recently, ionic battery-based energy storage has garnered considerable attention thanks to recent advances in their mega-scale commercialization. However, due to the large amount of raw material (such as nickel, cobalt, and lithium) required per unit energy and poor scalability of batteries into the GWh

range, their economical use is mostly limited to rather small-scale applications such as mobile devices, sedan-sized vehicles, and household energy storage.

Hydrogen is capable of overcoming the shortcomings of other energy storage schemes and emerges as the most promising form of energy carrier to form a clean energy ecosystem. Hydrogen can be utilized for both transportation and stationary applications in the form of electricity and heat without any damage to the environment.[1,5] As with conventional fuels, hydrogen can be combusted, and the chemical reaction that takes place during the combustion process emits only water as a byproduct, making hydrogen a "zero-emission fuel". Moreover, the hydrogen fuel cell is a technology that efficiently recombines hydrogen and oxygen and captures the electrical and thermal energy that is produced by this chemical reaction. There is no air pollution when hydrogen is used as fuel, which meets a major requirement as a clean energy medium.

Hydrogen is virtually a renewable resource unlike fossil fuels. Hydrogen is the most common element in the universe and can be extracted from water and methane gas on earth. Hydrogen has been widely used for various industrial processes and ammonia production, already reaching a market size of ~ $120 billion in 2010. While the majority of hydrogen is being produced through a CO_2-emitting steam reforming method, an intense effort is being made to achieve a cost competitiveness for water electrolysis, during which electrical energy is used to split water molecules into hydrogen and oxygen. On the other hand, a fuel cell operates in the reverse order of the water electrolysis process; inside of a fuel cell, hydrogen and oxygen spontaneously recombine to produce an electrical current, a little amount of thermal energy, and H_2O as a by-product. A fuel cell is intrinsically more efficient than internal combustion engines because a fuel cell converts the chemical energy in hydrogen into the electrical energy without other intermediate energy steps. If pure hydrogen is used, a fuel cell can provide clean electricity for both stationary and non-stationary applications, making the round-trip made of an electrolyzer and a fuel cell fully carbon emission-free.

Many organizations across the globe are already working to develop fuel cell technology, such as the Fuel Cell and Hydrogen Energy Association in the US, and the European Hydrogen Association and Fuel Cells and Hydrogen Joint Undertaking in Europe.[6] With further development of hydrogen fuel cells, this technology could initially supplement, and eventually replace the combustion of fossil fuels. While the renewable energy ecosystem aided by hydrogen is highly pursued by many countries, there are major hurdles to overcome. First, the production of clean hydrogen should achieve cost competitiveness. The US government recently announced the "Hydrogen Shot" initiative, aiming to produce green hydrogen at the cost of $1 per 1 kg of hydrogen by 2030. Second, both electrolyzers and fuel cells need to achieve a commercially viable durability that can warrant a stable and economical means of using hydrogen in the energy sector.

This dissertation focuses on advancing the performance and understanding of electrochemical processes at the surface and interface of solid oxide-based components in solid oxide electrolyzer and fuel cells (SOEC/SOFCs), an electrochemical energy conversion cell operating at a high temperature of 500 – 1000 ℃.

Chapter 2 discusses the fundamentals of SOFC (the operational principles and electrode materials), fabrication processes (atomic layer deposition, solution impregnation), macro-scale and nanoscale electrochemical characterization methods

(impedance spectroscopy, atomic force microscopy variants), and physical characterization methods (electron microscopy).

Chapter 3 presents a study on how a nanoscale surface engineering by infiltration method affects the electrochemical performance of an electrode of negligible ionic conductivity for intermediate-temperature SOFCs .

Chapter 4 discusses how a combined mechanical and electrical stimuli affect charge transport behavior at a nanoscale interface in a scanning probe microscopy setup, as a baseline study for the subsequent chapters.

Chapter 5 presents spatially resolved observations of oxygen exchange and ionic transport in the vicinity of solid oxide surface, which is directly relevant to the electrochemical performance of air electrodes, with a significantly customized scanning probe setup at different temperatures and gas environments.

Chapter 6 presents an overall summary of research work and future work.

Chapter 2

Background

2.1 SOFC overview

SOFC has been refocused attention for being a potential source of fuel-versatile electric power. It offers many potential advantages over polymer electrolyte membrane fuel cells (PEMFCs) under the high operating temperature, including high tolerance to typical catalyst poisons, reversible electrode reactions, low internal resistance, production of high-quality waste heat for reformation of hydrocarbon fuels, and the possibility of burning hydrocarbon fuel directly.[8]

2.1.1 Operation

SOFCs are highly efficient energy conversion devices which convert potential energy stored in chemical fuels directly into electrical power, which can subsequently be used for work. Unlike conventional combustion engines, which derive mechanical energy from heat generated in the combustion of chemical fuels, SOFCs derive electrical energy directly from chemical fuels, allowing them to be much more efficient and environmentally friendly than combustion engines.

An SOFC consists of three major components: anode, cathode, and electrolyte (shown in Figure 2.1). These components are connected in series, with the solid ceramic electrolyte sandwiched between the two electrodes. The electrodes are connected using a wire or current collector. Air enters the porous cathode, where oxygen molecules from the air are adsorbed onto the surface of the catalytic cathode material. The O_2 molecules are further dissociated into oxygen atoms, and the oxygen atoms are reduced to an O_2 state by electrons from the current collector attached to the anode.

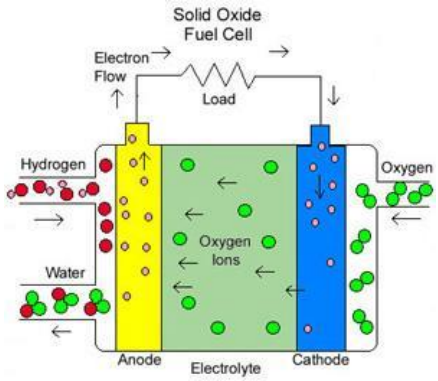

Figure 2.1: A schematic drawing of a SOFC.[9]

The cathode reaction is shown as:

$$\frac{1}{2}O_2 + 2e^- \rightarrow O^{-2} \qquad \text{(Equation 2.1)}$$

The oxygen ions diffuse through the solid ceramic electrolyte, which becomes a conductor for oxygen ions at high temperatures. Chemical fuel enters at the anode side (for this discussion, hydrogen gas will be assumed as the chemical fuel), and is catalyzed by the anode. Molecular hydrogen is adsorbed onto the surface of the catalyst, transports to the anode-electrolyte interface, where it combines with O_2 ions to form H_2O and heat, given by the reaction shown as:

$$H_2 + O^{-2} \rightarrow H_2O + 2e^- \qquad \text{(Equation 2.2)}$$

Combining the two half reactions gives the complete reaction for an SOFC as shown:

$$H_2 + \frac{1}{2}O_2 \rightarrow H_2O \qquad \text{(Equation 2.3)}$$

The difference in chemical potential between the hydrogen and oxygen ions drives the SOFC reaction, and the resulting flow of electrons from anode to cathode can be exploited to do work. The current collector connecting anode to cathode acts as an external circuit, and a load can be attached to the circuit to power an electronic device. In addition to generating free electrons and H_2O, heat is a byproduct of the reaction and is also generated in the SOFC by ohmic losses and electrode overpotentials. In other words, the movement of electrons and ions generates additional heat in the SOFC.[10] Therefore, a good thermal management system is necessary to achieve maximum efficiency in an SOFC, such as using recycled heat to maintain the high operating temperature that is needed. Alternatively, the exhaust heat can be used to power a turbine, provide heat for residential or automotive applications, produce hot water, or any number of applications. A proper thermal management system can increase SOFC efficiency by up to 40%, allowing for efficiencies as high as 85-90%.[11]

2.1.2 SOFC components

2.1.2-1 Electrolyte

SOFCs utilize a solid ceramic oxide-ion conductor as an electrolyte, which is sandwiched between the two electrodes. The primary purpose of the electrolyte is to transport O_2 ions from cathode to anode as well as provide mechanical support for the cell. A material must meet several requirements to be used as an effective SOFC electrolyte. Firstly, the material must exhibit high ionic conductivity, but negligible electronic conductivity. SOFC performance is generally limited by the ohmic resistance corresponding with the flow of ions through the electrolyte.[11] Therefore, a suitable electrolyte material should be as ionically conductive as possible, and it should exhibit sufficient stability to retain its conductivity after prolonged use. Additionally, any electrons shorting through the electrolyte will cause a voltage loss in the cell; therefore, a good SOFC

electrolyte is as electronically insulative as possible. Layer thickness is also an important factor for SOFC electrolytes as the resistance, and therefore ionic flow, is sensitive to electrolyte thickness. The resistance of the electrolyte material is given by:

$$R = \frac{\underline{t}}{\sigma_i A} \qquad \text{(Equation 2.4)}$$

Where $\underline{t}$ is the electrolyte thickness, σ_i is the ionic conductivity, and A is the cross-sectional area. This equation shows that the ohmic resistance of the electrolyte scales linearly with layer thickness; therefore, a thin electrolyte layer minimizing resistance is essential for optimal performance. However, an SOFC electrolyte that is too thin will allow electrons to short through the electrolyte. Thus, studies have shown that an optimal electrolyte thickness of around 15 μm will minimize ohmic resistance while preventing voltage losses due to electron shorting.[12] In addition to optimal layer thickness, an SOFC electrolyte should be as dense as possible; as a porous electrolyte results in the fuel mixing with the oxidant, which drastically decreases the voltage capacity of the cell.

Chemical and mechanical stability is another requirement for SOFC electrolyte materials. The electrolyte must be able to withstand the high-temperature reducing environment of the anode, as well as the high-temperature oxidation environment of the cathode, without experiencing any physical or chemical instability. The electrolyte should also be chemically inert, so that reactions between the electrolyte and electrodes do not occur. Reactions occurring between the electrolyte and either electrode could lead to a highly resistive phase forming, which dramatically hinders cell performance.[13] Additionally, the electrolyte will experience mechanical stress due to a mismatch in thermal expansion between electrolyte and electrodes. Therefore, electrolyte materials must have sufficient mechanical strength to withstand this stress, particularly for electrolyte-supported cells (cells which rely on a relatively thick electrolyte layer for mechanical stability). Finally, material and fabrication cost is an important barrier to mass commercialization of SOFC technology. Therefore, SOFC electrolytes should be relatively inexpensive to manufacture.

Yttrium-stabilized zirconia (YSZ) is the most widely used SOFC electrolyte material,[10] and is the primary electrolyte used for this study. YSZ is fabricated by doping a zirconia host (ZrO_2) with yttria molecules (Y_2O_3), resulting in a fluorite crystal structure. During the doping process, yttrium cations (Y^{+3}) diffuse into the zirconia host material and replace zirconium cations (Zr^{+4}) in the crystal lattice. Because of the charge difference between the cations, one oxygen vacancy (O^{-2}) is created each time two yttrium cations replace two zirconium cations in the lattice, so that charge balance is maintained. In Figure 2.2: Figure 2.2(a) shows the un-doped zirconia host, while Figure 2.2(b) shows an empty O^{-2} site created by replacing two Zr^{+4} cations with two Y^{+3} cations. These oxygen vacancies are what give YSZ its ionic conductivity; as oxygen ions created at the cathode hop from one empty O^{-2} site to the next, until they reach the anode. Increasing the amount of yttria doping increases the number of empty O^{-2} sites in the lattice, therefore increasing the ionic conductivity. However, there exists an upper limit to doping concentration, beyond which O^{2-} sites begin to interact with one another, and ionic conductivity decreases. Studies have shown that a doping concentration of 8 mol% Y_2O_3 is optimal for the ionic conductivity of YSZ, as shown in Figure 2.3(a).[11]

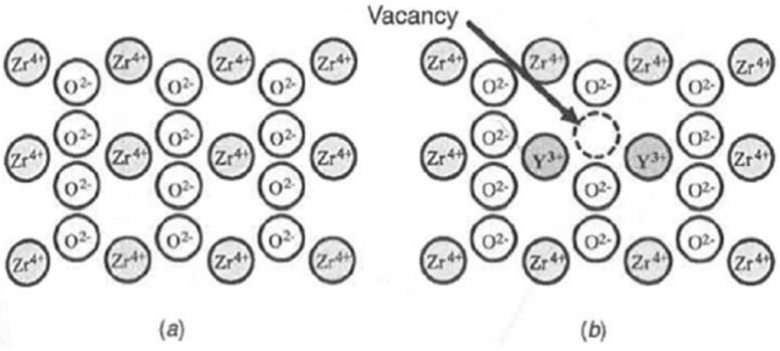

Figure 2.2: Oxygen vacancies created by doping zirconia with yttria: (a) the un-doped zirconia host and (b) an empty O^{-2} site created by replacing two Zr^{+4} cations with two Y^{+3} cations.[11]

Although YSZ is the primary electrolyte material used in this study, gadolinium-doped ceria (GDC) also plays an important role, and will be briefly introduced here. At temperatures above about 800°C, YSZ reacts with $LaNi_{0.6}Fe_{0.4}O_{3-\delta}$(LNF), which is the primary cathode material used in this study, to form an ionically insulating phase which dramatically impedes cell performance. A thickness of 5μm of GDC layer can be placed between the YSZ electrolyte and LNF cathode to prevent insulating phase formation from occurring during electrode sintering.[14] Like YSZ, GDC exhibits a fluorite crystal structure, and shares the same ion-hopping mechanism to facilitate ionic conductivity in the electrolyte. However, because the gadolinium dopant ions are similar in size to the host cerium ions, ceria can be doped with a higher concentration of dopant of up to 10-20% compared to the 8 mol% for YSZ. Therefore, GDC generally shows a higher ionic conductivity than YSZ, as seen in Figure 2.3(b), which shows the ionic conductivity as a function of temperature for these materials. However, GDC has several disadvantages compared to YSZ, which is why YSZ is the primary electrolyte used in this study. Firstly, GDC exhibits significant electronic conductivity in the high-temperature reducing environment of the anode, which leads to a dramatic decrease in available open circuit operating voltage (and thus a decreased overall power density). Sm (Samarium) and Gd (Gadolinium) are typical dopants for ceria that can be used as an SOFC electrolyte or as the interlayer between a cathode and an electrolyte or a composite active layer on the cathode or anode side. Although Sm- or Gd-doped ceria exhibits electrical conductivity in an anode atmosphere where the oxygen partial pressure (P_{O_2}) is around $10 - 18$atm, they are poor electrical conductors in the cathode atmosphere.[15,16,17] Additionally, GDC shows significant chemical expansion when exposed to a reducing environment, causing mechanical failure in the electrolyte.[11] Therefore, while YSZ is the primary electrolyte material used in this study, a thin layer of GDC is inserted to separate the YSZ electrolyte from the cathode to prevent ionically insulating phases from forming between the YSZ electrolyte and the cathode.

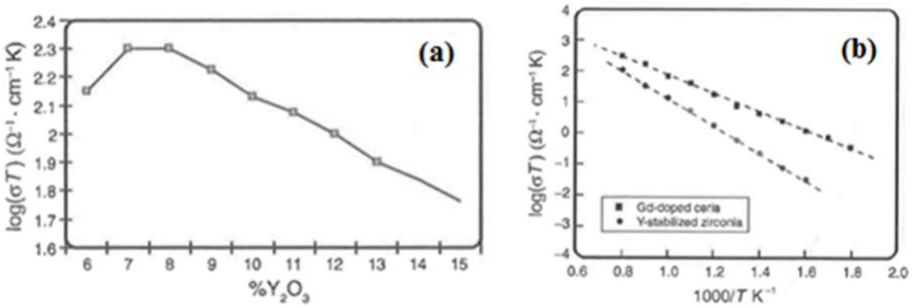

Figure 2.3: (a) Ionic conductivity vs yttria doping concentration for YSZ; (b) ionic conductivity vs temperature for YSZ and GDC.[11]

2.1.2-2 Cathode

The SOFC cathode has two main functions. It is responsible for reducing oxygen into O_2 ions and transporting these ions to the electrolyte. Secondly, it transports electrons from the external circuit to the triple phase boundary site where the oxygen reduction reaction occurs. Therefore, a suitable SOFC cathode will exhibit excellent catalytic activity and high electronic conductivity. In addition, the cathode material should exhibit reasonable ionic conductivity, so that the electrode reaction sites, or triple phase boundary (TPB) area, is maximized. The TPB (Figure 2.4) is the area at which the three important SOFC elements coincide: gas as an oxygen source, the electronic conductor, and the ionic conductor (or electrolyte). These are the sites at which essentially all electrode reactions occur; thus, maximizing this area is crucial to optimizing SOFC performance.

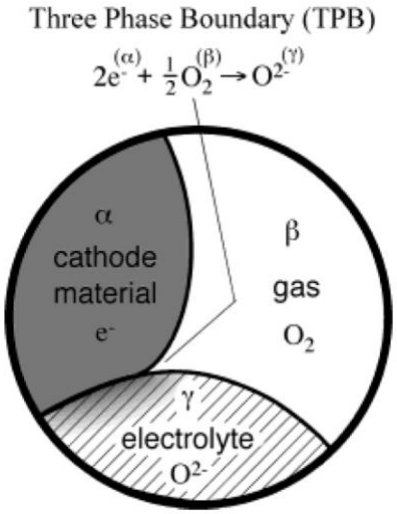

Figure 2.4: Phenomenological roles of the electronically conducting (electronic) phase (α), gas phase (β), and ionically conducting (ionic) phase (γ) in accomplishing oxygen reduction.[18]

Transition-metal oxides were originally investigated as SOFC cathodes due to their good electrical conductivity (most oxides are insulators) and as a relatively low-cost alternative to Pt, which prior to about 1965 was the only SOFC cathode material being considered extensively. One of the first such materials studied was $La_{1-x}Sr_xCoO_{3-\delta}$ (LSC), reported by Button and Archer in 1966.[19] This was followed quickly thereafter by a number of other materials having perovskite crystal structure, including $La_{1-x}Sr_xMnO_{3-\delta}$ (LSM), which as of ~1973 became the favored material for SOFC cathodes. Figure 2.5 illustrates the general perovskite crystal structure $ABO_{3-\delta}$ as it relates to the electronic and ionic transport properties of some transition-metal oxides. In this case, the B-site cation is a reducible transition metal such as Co or Fe (or mixture thereof) and the A-site cation is a mixture of rare and alkaline earth such as La and Sr. The octahedral symmetry around the transition metal often promotes a metallic or semiconducting band structure at high temperature, leading to high electronic conduction. This structure is also quite stable relative to other crystalline phases, and thus with a judicious choice of A and B-site cations, it can stably support a large number of oxygen ion vacancies(δ) at SOFC operating conditions, thus facilitating significant bulk ionic oxygen transport. Later years, LSM was found that it is not suitable for IT (intermediate temperature) -SOFC due to its low activity below 800 ℃ and the Cr-poisoning problem. One strategy for trying to improve performance has been to replace LSM with a single-phase mixed conductor (material which conducts both oxygen ions and electrons), such as $La_{1-x}Sr_xCo_{1-y}Fe_yO_{3-\delta}$ (LSCF).[20,21,22]

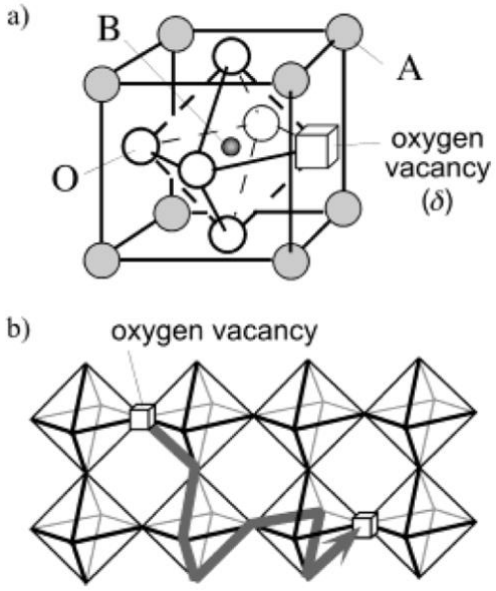

Figure 2.5: Atomic structure and oxygen transport in mixed conducting perovskites $ABO_{3-\delta}$. (a) Basic structural element, consisting of a corner-sharing BO_6 octahedron surrounded by charge-compensating A-site cations. (b) Bulk oxygen transport mechanism, involving random hopping of oxygen ion vacancies on the oxygen sub-lattice.[18]

For a standard cathode with negligible ionic conductivity, the TPB area is confined to the interface between the cathode and electrolyte, as shown in Figure 2.6(a). However, choosing a cathode material with a high ionic conductivity will extend the TPB area dramatically, allowing cathode reactions to occur at virtually any location on the cathode surface. This is illustrated in Figure 2.6(b), where the oxygen is reduced at any point on the surface of the cathode and the oxygen ions can then travel through the cathode to the electrolyte. Furthermore, fabricating a composite cathode using a mixture of electrolytic and cathodic materials can also dramatically increase performance by further increasing ionic conductivity.

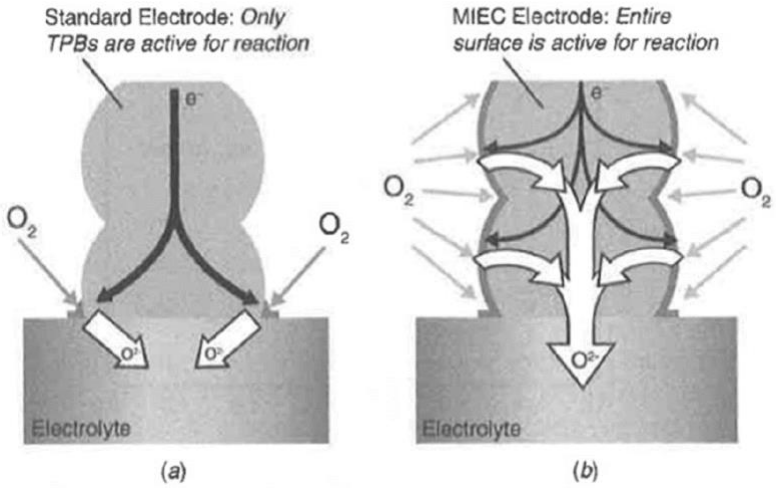

Figure 2.6: Schematic diagram showing triple phase boundary area for (a) a standard electrode; and (b) a mixed ionic-conducting electrode.[11]

In contrast to the electrolyte, the cathode should be sufficiently porous to allow oxygen gas to permeate the electrode, maximizing reaction sites. In addition, the cathode material needs to have sufficient mechanical and chemical stability to withstand the high temperature oxidation environment of the cathode. The thermal expansion of the cathode must match relatively well with the electrolyte to prevent electrode delamination, and the material should have the mechanical stability to withstand repeated heating/cooling cycles. The cathode should also be chemically compatible (nonreactive) with the electrolyte material and the interconnecting materials, and as with the electrolyte, should be relatively inexpensive to fabricate.

2.1.2-3 Anode

The focus of this study is primarily cathode optimization, with some focus on electrolytic materials as well. However, the final component of SOFCs is the anode, a detailed investigation of which is outside the context of this study. Many of the requirements of the SOFC anode are similar to those of the cathode. The anode material must exhibit high catalytic activity for the hydrogen oxidation reaction, should have excellent electronic conductivity for electron transport from TPB sites to the external

circuit, and should show at least marginal ionic conductivity to maximize the TPB site density. The anode material should have sufficient chemical and mechanical stability to withstand the high temperature oxidation environment of the anode and the repeated reduction/oxidation (redox) cycles required for regular operation. The material should be chemically compatible with other SOFC components such as the electrolyte and the circuit interconnect materials, and should have a thermal expansion coefficient that matches relatively well with other SOFC components. The anode should be sufficiently porous (> 30 vol%) to allow permeability of gaseous fuel, and should be sufficiently stable to maintain performance after extended operation (> 90,000 hours).[12]

The most extensively used SOFC anode material is a Ni-YSZ composite cermet material (material that is comprised of both a ceramic and a metal component). In Ni-YSZ anodes, nickel provides the high catalytic activity and electronic conductivity, and the YSZ provides the ionic conductivity, structural support, aids in the matching of thermal expansion between the anode and electrolyte, and suppresses agglomeration of nickel particles during operation (a common problem for pure Ni anodes). Ni-YSZ anodes are extremely stable in high temperature oxidation environments, and they essentially satisfy all of the requirements for an SOFC anode. As with the cathode, a multi-layer approach is often used to improve performance and maximize thermal expansion compatibility.[11]

2.2 Fabrication approaches for nanoscale

2.2.1 Solid Oxide Fuel Cells

The basics of SOFCs are provided in Section 2.1 . In this chapter, we will extend the discussion on SOFCs by reviewing previous publications. The structures and materials of SOFCs will be mentioned roughly, including electrolyte, cathode and anode sides. SOFCs are much closer to commercial real life than they were 30 years ago, due to technological advances in electrode material composition, microstructure control, thin-film ceramic fabrication, and stack and system design. These improvements have led to plenty of active SOFC development programs in both stationary and mobile power, and contributed to commercialization or development in a lot of related technologies. For examples, gas sensors,[23] solid-state electrolysis devices,[24] and ion-transport membranes for gas separation and partial oxidation.[25] There are a lot of reviews available which summarize the technological advances made in SOFCs over the last 25 – 45 year readers who are primarily interested in knowing the state-of-the art in materials, design, and fabrication (including the electrolytes and electrodes) are encouraged to consult these reviews.[19,26–34]

For the purposes of review, Figure 2.7 illustrates the basic function of SOFCs. Whether acting alone or as part of a stack of cells, each cell consisted of a free-standing or supported membrane of an oxygen-ion-conducting electrolyte, often yttria-stabilized zirconia (YSZ). It is what we used in this study as well. Usual as the air, oxygen, which is fed to one side of the membrane, is reduced by the cathode to oxygen ions via the overall half-cell reaction like Equation 2.1.

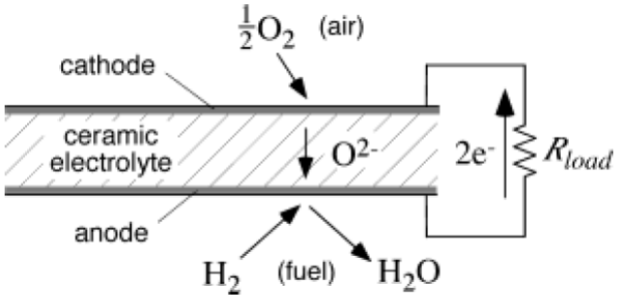

Figure 2.7: Schematic showing the roles of anode, cathode, and electrolyte in a SOFC.[18]

Oxygen ions thus migrate selectively through the membrane to the anode, where they undergo a similar half-cell reaction with a gaseous fuel either H_2, syngas, or a hydrocarbon to produce H_2O and CO_2. The flow of electrons is liberated and consumed at the anode and cathode sides, respectively, delivering some portion of the reversible work of the reaction to the external circuit. The percentage of reversible work converted to electrical work depends on the internal losses in the cell, including the ohmic resistance of the electrolyte, and the overpotential losses at the anode and cathode. While ohmic losses in oxide electrolytes are mostly understood today, the physics governing the electrode overpotential losses at the anode and cathode remain a gigantic focus of research, with significant progress being made only in the last 25-30 years. This change in emphasis from the electrolyte to the anode and cathode (electrodes) has been driven by an ability to make progressively thinner, less resistive, electrolyte films and also a drive toward lower operating temperatures where the electrodes are a higher percentage of the voltage loss due to higher activation energy. There is a lot of this work that has focused on the cathodes, most likely because oxygen reduction is generally thought to be the more difficult reaction to activate on SOFCs operating at commercially relevant temperatures. People have tried to not only understand electrode mechanisms, but also explore new electrode materials and micro-structures, explain structure-property-performance relationships, and comprehend how and why electrode performance changes with time, temperature, thermal cycling, operating conditions, impurities, or other factors that may be pertinent in the design of multi-cell stacks and systems.[18]

SOFCs generally consist of three layers: a porous cathode material, an ion conducting electrolyte, and an anode material. We are going to talk about the electrolyte part first. YSZ, scandia-stabilized zirconia (ScSZ) and SDC are the most common materials of electrolyte in recent years.[35] A sufficient quantity would migrate through the porous structure of the cathode and reach the cathode/electrolyte interface. The normal process at the cathode/electrolyte interface is the O_2 reduction reaction (ORR). In most cases, the materials for electrolyte usually have high ionic conductivities. the ionic conductivity of GDC is of the order of magnitude of 5×10^{-2} S cm^{-1} at SOFC operating temperatures (600-800 ℃).[36,37,38] This is higher than the typical corresponding ionic conductivity of YSZ.[39] The difference is more pronounced at lower temperatures. For example, at 700 ℃ the conductivity of GDC is 5.8×10^{-3} S cm^{-1} as compared to 1.4×10^{-4} S cm^{-1} for YSZ. We discussed YSZ more in Section 2.1.2-1 already, the reason we chose YSZ as our main

electrolyte is its low electronic conductivity. Although GDC has higher ionic conductivity than YSZ, its electronic conductivity is relatively high as a electrolyte material, which makes other particles go through the electrolyte not only ions.[40] We do choose GDC as our interlayer to prevent growing insulating layer like ZrO_2, also by its high ionic conductivity to help the electrolyte have better performance.

We will go into more detail on the cathode part in the next paragraph. The anode material must exhibit high catalytic activity for the hydrogen oxidation reaction, it should have excellent electronic conductivity for electron transport from TPB sites to the external circuit, and should show at least insignificant ionic conductivity to maximize the density of TPB. The anode material should have sufficient chemical and mechanical stability to endure the high temperature oxidation environment of the anode and the repeated reduction/oxidation (redox) cycles required for regular operation. We do not spend too much time on the anode sides because this study mainly focuses on the cathode sides. Eventually it has to be a full fuel cell, so it is necessary to know well about anode sides. YSZ and Pt are pretty common materials for the anode of SOFC. YSZ is coated by atomic layer deposition (ALD) and Pt is by sputtering, the thickness usually is about 500 nm and 200 nm, respectively.[41,42]

2.2.1-1 SOFC Cathodes

In recent years, potential cathode candidates have normally been based on mixed oxygen ionic and electronic conducting oxides (MIEC material), which have both high ionic and electronic conductivity, and have attracted a lot of attention in terms of their applications for fuel cell electrodes, oxygen separator membranes and membrane reactors for the partial oxidation of methane to syngas.[43,44,45] The mixed conductivity extends the active oxygen reduction sites from the typical electrolyte-electrode-gas triple phase boundary to the entire cathode surface, therefore greatly reducing the cathode polarization at low operating temperatures.[46]

Lately, $La(Ni,Fe)O_3$ perovskite (lattice structure $ABO_{3-\delta}$) material has been developed as one of the most favorable cathode materials in IT-SOFC operated at 600-800 ℃. Of particular interest is $LaNi_{0.6}Fe_{0.4}O_3$ (LNF) which exhibits high electronic conductivity, a thermal expansion coefficient close to that of the zirconia electrolyte, high electrochemical activity for the oxygen reduction reaction, resistance to cathode poisoning by chromia vapor from the metal separators,[47–60] and has been shown to outperform conventional cathode materials such as lanthanum strontium manganite or LSM. Kharton *et al.*[61] showed that the oxygen permeation through $LaNi_{1-x}Fe_xO_{3-\delta}$ ($x = 0.0 – 1.0$) membranes tended to increase with nickel content due to an increase of oxygen vacancy concentration and bulk ionic conductivity. The polarization resistance of the LNF cathode increased with time without a significant change in the ohmic resistance. According to Ref.,[51] the increase of polarization resistance with time could be explained by re-oxidation of sintered LNF material and consequent decrease of oxygen vacancy concentration. It is noted that the LNF cathodes tend to lose oxygen on heating, turning out oxygen vacancy formation.[52] LNF is a mixed ionic-electronic conductor (MIEC); in other words, in addition to being electronically conductive at intermediate temperatures, it also displays reasonably high ionic conductivity of 1.6×10^{-6} S cm^{-1} at 700 °C,[53] whereas LSM shows ionic

conductivity of 10^{-7} S cm^{-1} at 900 ℃.[54] Thus, LNF has a higher TPB area (more reaction sites) compared with LSM. LSM has a similar electronic conductivity as LNF(200 – 300 S cm^{-1} at 900 °C) but has much lower ionic conductivity, reportedly 4×10^{-8} S cm^{-1} at 800 ℃. $LaNi_{1-x}Fe_xO_{3-\delta}$ (x = 0.0 – 1.0) perovskites have received considerable interest for industrial applications such as cathodes for SOFCs[52,55,56] and catalyst for hydrogen production from biomass gasification,[57] steam reforming,[58] and partial oxidation of methane (POM).[59] Chiba *et al.*[55] was the first group to investigate LNF (x = 0.0 – 1.0) and $LaNi_{1-x}M_xO_{3-\delta}$ (M = Al, Cr, Mn, Fe, Co, and Ga) as cathode materials for IT-SOFC. $LaNi_{0.6}Fe_{0.4}O_{3-\delta}$ (LNF64) exhibits the greatest electronic conductivity over three times greater than the conventional cathode material of $La_{0.8}Sr_{0.2}MnO_3$. Moreover, the thermal expansion coefficient (TEC) of this composition is close to that of the doped zirconia electrolyte.[55]

However, the electrochemical catalytic performance of LNF cathode operated below 800°C was not adventageous.[60,62] In order to improve the cell performance, LNF-SDC ($Sm_{1-x}Ce_xO_{3-\delta}$) composite electrode was fabricated by Bevilacqua *et. al.*[63] and the ASR values for LNF-SDC were remarkably smaller with respect to pure LNF. Micro-structure optimization of LNF thus has also been intensively performed and the functionally gradient LNF cathode disclosed much better electrochemical performance compared to that of mechanically mixed composite cathode,[64] or by infiltration. Active layer of Pr_6O_{11} or Pr-doped CeO_2 was utilized in LNF cathodes and the interfacial resistance was reduced to 1/30 that of LNF-GDC ($Gd_{1-x}Ce_xO_{3-\delta}$) composite cathode at 800 ℃.[65] SDC and GDC are widely officially approved as excellent oxygen ionic conductors with high concentration of oxygen vacancy. Sm (samarium) and Gd (gadolinium) are typical dopants for ceria that can be utilized as an SOFC electrolyte or as the interlayer between a cathode and an electrolyte or a composite active layer on the cathode or anode side.[66] Although Sm- or Gd-doped ceria manifests good electrical conductivity in an anode side, where the oxygen partial pressure (P_{O_2}) is around $10 - 18$ atm. They behave poorly as electrical conductors in the cathode side.[62]

The combination methods of LNF64 perovskite have been investigated and reported by several research groups.[67,52,56,68] Diverse combination methods of LNF (x = 0.0 – 1.0) have been investigated in both conventional solid state techniques[55,69,70] and wet chemical procedure by way of citrate using ethanol,[52] nitric acid,[70] or water [68,71] as a solvent. From the foregoing works, the altered citrate procedure for the combination of $LaFeO_3$-based perovskites, which involves the compound formation of metal ions with citric acid and NH_3 and the unselfconscious combustion have been used in these works. The benefit of the altered citrate procedure over the indigenous citrate procedure is an accomplishment of high quality, homogeneous, and single phase powder.[72,73] Almost identical to the manner, Bontempi *et al.*[74] combined LNF37 by an altered citrate way using metal acetates rather than metal nitrates as beginning materials and decomposing the organic substances in mild condition at 400 ℃. Basu *et al.*[75] synthesized LNF64 by citrate and urea methods, the metal nitrates were dissolved and mixed with citric acid or urea, respectively. They found that the powder synthesized by citrate method has smaller particle size than from the urea method averagely. Quite the contrary, the electronic conductivity of membrane prepared by urea method is greater.[68] Among three different approaches; citrate method using ethanol as a solvent, glycine-nitrate method, and co-precipitate

method have been investigated by Bevilacqua *et al.*[52] The citrate and co-precipitate methods conduct to homogeneous powder while the powder prepared by the co-precipitate method was sintered easily. Nevertheless, the amount of base tetramethylammonium hydroxide used has to be four times the stoichiometry value to insure full precipitation for this co-precipitation method.

Sukpirom *et al.*[76] combined LNF64 by the citrate route using different methods. They used four different solvents to prepare samples; nitric acid as a solvent (NC), water as a solvent (WC), and two modified methods for both (MNC and MWC). The NC procedure was using stoichiometric amounts of La^{+3}, Ni^{+2}, and Fe^{+2} nitrates that were dissolved in nitric acid with the volume of 10 ml. Then citric acid was added to a citric : cationic mole ratio of 2:1. The citrate solution was stirred at room temperature for 3 hours, and evaporated on a hot plate at 200 ℃ until the mixture auto-ignites. A mortar and pestle were used to ground the solid, and followed by calcination at 700 – 1200 ℃ for 5 hours. The WC procedure was carried out following the NC method but using water as a solvent rather than nitric acid. The MNC procedure was carried out homogeneously to the NC method. Before the step of evaporation, NH_3 was added until the pH of the solution was 9 as reported in previous works.[72,73] The homogeneous solution was stirred for 3–5 hours before it evaporated. The MWC procedure was carried out following the MNC method but using water as a solvent rather than nitric acid. Figure 2.8 shows that their samples have been investigated by X-ray diffraction (XRD); all LNF64 powders synthesized from every method contain a single phase of rhombohedral structure similar to $LaNiO_3$[77] after calcination at 1000 ℃ for 5 hours. Although they have the same structure, the morphology is different for each synthesis method. From Figure 2.9, SEM micrographs show that all of the powders besides the one from the WC method show a uniform shape with a narrow size distribution. Additionally, the powders synthesized by both modified citrate methods have smaller particle size than that of the unmodified ones. Estimates from SEM micrographs were obtained from the powder prepared by MNC, WMC, and NC, the mean particle sizes of ~ 0.2, ~ 0.3, and ~ 0.4 μm, respectively.,

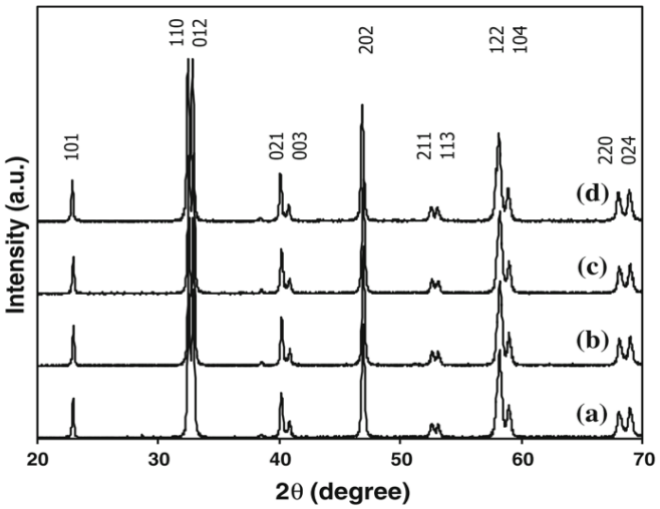

Figure 2.8: XRD patterns of LNF64 ($T_{calcination}$ = 1000 ℃ for 5 hours) synthesized by four methods: (a) WC, (b) MWC, (c) NC, and (d) MNC.[76]

To examine the effect of the synthesis methods on the internal resistance of the cells, Figure 2.10 shows the comparison of the Nyquist plots of LNF64 prepared by four methods at 700 ℃. The size of the semi-circle corresponds to the specific interfacial resistance between the cathode and electrolyte (we will discuss this more in Section 2.3.1), indicating its bigger values of LNF64 prepared by unmodified citrate methods than those prepared from modified citrate methods. The modified citrate methods provide smaller particle size powder which cause better particle packing and a higher degree of sintering. This may cause greater/more area of the triple phase boundary which is one reason for smaller resistances. The deliberation should include more studies and work to avoid technical dissension with at least two other aspects, for instance the triple phase boundary length and packing patterns.

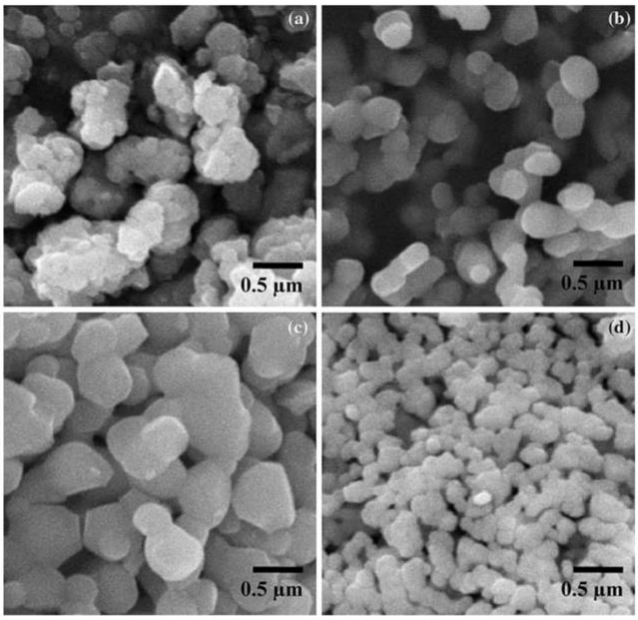

Figure 2.9: SEM micrographs of LNF64 ($T_{calcination}$ = 1000 ℃ for 5 hours) synthesized by four methods: (a) WC, (b) MWC, (c) NC, and (d) MNC.[76]

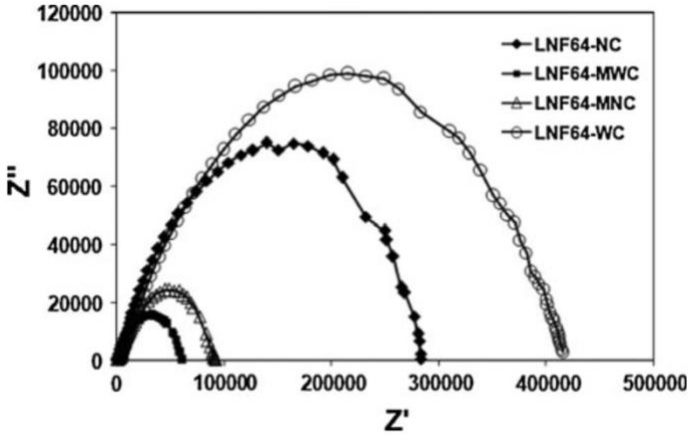

Figure 2.10: Nyquist plots of LNF64 cathodes prepared using four methods at 700 ℃.[76]

2.2.1-2 SOFC Anodes

The reaction of the anode side of SOFC is Equation 2.2. Hydrogen molecules obtain oxygen ions and release electrons and byproduct water. We are not going to discuss the anode sides too much in this Section because most of our anode sides are made by ALD. Materials include YDC and YSZ. In Section 2.2.3, there is more discussion about ALD and its applications.

2.2.2 Infiltration

2.2.2-1 Overview

The performance of SOFCs is often limited by the stagnant oxygen reduction reaction (ORR) process at the cathode side. It is also broadly believed that the surface exchange kinetics and surface area of cathodes play an important role in determining the overall cathodic performance. For this reason, various efforts have been made to improve these metrics through nanoscale materials engineering, most notably by the solvent infiltration method. Infiltration is the way that we use nitrate salt solutions, usually materials of MIEC (mixed ionic and electronic conductor), which have good ionic conductivity and electronic conductivity, syringe these solutions on porous cathode backbones. Then the samples were placed in the furnace for a few hours to grow nano-scale particles on or merge in the cathode backbones. Figure 2.11 demonstrates that matrix material (nitrate solution) is infiltrated into fibrous preforms (cathode backbones) by the use of reactive gasses at elevated temperature to form fiber-reinforced composites. There are two main reasons why we chose this method. First, Boosting the oxygen reduction reaction mechanism by catalytic functionalization. Enlarging the length of three phase boundary (TPB) and it might grain on or diffuse into backbones. Second, it potentially helps improve the stability and durability of backbone in cathodes of SOFCs (Figure 2.12).[8,78–80]

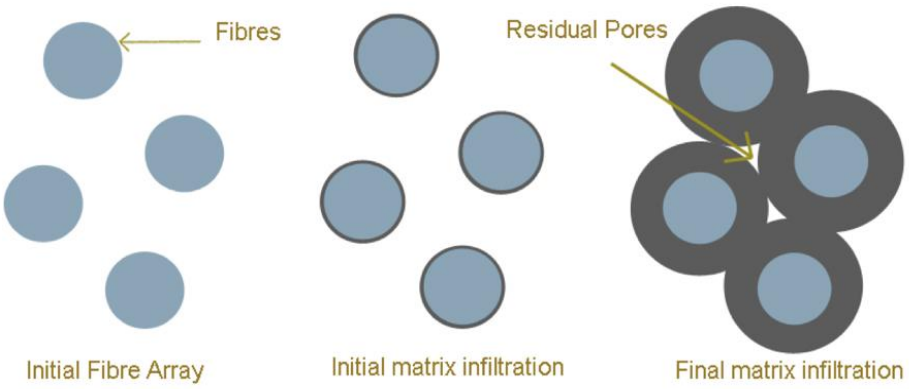

Figure 2.11: Infiltration growth mechanism.

This method, however, poses an intrinsic disadvantage of poor durability during high temperature operations. This is because the resulting perovskite infiltrates after a sintering process are known to be of true nanometer-scale (1–5 nm in diameter); they are very susceptible to thermal agglomeration. An atomic layer deposition (ALD) treatment on these infiltrates is hypothesized to be effective in suppressing the thermal degradation.

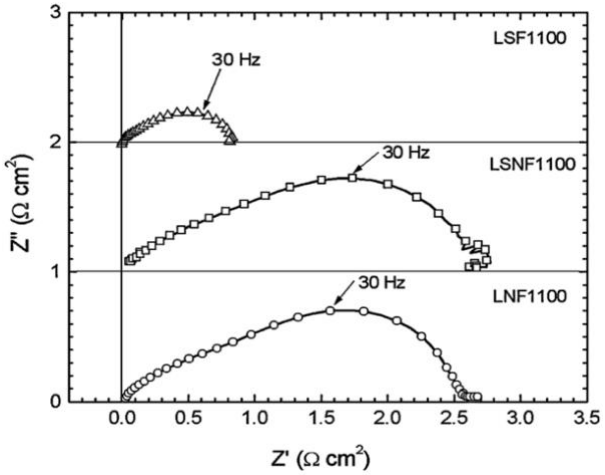

Figure 2.12: Cole-Cole plots for the cells with LNF-YSZ, LSNF-YSZ, and LSF-YSZ cathodes calcined to 1100 ℃. The measurements were performed at open circuit holding the cathodes in air at 700 ℃.[67]

2.2.2-1 Materials

Many materials have been used to infiltrate SOFC cathode backbones for the two main purposes previously mentioned: boosting the oxygen reduction reaction mechanism by catalytic functionalization (enlarge the length of three phase boundary (TPB) and it might grain on or diffused into backbones) and improving the stability and durability of backbone in cathodes of SOFCs. Most of these materials are MIEC (mixed ionic and electronic conductor) and they also are widely used for SOFC cathode backbones. In this chapter, I will mention a few publications about infiltration or composite for SOFC cathodes and then classify all information as a comparison table.

LSCo/LSF/LBF/LCF/LSCF/LSM infiltrated on YSZ

"High-Performance SOFC Cathodes Prepared by Infiltration" by John M. Vohs and Raymond J Gorte focuses[8] more closely on a relatively new method for cathode development, the fabrication of cathodes by infiltration. Back to 2009, this method had been acquiring more and more attention in the past few years. Still, the number of references in a recent review of the sphere was still a little small.[81] Preparatory work in their laboratory used this method to prepare Ni-free anodes in SOFCs that were able to oxidize hydrocarbon fuels without catalyzing the configuration of carbon fibers.[82–85] Nonetheless, infiltration method can also be used to prepare or alter high-performance

cathodes.

While LSM has good electronic conductivity of 200 S cm^{-1} at 800 ℃ and atmospheric conditions (oxygen supplied), its ionic conductivity has been revealed to be less than 4×10^{-8} S cm^{-1}.[15] On the other hand, YSZ has an ionic conductivity of 0.043 S cm^{-1} and insignificant electronic conductivity at 800 ℃.[86] Matching of ionic and electronic conductivities where LSM and YSZ come together implies that the electrode reaction can take place only at the three-phase boundary (TPB) line, the line of connection for the LSM, the YSZ, and the gas phase.[87] This is shown graphically in Figure 2.13(a). As anticipated, measurements have shown that electrode performance scales linearly with TPB length in LSM-YSZ electrodes.[88] Theoretically, the TPB line can have a finite width when one of the electrode elements has mixed electronic and ionic conductivity (MEIC); even so, the width of the TPB is probably of atomic dimensions at LSM-YSZ connect lines. LSM electrodes with the best electrochemical performance at lower temperatures are compounds of LSM and YSZ. As well as the reality that interfaces between electrodes and electrolytes have better mechanical characteristics with composite electrodes, electrodes that are mixtures of LSM and YSZ can have much more extended TPB lines, for reasons shown graphically in Figure 2.13(b). This figure indicates that the YSZ within the composite can supply pathways for oxygen ions to diffuse into the electrode. The distance from the electrolyte interface for which the YSZ pathways are powerful in making better electrode performance, relies on the composition of the composite and structure of the YSZ within the composite. Theoretical and experimental concerns advocate that the electrochemically active region in most cases extends 10 to 20 μm from the electrolyte into the electrode.[87],[89],[90]

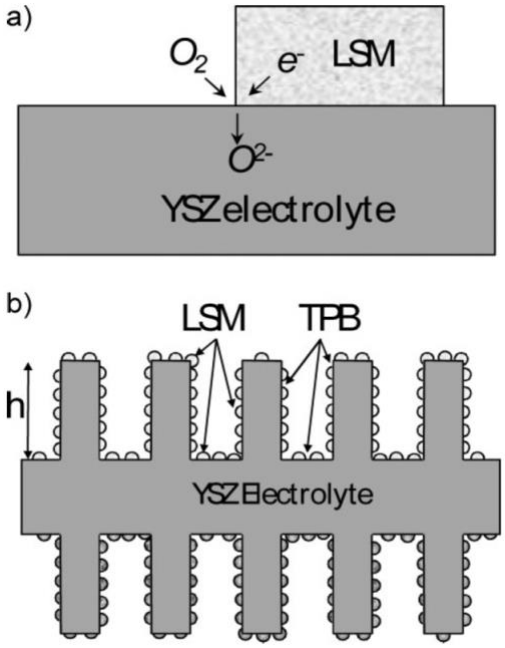

Figure 2.13: Schematic diagrams showing (a) the location of the three-phase boundary (TPB), i.e., the boundary between the YSZ electrolyte, LSM electro-catalyst and current conductor, and the gas phase, and (b) idealized structure of a cathode.[8]

The traditional method for fabricating electrodes, such as LSM-YSZ compounds on electrolyte- or anode-supported fuel cells, includes depositing a mixture of LSM and YSZ powders onto a dense YSZ electrolyte, then sintering that mixture onto the electrolyte. Deposition can be achieved by diverse methods. For example, spin coating and screen printing are common techniques for implementing an even coating of the mixture of LSM and YSZ particles.[91] The choice of sintering temperature for the cathode composite is more complicated.[92] There is a minimum sintering temperature for making ‘‘connection’’ between the YSZ in the electrode and the YSZ in the electrolyte, to build the YSZ channels that are shown graphically in Figure 2.13(b). Low-temperature processing would result in grain-boundary resistances that would avoid the free flow of oxygen anions from the electrolyte. For YSZ, this minimum temperature is roughly 1000 ℃. The maximum sintering temperature for composite electrodes is usually chosen so as to avoid solid-state reactions between the components of the cathode mixture. Particularly, one of the main reasons for using LSM instead of other conducting perovskites is that LSM-YSZ mixtures can be heated to as high as 1250 ℃ for reasonable times without forming insulating phases. For example, $La_2Zr_2O_7$.[92–95] Most other conducting perovskites cannot be prepared in the relatively narrow temperature window that is required.

Combination of composite electrodes by infiltration was at first developed in order to separate the calcination temperature of the YSZ from the sintering temperatures of the other electrode components.[96–98] However, other benefits have been noticed for electrodes prepared in this way.[81,99] With fabrication by infiltration, the composite is formed by first making a porous layer of the electrolyte material together with the electrolyte. The porous layer is used as a backbone for the electrode and the electronically conductive components are deposited into this layer in the following steps. The general strategy is shown graphically in Figure 2.14.[100,101]

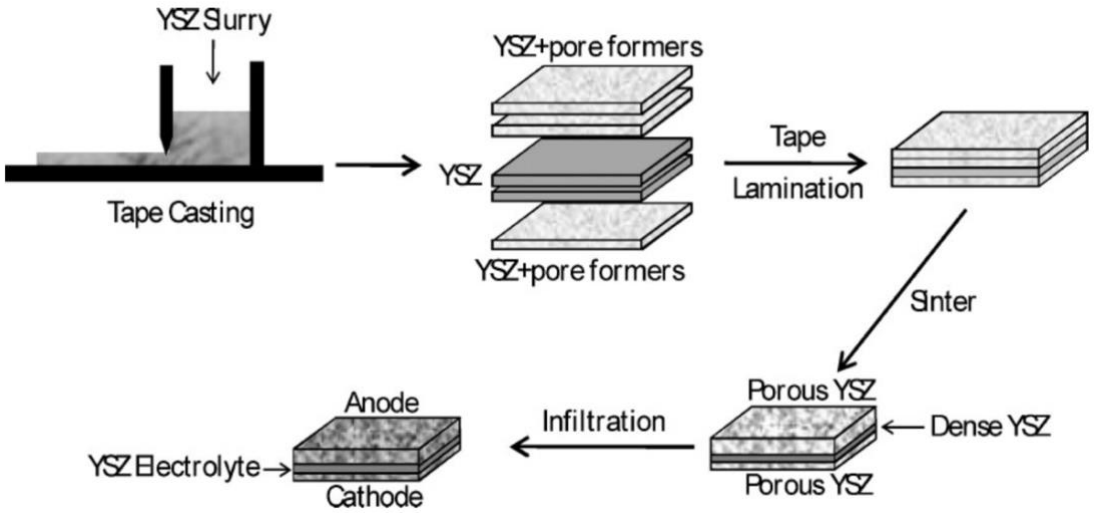

Figure 2.14: Diagram showing the steps used to fabricate an SOFC in which the electrodes are produced by infiltration of active components into a porous YSZ scaffold.[100,101]

The most-untimely work with LSM composites used infiltration of aqueous solutions of La^{+3}, Mn^{+3}, and Sr^{+2} nitrate salts.[99,102] Capillarity drives the salt-containing water into the porous layer; despite that, must be pay attention on the drying operation to avoid having the salts return to the external surface of the electrode.[103] The mixed oxides that form after decomposition of the nitrate ions can be calcined to form the perovskite inside the pores. Because $La(NO_3)_3$ and $Mn(NO_3)_3$ melt at relatively low temperatures, it is also possible to simply infiltrate a mixture of the liquefied salts.[104] From some previous works, suspensions of nanoparticles of the perovskite have been added straightly.[105–108] This has the profit of avoiding a separate calcination step to form the perovskite. In the case of LSM in YSZ, the electrodes formed by these three processes were shown to be essentially identical.[104]

Electrode fabrication by infiltration is relatively new and there are many problems that need to be solved. For instance, the amount of material that can be added in a single step using salt solutions is identical to the ion concentration in the infiltrating solution. Since 1 cm^3 of a solution that is one molar in both La^{+3} and Mn^{+3} salts will provide only 0.035 cm^3 of solid $LaMnO_3$, a single infiltration into a backbone that is 65 % porous will supply a composite that is only about 2.3 vol.% of the perovskite. Thus numerous steps are usually required in order to reach the necessary loading of the perovskite to make the electrode conductive. Although $La(NO_3)_3$ and $Mn(NO_3)_3$ have low melting temperatures, making it possible to infiltrate a mixture of the melted salts immediately,[104] the bulkiness of the nitrate anions still does not allow adequate amounts of the cations to be added in a single step. Besides, for some perovskites, like Sr-doped $LaFeO_3$ (LSF), extra bulky molecules, such as citric acid, must be added to the solution in order for the perovskite phase to form at lower temperatures.[109] There are reports that infiltration of nanoparticle solutions of LSM allows preparation of the composite electrodes in a single step.[105] Unquestionably, the use of nanoparticle solutions avoids the need for synthesizing the perovskite within the pores. Nevertheless, it is not easy to get concentrated solutions of particles small enough to fit into the pore structure of the backbone. Based on the information given by the authors for the preparation of their nanoparticles,[107] John M. Vohs and Raymond J Gorte estimated that the nanoparticle solutions used in that work were 15 wt.% (~ 3 vol.%) LSM, implying that the amount of LSM added in each step is much the same to that which would be added using 1.0 M solutions of the salts. The primary performance of electrodes prepared using a single infiltration of nanoparticles was notably better than that which could be achieved using a single infiltration step with the salt solutions.

Cathodes based on Sr-doped $LaCoO_3$ (LSCo) are known to be capable of high-quality cathode performance due to their high electronic and ionic conductivities.[110–113] The kinetics for the surface-exchange reaction, a measure of the catalytic activity of the cathode material, are also reported to be very excellent.[113] The reason LSCo is not broadly applied is that it reacts quickly with YSZ at 1000 ℃, the minimum sintering temperature for YSZ, to form insulating $La_2Zr_2O_7$ and $SrZrO_3$ phases.[112,114] There has been some successful results in stabilizing LSCo cathodes by subsuming layers of doped ceria between LSCo and YSZ in order to avoid these reactions;[115,116] but this method has not been completely triumphant.[117] Because the LSCo perovskite phase can be created simply at low temperatures, (for example, by heating the mixed nitrate salts to 700 ℃[109,118]), it is

feasible to prepare LSCo-YSZ electrodes with YSZ electrolytes by infiltration of the salts, without there being notable interfacial reaction between the YSZ and the LSCo. The infiltrated electrodes have the further benefit that the coefficient of thermal expansion (CTE) mismatch is less of a problem. Two groups have shown that the beginning electrochemical properties of these electrodes can be extraordinarily excellent. For instance, Armstrong and Rich demonstrated that a cell with a cathode constituted of 30 vol.% LSCo in a YSZ backbone, established by infiltration of the nitrate salts, showed a peak power density of 2.1 W cm^{-2} at 800 ℃ when operating in air and humidified H_2.[118]

In a study from John M. Vohs and Raymond J Gorte's laboratory, the impedance of an LSCo-YSZ electrode at 700 ℃ was calculated to be 0.03 Ω cm^2 with a composite electronic conductivity of 30 S cm^{-1}. This level of performance is high enough so that cathode losses can be considered unimportant compared to other losses in the cell. Unsurprisingly, the electrode impedance was detected to powerfully depend on the pore structure of the YSZ backbone.[109] The average pore size of the YSZ was increased from between 1 and 2 mm to roughly 20 μm, that increased the cathode impedance at 700 ℃ to 0.13 Ω cm^2. This increase is easily explained by the loss of TPB as suggested by Figure 2.13(b). Unluckily, fuel cells made with LSCo-YSZ electrodes were found to be unsteady, even at 700 ℃.[109,119] The loss in cell performance was related with an increase in the ohmic losses in the cell, constant with the formation of insulating phases within the electrode. Admittedly, evidence has been granted for the reaction of $LaCoO_3$ with YSZ at 700 ℃.[120] The instability of LSCo on YSZ electrolytes, even at low operating temperatures, most likely eliminates any possibility of using electrodes in which there is connect between LSCo and zirconia.

In their study, they have found that LSF-YSZ cathodes offer the best agreement between performance and stability for electrodes created by infiltration.[119,121] Before considering the results for infiltrated LSF-YSZ compounds, it is profitable to consider briefly the properties of LSF and the electrode materials that have been prepared by ordinary methods. The electronic conductivity of LSF is lower than that of LSM but still above 50 S cm^{-1} at usual SOFC operating conditions.[122–124] Because conductivity is lost in forming a composite with a nonconductor, LSF may not be satisfactory for the conduction layer of the electrode but its conductivity would materialize to be enough high for use in the functional layer of SOFC cathodes. The lack of electronic conductivity should be more than counterbalanced by the high ionic conductivity of LSF, reported to be 5×10^{-3} S cm^{-1} at 800 ℃ and atmospheric pressures for $La_{0.8}Sr_{0.2}FeO_3$.[124] Even higher conductivities are possible with increased Sr-doping.[61] These values are ten times of magnitude lower than that of YSZ but many orders of magnitude higher than that of LSM.

LSF is often combined with LSCo as being reactive with YSZ; Nevertheless, inspection of the available evidence indicates that it has a lower activity with zirconia-based electrolytes. A lot of groups have tried to find solid-state reactions between LSF and YSZ but have not found proof for new phases below 1200 ℃,[121,125,126] with some recommending phase steadiness at temperatures as high as 1400 ℃. Co-firing a mixture of LSF and YSZ to 1200 ℃ has been reported to cause an enlargement of the perovskite lattice, a finding which has been explained as being due to Zr-doping of the perovskite phase at the higher temperatures.[126] Still, 1200 ℃ is a comparatively high temperature, similar to the temperature at that solid-state reactions are observed with LSM and YSZ.

Moreover, $La_{0.8}Sr_{0.2}Fe_{0.9}Zr_{0.1}O_3$ has electronic conductivity and has been shown to provide reasonable performance as a cathode material when introduced to porous YSZ by infiltration.[121] These studies would advocate LSF-YSZ composites should be outstanding SOFC cathodes.

Infiltration strategies perform optimally in low-temperature fabrications of LSF-YSZ composites. In the study of John M. Vohs and Raymond J Gorte, electrodes were prepared by impregnating a 65% porous YSZ layer with the nitrate salts in the desired stoichiometry, to form the correct phase (the Pechini method) by using citric acid.[121,127] The citric acid forms a compound with the cations so that the La^{+3}, Sr^{+2}, and Fe^{+3} ions are well mixed in the oxide that is formed by heating to get rid of the nitrate salts. The perovskite phase was formed by additional heating to 850 ℃. The composite electronic conductivity increased with the loading of LSF but it was necessary to have 40 wt.% LSF (~ 23 vol.%) as a mean to achieve a conductivity greater than 1 S cm^{-1}.[127] The SOFC cathode impedance of the LSF-YSZ electrode with 40 wt.% LSF was estimated to be 0.1 Ω cm^2 and independent of current density at 700 ℃ in air.

The most important problem around these electrodes worries their stability. In symmetric-cell tests at 700 ℃ in air, it was found that the open circuit voltage (OCV) of the infiltrated LSF-YSZ electrode, initially calcined at 850 ℃, increased from 0.1 Ω cm^2 to 0.6 Ω cm^2 after 2500 hours.[121] Besides, the impedance of the deactivated electrode was found to be a strong function of current density and the average impedance of the deactivated electrode at a current density of 0.6 A cm^{-2} was found to be 0.15 Ω cm^2, as shown in Figure 2.15. Noticeably, in the presence of an applied current, a "symmetric" cell is no longer symmetric, since one electrode must be polarized anodically and the other cathodically. Consequently, the lowered impedance must apply to the LSF-YSZ electrode under both anodic and cathodic polarization. Ultimately, the characteristics of the inactivated LSF-YSZ electrode, including the increased open-circuit impedance and the strong current dependence, were identical in the initial performance of LSF-YSZ electrodes calcined at 1100 ℃.

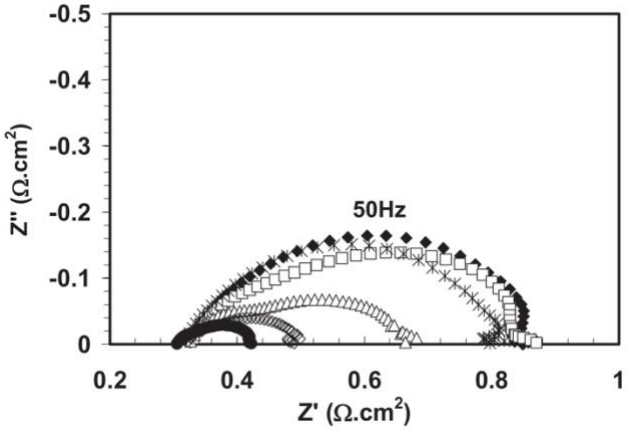

Figure 2.15: Cole-Cole plots of impedance spectra collected at 700 ℃ for a symmetric cell with two LSF-YSZ electrodes fabricated by infiltration as a function of the current density applied to the cell: (⬥) OCV, () 100 mA cm^{-2}, (△) 200 mA cm^{-2}, (◇) 400 mA cm^{-2} (•) 600 mA cm^{-2}, and (*) OCV immediately after applying 600 mA cm^{-2}. Prior to measuring the impedance spectra the electrodes were aged by annealing in air at 700 ℃ for 2500 hours.[121]

An alternate picture for understanding deactivation of the LSF-YSZ electrodes is shown schematically in Figure 2.16. Based on the SEM results, the LSF deposits calcined at 850 ℃ exist as small particles on the YSZ backbone, separated by gaps that allow gas phase oxygen to diffuse to the LSF-YSZ interface. This is depicted in Figure 2.16(a), which is similar to the diagram in Figure 2.13(b). When these particles sinter, either over time at operating conditions or following high-temperature calcination, the LSF forms a dense, polycrystalline layer over the YSZ backbone, as presented in Figure 2.16(b). Because the ionic conductivity of LSF is much lower than that of YSZ (8×10^{-4} S cm^{-1} for LSF and 1.89×10^{-2} S cm^{-1} for YSZ at 700 ℃ [128,124]). the transport of oxygen ions through the LSF could be restricted. The coupling of oxygen-ion transport up the YSZ "fingers" and through the LSF film would then be responsible for the current-dependent impedances.

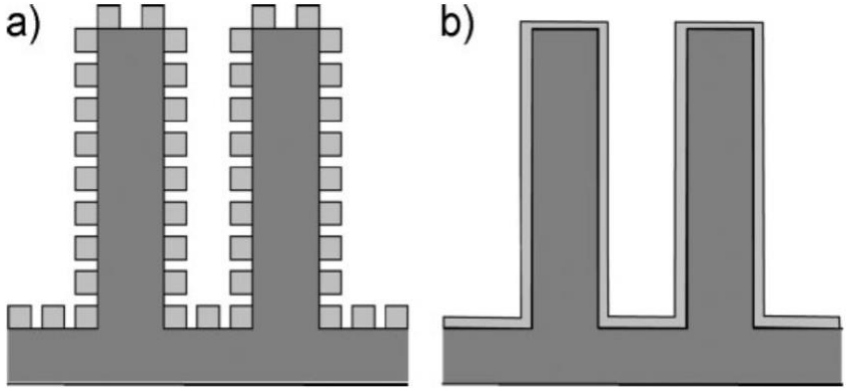

Figure 2.16: Schematic diagram of infiltrated LSF-YSZ cathode (a) after calcining in air at 850 ℃ and (b) after calcining at higher temperatures (>1000 ℃) or long term aging.[8]

Data for cathode performance with infiltrated Ca- and Ba-doped $LaFeO_3$ (LCF and LBF) deliver auxiliary support for the picture in Figure 2.16.[124] LCF and LBF have nearly identical electronic conductivities as that of LSF, but their ionic conductivities are remarkably lower. Especially LCF has an ionic conductivity that is 50 times lower than that of LSF at 700 ℃. Following calcination at 850 ℃, the initial performance of LCF-YSZ and LBF-YSZ electrodes was difficult to tell apart from that observed with LSF-YSZ electrodes. Assuming the morphology of the electrodes is similar to that shown in Figure 2.16(a), it is rational that the ionic conductivity would not be crucial in this case. Following calcination at 1100 ℃, SEM showed that LSF, LCF, and LBF each most likely tended to form a dense film over the YSZ, similar to that pictured schematically in Figure 2.16(b). Cathode performance for each of the three composite cathodes also decreased considerably.

Figure 2.17 shows impedance data at open circuit and at 100 mA cm^{-2} for three cells made with duplicate anodes and electrolytes, but with infiltrated cathodes based on LSF, LBF, or LCF.[124] The impedance at open circuit was much larger for the electrodes based on LCF and LBF, as would be anticipated for the model in Figure 2.16, given the remarkably lower ionic conductivities of the LCF and LBF. Similar to the findings with LSF, the impedance of LCF-YSZ and LBF-YSZ cathodes showed a strong current

dependence. With LCF-YSZ, the cathode impedance decreased from greater than 3 Ω cm^2 to less than 0.5 Ω cm^2 upon application of a cathodic potential.

Sr-doped $LaFe_{0.8}Co_{0.2}O_3$ (LSCF) can be considered a subcategory of LSF. LSCF has better electronic conductivity than LSF and a similar ionic conductivity.[129–131] It shows very excellent initial performance as an SOFC cathode when a doped-ceria layer is used to separate it from the YSZ.[132,133] It is also used in the current collecting layer of some fuel-cell designs.[134] Work has performed in which an LSCF cathode was fabricated by infiltration into porous YSZ backbones.[135] Chen *et al*.[135] have indicated that an infiltrated LSCF-YSZ electrode had an impedance as low as 0.047 Ω cm^2 at 800 ℃, approximate to the performance of infiltrated LSCo-YSZ and LSF-YSZ electrodes.[109,127] Given the lack of stability of LSF-YSZ and LSCo-YSZ electrodes, it seems most likely that there would be stability problems with LSCF as well. The major problem is whether or not the Co in the LSCF would remain in the perovskite phase, so that $La_2Zr_2O_7$ formation would be prevented. A study of $La_{0.8}Sr_{0.2}Mn_{0.8}Co_{0.2}O_3$ (LSCM) infiltration into porous YSZ showed sensible initial performance; however, the LSCM–YSZ electrodes were found to exhibit stability much the same to that of LSCo-YSZ electrodes. Performance declined remarkably, even at 700 ℃.[119]

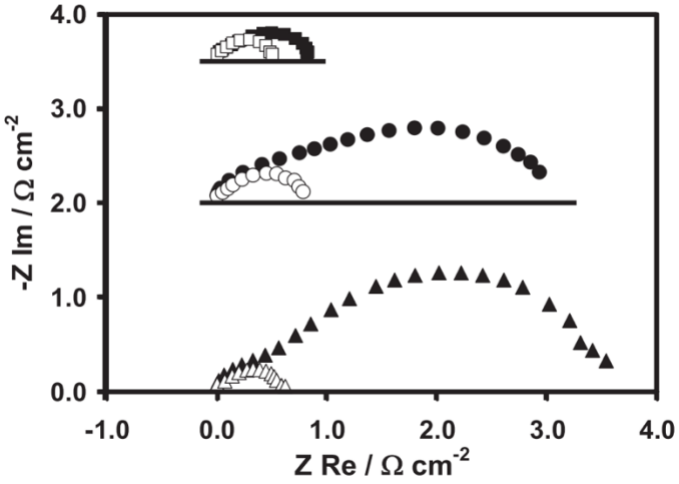

Figure 2.17: Impedance spectra obtained from fuel cells with infiltrated electrodes as a function of the active component, LSF (■), LBF (•), and LCF (▲), used in the cathode. The composite cathodes in each of, these cells were calcined at 1100 ℃. The filled symbols show data measured at open circuit while the open symbols were obtained at a current density of 100 mA cm^{-2}. Reproduced with permission from reference.[124]

Some of the main characteristics of LSM have already been discussed earlier in this Section and have been reviewed substantially elsewhere.[18] Under typical cathode conditions, LSM has an electronic conductivity greater than 200 S cm^{-1} at 800 ℃ but has minor ionic conductivity (4×10^{-8} /10^{-7} S cm^{-1} at 800/900 ℃). It experiences a solid-state reaction with YSZ to $La_2Zr_2O_7$ (insulating layer) above 1250 ℃, but LSM-YSZ mixtures are stable at lower temperatures. Since LSM-YSZ composites are the standard material for

cells with YSZ electrolytes, there is a very large amount of work examining the performance of these electrodes.[94] The performance of electrodes fabricated by infiltration of LSM is very good and approximate to that of regular LSM-YSZ composites. For instance, Armstrong and Virkar prepared infiltrated LSM electrodes using nitrate-salt solutions and achieved power densities as high as 1.2 W cm^{-2} for a cell operating in hydrogen at 800 ℃.[102] The performance characteristics of the infiltrated LSM-YSZ electrodes also changed remarkably with increasing calcination temperature.[136] In spite of symmetric-cell data is not a really reliable measurement of the performance acquired in actual full fuel cells with LSM electrodes due to activation by polarization,[137] the impedance determined from symmetric cells at 700 ℃ increased from 0.45 Ω cm^2 to nearly 3 Ω cm^2 when the calcination temperature was changed from 850 ℃ to 1050 ℃. Huang *et al.*[136] have also studied infiltrated LSM-YSZ electrodes that were fabricated by using three different methods: (1) infiltration of aqueous nitrate salt solutions; (2) infiltration using a molten mixture of La and Mn nitrate salts, with dissolved $Sr(NO_3)_2$; and (3) infiltration of LSM nanoparticles. The performance of electrodes prepared by each of these methods was very similar when the same calcination conditions (temperature and time) were used.[104,136] However, the properties of the infiltrated composites were found to depend powerfully on the temperature of calcination.

Moreover, composite electrodes above 1050 ℃ of calcination temperature showed strong hysteretic behavior, while the 850 ℃ electrode did not. Since 1050 ℃ is a little below the temperature (1200 ℃) at which one might expect LSM to undertake solid-state reactions with YSZ, it is believed the hysteretic behavior provides clues about what is likely happening in the electrode. Figure 2.18 shows an example of this behavior for a cell with an LSM-YSZ electrode prepared by conventional methods.[137] The figure shows two-electrode impedance spectra, measured at open circuit, with the ohmic contribution removed. The spectra were obtained following the application of the listed current densities for ten minutes. Under 700 ℃, the initial impedance spectrum shows a large, 3 Ω cm^2 non-ohmic contribution, of which roughly 0.5 Ω cm^2 is believed to be related with the Cu-ceria anode.[138] After applying the various currents, the open-circuit electrode impedances decreased remarkably. After ten minutes at 850 mA cm^{-2}, the total impedance decreased to 0.8 Ω cm^2, with 0.3 Ω cm^2 coming from the cathode. When the cell was held at an open circuit overnight, the electrode impedance returned to its initial high value 3 Ω cm^2.

The following are some of the clarifications that have been given for LSM electrode activation: (1) partial reduction of Mn^{+3} and generation of oxygen vacancies that extend the three phase boundary (TPB) by providing sites for O_2 reduction;[139] (2) reduction of LSM at the LSM/YSZ interface provides a driving force to reduce any $La_2Zr_2O_7$ that could have formed at the LSM/YSZ interface;[140,141] (3) reducing conditions at the TPB remove other species that might passivate the interface;[142,143] (4) cathodic polarization results in the formation of nano-pores and causes other micro-structural changes that improve diffusion of oxygen species;[139,144] (5) cathodic polarization results in a thin La_2O_3 oxide film at the LSM/YSZ interface which decreases polarization for unspecified reasons.[145] The reduction potential at TPB sites is lowered from atmospheric conditions by the cathode overpotential at most. From the data in Figure 2.18, changes in the open-circuit impedance are measured for polarization resistance less than 0.2 V and at a comparatively mild temperature of 700 ℃, conditions for which bulk thermodynamic studies of LSM indicate

the perovskite should be stable and have an oxygen stoichiometry near 3. Take $La_{0.8}Sr_{0.2}MnO_{3-\delta}$ for example, δ is zero. Indeed, based on the thermodynamic data of Mizusaki *et al.*[146] in Figure 2.19 and using a Nernst-like expression to relate $P(O_2)$ to potential, 3-δ is actually greater than 3 for low overpotentials.[146]

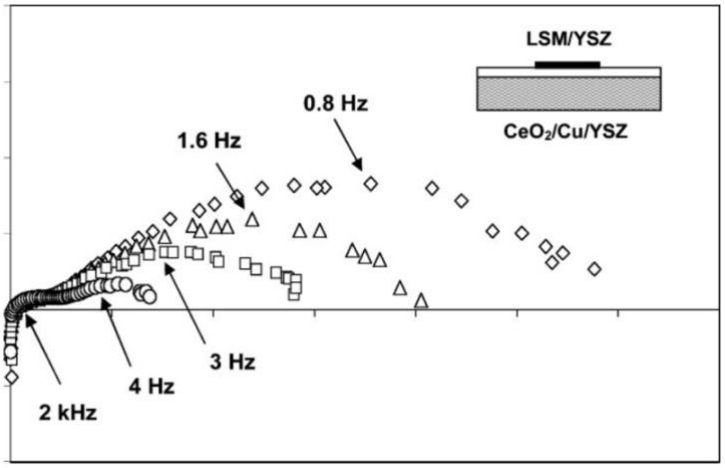

Figure 2.18: Impedance spectra for a SOFC with an LSM-YSZ cathode and Cu-CeO_2-YSZ anode at 700 ℃ in humidified H_2 (3% H_2O). The cathode in this cell was fabricated by co-sintering LSM and YSZ powders. All of the spectra were measured at open circuit immediately after applying a current for 10 min. The current densities were applied in the following order: (◇) after heating at OCV, (△) 60 mA cm^{-2}, () 150 mA cm^{-2}, (○) 850 mA cm^{-2} (short circuit). The constant ohmic resistance of the cell has been subtracted from each spectrum.[137]

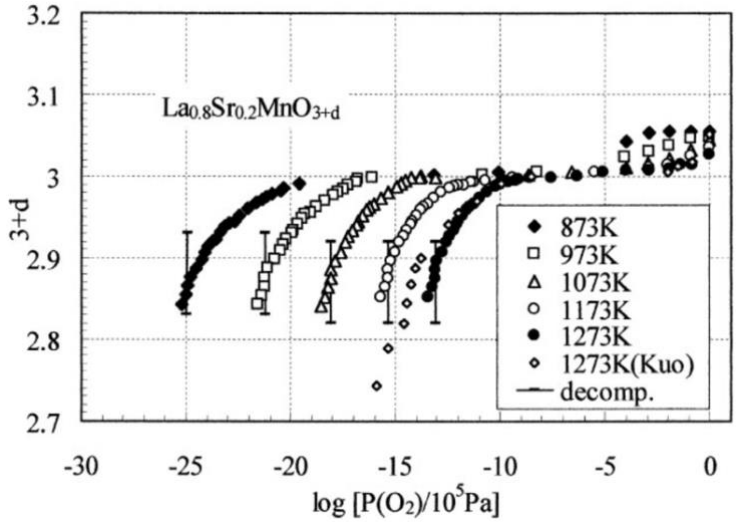

Figure 2.19: Equilibrium composition of $La_{0.8}Sr_{0.2}MnO_{3+d}$ as a function of $P(O_2)$.[146]

Based on work in John M. Vohs and Raymond J Gorte's laboratory with LSM-YSZ electrodes fabricated by infiltration, they have argued that the primary mechanism for impedance reduction upon electrode polarization is introduction of micro-porosity within the LSM.[104,136] According to this model, the LSM tends to create a dense layer over the YSZ, with diffusion of ions through this layer restraining performance (because LSM has poor ionic conductivity). Cathodic polarization causes partial reduction of the LSM layer, introducing micro-pores that allow oxygen to reach the YSZ interface. The evidence for this model is as follows: (1) LSM-YSZ composites fabricated by infiltration and calcined to only 850 ℃ were highly porous and not activated by polarization, while in composites calcined at 1050 ℃ the LSM created a dense layer over the YSZ backbone and were activated by polarization. (2) Brief reduction of an LSM-YSZ composite in humidified H_2 at 700 ℃, a treatment that had minimal effect on the LSM phase as measured by XRD, produced a decrease in electrode impedance much the same to that obtained by electrode polarization. BET measurements also indicated that reduction introduced micro-porosity, as proved by a large increase in the surface area of the composite. (3) The impedance curves that disappeared with activation have a low characteristic frequency and are much the same to the classical Warburg shape that is typical of diffusional limitations. This change cannot be due to gas-phase diffusion limitations since polarization does not change the all pore structure in the electrode and therefore suggests a decrease in the barrier for diffusion of oxygen through the LSM cathode to the YSZ electrolyte.

John M. Vohs and Raymond J Gorte have focused on adding all of the electrode components except the electrolyte backbone by infiltration. Because the necessity for conductivity requires relatively high loadings of the electronically conductive phase, it is imperative to add noteworthy amounts of material to the electrode. Nevertheless, it is possible to modify the characteristics of a conventional LSM-YSZ composite by infiltrating components for enhanced catalytic properties or ionic conduction. This method has been getting an increasing amount of attention a short time ago due to some very encouraging observations and examinations.

Composite of LNF and Pr_6O_{11}, PDC, or GDC

H. Taguchi *et al.*[65] fabricated electrolyte supported single cells with three types of cathodes that consisted of a $Ce_{0.1}Gd_{0.1}O_{1.95}$ (GDC) buffer layer, a $LaNi_{0.6}Fe_{0.4}O_3$ (LNF) cathode and an active layer. Single cells with cathodes consisting of a LNF current collection layer with thickness of 40 mm and an active layer with thickness of 3 mm on a 1.0 mm thick $0.89ZrO_2$-$0.10Sc_2O_3$-$0.01Al_2O_3$ or scandia alumina stabilized zirconia (SASZ) electrolyte sheet. The buffer layer-GDC was screen printed on the SASZ electrolyte and sintered at 1150 ℃ in air, then the active layer was screen printed and dried at 100 ℃, and an current collection layer-LNF was screen printed on it and sintered at 1000 ℃. The mean diameters of the LNF, GDC, and $Ce_{1-x}Pr_xO_{2-\delta}$ (x = 0.1, 0.3, 1.0) powders were roughly 1.3, 0.1, and 0.3 μm, respectively ($Ce_{1-x}Pr_xO_{2-\delta}$ (x = 1.0) is Pr_6O_{11}). They also printed a Pt anode on the other side of the electrolyte and a Pt reference electrode covering the entire peripheral part of the electrolyte disk. Lastly, the samples were fired at 1000 °C. The effective area of the anode and cathode was 0.785 cm^2.

The only dissimilarity between the three cathodes is that each was screen-printed a divergent active layer. Figure 2.20 shows backscattered electron images of cross sections of three types of cells acquired around the active layer. These cells have cathodes with a GDC-LNF composite active layer, a $Ce_{1-x}Pr_xO_{2-\delta}$ (x = 0.1, 0.3, 1.0)-LNF composite active layer, and a Pr_6O_{11} active layer. Figure 2.20(a) shows a cathode whose active layer is a GDC (50wt.%) and LNF (50 wt.%) composite.[147] Figure 2.19(b) shows a cathode whose active layer is a composite of $Ce_{1-x}Pr_xO_{2-\delta}$ (x = 0.1, 0.3, 1.0) (50 wt.%) and LNF (50 wt.%). The cathode shown in Figure 2.20(c) has a Pr_6O_{11} ($Ce_{1-x}Pr_xO_{2-\delta}$ (x = 1.0)) active layer (without LNF particles in the active layer). GDC was used to be a buffer layer to prevent any reaction between the SASZ electrolyte and LNF or Pr_6O_{11}. Pr_6O_{11} and $Ce_{1-x}Pr_xO_{2-\delta}$ particles are incorporated in the active layer like an insulating layer. These particles might react with the LNF or GDC. In other words, if the GDC buffer layer does not operate appropriately, Pr_6O_{11} and $Ce_{1-x}Pr_xO_{2-\delta}$ might react with the SASZ zirconia electrolyte.

In Figure 2.21, it shows the EIS measurement of these samples. The interface resistance (R_{inf}) and overvoltage (η_c) of the cathodes were investigated and analyzed. At 800 ℃, the $R_{inf}$of the cathode with the Pr_6O_{11} active layer was decreasing to 1/30 that of the cathode with the GDC-LNF composite active layer. The R_{inf} at 800 ℃ for the cathode with the Pr_6O_{11}-LNF composite active layer was decreasing to 1/8 that of the cathode with the GDC-LNF composite active layer. The R_{inf} values of the cathode with an active layer between 650 and 750 ℃ were also much better than those of the cathode with the GDC-LNF composite active layer. By using the cathode with the Pr_6O_{11} active layer, the operating temperature can be made smaller to 700 ℃ while maintaining the same performance (same overvoltage at 254 mA/cm^2) as a cathode with a GDC-LNF composite active layer at 800 ℃.

Bo Huang and their group[64] investigated the electrochemical properties of three different configurations of $LaNi_{0.6}Fe_{0.4}O_3$ (LNF)-based cathodes for SOFC (Shown in Figure 2.22). The LNF material is a chemically stable cathode material for ScSZ electrolyte-based SOFC when the calcined temperature was below 1100 ℃.[148] Therefore, the LNF-GDC composite is also a chemically stable cathode material for ScSZ electrolyte-based SOFC when the calcined temperature is below 1100 ℃. and the compositions of three cathode samples are summarized in Table 2.1. For the preparation of the functionally gradient LNF cathode, the first layer attached on the ScSZ electrolyte is composed of 60 wt.% LNF + 40 wt.% GDC, the second one is composed of 70 wt.% LNF + 30 wt.% GDC, and the top layer consists of 100 wt.% LNF. For the preparation of the GDC-impregnated LNF, stoichiometric amounts of gadolinium nitrate ($Gd(NO_3)_3 \cdot 6H_2O$) and cerium nitrate ($Ce(NO_3)_3 \cdot 6H_2O$) were dis- solved in distilled water with constant stirring. Then, a stoichiometric amount of citric acid ($C_6H_8O_7 \cdot H_2O$), which is a chelating agent and fuel, was also dissolved in this solution. The stoichiometric ratio of citric acid to nitrates was calculated according to S. C. Jain *et al.*[149]

Figure 2.23 shows the XRD patterns of 50 wt.% LNF + 50 wt.% GDC calcined at 1100 ℃ for 5 hours. Pure LNF contains a perovskite structure, while GDC contains a cubic fluorite-type structure. The results disclose that no apparent reaction between interface of the electrode and electrolyte appeared for LNF + GDC composites when heated up to 1100 ℃ for 5 hours and concur with those of Chiba.[48] Usually, a composite cathode material sintered at high temperature with a larger grain size causes to a decrease in the number of

the cathode-electrolyte-gas interface (triple phase boundary, TPB) sites, which results in high polarization resistance.[150,151] Meantime, due to the high sintering temperature, the cathode materials cohere firmly to the electrolyte surface, resulting in better contact with the electrolyte and better current collection. This represents a compromising relationship with regard to the sintering temperature to obtain cathode materials with fine microstructure and sturdy adherence to the electrolyte. Figure 2.24 shows the micro-structure of composite LNF-based cathode (70LNF-30GDC) with weight ratio of LNF:GDC being 70:30, which disclosed the uniform grains size of LNF are in the range of 0.4 – 1.0 μm. At the same time, the agglomeration situation of GDC particles was detected, the particle size distribution was in the range of 0.1 – 0.3 μm. After the ion impregnation with $Gd_{0.2}Ce_{0.8}(NO_3)_x$ solution, nano-size GDC particles were introduced to the LNF backbone as shown in Figure 2.24(b). The GDC particles were comparatively uniform and the grain size was in the range of 40-50 nm, as estimated from the SEM pictures (Figure 2.24(b)). Obviously, the impregnated GDC particles are much smaller than that of LNF particles.

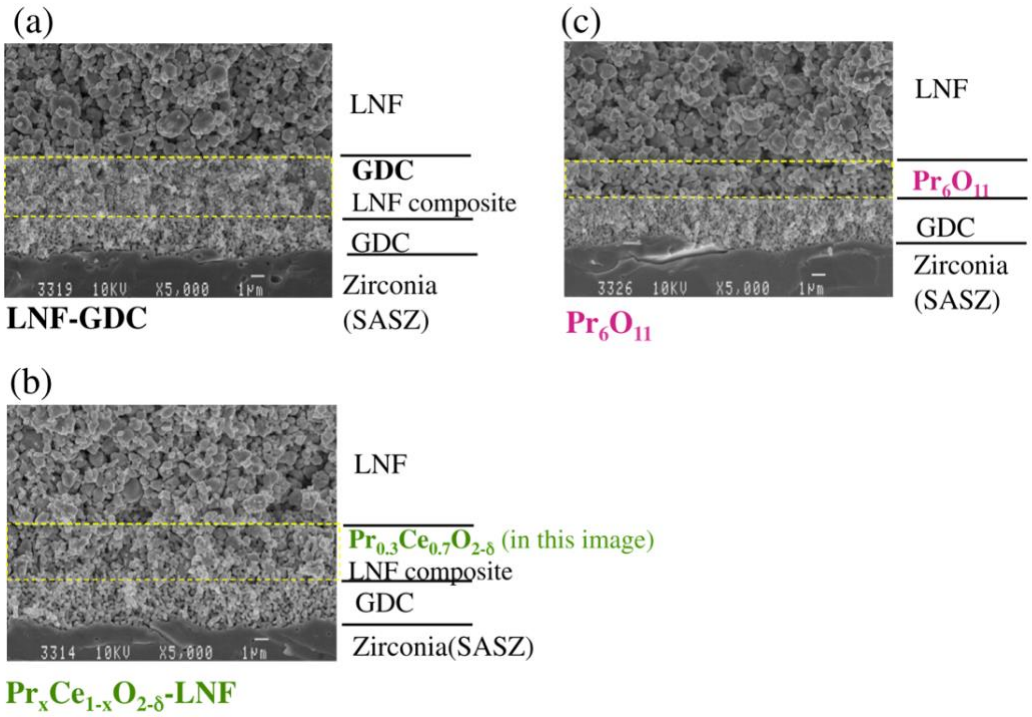

Figure 2.20: Cross-section of three types of cathode near the electrolyte. (a) Cathode with GDC-LNF composite active layer, (b) cathode with $Pr_xCe_{1-x}O_{2-\delta}$ (x = 0.1, 0.3, 1.0)-LNF composite active layer, and (c) cathode with Pr_6O_{11} active layer.[65]

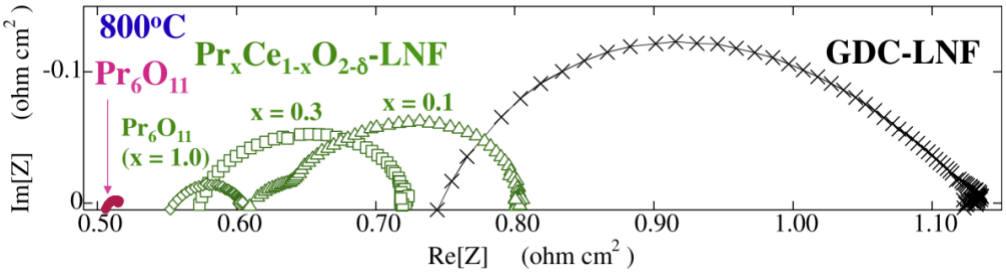

Figure 2.21: AC impedance plots for cathodes with different active layers. The effective area was 0.785 cm^2.[65]

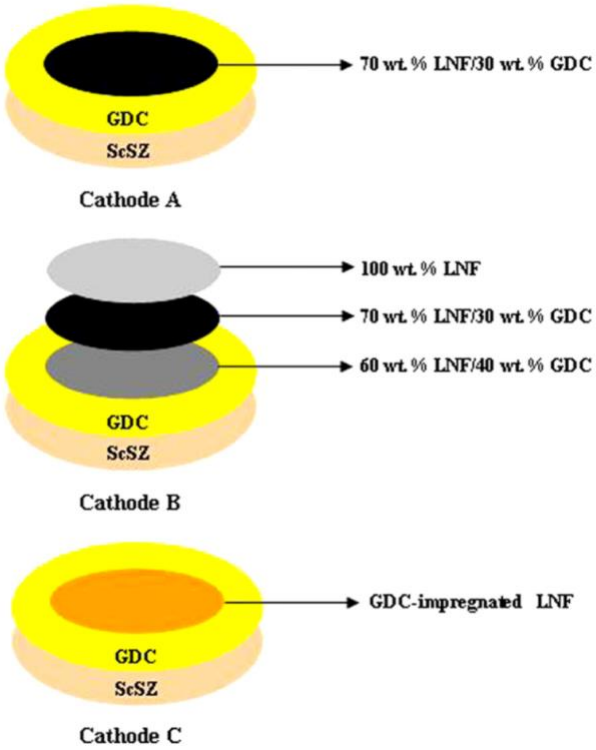

Figure 2.22: Schematic diagram of one side of the symmetric cell structure for cathode A, cathode.[64]

Summary of three configuration cathode samples.

Sample	Compositions		
	Layer 1	Layer 2	Layer 3
Cathode A	70 wt.% LNF/30 wt.% GDC	70 wt.% LNF/30 wt.% GDC	100 wt.% LNF
Cathode B	60 wt.% LNF/40 wt.% GDC		
Cathode C	GDC-impregnated LNF		

Table 2.1: The compositions of three cathode samples.[64]

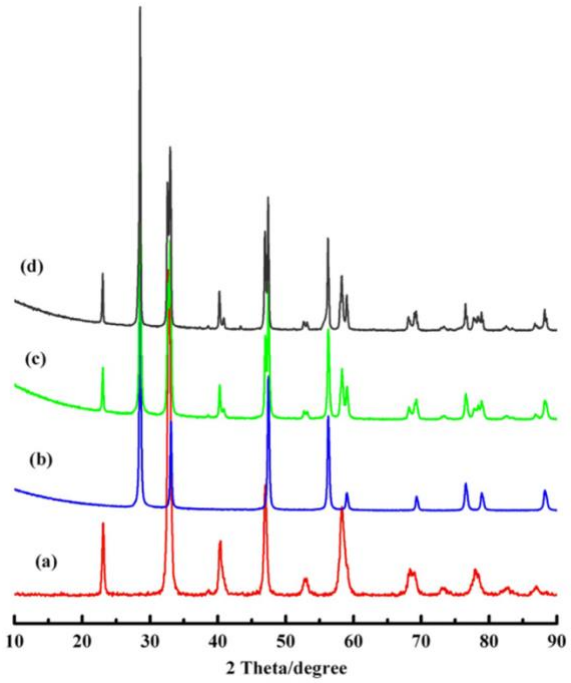

Figure 2.23: X-ray diffraction pattern of the powder of (a) LNF, (b) GDC, (c) 50 wt.% LNF + 50 wt.% GDC at room temperature and (d) 50 wt.% LNF + 50 wt.% GDC calcined at 1100 ℃ for 5 hours.[64]

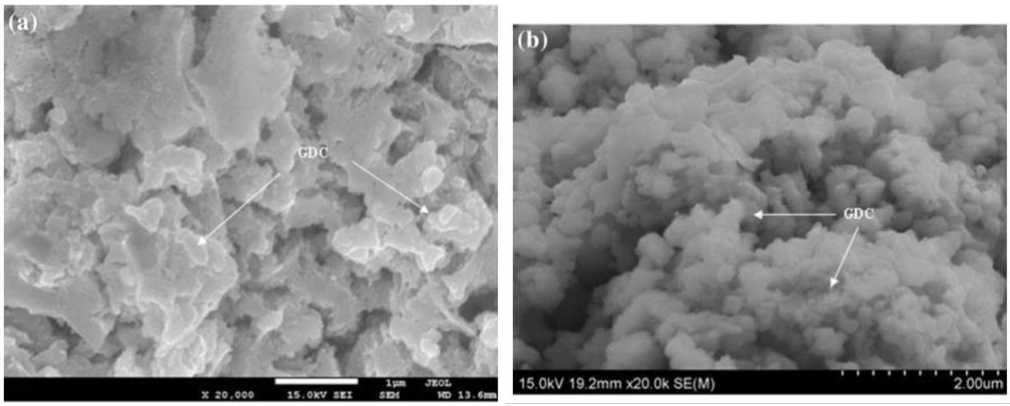

Figure 2.24: SEM images of (a) composite LNF-based cathode (70 wt.% LNF:30 wt.% GDC) and (b) GDC-impregnated LNF.[64]

Figure 2.25(a)-(e) show the general impedance spectroscopies for the LNF-based cathodes are investigated based on a symmetrical cell sintered at 1050 ℃ for 2 hours and cataloged under open-circuit conditions in the temperature range of 650-850 ℃ in air. Figure 2.25(f) uses an equivalent circuit to explain the impedance curves of symmetrical cells. This will be introduced with more details in Section 2.3.1. Figure 2.25(g) shows an

impedance sketch map on the compound plane. In the circuit, CPE and R denote constant phase element and cathode resistance, respectively. Fitting parameters for ORR on the LNF-based cathodes were listed in Table 2.2. It is clear to find that cathode A disclosed the largest R_p among the three cathode samples. In particular, cathode B performed an roughly 10 – 30% improvement in R_p, compared with cathode A. R_p of cathode C reduced approximately 70 – 80% compared with cathode A. Furthermore, as shown in Table 2.3, the value of the gas phase diffusion resistance (R_2) is always significantly larger than that of the charge transfer resistance (R_1). This indicates that R_2 dominates the total specific cathode polarization resistance (R_p) at temperatures within the range of 650 – 850 ℃. On the other hand, resistances (R_1 or R_2) gradually reduced from cathode A to cathode C. Evidently, with an increase in the number of cathode layers, there was a significant decrease in the total specific cathode polarization, implying a decrease in the impedance of ORR on the ScSZ electrolyte, i.e., the enhancement of electrochemical activity for the kinetics of ORR. Compared with composite LNF-based cathode (70 wt.% LNF-30 wt.% GDC), the functionally gradient LNF cathode with gradual changes in composite between ScSZ electrolyte and LNF cathode exhibited better adhesion resulting in the reduction in charge transfer resistance (R_1). In addition, the decrease in gas phase diffusion resistance (R_2) may be related to the area of triple phase boundaries (TPBs). The decrease in R_p for cathode B is mainly due to the gradual change rather than abrupt change in composition between ScSZ electrolyte and LNF cathode with dissimilar material structure. For the functionally gradient LNF cathode configuration, the composition changes gradually from one material to the other.

Specimens	650 °C R_P (Ω cm^2)	700 °C R_P (Ω cm^2)	750 °C R_P (Ω cm^2)	800 °C R_P (Ω cm^2)	850 °C R_P (Ω cm^2)
Cathode A	3.405	1.363	0.581	0.242	0.101
Cathode B	2.489	1.009	0.452	0.202	0.091
Cathode C	0.702	0.285	0.115	0.054	0.028

Table 2.2: Fitting parameters for ORR on the LNF-based cathodes.[64]

Specimens	650 °C		700 °C		750 °C		800 °C		850 °C	
	R_1 (Ω cm^2)	R_2 (Ω cm^2)	R_1 (Ω cm^2)	R_2 (Ω cm^2)	R_1 (Ω cm^2)	R_2 (Ω cm^2)	R_1 (Ω cm^2)	R_2 (Ω cm^2)	R_1 (Ω cm^2)	R_2 (Ω cm^2)
Cathode A	0.987	2.418	0.368	0.995	0.145	0.436	0.061	0.181	0.026	0.075
Cathode B	0.742	1.747	0.283	0.726	0.122	0.330	0.046	0.156	0.016	0.075
Cathode C	0.227	0.475	0.073	0.212	0.035	0.080	0.011	0.043	0.004	0.024

Table 2.3: The value of the gas phase diffusion resistance (R_2).[64]

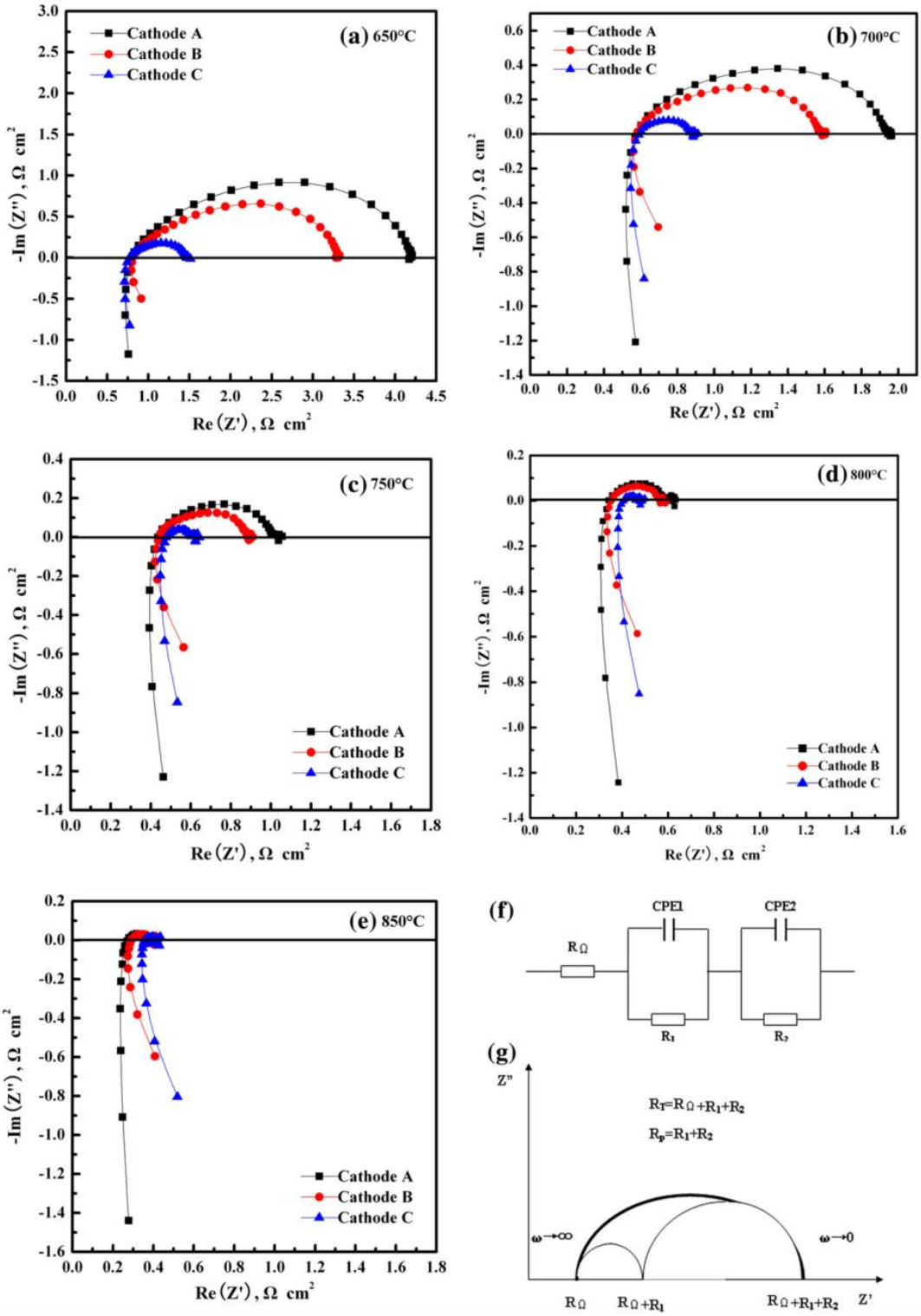

Figure 2.25: Electrochemical impedance spectra of LNF-based cathodes measured at different temperatures in air: (a) 650 ℃, (b) 700 ℃, (c) 750 ℃, (d) 800 ℃ and (e) 850 ℃. EIS was measured at open circuit. (f) The equivalent circuit for data fitting. (g) Impedance sketch map on the complex plane.[64]

Figure 2.26 shows the activation energies of the specific cathode polarization resistance for three LNF-based cathode configurations. It was found that specific cathode polarization resistance (R_p) decrease remarkably with increasing temperature for three cathode samples. The activation energies of the specific cathode polarization resistance for LNF-based cathodes were in the range of 138.83 – 151.59 kJ/mol. These values are comparable to that of the $La_{0.8}Sr_{0.2}Co_{0.8}Fe_{0.2}O_3$ (LSCF) (~130 kJ/mol) cathode deposited on $Ce_{0.8}Sm_{0.2}O_{1.9}$ electrolyte reported in Ref.[152] This suggests that LNF-based cathodes exhibit compatible activation energies of the specific cathode polarization resistance with that of LSCF cathode. The activation energies of the specific cathode polarization resistance for cathode A, cathode B and cathode C were 151.59, 142.58 and 138.83 kJ/mol, respectively. Noticeably, the activation energy values for functionally gradient and GDC-impregnated LNF cathodes (cathode B and cathode C) both are lower than that of composite LNF-based cathode (cathode A). This implied that the two approaches would effectively improve the cathode performance. Especially for the GDC-impregnated LNF cathode (cathode C), its configurations with a continuous and three-dimensional networks could greatly accelerates the oxygen dissociation and diffusion processes, substantially enhance the triple phase boundaries for the ORR, thereby reducing in the activation energies of the specific cathode polarization resistance.

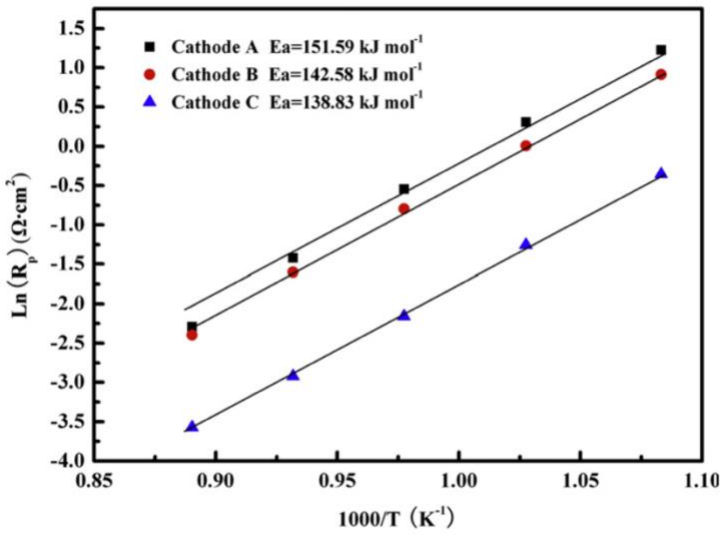

Figure 2.26: Arrhenius plots of the specific polarization resistance (R_p) for three different configurations of LNF-based cathodes.[64]

<u>BLF/BSCF/SDC/LNF/Pr_6O_{11} infiltrated on LNF</u>

Xifeng Ding and the research group[78] report the application of novel infiltration method to enhance the oxygen reduction reaction of $LaNi_{0.6}Fe_{0.4}O_{3-\delta}$ (LNF) cathode fabricated with different nano-catalysts, they are: $Ba_{0.5}Sr_{0.5}Co_{0.8}Fe0.2O_{3-\delta}$ (BSCF), $Ba_{0.9}La_{0.1}FeO_{3-\delta}$ (BLF), $Sm_{0.2}Ce_{0.8}O_{3-\delta}$ (SDC), and Pr_6O_{11}. Electrolyte-supported

symmetric cells for impedance measurement were prepared by screen printing. The cathode slurry of LNF powder mixed with ethyl cellulose and terpineol was printed onto both sides of SDC disks, followed by calcinations at 1000 ℃, 1100 ℃, 1200 ℃ for 3 hours in air, respectively. The weight ratio of cathode powder, ethyl cellulose and terpineol is 1:0.05:3. The surface fabrication of the LNF electrode was managed by ionic infiltration of nitrate solutions of BSCF, BLF, SDC and Pr_6O_{11}, respectively. Stoichiometric amounts of each ingredient of nitrate solutions for the impregnation process were dissolved in de-ionized water. The impregnated samples were calcined at 750 ℃, 800 ℃ and 850 ℃ for 2 hours, respectively. The infiltration and calcination processes were replicated until the necessary amount of nano-catalysts was achieved. Both of the two LNF electrodes were infiltrated concurrently. The infiltration loading was calculated by the mass of LNF electrodes before and after infiltration, and the mass of LNF electrodes were firstly calculated by SDC pellets with and without coated LNF electrodes. Ag paste was printed on electrode surfaces as the current collector layer and sintered at 700 ℃ for 30 minutes.

Figure 2.27 illustrated the XRD patterns of LNF and SDC calcined at 1000 ℃ and 1200 ℃. There were no secondary phases detected in the SDC powders. And a small peak appeared at 2θ = 32º in the LNF diffraction pattern which was recognized as La_2NiO_4 perovskite-related phase. Blank LNF electrode was first probed on SDC electrolyte using a symmetrical cell sintered at 1000-1200 ℃ to obtain well bonded and stable electrode film. The polarization resistances of blank LNF electrode got from electrochemical impedance spectra (EIS) measurement are shown in Figure 2.28.

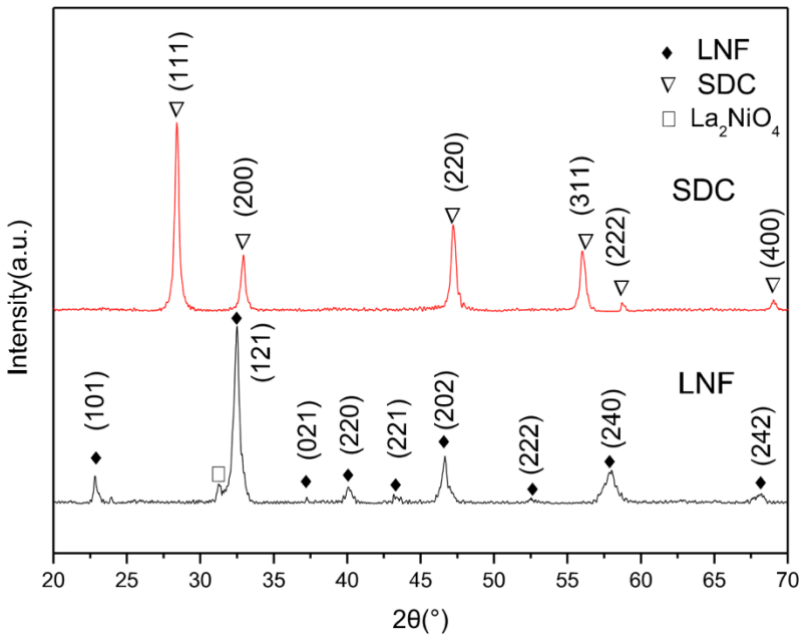

Figure 2.27: XRD of LNF powders synthesized by glycine nitrate process and calcined at 1000 ℃ and SDC powders prepared by solid state reaction calcined at 1200 ℃. The index of crystallographic plane was marked.[78]

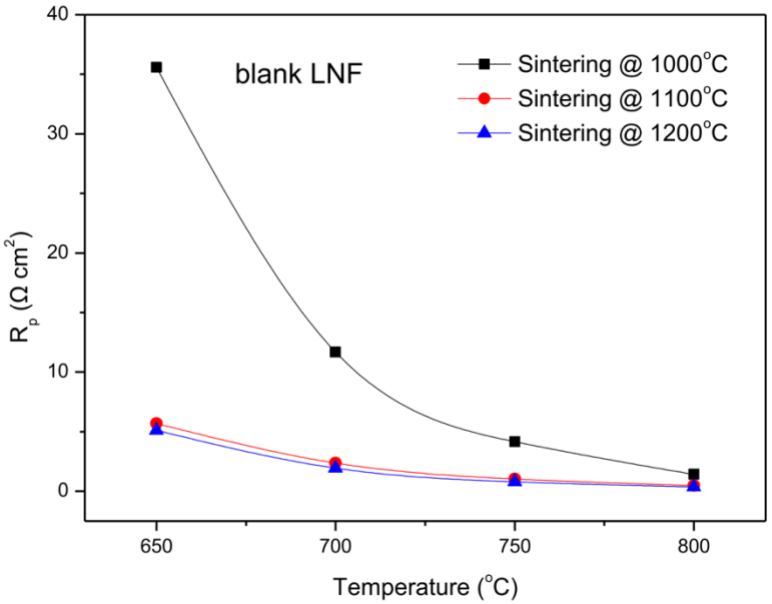

Figure 2.28: Polarization resistance (R_p) of blank LNF cathode sintered at 1000 ℃, 1100 ℃ and 1200 ℃ for 2 hours in air.[78]

R_p of LNF sintered at 1000 ℃ is much higher than that fired at 1100 and 1200 ℃, which may be ascribed to poor contact of the LNF electrode particles. The ohmic resistance (R_s) of blank LNF cathode sintered at 1000, 1100 and 1200 ℃ for 2 hours in air is shown in Table 2.4. And the R_s the value of SDC electrolyte supported cell calcined at 1000 ℃ is higher than that of the others, specifying the interfacial resistance is high for the former. They also mentioned that the adhesion between the LNF film and SDC substrate is awful and easily peeled off for the sample fired at 1000 ℃. The R_s value is 1.49 Ω cm^2 at 750 ℃ for the cell fired at 1100 ℃, that is close to a recent reported 1.33 Ω cm^2 for $BaFeO_{3-\delta}$/SDC/$BaFeO_{3-\delta}$ symmetric cell in the earlier publication of Feifei Dong and their research group.[153] While for LNF sintered at 1100 ℃ and 1200 ℃, the R_p values are very similar and show a clear reduction compared to that fired at 1000 ℃, typically at lower operating temperature, designating an improvement of electrochemical performance for oxygen reduction reaction. In addition, the interface reaction between LNF and Pr_6O_{11} was even worse when the firing temperature was higher than 1200 ℃.[65]

Temperature (°C)	R_s (Ω cm^2)		
	1000 °C	1100 °C	1200 °C
650	4.62	3.65	3.98
700	2.73	2.22	2.42
750	1.74	1.49	1.58
800	1.16	1.04	1.03

Table 2.4: The ohmic resistance (R_s) of blank LNF cathode sintered at 1000, 1100 and 1200 ℃ for 2 hours in air.[78]

Table 2.5 shows the raw impedance spectroscopy data with ohmic resistance R_s, polarization resistance R_p of blank LNF and LNF infiltrated with BLF, BSCF, SDC, Pr_6O_{11} and LNF nano-catalysts measured at 750 ℃, 700 ℃ and 650 ℃. The thickness of the electrolyte was quite dissimilar for each sample, which causes different R_s values in a little difference interval. Thereby, as a means to straightly compare the polarization resistance R_p of electrodes with and without infiltration.

Sample	750 °C		700 °C		650 °C	
	R_s (Ω cm^2)	R_p(Ω cm^2)	R_s(Ω cm^2)	R_p(Ω cm^2)	R_s(Ω cm^2)	R_p(Ω cm^2)
Blank LNF	1.58	0.62	2.42	1.89	3.98	5.22
BLF infiltrated	1.21	0.35	1.84	0.81	3.03	2.38
SDC infiltrated	0.92	0.19	1.35	0.45	2.25	1.47
BSCF infiltrated	0.95	0.12	1.46	0.26	2.41	0.75
Pr_6O_{11} infiltrated	1.05	0.09	1.53	0.23	2.31	0.62
LNF infiltrated	1.25	0.82	1.97	1.98	3.90	5.37

Table 2.5: Ohmic resistance R_s and polarization resistance R_p of SOFC cathode materials.[78]

In Figure 2.29, the electrolyte ohmic resistance (R_s) has been removed. R_p values could be approximately procured from the intervals of impedance spectra at Real[Z] axis. R_p is 0.62 Ω cm^2 for blank LNF electrode at 750 ℃, which is close to reported LNF electrode with the same composition by Manuela Bevilacqua and their research group.[63] After infiltrated with MIEC or ionic conducting catalysts, the electrochemical catalytic activity for oxygen reduction reaction of LNF electrodes was improved apparently. R_p is 0.09 Ω cm^2, 0.12 Ω cm^2, 0.19 Ω cm^2 and 0.35 Ω cm^2 at 750 ℃ for Pr_6O_{11}, BSCF, SDC and BLF decorated LNF electrode, respectively. Moreover, it increased to 0.23 Ω cm^2, 0.26 Ω cm^2, 0.45 Ω cm^2, 0.81 Ω cm^2 at 700 ℃ and to 0.62 Ω cm^2, 0.75 Ω cm^2, 1.47 Ω cm^2, 2.38 Ω cm^2 at 650 ℃ for Pr_6O_{11}, BSCF, SDC and BLF decorated LNF electrode, respectively.

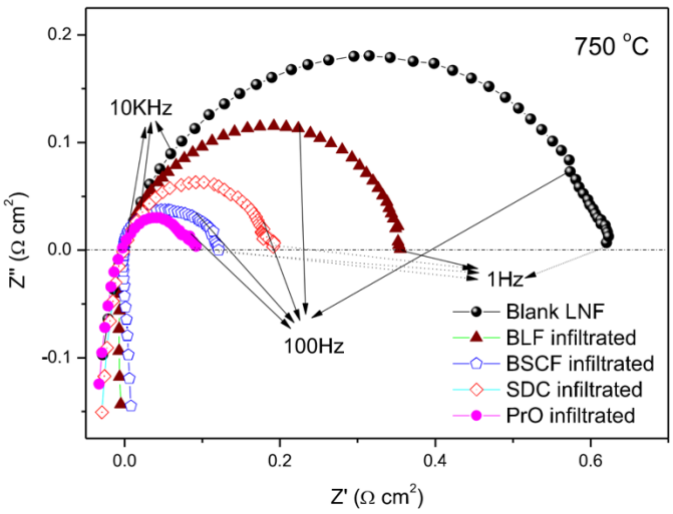

Figure 2.29: Electrochemical impedance spectra of blank LNF and BLF infiltrated with BLF, BSCF, SDC and Pr_6O_{11} nano-catalysts measured at 750 ℃.[78]

Additionally, for separating the effect of microstructure and ionic conductivity, the LNF electrodes were infiltrated with LNF particles itself because LNF is very close to pure electronic conductor (EC: 200-300 Scm^{-1} at 900 ℃ and IC: 1.6×10^{-6} Scm^{-1} at 700℃), and the polarization resistance of LNF-infiltrated-LNF in Table 2.5 is even slightly higher than that of blank LNF electrode, because of the concentration polarization stirred up from decreased porosity after infiltration, and the improved electrochemical catalytic activity of LNF infiltrated by former four catalysts was attributed to the enhanced oxygen ionic conductivity.

The micro-structures of the electrodes with different infiltration materials are shown in Figure 2.30. The electrodes fabricated(infiltrated) with BSCF and BLF were calcined at 800 ℃ and those infiltrated with Pr_6O_{11} and SDC were fired at 750 ℃ at which firing temperature the electrode performed the best electrochemical catalytic activity. The micro-structures of the electrodes with different infiltration materials look dissimilar. For the electrodes decorated with BSCF in Figure 2.30(a) and BLF in Figure 2.30(b), BSCF (about 20 nm) and BLF (about 60 nm) nano-particles were infiltrated on the boundary of LNF grains. For the electrodes infiltrated with Pr_6O_{11} in Figure 2.30(c) and SDC in Figure 2.30(d), nano Pr_6O_{11} bars (about 30 nm in diameter) and SDC (60 nm in diameter) were infiltrated in the pores of LNF backbone. The large surface area-to-volume ratio of nano-bar or nano-fiber allowed greater surface adsorption of oxygen and provided continuous pathways for charge transport throughout the cathode, thus hold excellent potential for intermediate-temperature SOFCs.[154]

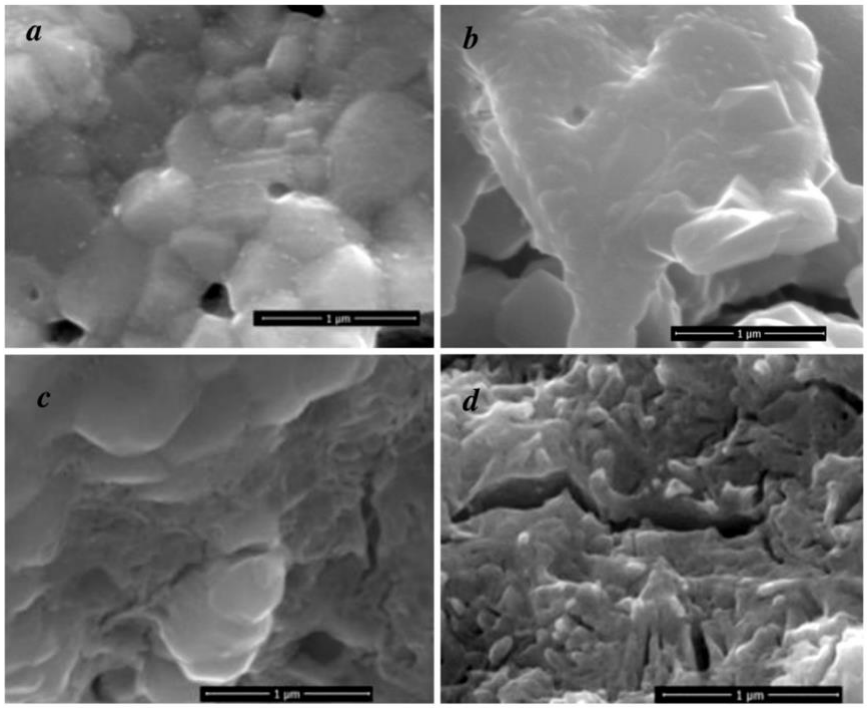

Figure 2.30: SEM of LNF electrode infiltrated different promoting agents (a) BSCF infiltrated cathode calcined at 800 ℃, (b) BLF infiltrated cathode calcined at 800 ℃, (c) Pr_6O_{11} infiltrated cathode calcined at 750 ℃ and (d) SDC infiltrated cathode calcined at 750 ℃.[78]

2.2.3 ALD Method

2.2.3-1 Overview

Atomic layer deposition (ALD) is a relatively new vapor deposition technique for depositing a large variety of ultra-thin films with extreme precision. It has become an important tool in many research-oriented and industrial applications, such as semiconductor manufacturing, photovoltaics, lithium-ion batteries, heterogeneous catalysts, and solid oxide fuel cells.[155] Because of the sequential, self-limiting nature of the reaction process, ALD allows for the deposition of highly uniform layers of carefully controlled thickness, down to the angstrom (Å) level. A typical ALD process is shown in Figure 2.31. The substrate is first placed in an evacuated chamber, generally between 200-350°C.[7,156] The surface of the substrate may be naturally functionalized, or may have to be treated for functionalization to facilitate reactions with the precursor functional groups. The first precursor (Precursor A) fills the chamber, and the precursor functional groups attach to reaction sites on the functionalized surface of the substrate.

The ligands attached to the precursor molecules can only react with reaction sites on the substrate; they cannot react with each other. Therefore, assuming that the dwell time (amount of time that precursor molecules are allowed to remain in the chamber) is sufficiently long, all reaction sites on the substrate surface will be occupied by one single layer of precursor molecules. It is this characteristic of the atomic layer deposition process that allows for uniform, highly conformal deposition of the most complex high-aspect ratio and nano-porous structures.

After Precursor A has been given sufficient time to react with the surface of the substrate, an inert gas such as nitrogen or argon flows through the chamber to purge any remaining byproducts or precursors that did not react with the surface, as shown in Figure 2.31(c). After the purging of Precursor A is complete, Precursor B is pulsed through the chamber, shown in Figure 2.31(d). As before, Precursor B contains functional groups that react selectively and exclusively with the functional groups attached to Precursor A. Thus, a monolayer of Precursor B is deposited on top of Precursor A, such that all reaction sites become occupied and no accumulation occurs on top of the monolayer. The remaining byproducts and Precursor B molecules are purged from the chamber with inert gas, as shown in Figure 2.31(e). For a binary system, the purging of Precursor B would mark the end of one single cycle. For ALD processes, the number of cycles controls layer thickness, so cycles can be repeated until the desired thickness is reached. Typical ALD deposition rates are generally less than one angstrom (Å) per cycle, and depending on the specific process, can vary between 100-300nm every hour.[157,158]

To further illustrate a common ALD process for SOFC application is the deposition of YSZ thin films electrolytes. This can be achieved by alternating deposition of precursors yttria (Y_2O_3) and zirconia (ZrO_2). As mentioned in Section 2.1.2-1, the optimal composition or YSZ contains 8 mol% yttria. This composition can be accurately achieved with ALD by pulsing the precursors in specific ratios.[159] This observation leads to another important advantage of ALD: composition control. The nature of the ALD process allows for the deposition of thin films with highly tunable compositions, allowing for deposition of many different types of metal and metal-oxide materials.

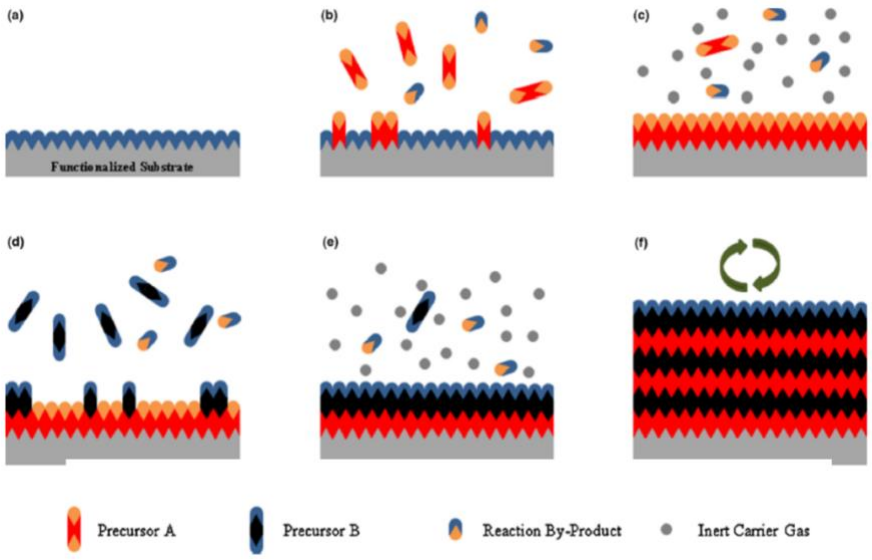

Figure 2.31: Typical atomic layer deposition cycle: (a) Bare functionalized substrate; (b) precursor A attaches to substrate; (c) Inert gas purges chamber and evacuates remaining precursor A; (d) precursor B fills chamber and attaches to precursor A; (e) remaining precursor B is purged from chamber with inert gas; (f) cycle is repeated until desired thickness is reached.[7]

2.2.3-2 Applications

Atomic layer deposition (ALD) is a thin-film deposition approach build on the sequential use of a gas phase chemical procedure. ALD is believed a sub-class of chemical vapor deposition. The most of ALD reactions use two chemicals, in most cases called precursors. These precursors react with the surface of a material one at a time in a continuous, self-limiting method. Through the replicated subjection to detach precursors, a thin film is deposited at a slow pace. ALD is a key procedure in the fabrication of semiconductor devices, and part of the set of tools obtainable for the synthesis of nano-materials. The basic working function we already discussed in Section 2.2.3-1, so here we focus on some literature review and applications.

In the review by Richard W. Johnson *et al.*[7], they mentioned that ALD could be used in diverse directions with multiple purposes. For example, $Cu(In,Ga)Se_2$ solar cell devices, high-k transistors, and solid oxide fuel cells. The range of materials that ALD can deposit-from metal oxides such as $Zn_{1-x}Sn_xO_y$, ZrO_2, Y_2O_3, to noble metals like plutonium. The main benefits of ALD are all derived from the chronological, self-saturating, gas-surface reaction control of the deposition process. First of all, the conformity of ALD-deposited films is often the critical factor in choosing ALD over competing deposition techniques such as chemical vapor deposition (CVD) or sputtering. Conformity of high aspect ratio and three dimensionally-structured materials is made possible by its self-

limiting characteristic that restricts the reaction at the surface to no more than one layer of precursor. With adequate precursor pulse times, the precursor can be distributed into deep narrow ditches, permitting for an entire reaction with the whole surface. Following cycles give permission for uniform growth on high aspect ratio structures, whereas CVD and physical vapor deposition (PVD) may have trouble with non-homogeneity due to rapid surface reactions or shadowing effects. Figure 2.32(a) and (b) for SnS_x films on Au nanoparticles and $Ge_2Sb_2Te_5$ films over SiO_2 trenches; the ability of the process to equally coat the substrate morphology is visible. The second palpable value of ALD is the thickness control of the deposited thin films. Another well-known benefit of ALD is composition control. Composition control has been demonstrated with materials such as zinc tin oxide (ZTO)[160] and $SrTiO_3$,[161] among many others.[162–164] These films could be deposited and compositionally managed by tailoring ALD "super cycles", which are composed of numerous ALD operations. For instance, in ZTO deposition, altering the super cycle ratios for SnO_x and ZnO can tailor different conduction behavior and optical characteristics of the film.[160] In depositing $SrTiO_3$, ALD procedures for TiO_2 and $SrCO_3$ are given turns to in a super cycle at a 1:1 proportion, constructing a stoichiometric $SrTiO_3$ film after annealing. In spite of that, it should be noticed that a nonlinear association between the cycle ratio and the film's atomic ratio is ordinary for the ternary oxide procedures,[163,164] causing it to be less simple to deposit a film with a certain required composition. By way of illustration, more and more studies on $SrTiO_3$, ALD have specified that a 1:1 Sr:Ti atomic ratio in films is also feasible for ALD cycle ratios between 0.67 and 0.82.[162]

The materials enclose metals, insulators and semiconductors in both crystalline and amorphous phases. Furthermore, ALD provides a massive option of elements to choose from to create the material of choice, as listed in Table 2.6.[165–171] This table displays that the most conventional types of ALD-grown materials so far are oxides, nitrides, sulfides and pure elements. In spite of the fact that the selection of materials listed in Table 2.6 is magnificent, obviously it also discloses that it is not yet practicable to grow every material by ALD. The major restraint of the availability of a material by ALD is the finite selection of effective reaction pathways. The selection is further restrained by the availability of reactants that can make the suitable reaction pathway.

Ikwhang Chang *et al.*[41] bespoke that an attempt to avoid thermal agglomeration of metal electrodes, an extremely thin yttria-stabilized zirconia (YSZ) is coated on the porous metal (Pt) cathode by the atomic layer deposition, a scalable, and potentially high-throughput deposition technique. A very thin YSZ coating is found to maintain the morphology of its underlying nano-porous Pt during high temperature performances (over 500 °C); figure 2.33 displays some SEM images to illustrate this. More appealingly, the YSZ coating is also found to improve oxygen reduction reaction (ORR) activity by about 2.5 times better. This improvement is ascribed to an increased triple phase area, principally in the surrounding area of the Pt-electrolyte interface. Cross-sectional electron microscopy images in Figure 2.34 specify that the initially uniform extremely thin YSZ layer becomes a not entirely agglomerated coating, an advantageous structure for a maximized reaction area and free-flowing oxygen access to the Pt-electrolyte interface.

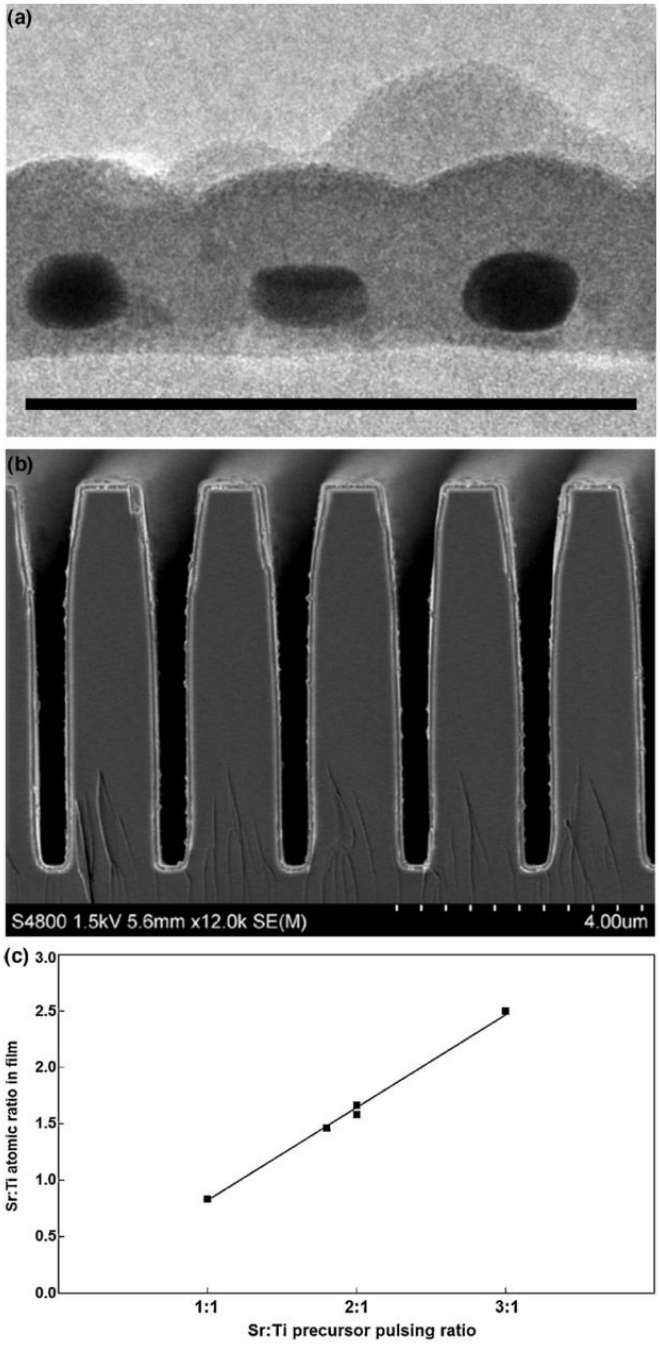

Figure 2.32: Examples of ALD strengths. (a) TEM image of conformal SnS_x ALD film on Au nanoparticles. Scale bar is 100 nm. (b) SEM cross-sectional image of conformal $Ge_2Sb_2Te_5$ ALD film in trenches.[165] (c) $SrTiO_3$ stoichiometry as a function of $SrCO_3$ and TiO_2 ALD super cycle ratio.[161]

List of materials grown by ALD				
Elemental	**Oxides**	**Nitrides**	**Sulfides**	**Other compounds**
C, Al, Si, Ti, Fe, Co, Ni, Cu, Zn, Ga, Ge, Mo, Ru, Rh, Pd, Ag, Ta, W, Os, Ir, Pt	Li, Be, B, Mg, Al, Si, P, Ca, Sc, Ti, V, Cr, Mn, Fe, Co, Ni, Cu, Zn, Ga, Ge, Sr, Y, Zr, Nb, Ru, Rh, Pd, In, Sn, Sb, Ba, La, Ce, Pr, Nd, Sm, Eu, Gd, Tb, Dy, Ho, Er, Tm, Yb, Lu, Hf, W, Ir, Pt, Pb, Bi	B, Al, Si, Ti, Cu, Ga, Zr, Nb, Mo, In, Hf, Ta, W	Ca, Ti, Mn, Cu, Zn, Sr, Y, Cd, In, Sn, Sb, Ba, La, W	Li, B, Mg, Al, Si, P, Ca, Ti, Cr, Mn, Co, Cu, Zn, Ga, Ge, As, Sr, Y, Cd, In, Sb, Te, Ba, La, Pr, Nd, Lu, Hf, Ta, W, Bi

Table 2.6: The most conventional types of ALD-grown materials [165–171]

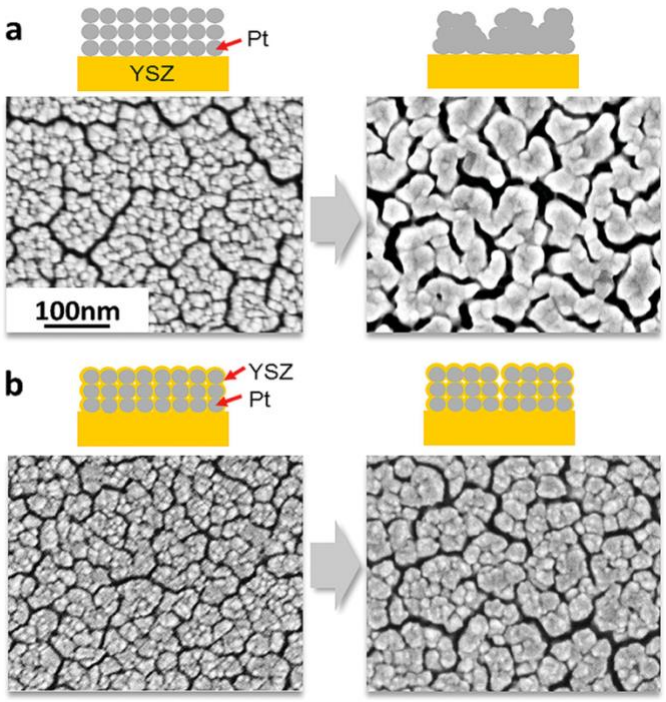

Figure 2.33: Top-view SEM images of Pt films (a) without and (b) with a nanoscale YSZ coating before (left) and after an annealing process (right) at 500 °C for 20 hours. Upper schematic diagrams depict conceptual microstructures of each sample. For this characterization, the Pt film was deposited on a Si substrate.[41]

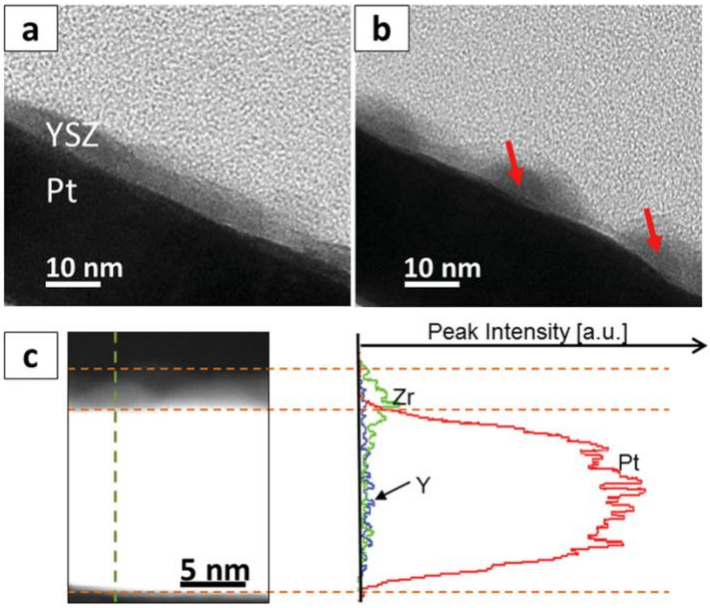

Figure 2.34: Cross-sectional TEM images of a YSZ-coated Pt film (a) before and (b) after an annealing at 600 °C for 10 hours. A thermally induced agglomeration of YSZ coating is observed. (c) An EDS line mapping scanned through the dotted vertical line in the TEM image on the left side.[41]

2.3 Characterization Methods

There are a lot of methods for characterizing the performance of solid oxide fuel cells, including but not limited to: electrochemical impedance spectroscopy (EIS), current-voltage (*i*-V) characterization, open circuit voltage (OCV) measurements, and scanning electron microscopy (SEM) for characterizing electrode microstructure. In the present study, only cathode performance is studied, and all experiments are conducted using symmetric cells (a symmetric cell has two cathode electrodes, whereas a full cell has one cathode and one anode). Current-voltage characterization and open circuit voltage measurements are generally only used for full cell characterization. Thus, electrochemical impedance spectroscopy and scanning electron microscopy are the primary characterization methods used in this study.

2.3.1 Electrochemical Impedance Spectroscopy

The electrochemical reactions in a single solid oxide fuel cell can theoretically generate up to 1.23 V of electric potential.[19] In practice, however, an SOFC suffers performance losses due to anode and cathode activation losses (caused by electrochemical reaction kinetics) and electrolyte/electrode ohmic losses (caused by electronic and ionic conduction). EIS is a popular characterization method that allows the user to accurately differentiate between the major sources of loss in the cell. Impedance is the ability of a system to impede the flow of electrical or ionic current. Impedance is an extension of resistance, in that it also deals with time-dependent phenomena. The impedance Z of a system is defined as the ratio of voltage to current as is shown as:

$$Z = \frac{V(t)}{i(t)} \qquad \text{(Equation 2.5)}$$

As mentioned, the voltage and current need not be steady state values; they are time (frequency) dependent functions. To measure the impedance of a system, the system is subjected to a small sinusoidal voltage perturbation, and the resulting current is measured. In general, the current response may lag behind the voltage input, which introduces the phase shift ϕ. The impedance of a system can then be described in terms of magnitude Z_0 and phase angle ϕ, or alternatively as a real component $Z_0 \cos \phi$ and imaginary component $Z_{0j} \sin\phi$. Purely resistive circuitry elements such as resistors have only real components of impedance, whereas time-dependent elements such as capacitors have both real and imaginary components of impedance.

To perform electrochemical impedance spectroscopy, the impedance of the system is measured over several orders of magnitude of AC voltage frequencies (for this present study, the range is 50 mHz – 7 MHz). The resulting data is plotted in terms of the real and imaginary components of the impedance values, with the real components (Z_{real}) plotted on the x-axis and the negative imaginary components (-Z_{image}) plotted on the y-axis. The useful imaginary components generally have negative values, and therefore it makes more sense graphically to plot these values on the positive axis. This graphical representation of impedance data is known as a Nyquist plot (Figure 2.39), and it summarizes the impedance behavior of a system over a wide range of frequencies.

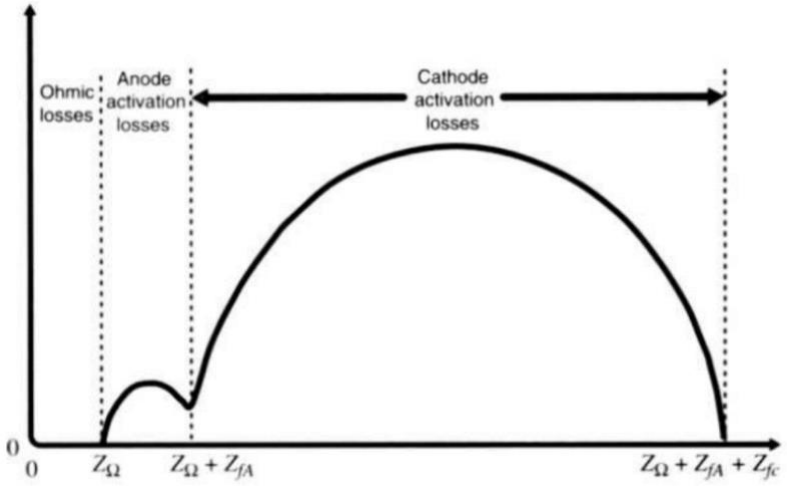

Figure 2.35: Nyquist plot showing sample SOFC electrochemical impedance spectroscopy data for illustration; Z_Ω is the cell ohmic resistance, Z_{fA} is the anodic polarization resistance, and Z_{fC} is the cathodic polarization resistance.[11]

To understand the shape of the Nyquist plot for an SOFC, some fuel cell modeling principles must be described first. An SOFC can be represented by an equivalent circuit, the elements of which describe the actual physical processes occurring during fuel cell operation (Figure 2.36). Each electrode can be represented by a parallel resistor-capacitor (RC) circuit. The resistor represents resistance to the electrochemical reactions occurring at the electrode. In other words, the resistance value is directly related to the electrode kinetics, or the speed of the electrochemical reactions.

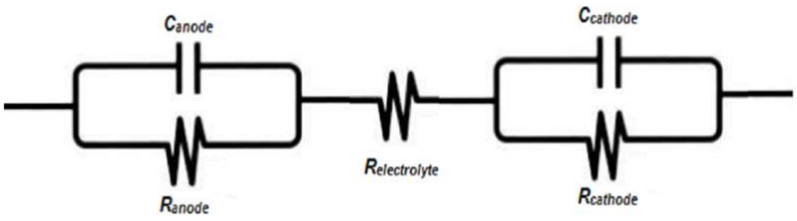

Figure 2.36: simplified equivalent circuit for an SOFC.

At the electrode-electrolyte interface, a buildup of ions in the electrolyte causes a buildup of electrons in the electrode to balance the charge, in much the same way that the accumulation of charge in one capacitor electrode causes a buildup of charge in the opposing electrode. Thus, SOFC electrodes exhibit electronic behavior that is similar to a parallel RC circuit. The two electrodes are connected serially, with the electrolyte in between them, which can be modeled as a simple resistor.

Now that the basic concepts of SOFC equivalent circuitry have been explained, the shape and significance of the Nyquist plot of Figure 2.35 can be described. As mentioned, the Nyquist plot is generated by measuring the impedance of the SOFC over many orders of magnitude of input voltage frequencies. The resistive elements of the SOFC have purely real components of impedance, and the capacitive elements have purely imaginary components. At very low frequencies (data shown on the right side of the Nyquist plot), the capacitive elements act as open circuits, and all current flows through the resistive component of the electrode. Thus, the impedance values have no imaginary components and lie on the Z_{real} axis (x-axis), representing the effective impedance of the resistor. Conversely, at very high frequencies (furthest to the left side of the Nyquist plot), the capacitive elements act as short circuits, with all current flowing through the capacitive element of the electrode. Thus, the effective impedance of the electrode is zero.[11]

As Figure 2.35 illustrates, a standard Nyquist plot for an SOFC shows two semi-circular arcs, one larger than the other. The SOFC Nyquist plot provides many pieces of useful information regarding cell performance, a few of which will be described here. The cathodic activation resistance (resistance related to electrochemical reaction speed) is given by the difference in the two Z_{real} intercepts of the large arc; in other words, the distance between the two intercepts gives a direct measurement of the electrochemical reaction speed taking place at the cathode. Similarly, the anodic activation resistance is given by the distance between the two Z_{real} intercepts of the smaller arc. It should be noted that the semicircle corresponding to cathodic activation loss is much larger than the semicircle corresponding with the anodic activation loss. This is because the oxygen reduction reaction taking place at the cathode is much more sluggish than the hydrogen oxidation reaction taking place at the anode. Thus, the cathodic activation resistance is generally the limiting factor in SOFC performance, and therefore much SOFC research is dedicated to decreasing cathodic activation resistance to improve overall cell performance. One additional piece of information that can be gleaned from an SOFC Nyquist plot is the ohmic resistance, or resistance to the flow of ions and electrons, of the cell. As was mentioned, at very high frequencies, the activation impedance of the electrodes is effectively zero, and the resulting intercept on the Z_{real} axis (x-axis) represents the ohmic resistance of the cell. In general, electronic resistance is negligible, and the ohmic resistance represents resistance to the flow of oxygen ions. Furthermore, much of the ohmic resistance in an SOFC generally comes from the electrolyte. In summary, EIS provides a method for quantifying the major sources of loss in a fuel cell. It is an extremely useful tool for experimental SOFC work, as it allows the user to quantitatively compare the effects of different SOFC fabrication processes and compositions, and it is the primary characterization technique used in this study. It should be noted that since all cells in this study were symmetric (having a cathode on either side of the electrolyte) the Nyquist plot shows only a single arc, from which cathode activation resistance and ohmic resistance can be obtained.

2.3.2 Electrode Performance

Of greater significance for the present discussion is the fact that SOFCs and SOEs can convert between chemical and electrical energy with very high efficiency.[172] In an ideal SOFC or SOE, the potential difference between the electrons consumed at the cathode and

those produced at the anode is given by the Nernst equation:

$$E_{Nernst} = E^0 + \frac{\tilde{R}T}{2F} \times ln\ ln \left(\frac{P_{H_2,anode}(P_{O_2,cathode})^{\frac{1}{2}}}{P_{H_2O,anode}} \right) \qquad \text{(Equation 2.6)}$$

where F is Faraday's constant (96400 C/mol), $\tilde{R}$ is a universal gas constant (8.314 J/K mol), T is absolute temperature in K, and E^0 is the equilibrium potential for reactants at the standard state. This equation is simply an expression for the reversible work associated with a charged particle moving from the $P(O_2)$ at the cathode to the $P(O_2)$ at the anode. The anode $P(O_2)$ in the Nernst equation, Equation 1, is a fugacity, rather than a true oxygen partial pressure, and is determined from the equilibrium expression for the H_2 oxidation reaction.

In real devices, some of the potential energy is lost in the electrodes and in the electrolyte. For understanding these losses, the electrolyte can usually be treated as a simple resistor, with a resistance R_e, so that the lost potential energy is proportional to the current and equal to iR_e. Minimizing the electrolyte losses is accomplished by making the ceramic membrane very thin and by choosing a material with a high ionic conductivity. Most research in SOFCs continues to focus on yttria-stabilized zirconia (YSZ) as the electrolyte. While there are materials that have higher ionic conductivities,[26,47,173] most of these either exhibit electronic conductivity under reducing conditions or are reactive with commonly used electrode materials. Because the electrodes should be good electric conductors, the lost potential energy, or overpotential, in an electrode results from the fact that the effective $P(O_2)$ at the electrode-electrolyte interface differs from the $P(O_2)$ within the electrode compartment.[174] At an SOFC cathode for example, this difference in $P(O_2)$ has two primary origins. First, gas-phase diffusion of oxygen through the porous electrode causes the $P(O_2)$ to be lower near the electrolyte interface. This electrode loss, referred to as concentration polarization, is weakly dependent on temperature and is only important at high current densities on electrodes with low porosities.[175] Second, finite oxidation rates for the electro-catalyst in the cathode, coupled with diffusion of oxygen anions to sites where the cathode and electrolyte are in contact, prevent the electrolyte interface from being in equilibrium with the gas phase. These processes are expected to show a strong Arrhenius temperature dependence and depend on the choice of materials used in the electrode.

The classical picture for understanding electrode overpotential indicates that there should be an exponential decrease in cell voltage with current density near an open circuit. This decrease is expected because of shifts in the reaction coordinate in the presence of large potential gradients at the electrode/electrolyte interface. In essence, potential gradients are viewed as playing a similar role in the electrochemical reaction as that of temperature in thermal reactions, helping reactants overcome the reaction activation barrier. Therefore, the electrode losses are often modeled using Butler-Volmer kinetics (equation 2.29), a simple exponential expression relating electrode potential and current density.[176]

$$j = j_0 \times \left\{ exp\left[\frac{n\alpha_{anode}F\eta}{RT} \right] - exp\left[-\frac{n\alpha_{cathode}F\eta}{RT} \right] \right\} \qquad \text{(Equation 2.6)}$$

In this equation, j is electrode current density (defined as $j = i/A$, [A/m^2]), j_0 is exchange current density, n is the number of electrons involved in the electrode reaction, α_{anode} and $\alpha_{cathode}$ are so-called anodic and cathodic charge transfer coefficients (dimensionless), and η is activation overpotential (unit is V, defined as $\eta = E - E_{eq}$, the difference between electrode potential and equilibrium potential).

However, in solid-oxide devices, the relationship between cell potential and current density is often linear over a very wide range of currents, as shown by the example in Figure 2.42(a). This example shows that the *i*-V relationship has a similar slope under both fuel-cell and electrolysis conditions. The change in slope at high electrolysis currents is likely due to diffusion limitations, since the water concentration sent to the cell was low. This example, along with many others from the literature,[177–179] does not even show an offset or change in slope when going from fuel-cell to electrolysis modes, a result that is difficult to rationalize in terms of the Butler-Volmer picture. Note: the data in Figure 2.42 were obtained on a cell with an LSF-YSZ cathode.

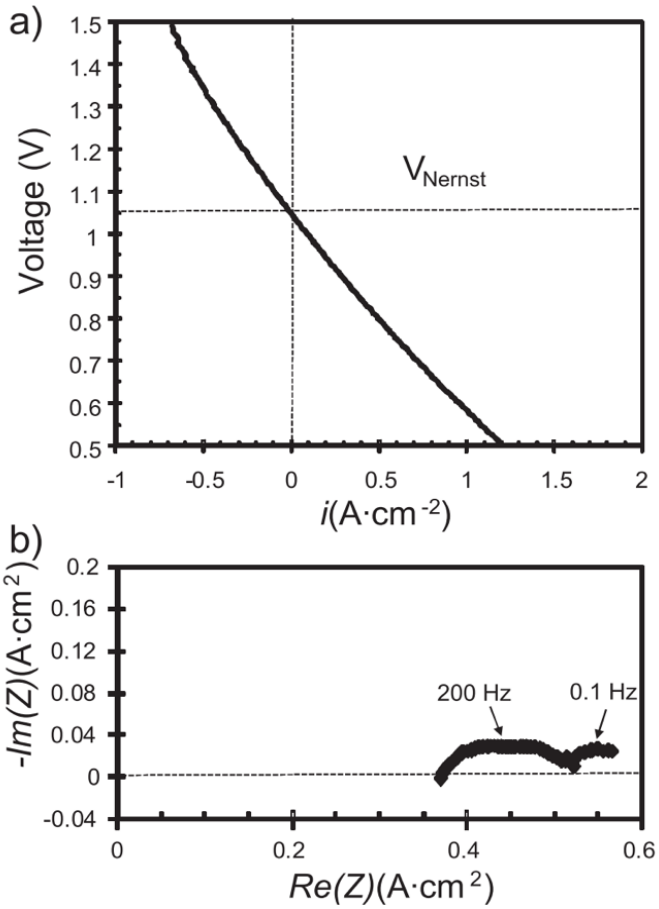

Figure 2.37: (a) *i*-V polarization curve and (b) Cole-Cole impedance spectrum for a SOFC/SOE operating at 700 ℃ on a fuel consisting of 90% H_2 and 10% H_2O. The cell composition was as follows: 40 wt.% LSF in YSZ/YSZ (65 mm)/0.5 wt.% Pd, 5 wt.% $Ce_{0.48}Zr_{0.48}Y_{0.04}O_2$, and 45 wt.% LSCM in YSZ. More details on the cell fabrication can be found in reference.[177]

If the voltage-current relationship is linear, it is convenient to describe the anode and cathode losses using the zero-frequency electrode impedances, R_a and R_c, with the anode and cathode overpotentials given by iR_a and iR_c. With these assumptions, the cell voltage, V, is given by Equation 2.7.

$$E = E_{Nernst} - i(R_e + R_a + R_c) \qquad \text{(Equation 2.7)}$$

When normalized to the active area of the fuel cell, the electrode impedances are sometimes referred to as area specific resistances (ASR). An example where impedance spectroscopy has been used to determine electrode and electrolyte losses is shown in Figure 2.42(b). This is a Cole-Cole plot of the impedance spectrum, taken at open circuit, corresponding to the V- i curve in Figure 2.42(a). The high-frequency intercept with the real axis at 0.36 Ωcm^2 is equal to the ohmic losses in the cell and is close to the value except for R_e based on the electrolyte thickness and the known conductivity of YSZ.[128] The length of the arc separating the zero-frequency and high-frequency intercepts on the real axis is equal to R_a + R_c, approximately 0.2 Ωcm^2 in this example. Separating R_a from R_c is more difficult. In principle, one can determine the individual cathode and anode impedances using reference electrodes; however, improper placement of reference electrodes can cause the measurements to be inaccurate.[35,180–183] It has been suggested that a significant portion of the published data obtained using reference electrodes is unreliable.[184] Alternatively, one can easily measure the sum of R_a and R_c and determine R_c (or R_a) by measurements on a cell for which R_a (or R_c) is already known. For example, there are cathode materials that exhibit negligible losses,[109] at least for short times, so that the total electrode losses would be equal to R_a.

The electrode impedance is a useful way to describe performance. If V decreases linearly with i, the maximum power density of the cell in W cm^{-2} is given by Equation 2.8. with the impedances in units of V cm^2. If one targets a power density of 1 W cm^{-2}, each of the individual impedances need to be less than approximately 0.1 V cm^2. For electrolytes, where resistivity is a materials property that is strongly dependent on temperature, it is relatively easy to use the maximum- impedance target to calculate the allowable electrolyte thickness as a function of temperature.[172]

$$P = \frac{(E_{Nernst})^2}{4(R_e+R_a+R_c)} \qquad \text{(Equation 2.8)}$$

2.3.3 Rate-determining step

Rate-determining step (RDS), also known as rate-limiting step. It is a common method to apply to SOFC research. In Equation 2.6, j_0 is the exchange current density. From previous publications[185–188] we know that it is as a function of P_{O_2} and temperature shows that oxygen for the charge-transfer process is supplied through adsorbed adatoms on the Pt electrode surface, obeying the Langmuir isotherm. At high P_{O_2}, the η-I curves obey the Bulter-Volmer equation, with transfer coefficients of unity, both for anodic and cathodic polarizations. This result implies a charge-transfer (or activation) mechanism. In addition, at low P_{O_2}, limiting current behavior is obtained for the cathodic polarization. We

can derive from $I_0 \propto \left(P_{O_2}\right)^m$ to Equation 2.9:

$$R_p \propto \left(P_{O_2}\right)^{-m} \qquad \text{(Equation 2.9)}$$

When $m = 0 - 0.25$ means Langumuir's type oxygen atom adsorption. The fraction of adsorption sites, θ, is very low; high temperature and/or low P_{O_2} (From a reaction $A_{gas} + S \rightleftharpoons A_{ads}$, Langumuir equation: $\theta_A = \frac{V_m}{V_m} = \frac{K_{eq}^A P_A}{1+K_{eq}^A P_A}$, where S represents an empty adsorption site and A_{ads} is an absorbed complex, θ_A is the fractional occupancy of adsorption sites, V_m is the volume of monolayer, K_{eq}^A is an associated equilibrium constant of complex A, and P_A is the adsorbate's partial pressure). When $m = 0$ means electrode resistance is not the function of P_{O_2}, the value of electrode resistance is a constant, we could assume that this process is dominated by the reaction between electrode and electrolyte ($O_{electrode}^{2-} \rightleftharpoons O_{electrolyte}^{2-}$, when $m = 0.125$ means $O_{ads}^- + e^- + V_{o"} \rightleftharpoons O_O^{2-}$ and $m = 0.5$ means $O_{ads,\,ERS} + 2e^- + V_{o"} \rightleftharpoons O_{O^x}$). When $m = 0.375$ means oxide ion diffusivity ($O_{ads} \rightleftharpoons O_{ads}^-$). When $m = 0.5$ means dissociation ability of oxygen molecules ($O_{2,ads} \rightleftharpoons 2O_{ads}$). When $m = 1$, the adsorption ability of oxygen molecules ($O_{2(g)} \rightleftharpoons O_{2,ads}$). ERS means electrochemical reaction site, where $V_{o"}$ and O_{O^x} indicate an oxide ion vacancy and an oxide ion in normal lattice sites (Kröger-Vink notation). By analyzing the value of this reaction order m, we are able to know which reaction dominates the work process. Once we know it we can focus on it and make some improvement.

2.4 Microstructure characterization

2.4.1 Scanning Electron Microscopy

In addition to characterizing fuel cell performance using electrochemical characterization methods, it is also important to examine the microstructure of SOFC electrodes, in order to explore the relationships between electrochemical performance and the physical structure of the electrode. Some microstructural characteristics that effect electrode performance include particle size and interconnectivity, electrode porosity and tortuosity, electrode layer thickness and uniformity, and electrode/electrolyte adhesion. High magnification (> 10,000x) and excellent image resolution is required to properly observe these features. The scanning electron microscope (SEM) allows for detailed observation of features on a micrometer or even a nanometer scale. Although a detailed description of SEM operation is beyond the scope of this thesis, a brief overview will be given.

In the SEM, a finely focused beam of electrons is scanned across the surface of the sample to be examined. Several types of interactions occur between the electrons and the sample, including (but not limited to) backscattered electron interactions and secondary electron interactions, which provide information about sample composition and surface topography, respectively.[189] Backscattered electrons come directly from the focused electron beam, are detected by the molecules or atoms making up the sample, and are

collected by a backscattered electron detector. The number of backscattered electrons that are detected depends upon the atomic number of the elements making up the sample; heavier elements detect more electrons. Therefore, backscattered electron signals give information about the sample composition; darker spots on the formed image represent the heavier elements in the sample, and lighter spots represent lighter elements. In contrast, secondary electron interactions do not come directly from the focused electron beam. Secondary electrons are outer shell electrons belonging to the atoms making up the specimen. Electrons with sufficient energy coming from the electron beam can knock these outer electrons out of orbit, allowing them to pass through the specimen and to be collected by the secondary electron detector. Secondary electron collection is highly directional; that is, most of the electrons that are collected are ones that exit the specimen facing the detector. Because of this, secondary electron signals provide information about the surface topography of the specimen; surfaces facing the detector appear to be illuminated, while surfaces facing away from the detector appear to be shaded. Additionally, because of the relatively low energy of the outer shell electrons, only secondary electrons emitted near the surface of the specimen are collected. Because of the small sampling depth, secondary electron signals provide very detailed, high resolution images of the surface of the specimen. Using a combination of backscattered electron and secondary electron signals, the SEM can generate highly detailed images of the specimen to be studied, allowing for extensive study of microstructural characteristics of the material. In this study, SEM is used extensively in conjunction with EIS to investigate correlations between electrode microstructure and electrochemical performance.

2.4.2 X-Ray Diffraction

X-ray diffraction (XRD, also known as X-ray crystallography) is a technique used for determining the atomic and molecular structure of a crystal, in which the crystalline atoms cause a beam of incident X-rays to diffract into many specific directions. By measuring the angles and intensities of these diffracted beams, a crystallographer can produce a three-dimensional picture of the density of electrons within the crystal. From this electron density, the mean positions of the atoms in the crystal can be determined, as well as their chemical bonds, their disorder, and various other information.[190–192] In other words, we used XRD analyze to make sure what we have in our samples.

Crystals are regular arrays of atoms, and X-rays can be considered waves of electromagnetic radiation. Atoms scatter X-ray waves, primarily through the atoms' electrons. Just as an ocean wave striking a lighthouse produces secondary circular waves emanating from the lighthouse, so an X-ray striking an electron produces secondary spherical waves emanating from the electron. This phenomenon is known as elastic scattering, and the electron (or lighthouse) is known as the scatterer. A regular array of scatterers produces a regular array of spherical waves. Although these waves cancel one another out in most directions through destructive interference, they add constructively in a few specific directions, determined by Bragg's law:

$$2d\ sin\ sin\ \theta\ = n\lambda \qquad \text{(Equation 2.10)}$$

Here d is the spacing between diffracting planes, θ is the incident angle, n is any integer, and λ is the wavelength of the beam (Figure 2.38). These specific directions appear as spots on the diffraction pattern called reflections. Thus, X-ray diffraction results from an electromagnetic wave (the X-ray) impinging on a regular array of scatterers (the repeating arrangement of atoms within the crystal). As shown in Figure 2.38, the incoming beam (coming from upper left) causes each scatterer to re-radiate a small portion of its intensity as a spherical wave. If scatterers are arranged symmetrically with a separation d, these spherical waves will be in sync (add constructively) only in directions where their path-length difference $2d\ sin\ sin\ \theta$ equals an integer multiple of the wavelength λ. In that case, part of the incoming beam is deflected by an angle 2θ, producing a reflection spot in the diffraction pattern.

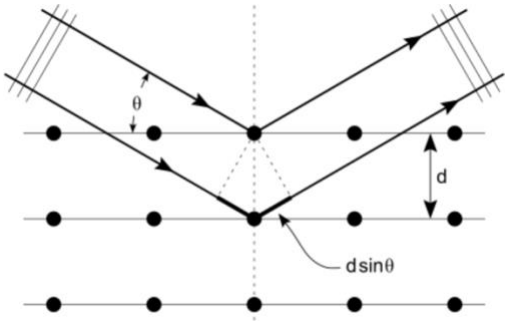

Figure 2.38: A regular array of scatterers (atoms' electrons) produces a regular array of spherical waves when X-ray waves come from some specific angle.

2.4.3 Atomic Force Microscopy

Atomic force microscopy (AFM) or scanning force Microscopy (SFM) is a very-high-resolution type of scanning probe microscopy (SPM), with demonstrated resolution on the order of fractions of a nanometer, more than 1000 times better than the optical diffraction limit. The information is gathered by "feeling" or "touching" the surface with a mechanical probe. Piezoelectric elements that facilitate tiny but accurate and precise movements on (electronic) command enable precise scanning.

The AFM has three major abilities: force measurement, imaging, and manipulation. In force measurement, AFMs can be used to measure the forces between the probe and the sample as a function of their mutual separation. This could be applied to perform force spectroscopy, to measure the mechanical properties of the sample, such as the sample's Young's modulus, a measure of stiffness. For imaging, the reaction of the probe to the forces that the sample imposes on it could be used to form an image of the three-dimensional shape (topography) of a sample surface at a high resolution. This is achieved by raster scanning the position of the sample with respect to the tip and recording the height of the probe that corresponds to a constant probe-sample interaction (see section topographic imaging in AFM for more details). The surface topography is frequently displayed as a pseudo-color plot. In manipulation, the forces between tip and sample can also be used to change the properties of the sample in a controlled way. Examples of this

include atomic manipulation, scanning probe lithography and local stimulation of cells. Simultaneous with the acquisition of topographical images, other properties of the sample can be measured locally and displayed as an image, often with similarly high resolution. Examples of such properties are mechanical properties like stiffness or adhesion strength and electrical properties such as conductivity or surface potential. In fact, the majority of SPM techniques are extensions of AFM that use this modality.[193]

Figure 2.39 shows an AFM, which typically consists of the following features. Numbers in parentheses correspond to numbered features in Figure 2.39. Coordinate directions are defined by the coordinate system (0). The small spring-like cantilever (1) is carried by the support (2). Optionally, a piezoelectric element (typically made of a ceramic material) (3) oscillates the cantilever (1). The sharp tip (4) is fixed to the free end of the cantilever (1). The detector (5) records the deflection and motion of the cantilever (1). The sample (6) is mounted on the sample stage (8). An xyz drive (7) permits the displacement of the sample (6) and the sample stage (8) in x, y, and z directions with respect to the tip apex (4). Although it shows the drive attached to the sample, the drive can also be attached to the tip, or independent drives can be attached to both, since it is the relative displacement of the sample and tip that needs to be controlled. Controllers and plotters are not shown in Figure 2.39.

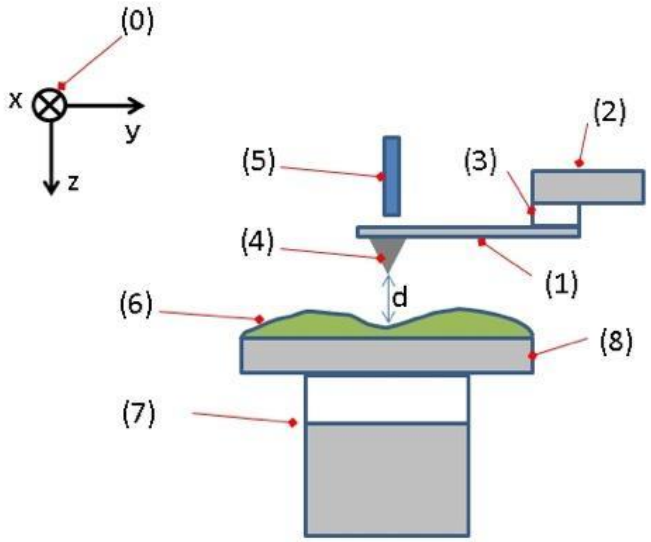

Figure 2.39: Typical configuration of an AFM. (1): Cantilever, (2): Support for cantilever, (3): Piezoelectric element(to oscillate cantilever at its eigen frequency.), (4): Tip (Fixed to open end of a cantilever, acts as the probe), (5): Detector of deflection and motion of the cantilever, (6): Sample to be measured by AFM, (7): xyz drive, (moves sample (6) and stage (8) in x, y, and z directions with respect to a tip apex (4)), and (8): Stage.

According to the disposition described above, the interaction between tip and sample, which can be an atomic scale phenomenon, is transduced into changes of the motion of the cantilever which is a macro scale phenomenon. Several different aspects of

the cantilever motion can be used to quantify the interaction between the tip and sample, most commonly the value of the deflection, the amplitude of an imposed oscillation of the cantilever, or the shift in resonance frequency of the cantilever. The detector (5) of AFM measures the deflection (displacement with respect to the equilibrium position) of the cantilever and converts it into an electrical signal. The intensity of this signal will be proportional to the displacement of the cantilever. Various methods of detection can be used, e.g. interferometry, optical levers, the piezo-resistive method, the piezoelectric method, and STM-based detectors.

The cantilever is typically silicon or silicon nitride with a tip radius of curvature on the order of nanometers. When the tip is brought into proximity of a sample surface, forces between the tip and the sample lead to a deflection of the cantilever according to Hooke's law.[194] Depending on the situation, forces that are measured in AFM include mechanical contact force, van der Waals forces, capillary forces, chemical bonding, electrostatic forces, magnetic forces (see magnetic force microscope, MFM), Casimir forces, solvation forces, etc. Along with force, additional quantities may simultaneously be measured through the use of specialized types of probes. The AFM can be operated in a number of modes, depending on the application. Generally, possible imaging modes are divided into static (also called contact) modes and a variety of dynamic (non-contact or "tapping") modes where the cantilever is vibrated or oscillated at a given frequency.[193]

The disparity of contact area with load between adhesive elastic spheres (tip apexes) depends upon the effective range of attractive surface forces. Comparatively simple formations to illustrate limiting cases occur, but the general intermediate case involves a more complicated analysis and investigation. Robert W. Carpick *et al.*[195] present a more straightforward general equation that approximates *Maugis' solution* exceedingly closely. The general equation is susceptible to traditional curve fitting software routines and offers an instantaneous way of calculating the value of the "transition parameter" which delineates the range of surface forces. Continuum models which anticipate the contact area for diverse geometries have been worked out beginning with the initiating work of Hertz.[196] Experimental techniques that quantify contact area for elastic single severities; in other words, the surface forces apparatus (SFA).[197,198] The atomic force microscope (AFM), can be reported by the geometry of contacting spheres (approximated as paraboloids). In the case of the AFM, one sphere appears for the sample, with an infinite radius of curvature, while the other sphere appears for the tip, which in many cases matches to a paraboloid shape.[199] In the nonattendance of adhesion, the Hertz model has been shown to accurately relate the contact area between elastic spheres.[200] Nevertheless, at small scales the surface-to-bulk ratio becomes remarkable. Consequently, adhesion emerging from attractive surface forces is usually not insignificant and must be concerned in any illustration of the contact area.

The spatial range over which surface forces act depends upon the chemistry of the materials in contact, as well as may or may not be long range compared to the scale of elastic deformations due to these forces,[201] they are shown in Figure 2.40. Two limiting cases are obvious. When the surface forces are short range in comparison to the elastic deformations they cause (for examples, compliant materials, strong adhesion forces, large tip apex radii), the contact area is described by the Johnson–Kendall–Roberts (JKR) model.[202] The opposite limit like stiff materials, weak adhesion forces, small tip apex radii

is concerned to as the Derjaguin-Müller-Toporov (DMT) pattern[203] and the configuration of the contact area is submitted in the work of Maugis[204] It is appropriate to harness a non-dimensional physical parameter to calculate these limits and cases in between. Often referred to as Tabor's parameter μ , this transition parameter is defined as Equation 2.11.[205]

$$\mu = \left(\frac{16R\gamma^2}{9K^2 z_0^3}\right) \qquad \text{(Equation 2.11)}$$

where z_0 is the equilibrium separation of the surfaces, *R* is the tip curvature radius, γ is the interfacial energy per unit area (work of adhesion), and *K* is the combined elastic modulus of tip and sample, given by:

$$K = \frac{4}{3}\left(\frac{(1-v_1^2)}{E_1} + \frac{(1-v_2^2)}{E_2}\right)^{-1} \qquad \text{(Equation 2.12)}$$

where E_1 and E_2 are the tip and sample Young's moduli, and v_1 and v_2 are the tip and sample Poisson ratios, respectively. The quantity μ is in fact equal to the ratio of the elastic deformation just before the surfaces separate to the equilibrium separation z_0. To approach an actual interaction potential like that depicted in Figure 2.40, Maugis[204] reflects on a "Dugdale" (square well) potential to describe attractive forces between contacting spheres (Figure 2.41), where a constant adhesive stress σ_0 acts over a range δ_t.

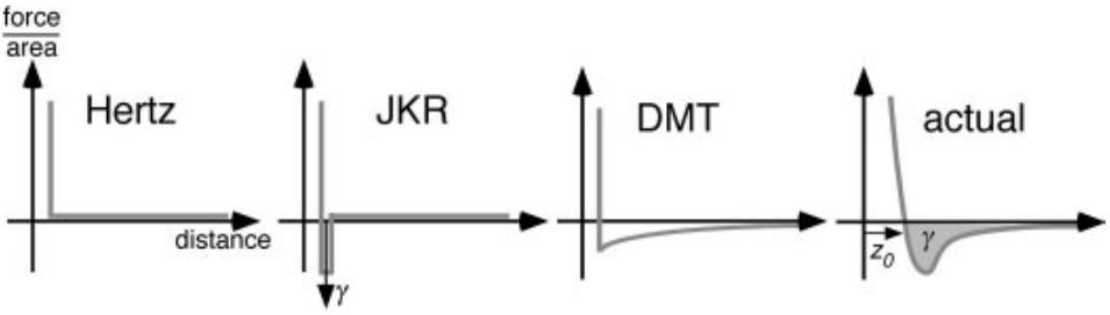

Figure 2.40: Interaction forces (per unit area) for the Hertz, JKR, and DMT models, compared to a realistic interaction. There is no attractive force in the Hertz model, only hard wall repulsion at contact. The JKR model includes short range adhesion which is essentially a delta function with strength γ and thus acts only within the contact zone. The DMT curve shown represents a long-range surface force. A volume-integrated force, like the van der Waal's force, can also lead to a DMT dependence, where the contact profile remains Hertzian and the attractive forces act like an additional external load. For an actual interaction force, the integral of the force–distance attractive well corresponds to the work of adhesion, γ.[195]

Thus, the work of adhesion is $\gamma = \sigma_0 \times \delta_t$. Maugis defines a parameter, λ, which is similar to μ, given by:

$$\lambda = 2\sigma_0 \left(\frac{R}{\pi\gamma K^2}\right)^{\frac{1}{3}} \qquad \text{(Equation 2.13)}$$

By choosing σ_0 to coordinate with the minimum adhesive stress of a Lennard-Jones potential (with equilibrium separation z_0), it obeys that δ_t=0.97z_0, and so λ =1.1570 μ . Thereby, λ and μ are approximately identical. For convenience they (so do we) referred to λ in their study as the "transition parameter". If $\lambda > 0.1$, the DMT model applies, and if $\lambda > 5$, the JKR model applies. Values between 0.1 and 5 would be assigned to the "transition regime" between JKR and DMT. A review of various conventions used for defining this "transition parameter" is reported by Greenwood.[205] The Hertz model applies when there are no attractive surface forces ($\gamma = 0$).

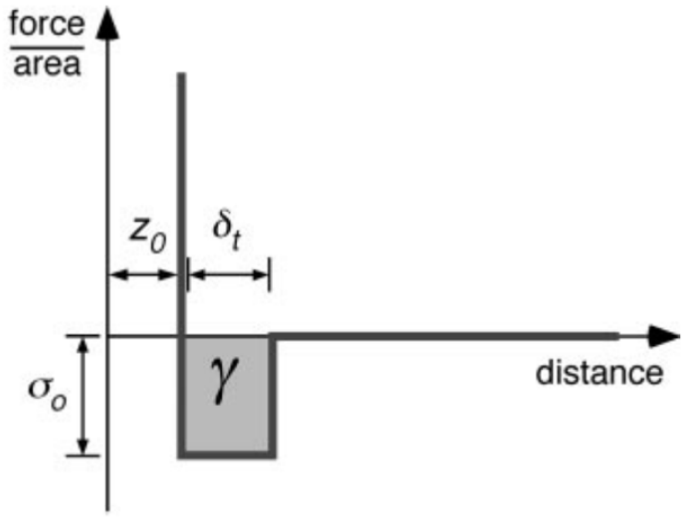

Figure 2.41: The force-distance relation for the Dugdale model used by Maugis. A constant adhesive stress (force per unit area) σ_0 acts between the surfaces over a range δ_t. At greater distances, the attractive force is zero. The work of adhesion is thus $\gamma = \sigma_0 \times \delta_t$.[195]

The dissimilarity of contact area with load for various values of λ, and for the Hertz model, is graphed in Figure 2.42. In the non-zero adhesion cases, there is a well-defined "pull-off force" or negative "critical load" at which the surfaces separate when being pulled apart. This applies for the case of "fixed loads" where one of the spheres is attached to an acquiescent spring (the cantilever of AFM would be in the case). Robert W. Carpick *et al.* referred to this negative critical load as L_C,and for the two limiting cases it is given by:

$$L_{C(JKR)} = -\frac{3}{2}\pi\gamma R \qquad \text{(Equation 2.14a)}$$

$$L_{C(DMT)} = -2\pi\gamma R \qquad \text{(Equation 2.14b)}$$

The models also predict particular values for the contact radius at zero load a_0, given by:

$$a_{0(JKR)} = \left(\frac{6\pi\gamma R^2}{K}\right)^{\frac{1}{3}} \qquad \text{(Equation 2.15a)}$$

$$a_{0(DMT)} = \left(\frac{2\pi\gamma R^2}{K}\right)^{\frac{1}{3}} \qquad \text{(Equation 2.15b)}$$

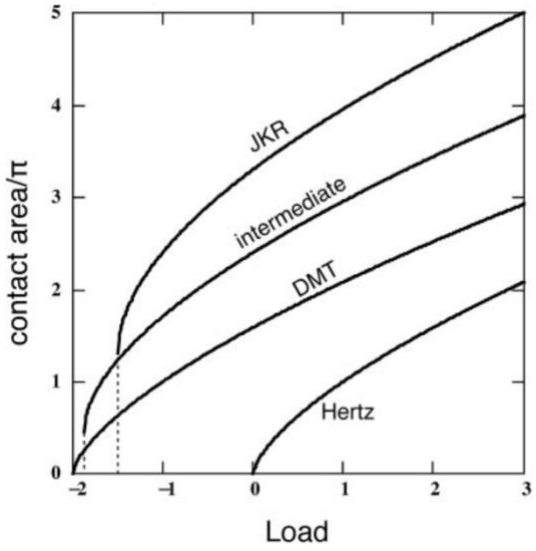

Figure 2.42: The Hertz area-load curve, and the JKR-DMT transition, plotted in Maugis' units (Equation 2.20). Area-load curves for the JKR limit, the DMT limit, and an intermediate case are shown. These approach the Hertz curve in the limit $\gamma \to 0$ (no adhesion). Adhesion increases the contact area from the Hertz case for a given load by an amount dependent upon the range of attractive forces.[195]

The difference of contact radius a with load L for the JKR and DMT cases are each described by relatively simple equations:

$$\frac{a}{a_{0(JKR)}} = \left(\frac{1+\sqrt{1-\frac{L}{L_{C(JKR)}}}}{2}\right)^{\frac{2}{3}} \qquad \text{(Equation 2.16a)}$$

$$\frac{a}{a_{0(DMT)}} = \left(1 - \frac{L}{L_{C(DMT)}}\right)^{\frac{1}{3}} \qquad \text{(Equation 2.16b)}$$

Since the tip is axially symmetric, the contact area A is simply given by:

$$A = \pi a^2 \qquad \text{(Equation 2.17)}$$

It is obvious that Equations 2.16a and 2.16b could be generalized to form an equation which describes the contact radius for both cases,

$$\frac{a}{a_{0(\alpha)}} = \left(\frac{\alpha + \sqrt{1 - \frac{L}{L_{C(\alpha)}}}}{1+\alpha} \right)^{\frac{2}{3}} \qquad \text{(Equation 2.18)}$$

where $\alpha = 1$ exactly correlates with the JKR case, and $\alpha = 0$ exactly agrees with the DMT case. Included in Equation 2.18 is the fact that L_C and a_0 depend on as well. They referred to Equation 2.18 as the generalized transition equation. They showed that for intermediate cases ($0 < \alpha < 1$), the generalized transition equation is in agreement with very closely to solutions for the transition regime ($0.1 < \lambda < 5$) sophisticatedly worked out by Maugis using the *Dugdale model*.[204] Using the *Dugdale mode*l is a fair-minded way for approximating the value of the contact radius (and other quantities) as a function of load. The solution is referred to as the "MD" solution (*Maugis-Dugdale*). Two equations are needed to relate a and L:

$$\frac{\lambda \hat{a}^2}{2}\left[\sqrt{m^2-1} + (m^2-2)\left(\frac{1}{m}\right)\right] + \frac{4\lambda^2 \hat{a}}{3}\left[\sqrt{m^2-1}\left(\frac{1}{m}\right) - m + 1\right] = 1 \qquad \text{(Equation 2.19a)}$$

$$\hat{L} = \hat{a}^3 - \lambda \hat{a}^2\left[\sqrt{m^2-1} + m^2\left(\frac{1}{m}\right)\right] \qquad \text{(Equation 2.19b)}$$

where $\hat{L}$ and $\hat{a}$ are simple parameterizations of L and a,

$$\hat{L} = \frac{L}{\pi \gamma R} \qquad \text{(Equation 2.20a)}$$

$$\hat{a} = a\left(\frac{K}{\pi \gamma R^2}\right)^{\frac{1}{3}} \qquad \text{(Equation 2.20b)}$$

and the parameter m represents the ratio between the contact radius a and an outer radius c at which the gap between the surfaces reaches δ_t (i.e., where the adhesive stress no longer acts). *Maugis' equations* satisfactorily predict the JKR and DMT limits.

The struggle in utilizing the MD equations lies in the lack of a single expression relating only a and L. To plot the MD solution or fit it to the data, one needs to simultaneously solve Equations 2.19a and 2.19b by making m change properly between limits which depend upon λ. Moreover, the connection for the pull-off force must be calculated through repetition[205] if the value of λ is not known as a primary factor (the usual case with experimental measurements). In application, this is rather unmanageable if not

impossible to carry out with common software programs that utilize automated statistical fitting procedures. Table 2.7 displays the optimized values of α for various values of λ. An experiential formula was fit to this table of values to provide a conversion equation from α to λ, it is also shown in Figure 2.43, which is given by:

$$\lambda = -0.924\, ln\, ln\, (1 - 1.02\alpha) \qquad \text{(Equation 2.20)}$$

α	λ	$\hat{L}_c(\lambda)$	$\hat{a}_0(\lambda)$
DMT: 0	0	-2	$\sqrt[3]{2} = 1.260\cdots$
0.074	0.1	-1.951	1.336
0.158	0.2	-1.881	1.394
0.256	0.4	-1.816	1.442
0.433	0.5	-1.718	1.517
0.609	0.8	-1.634	1.598
0.692	1.0	-1.601	1.636
0.817	1.5	-1.556	1.700
0.886	2.0	-1.535	1.738
0.922	2.5	-1.523	1.760
0.944	3.0	-1.517	1.775
0.958	3.5	-1.513	1.785
0.967	4.0	-1.510	1.792
0.979	5.0	-1.506	1.800
JKR: 1	∞	$-3/2$	$\sqrt[3]{6} = 1.817\cdots$

Table 2.7: The optimized values of α for various values of λ.[195]

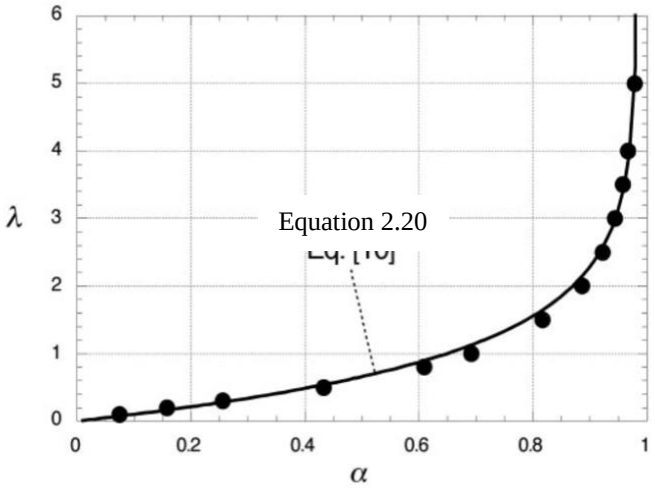

Figure 2.43: Plot of α vs λ from Table I (filled circles) and the empirical conversion equation, Equation 2.20 (solid line), fit to the data.[195]

2.4.4 Conductive atomic force microscopy

Conductive atomic force microscopy (CAFM) has been extensively applied to study the localized electrical properties of a vast range of substrates in non-vacuum conditions by the use of noble metal-coated tips such as platinum and gold. In this Section, I will review some reports about the discussion of mechanical change while AFM is working and electrical behavior of CAFM by metallic tips. We try to find the relation between mechanism and conductive fluctuation of the working conductive AFM tip.

So far we know how to calculate the contact area of AFM while it is working. We are going to cover conductance fluctuation and degeneracy in nano-contact between a conductive AFM tip. Bietsch *et al*.[206] investigated the nano-contacts between a Pt-coated AFM tip and gold film and found that the conductance is stable only under large contact force (about 500 – 600 nN) and large contact width (about 20 nm) conditions, but unsteady under small-load situation (less than 100 nN). Houzé *et al*.[207] reported that the contact resistances are highly scattered (from 102 to 1010 V) by scanning a W-coated CAFM tip on the sample of W film. However, they explained the resistance variation only from the different oxidation states of the surface grains, instead of the inherent instabilities of this type of nano-contact. Actually, the unpredictability of resistance; in the other words, conductance fluctuation, in nano-contacts in scanning tunneling microscopy (STM),[208] in mechanically controllable break junctions (MCBJ)[209] and in metal nano-bridges,[210,211] have already been observed. In the publication of Deng-Zhu Guo *et al*.[212] they experimentally investigated the electrical properties of the nano-contact between a W_2C-coated CAFM tip and grainy gold film under small-load (about 5 nN) at ambient air conditions. They found that under a constant bias voltage (10 V), the electrical current passing through the tip-sample junction at a fixed location of the sample surface significantly fluctuated and degenerated. By quantitatively calculating the mechanical and electrical facets of the nano-contact, they explained the observed phenomena as mechanical instabilities, electron tunneling transport and atomic rearrangements at the contact junction. They think that the results are important for the realistic application of CAFM in nano-electronic measurement. They also found that under the ambient air conditions, the iteration of I-V measurement for most kinds of samples is really bad. Figure 2.44 shows three typical I-V curves obtained at the same surface location of the sample of gold film with W_2C-coated CAFM tip under about 5 nN load condition. The curves A, B and C are pretty various from each other: in curve A, there is no detectable current within all the ±10 V voltage range; in curve B, current appears only above positive voltage +8 V; and in curve C, except for a dead bias region (-2.5 to +6.5 V), current appears asymmetrically at both positive and negative bias end. In addition, it is strange to note the negative resistance peaks (current decreases with voltage increasing) in curves B and C. Clearly, these I-V curves are not usable in judging the sample electrical properties, but imply that the tip-sample contact system might be electrically unreliable.

In order to investigate the reliability of the tip-sample electrical contact, they applied 10 V bias voltage between the tip and sample (sample negative) at a fixed surface location and recorded the current-time curves. They found that the current is not steady under the constant bias voltage and, alternatively, behaves like random pulses, as shown in Figure 2.45. During the first few minutes, the pulse density increases gradually and then it

begins to decrease. The typical pulse behavior after biased 1 minute, 15 minutes, 30 minutes and 40 minutes are respectively exhibited in Figure 2.50(a)-(d), indicating that the current pulses have the tendency to change from dense to sparse with time and their amplitude also gradually decreases. The apparent contact resistance, estimated by V/I, is changed between 400 MΩ and 10 GΩ for most time. After 45 min, the current attenuated to an undetectable value and no current recovered afterwards. The whole procedure is shown in Figure 2.46. which displays that the average current, obtained by arithmetically averaging the current data within every minute, degenerates in oscillation with time.

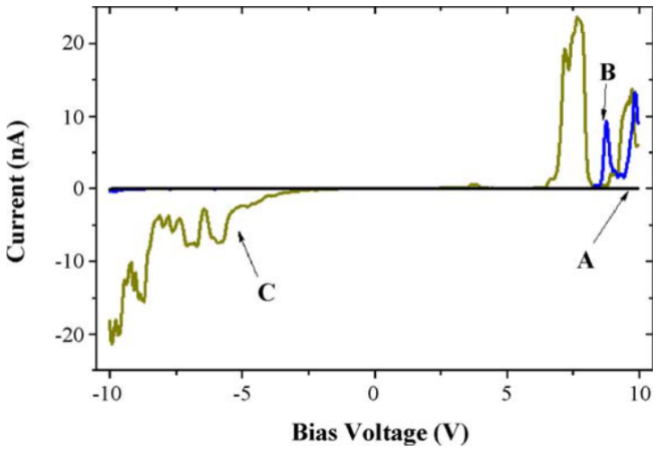

Figure 2.44: Non-repeatability of I-V curves measured in the same location of the sample surface.[212]

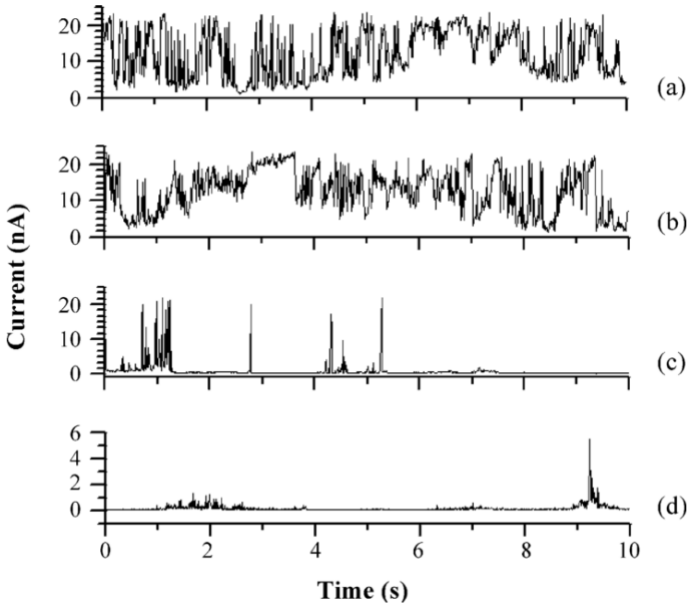

Figure 2.45: Current fluctuation and degeneracy behaviors in the nano-contact under constant ~ 5 nN contact load and 10 V bias voltage. The I–t curves after biased 1 min (a), 15 min (b), 30 min (c) and 40 min(d) are shown, respectively.[212]

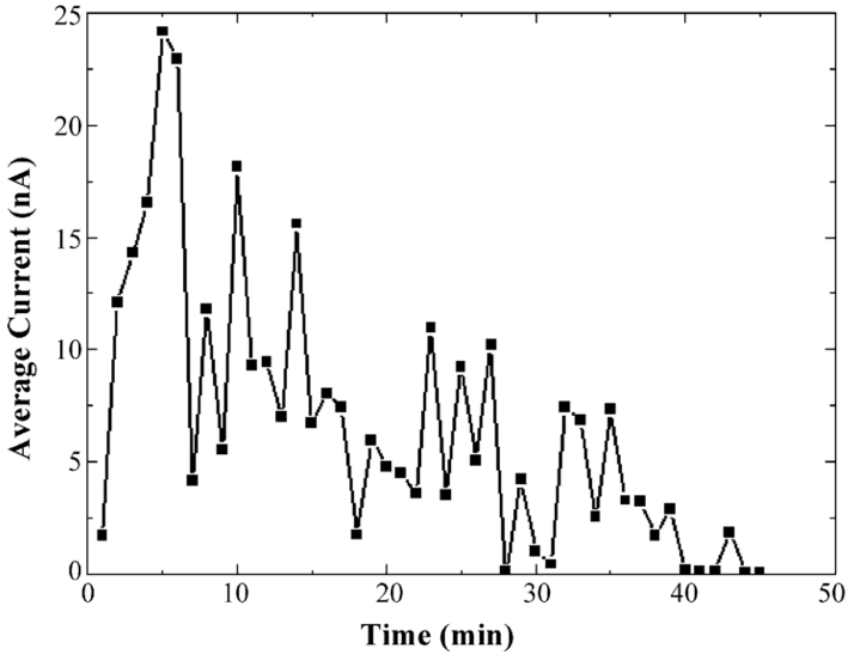

Figure 2.46: The degenerative behavior of the average current, noting it becomes completely undetectable after biased 45 min.[212]

They consider the electron transport modes in the tip–sample contact. If a real electrical contact is established between the AFM tip and particle surface, for example, no insulating layer exists between the two conductors, the electrons transport through the contact junction very likely by scattering and/or ballistic modes. The size-dependent contact resistance of each contact point comes from the constriction resistance R_C, which is the solution of a Laplace equation with appropriate boundary conditions:[213]

$$R_C = \frac{4(\rho_1+\rho_2)\lambda}{9\pi r^2} + \frac{\rho_1+\rho_2}{2\pi r}\int_0^\infty e^{-\frac{x\lambda}{r}}\frac{\sin(\pi x)}{\pi x}\,dx \qquad \text{(Equation 2.21)}$$

where ρ_1 and ρ_2 are the specific resistivities of the materials in contact, respectively, λ is the average electron free path, i.e., $\lambda = (\lambda_1 + \lambda_2)$ and r is the contact radius. if $r < \lambda$, R_C is dominated by *Sharvin's ballistic mechanism*[214] and the equation reduces to:

$$R_S = \frac{\lambda(\rho_1+\rho_2)}{2\pi r^2} \qquad \text{(Equation 2.22)}$$

if $\lambda < r$, the scattering mode is dominant and the contact resistance is reduced to the Maxwell formula:[215]

$$R_S = \frac{\rho_1+\rho_2}{4r} \qquad \text{(Equation 2.23)}$$

Ryan O'Hayre *et al.*[216] indicated that a methodology is suggested that empowers the withdrawal of quantitative information from the AFM impedance technique. This methodology applies results from nano-indentation experiments and contact mechanics theory to characterize AFM probe contacts. Using these results, contact forces between probe and sample (which can be accurately measured in the AFM) may be converted into probe-sample contact area approximations. These contact area approximations, when included in the model of the probe-sample contact, enable the withdrawal of quantitative data. This methodology is applied to the recently developed AFM impedance measurement technique, enabling a quantitative study of the oxygen reduction reaction (ORR) at nanometer length scales. Using the AFM impedance system, kinetic data for the (ORR) at nanoscale Platinum-Nafion contacts is withdrawn.

A general schematic graph of the AFM-impedance concept is shown in Figure 2.47. The system is built from a commercially obtainable AFM coupled to an electrochemical measurement instrument. The AFM unit is equipped with a conductive tip that provides the probe electrode for the desired electrical(electrochemical) measurements. The signal measured by the system depends essentially on the nature of the contact of tip and sample. For an identical sample, the spreading resistance equated with a small volume of material near the contact point between tip and sample, usually dominates the total impedance response of the system. Figure 2.48 proposes a simple equivalent circuit model of the contact between tip and sample. The contact is modeled as a parallel RC element with additional series resistors included to account for the tip and sample spreading resistances. The resistance of the tip (R_{tip}) is usually remarkable given the small sizes of AFM probes.

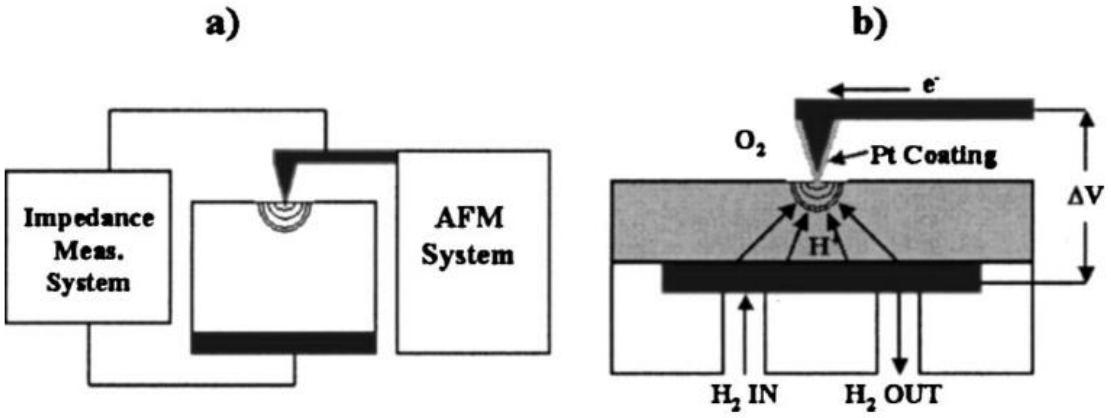

Figure 2.47: AFM impedance measurement. (a) General concept. Impedance is measured between a local probe (the AFM tip) and a bulk electrode. A significant spreading resistance contribution at the AFM tip/sample contact point ensures local characterization. (Shown schematically by the hemi- spherical lines.) (b) Detail of the Pt/Nafion impedance experiment. ORR kinetics at the interface between a Pt-coated AFM tip and a Nafion electrolyte membrane are measured using AFM impedance. Electrochemical bias is applied relative to the bulk bottom electrode (a reversible hydrogen electrode) which is hermetically sealed and supplied with hydrogen gas.[216]

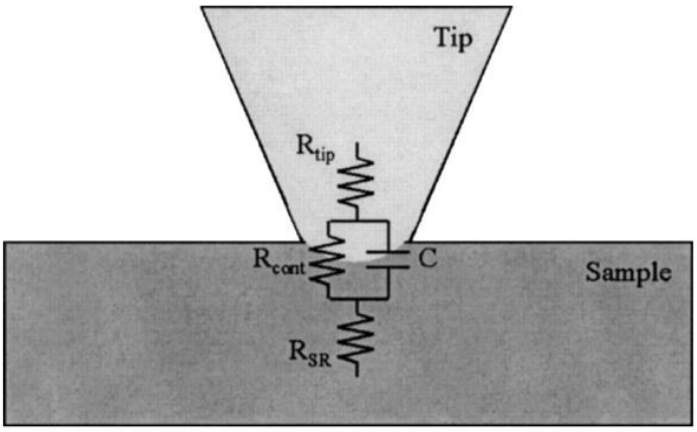

Figure 2.48: Simple equivalent circuit model of the tip/sample contact. R_{tip} represents the resistance contribution from the tip, R_{cont} accounts for the tip/sample interfacial resistance, which may include Schottky or Faradaic effects if the contact is non-ohmic. C represents the tip/sample capacitance. R_{SR} accounts for the spreading resistance associated with a small volume of material just beyond the tip/sample contact.[216]

2.4.5 Kelvin probe force microscopy

Kelvin probe force microscopy (KPFM) is a tool that enables the user to measure the local contact potential difference between a CAFM tip and the sample, thereby mapping the work function or surface potential of the sample with high spatial resolution. There are three stages of electronic energy levels of the AFM probe and sample: (shown in Figure 2.49) (a)before contacting: AFM probe and sample area separated in distance *z* with no electrical contact, (b)during contacting: AFM probe and sample are in electrical contact, and (c)bias applied: external bias (V_{DC}) is applied between AFM probe and sample to nullify the contact potential difference (V_{CPD}). (Figure 2.49)We provided AC with specific frequencies and DC bias (Equation 2.24) as well to nullify the contact potential difference. Then expanded the electrostatic force equation (Equation 2.25a) and put that ΔV equals the difference between the bias we provided to the probe and contact potential difference. We used the third part of this equation to measure the contact potential difference. By doing this, we are able to measure the sample's surface potential. We used the third part of Equation 2.25b to measure the contact potential difference.

$$V_{probe} = V_{AC}\, sin\, sin\, (\omega t)\ + V_{DC} \qquad \text{(Equation 2.24)}$$

$$F_{es} = -\frac{1}{2}\Delta V^2 \frac{dC(z)}{dz} \quad \text{(Equation 2.25a)}$$

$$F_{es} = -\frac{1}{2}\frac{dC(z)}{dz}\left(V_{probe} - V_{CPD}\right)^2 = -\frac{1}{2}\frac{dC(z)}{dz}[(V_{DC} - V_{CPD}) + V_{AC}\, sin\, sin\, (\omega t)\,]^2$$
$$= -\frac{1}{2}\frac{dC(z)}{dz}(V_{DC} - V_{CPD})^2 - \frac{1}{4}\frac{dC(z)}{dz}{V_{AC}}^2[1 + cos(2\omega t)] - \frac{dC(z)}{dz}(V_{DC} - V_{CPD})V_{AC}$$
$$sin\, sin\, (\omega t) \quad \text{(Equation 2.25b)}$$

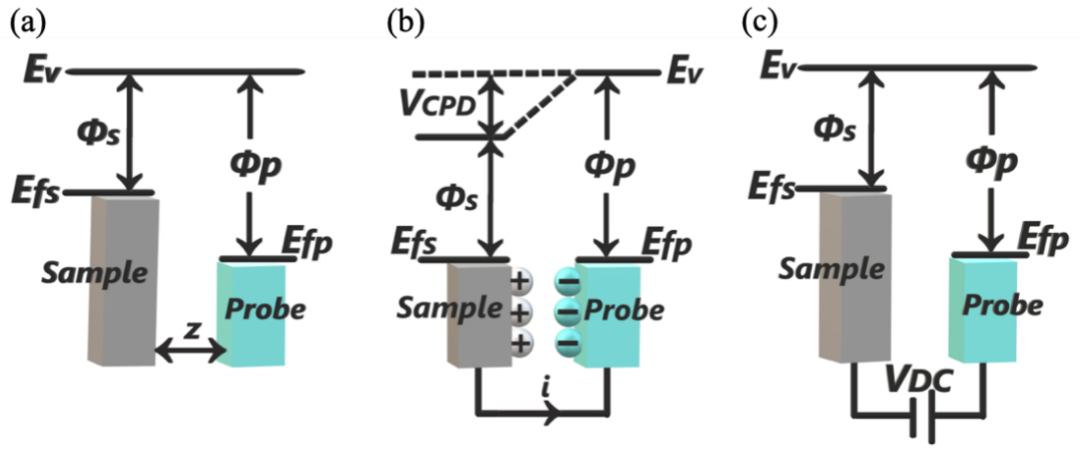

Figure 2.49: Three stages of electronic energy levels of the AFM probe and sample: (a) before contacting the AFM probe with a sample area separated by distance z with no electrical contact; (b) while in contact the AFM probe and samples also conduct electricity; and (c) the external bias (V_{DC}) is applied between AFM probe and sample to nullify the contact potential difference (V_{CPD}). E_v is the vacuum energy level, E_{fs} is the Fermi energy level of sample, and E_{fp} is the Fermi energy level of the AFM probe.)

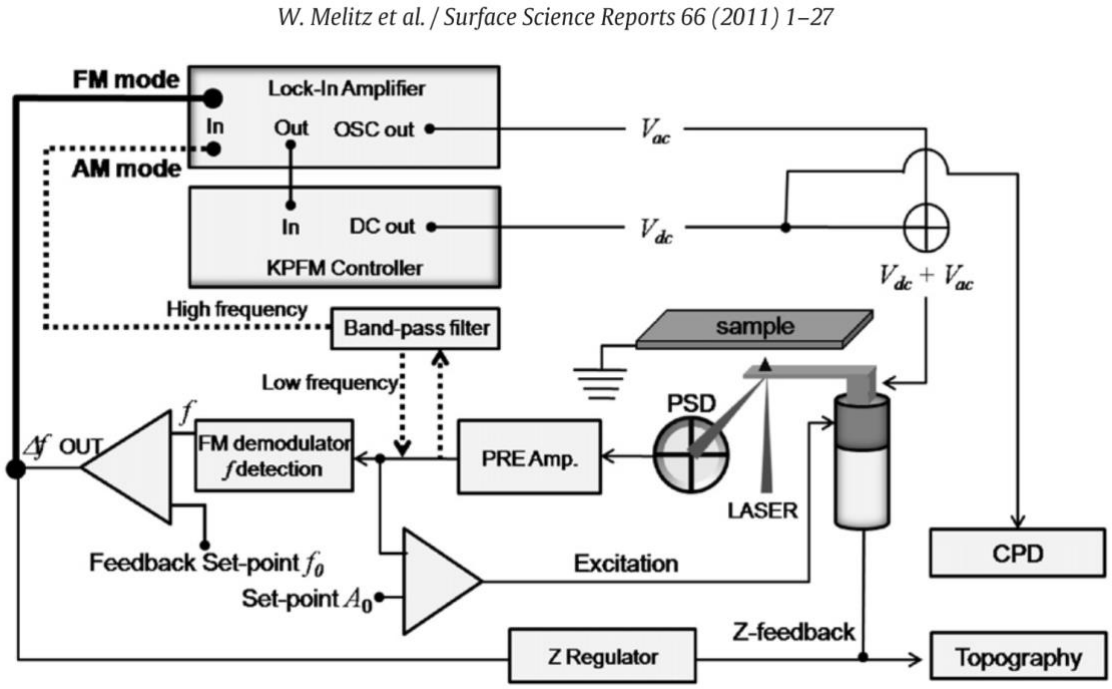

Figure 2.50 Schematic graph of KPFM system with AM and FM modes. The lower side of the graph is an FM mode AFM system for topography imaging and the upper side is a KPFM system for contact potential difference (V_{CPD}). [217]

Figure 2.50 shows the schematic graph of a KPFM experimental apparatus. The lower side of the graph shows the frequency modulation (FM) mode AFM system for topography measurement, and the upper side of the graph shows the components for contact potential difference (V_{CPD}) mapping, including the KPFM controller and lock-in amplifier. The dashed line and bold straight line in the graph show the amplitude modulation (AM) mode KPFM set-up. V_{AC} is applied to the tip from the lock-in amplifier reference signal voltage output (OSC out). In FM mode, the frequency shift signal(f) is split into: (1) one goes to the z regulator for topographical imaging, and (2) the other is sent to the lock-in amplifier. The lock-in amplifier splits the signal with the same frequency as V_{AC} and sends the signal into the KPFM controller. The KPFM controller keeps feedback to nullify the lock-in output signal, by applying V_{DC} to the tip. In AM mode, V_{AC} with the same frequency as the secondary resonant peak of tip, oscillation is applied to the AFM tip to motivate the tip with electrical force. The amplitude of tip oscillation has two parts: (1) low frequency (the first resonance peak) tuned by mechanical oscillation and (2) high frequency (the secondary resonance peak) tuned by V_{AC}. A band-pass filter filters the low and high frequency signals. The low frequency signal is used for topographical data regulation. The high frequency signal is sent directly to the lock-in amplifier. The KPFM controller measures contact potential difference (V_{CPD}) using the secondary resonance frequency component. [217]

Chapter 3

Topic I: Nanoscale engineering-effects on cathodes for intermediate-temperature SOFCs

3.1 Introduction

The performance of solid oxide fuel cells (SOFCs) is often limited by the sluggish oxygen reduction reaction (ORR) process at the cathode. It is also widely accepted that the surface exchange kinetics and surface area of cathodes play a crucial role in determining the overall cathodic performance. For this reason, various efforts have been made to improve these metrics through nanoscale materials engineering, most notably by the solvent infiltration method. This method, however, poses an intrinsic disadvantage of poor durability during high temperature operations. This is because the resulting perovskite infiltrates after a sintering process are known to be of true nanometer-scale (1 – 5 nm in diameter), they are very susceptible to thermal agglomeration. An atomic layer deposition (ALD) treatment on this infiltrates is hypothesized to be effective in suppressing the thermal degradation.

In this topic, we mainly focuses on improving performance of $LaNi_{0.6}Fe_{0.4}O_{3-\delta}$ (LNF)-based SOFC cathodes by initially infiltrating various kinds of solvents including praseodymium oxide (Pr_6O_{11}). In the last several months, I investigated the effects of using not only Pr_6O_{11}, but also $LaNi_{0.6}Fe_{0.4}O_{3-\delta}$ (LSCF) and LNF nitrate solvents to infiltrate on LNF-based function layers, and showed that an unprecedented improvement of cathodic performance by a factor of ~100 at 700 °C by a single-step infiltration. It is hypothesized that the improvement originates from larger surface area and higher surface exchange rate by the infiltrates. In the coming months, I will expand the choice of infiltrate materials into LSM ($La_{1-x}Sr_xMnO_{3-\delta}$), GDC ($Gd_{1-x}Ce_xO_{2-\delta}$), SDC ($Sm_{1-x}Ce_xO_{3-\delta}$), and PDC ($Pr_{1-x}Ce_xO_{3-\delta}$) nitrate solvents. For example, LSM is a conductor for electrons but an insulator against ions while GDC exhibits the opposite trend. PDC is expected to show higher electrochemical kinetics over the others. In addition to the dependency on material, the dependencies of cathodic performance on overpotential, temperature and oxygen partial pressure will help to reveal the critical factors of performance. An optimization for performance will be also performed in parallel by controlling e.g. the solvent concentration, number of infiltration processes and sintering temperature.

Further electrochemical measurement and structure analyses like electrochemical impedance spectroscopy (EIS), x-ray diffraction (XRD), and scanning electron microscope (SEM) will be also presented in the later part of this topic. Oxygen partial pressure dependency ($P(O_2)$) will be measured and the result of it will be analyzed, too. We provide some reasons and hypotheses to explain the performance of every different infiltrated sample we have observed in the end as well.

3.2 Experimental

3.2.1 Cell preparation

Cells consist of YSZ electrolyte, GDC interlayer, LNF with different infiltration material functional layers, and LNF current collecting layer (Figure 3.1) with the reaction area 0.35 cm^2. Each layer was sintered from slurry and screen-printed on the YSZ electrolyte layer by layer. For making GDC slurry, GDC nanopowder (surface area: 30 – 40 m^2/g; d_{50} particle size: 0.1 – 0.4 μm; FuelCellMaterials) and ethyl cellulose were added and mixed at room temperature overnight. Final slurry was composed of 40 wt.% terpineol, 10 wt.% hypermer KD-1, 2 wt.% ethyl cellulose, and 48 wt.% GDC nanopowder. GDC slurry was screen-printed onto both sides of 8 mol% YSZ electrolyte substrate (270 μm thickness, FuelCellMaterials), dried at 80 °C for 1 hour and sintered at 1150 °C for 5 hours. For sintering, the sample was heated to 500 °C in 2 °C/min, and held at 500 °C for 30 min to facilitate binder burn-off. Sample continued heating at 3 °C/min to sintering temperature, and cooled at 3 °C/min after sintering.

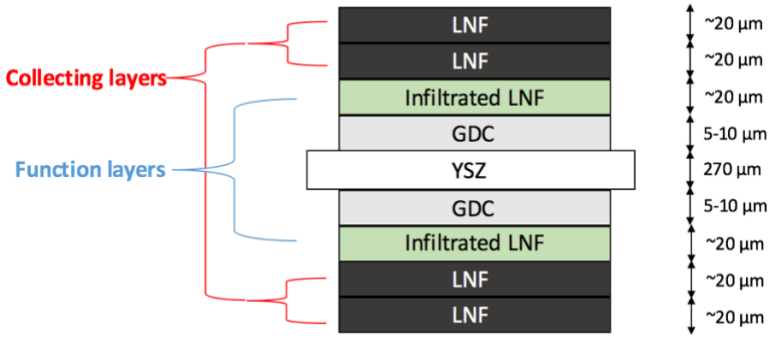

Figure 3.1: The configuration of a symmetric cathode fuel cell.

For making LNF slurries, we have to make LNF powder first. Materials for LNF powder are lanthanum (III) nitrate hexahydrate, nickel (II) nitrate hexahydrate, iron (III) nitrate nonahydrate, glycine, and deionized water. First, measure out the nitrate precursors in the following weight ratio: 1 : 0.403 : 0.373 (La : Ni : Fe). Dissolve the precursors in a minimal amount of deionized water while stirring on a hot plate. Then measure out glycine, for a metal ion : glycine mole ratio of 1:1, the weight ratio would be 1 : 0.877 (mass of all precursors used : mass of glycine). Add glycine slowly into the solution while stirring, and the color of the solution turns dark red. Once everything has dissolved, set the temperature to 100 – 150 °C to evaporate all the water, and once all the water has dissolved, remove the stir bar. At this step, the content will get more and more viscous, and a good indication that all the water has dissolved is when the stirrer would not stir properly anymore. Once the mixture is gel-like, set the temperature to 300 – 350 °C. The combustion should happen when the gel reaches ~ 250 °C, during this process there should be a lot of bubbling, and there will be a lot of gas released when the reaction happens. When the reaction seems to have settled down, use a spatula to stir around until all the content in the beaker seems to have reacted. Turn off the heat and wait for the contents to cool down. After crushing the

large pellets and transferring all the contents into a ceramic container, and calcining the powders at 850 °C for 3 hours. The color of the powder should be dark brown, and the final product should be pure black. After finishing preparing LNF powders, measure out hypermer, terpineol, ethyl cellulose, and LNF powders in the following weight ratio: 5 : 35 : 3 : 57. Hypermer is dissolved in terpineol using a magnetic mixer at 50 ^{0}C overnight. Then ethyl cellulose and LNF powders are then added into the mixture, and ball milled with a planetary ball mill for a total of 3 hours. LNF slurry was screen-printed onto both sides of GDC layers we made earlier, dried at 80 °C for 1 hour and sintered at 850 °C for 5 hours.

3.2.2 Infiltration solvent preparation

For making infiltration solutions, LNF, Pr_6O_{11}, LSCF, LSM, GDC, PDC nitrate solvents were made by either La^{+3}, Ni^{+2}, Fe^{+3}, or Pr^{+3}, or La^{+3}, Sr^{+2}, Co^{+2}, Fe^{+3}, or La^{+3}, Sr^{+2}, Mn^{+2}, Gd^{+3}, Ce^{+3}, or Pr^{+3}, Ce^{+3} nitrate colloid. Then, make different concentrations of these infiltration solvents. Syringe these infiltration solvents on LNF cathode backbones (function layers) and put them in the vacuum desiccator (Bel-art "space saver" polycarbonate vacuum desiccator) for at least one hour then dried at 450 ℃ for 30 minutes in the furnace. Finally, two LNF layers were screen printed on top of the infiltrated LNF functional layer, and dried at 80 ℃ for 1 hour. Completed symmetric cells were sintered at 850 ℃ for 2 hours, with the same heating profile as described. Samples were loaded into a SOFC test station after sintering. A mesh was used as a current collector (250 μm nominal aperture, Goodfellow.com), and a 5 kg weight was placed on top to ensure good contact between the electrode and mesh. Dry O_2 was fed to both electrodes at 100 sccm. Samples were heated to operating temperature at 3 °C/min, and held for at least 50 min before testing. EIS was performed with 20 mV ac perturbation from 3 MHz to 1 mHz (Bio-Logic SP-240). A Zeiss Gemini 500 FEG-SEM was used for microstructural characterization at ~ 0.64 kV operating voltage.

3.2.3 Equivalent circuit

Figure 3.2 shows the equivalent circuit we used for fitting our data. Because we fabricated a symmetric cathode fuel cell (half-cell). We used the equivalent circuit that is composed of two parallel capacitors (constant phase element) and resistor sets and series with a resistor. The single resistor (R_O) that series connect with the sets is ohmic resistor and represents the equivalent ohmic resistance from the electrolyte. R_H and R_L represent equivalent high resistance and low resistance from the cathodes. CPE_H and CPE_L are equivalent high and low constant phase elements from the cathodes (Equation 3.1), where Q is non-ideal capacitor and the associated α parameter indicates the Q's similarity to a true capacitor (CPE) (α =1 corresponds to an ideal capacitor). The values of polarization resistance (R_p) are calculated from R_H and R_L ($R_p = \frac{(R_H+R_C)}{2}$).

$$C = \frac{(RQ)^{-\alpha}}{R} \qquad (Equation\ 3.1)$$

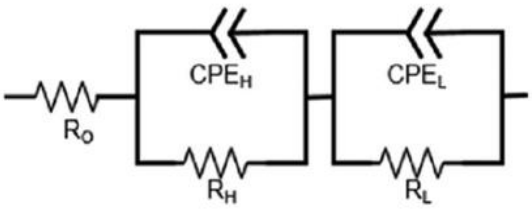

Figure 3.2: The equivalent circuit for a symmetric cathode fuel cell (half-cell).

3.3 Results and discussion

3.3.1 Electrochemical and microstructure characterization

Polarization resistance

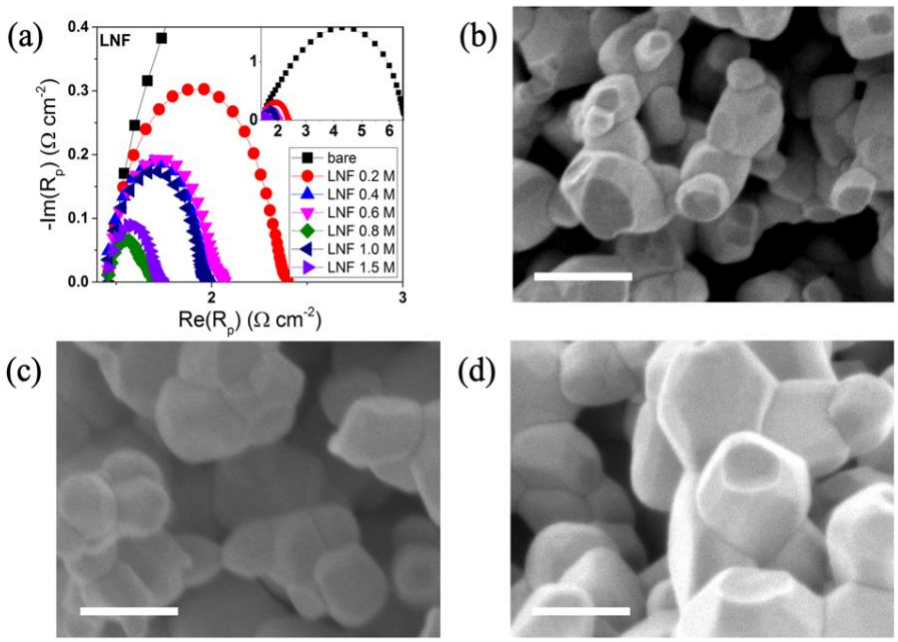

Figure 3.3: The EIS performance and SEM images: (a) shows the graph of all LNF-infiltration LNF-based cathodes with different concentrations. The graph on the upper right shows the LNF-infiltration LNF-based cathodes, compared to the blank LNF-based cathodes. (b) shows the SEM image of blank LNF backbones of LNF-base cathodes. (c) and (d) show the SEM images of LNF-infiltration LNF-base cathodes with concentrations of 0.2 M and 0.6 M, respectively. The scale bar indicates 200 nm.

LNF-infiltrated LNF-based cathodes show that LNF does improve the performance of not only polarization resistance but also ohmic resistance compared to blank (without infiltration) LNF-based cathodes. Figure 3.2(a) shows the best performance happened when concentration is 0.8 M (~ 43.7 wt.%) and the polarization resistance values are 0.0852 Ωcm^2 at 750 °C, 0.1522 Ωcm^2 at 700 °C, 0.3317 Ωcm^2 at 650 °C, and 0.781 Ωcm^2 at 600 °C. The polarization resistance is only 1/11 of blank LNF-based at 750 °C, 1/17 at 700 °C, 1/24 at 650 °C, and 1/37 at 600 °C. ohmic resistance for this sample is 0.8509 Ωcm^2 at 750 °C, 1.2859 Ωcm^2 at 700 °C, 2.0794 Ωcm^2 at 650 °C, and 3.717 Ωcm^2 at 600 °C, respectively. Figure 3.2(c) and (d) show SEM images of LNF-based cathodes without and with different concentrations of LNF infiltration solvents.

LSCF-infiltrated LNF-based cathodes show that LSCF also can improve the performance not only polarization resistance but also ohmic resistance compared to blank LNF-based cathodes, and even better than LNF-infiltrated LNF-based cathodes. Figure 3.3(a) shows the best performance happened when concentration is 1.0 M (~ 51.2 wt. %) and the polarization resistance values are 0.056 Ωcm^2 at 750 °C, 0.1009 Ωcm^2 at 700 °C, 0.1926 Ωcm^2 at 650 °C, and 0.4472 Ωcm^2 at 600 °C. The polarization resistance is only 1/17 of blank LNF-based at 750 °C, 1/25 at 700 °C, 1/42 at 650 °C, and 1/65 at 600 °C. ohmic resistance for this sample is 0.84 Ωcm^2 at 750 °C, 1.2338 Ωcm^2 at 700 °C, 2.001 Ωcm^2 at 650 °C, and 3.535 Ωcm^2 at 600 °C, respectively. Figure 3.3(c) and (d) show SEM images of LNF-based cathodes without and with different concentrations of LSCF infiltration solvents.

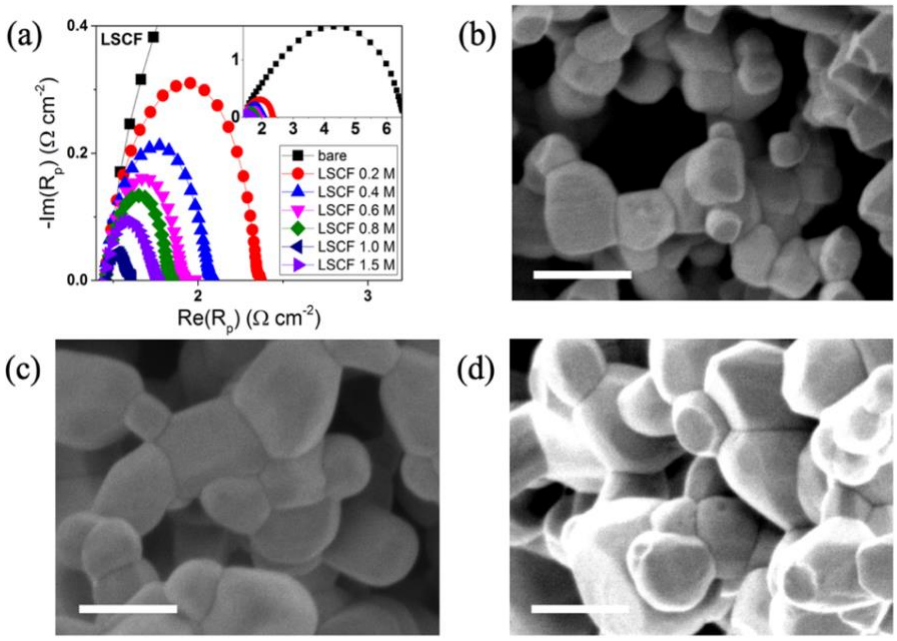

Figure 3.4: The EIS performance and SEM images: (a) shows the graph of all LSCF-infiltration LNF-based cathodes with different concentrations. The graph on the upper right shows the overall of LSCF-infiltration LNF-based cathodes, compared to the blank LNF-based cathodes. (b) shows the SEM image of blank LNF backbones of LNF-base cathodes. (c) and (d) show the SEM images of LSCF-infiltration LNF-base cathodes with concentrations of 0.2 M and 0.8 M, respectively. The scale bar indicates 200 nm.

Pr_6O_{11} (PrO_x)-infiltrated LNF-based cathodes show that LSCF also can improve the performance not only polarization resistance but also ohmic resistance compared to blank LNF-based cathodes, and even better than LNF-infiltrated and LSCF-infiltrated LNF-based cathodes. Figure 3.4(a) and (b) show the best performance happened when concentration is 1.0 M (~ 51.2 wt.%) and the polarization resistance values are 0.0326 Ωcm^2 at 750 °C, 0.0552 Ωcm^2 at 700 °C, 0.1088 Ωcm^2 at 650 °C, and 0.3294 Ωcm^2 at 600 °C. The polarization resistance is only 1/17 of blank LNF-based at 750 °C, 1/25 at 700 °C, 1/42 at 650 °C, and 1/65 at 600 °C. ohmic resistance for this sample is 0.8631 Ωcm^2 at 750 °C, 1.2576 Ωcm^2 at 700 °C, 1.9929 Ωcm^2 at 650 °C, and 3.303 Ωcm^2 at 600 °C, respectively. Figure 3.4(c)-(e) show SEM images of LNF-based cathodes without and with different concentrations of Pr_6O_{11} infiltration solvents.

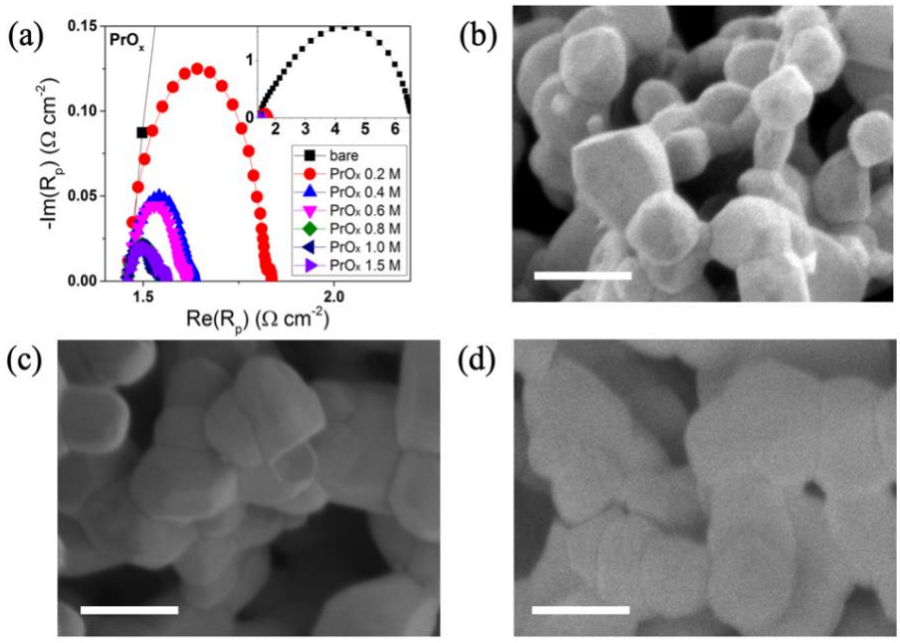

Figure 3.5: The EIS performance and SEM images: (a) shows the graph of all Pr_6O_{11}(PrO_x)-infiltration LNF-based cathodes with different concentrations. The graph on the upper right shows the overall of Pr_6O_{11}(PrO_x)-infiltration LNF-based cathodes, compared to the blank LNF-based cathodes. (b) shows the SEM image of blank LNF backbones of LNF-base cathodes. (c) and (d) show the SEM images of Pr_6O_{11}(PrO_x)-infiltration LNF-base cathodes with concentrations of 0.8 M and 1.5 M, respectively. The scale bar indicates 200 nm.

LSM ($La_{1-x}Sr_xMnO_{3-\delta}$)-infiltrated LNF-based cathodes show that LSM also can improve the performance of polarization resistance compared to blank LNF-based cathodes. However, it makes a worse improvement compared to other infiltrated LNF cathode samples. Especially in higher temperatures (~ 750 °C) From Figure 3.5(c) and (d). We can see there are some agglomeration materials grown during this infiltration process. The best performance happened when concentration is 0.8 M (~ 36.19 wt.%) and the

polarization resistance values are 0.2315 Ωcm^2 at 750 °C, 0.5279 Ωcm^2 at 700 °C, 1.5288 Ωcm^2 at 650 °C, and 4.5497 Ωcm^2 at 600 °C. The polarization resistance is only about 1/4 of blank LNF-based at 750 °C, 1/5 at 700 °C, 1/6 at 650 °C, and 1/6 at 600 °C. ohmic resistance for this sample is 1.0563 Ωcm^2 at 750 °C, 1.5288 Ωcm^2 at 700 °C, 2.5095 Ωcm^2 at 650 °C, and 4.473 Ωcm^2 at 600 °C, respectively. Figure 3.5(b)-(c) show SEM images of LNF-based cathodes without and with different concentrations of LSM infiltration solvents.

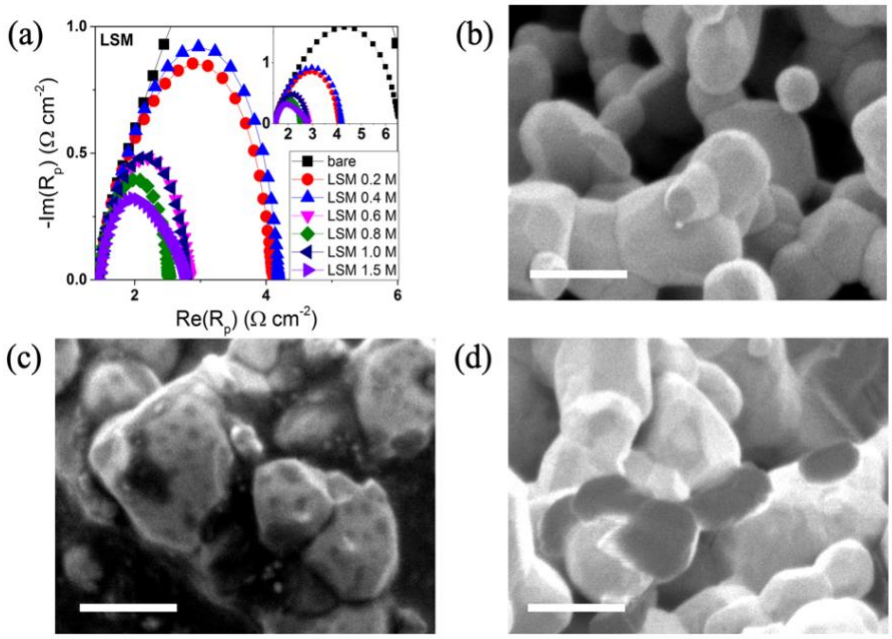

Figure 3.6: The EIS performance and SEM images: (a) shows the graph of all LSM-infiltration LNF-based cathodes with different concentrations. The graph on upper right shows the overall of LSM-infiltration LNF-based cathodes, compared to the blank LNF-based cathodes. (b) shows the SEM image of blank LNF backbones of LNF-base cathodes. (c) and (d) show the SEM images of LSM-infiltration LNF-base cathodes with concentrations of 0.2 M and 0.8 M, respectively. The scale bar indicates 200 nm.

GDC ($Gd_{1-x}Ce_xO_{2-\delta}$)-infiltrated LNF-based cathodes show that GDC also can improve the performance not only polarization resistance but also ohmic resistance compared to blank LNF-based cathodes, and even better than LNF-infiltrated, LSCF-infiltrated, and LSM-infiltrated LNF-based cathodes. A little worse than PDC-infiltrated and Pr_6O_{11}(PrO_x)-infiltrated LNF-based cathodes. Moreover, from Figure 3.6(c) and (d). We can see there are some small grains grown during this infiltration process. The best performance happened when concentration is 1.0 M (~ 35.0 wt.%) and the polarization resistance values are 0.0513 Ωcm^2 at 750 °C, 0.0993 Ωcm^2 at 700 °C, 0.2056 Ωcm^2 at 650 °C, and 0.4189 Ωcm^2 at 600 °C. The polarization resistance is only about 1/20 of blank LNF-based at 750 °C, 1/25 at 700 °C, 1/40 at 650 °C, and 1/66 at 600 °C. ohmic resistance for this sample is 0.9814 Ωcm^2 at 750 °C, 1.4280 Ωcm^2 at 700 °C, 2.2729 Ωcm^2 at 650 °C,

and 4.0145 Ωcm^2 at 600 °C, respectively. Figure 3.6(b)-(c) show SEM images of LNF-based cathodes without and with different concentrations of GDC infiltration solvents.

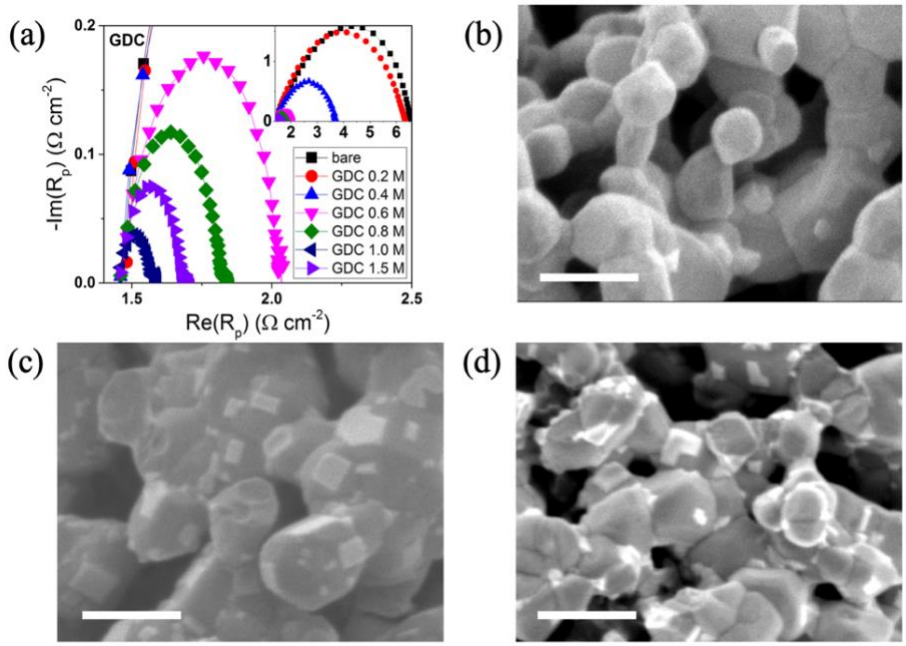

Figure 3.7: The EIS performance and SEM images: (a) shows the graph of all GDC-infiltration LNF-based cathodes with different concentrations. The graph on the upper right shows the overall of GDC-infiltration LNF-based cathodes, compared to the blank LNF-based cathodes. (b) shows the SEM image of blank LNF backbones of LNF-base cathodes. (c) and (d) show the SEM images of GDC-infiltration LNF-base cathodes with concentrations of 0.4 M and 1.5 M, respectively. The scale bar indicates 200 nm.

PDC($Pr_{1-x}Ce_xO_{3-\delta}$)-infiltrated LNF-based cathodes show that PDC also can improve the performance not only polarization resistance but also ohmic resistance compared to blank LNF-based cathodes, and even better than LNF-infiltrated, LSCF-infiltrated, and LSM-infiltrated LNF-based cathodes. Same as GDC-infiltrated and Pr_6O_{11}(PrO_x)-infiltrated LNF-based cathodes, they all have lower polarization resistance more than an order of magnitude. Moreover, from Figure 3.7(c) and (d). We can see there are some small grains grown during this infiltration process. The best performance happened when concentration is 1.5 M (~ 49.3 wt.%) and the polarization resistance values are 0.0368 Ωcm^2 at 750 °C, 0.0597 Ωcm^2 at 700 °C, 0.1203 Ωcm^2 at 650 °C, and 0.3433 Ωcm^2 at 600 °C. The polarization resistance is only about 1/84 of blank LNF-based at 750 °C, 1/40 at 700 °C, 1/67 at 650 °C, and 1/65 at 600 °C. ohmic resistance for this sample is 1.1659 Ωcm^2 at 750 °C, 1.6807 Ωcm^2 at 700 °C, 2.6971 Ωcm^2 at 650 °C, and 4.893 Ωcm^2 at 600 °C, respectively. Figure 3.7(b)-(c) show SEM images of LNF-based cathodes without and with different concentrations of PDC infiltration solvents.

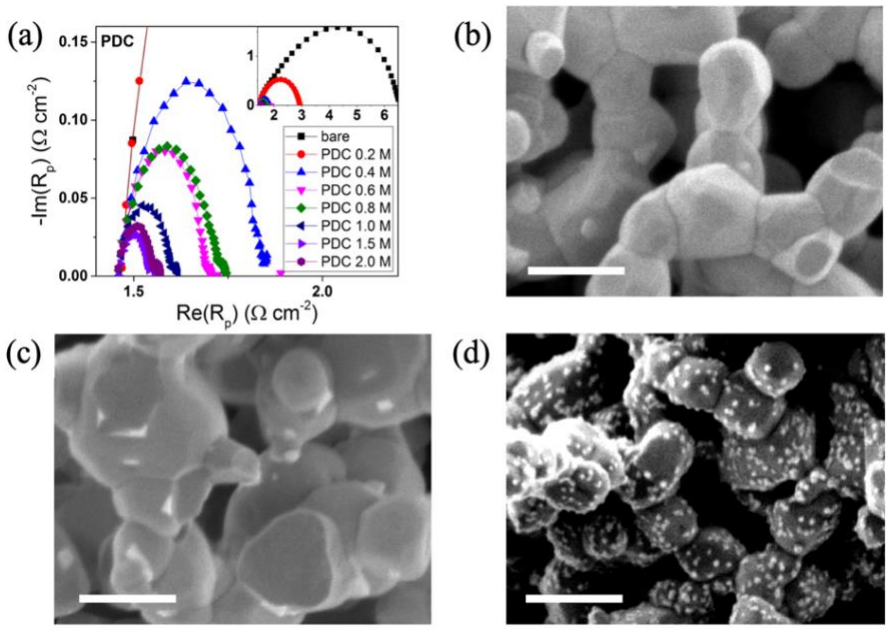

Figure 3.8: The EIS performance and SEM images: (a) shows the graph of all PDC ($Pr_{1-x}Ce_xO_{3-\delta}$)-infiltration LNF-based cathodes with different concentrations. The graph on the upper right shows the overall PDC-infiltration LNF-based cathodes, compared to the blank LNF-based cathodes. (b) shows the SEM image of blank LNF backbones of LNF-base cathodes. (c) and (d) show the SEM images of PDC-infiltration LNF-base cathodes with concentrations of 0.2 M and 1.0 M, respectively. The scale bar indicates 200 nm.

Figure 3.8(a) and (b) show the polarization resistance of R_H and R_L of infiltrated LNF-based cathode samples. Where the X axis is concentration (M) and Y axis is polarization resistance R_H and R_L (Ωcm^2). Table 3.1 shows the values of ohmic and polarization resistance at different temperatures. It is easy to tell that Pr_6O_{11} (PrO_x ,with a concentration of 1.0 M) made the best effort to improve the performance of LNF-based cathodes. PDC ($Pr_{1-x}Ce_xO_{3-\delta}$) also decreases the polarization resistance a lot. Meanwhile, we can notice that all ohmic resistance values are pretty similar at the same temperature for all samples with different infiltration materials and different concentration. We think this point makes this whole experiment more reliable.

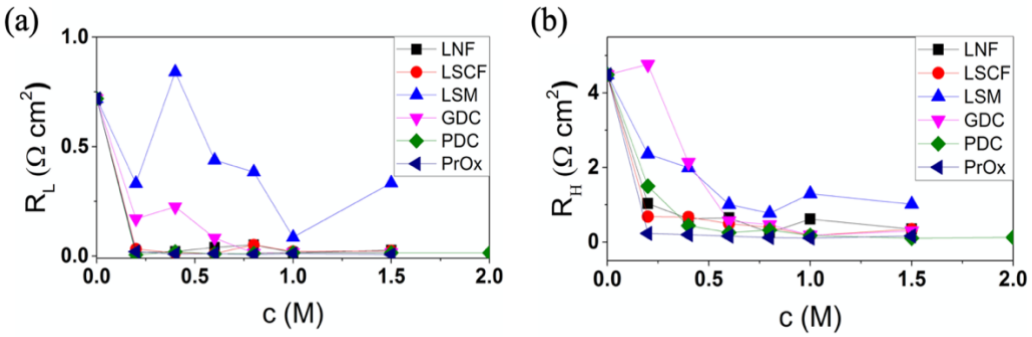

Figure 3.9: (a) The equivalent circuit we used for fitting our data, and (b) and (c) show the polarization resistance of the infiltrated LNF cathode.

Sample	600°C		650°C		700°C		750°C	
	R_{ohmic} (Ω cm^2)	R_{polar} (Ω cm^2)	R_{ohmic} (Ω cm^2)	R_{polar} (Ω cm^2)	R_{ohmic} (Ω cm^2)	R_{polar} (Ω cm^2)	R_{ohmic} (Ω cm^2)	R_{polar} (Ω cm^2)
Blank (no infiltration)	3.9165	28.9322	2.2071	8.1029	1.3713	2.6028	0.9223	0.9683
PrO_x (0.2 M ~5.02 wt.%)	3.8535	0.93	1.9719	0.4964	1.3031	0.2158	0.8911	0.1179
PrO_x (0.4 M ~9.7 wt.%)	3.591	0.5156	1.9646	0.2342	1.2975	0.1037	0.8848	0.0574
PrO_x (0.6 M ~14 wt.%)	3.507	0.4548	1.9411	0.2379	1.2947	0.0859	0.8813	0.0488
PrO_x (0.8 M ~18 wt.%)	3.8395	0.2857	2.1042	0.1617	1.357	0.0642	0.9366	0.0346
PrO_x (1.0 M ~21.8 wt.%)	3.303	0.3294	1.8932	0.1610	1.2467	0.0606	0.8631	0.0326
PrO_x (1.5 M ~30.1 wt.%)	3.3152	0.3037	1.918	0.121	1.1641	0.0857	0.8047	0.0494
LNF (0.2 M ~14.1 wt.%)	3.843	2.1547	2.1287	1.0625	1.3101	0.5238	0.8915	0.2534
LNF (0.4 M ~25.7 wt.%)	3.0373	1.5962	1.9523	0.6701	1.2541	0.3208	0.8505	0.1654
LNF (0.6 M ~35.4 wt.%)	3.927	1.4095	2.2253	0.6941	1.39335	0.3429	0.9653	0.1652
LNF (0.8 M ~43.7 wt.%)	3.717	0.781	2.0794	0.3317	1.2859	0.1522	0.8509	0.0852
LNF (1.0 M ~50.8 wt.%)	4.046	1.333	2.2516	0.64	1.3832	0.3157	0.937	0.1527
LNF (1.5 M ~64.8 wt.%)	3.7275	0.7494	2.1935	0.3681	1.407	0.1873	0.9751	0.0966
LSCF (0.2 M ~14.4 wt.%)	4.2315	2.8807	2.3062	1.1858	1.4098	0.5015	0.9758	0.2121
LSCF (0.4 M ~26.1 wt.%)	3.78	2.0395	2.1497	0.7936	1.329	0.341	0.8824	0.1654
LSCF (0.6 M ~35.8 wt.%)	4.165	1.5478	2.3506	0.6206	1.5194	0.2503	1.0518	0.1162
LSCF (0.8 M ~44.1 wt.%)	3.878	1.3647	2.1735	0.5392	1.3783	0.2216	0.9286	0.0962
LSCF (1.0 M ~51.2 wt.%)	3.394	0.5136	1.9523	0.2154	1.2408	0.0983	0.8397	0.0561
LSCF (1.5 M ~65 wt.%)	3.6225	1.0759	2.1326	0.4235	1.386	0.1837	0.9737	0.0976
LSM (0.2 M ~10.7 wt.%)	3.9235	5.7873	2.2225	2.8075	1.4039	1.345	0.9394	0.6304
LSM (0.4 M ~20.14 wt.%)	4.711	8.323	2.5785	3.2953	1.7217	1.4172	1.281	0.6377
LSM (0.6 M ~28.61 wt.%)	3.7345	5.3930	2.1361	1.8722	1.3505	0.7228	0.9457	03013
LSM (0.8 M ~36.19 wt.%)	4.473	4.5497	2.5095	1.5001	1.5288	0.5279	1.0563	0.2315
LSM (1.0 M ~42.95.8 wt.%)	4.1515	5.6296	2.3254	1.8457	1.4536	0.6898	1.0028	0.2846
LSM (1.5 M ~58.61 wt.%)	4.872	3.4557	3.0608	1.4221	1.9009	0.6734	1.2212	0.3287
GDC (0.2 M ~8.25 wt.%)	5.229	18.8578	2.9565	6.7321	1.8806	2.465	1.3556	0.7349
GDC (0.4 M ~15.7 wt.%)	48.23	5.726	24.2375	2.3824	15.3685	1.1784	9.772	0.5735
GDC (0.6 M ~23.03 wt.%)	12.1135	1.5449	6.181	0.7172	3.3663	0.3231	2.3517	0.1578
GDC (0.8 M ~28.92 wt.%)	4.8335	0.9926	2.8011	0.4478	1.8746	0.239	1.3955	0.1347
GDC (1.0 M ~35.0 wt.%)*	4.0145	0.4189	2.2729	0.2056	1.428	0.0993	0.9814	0.0513
GDC (1.5 M ~49.82 wt.%)	7.168	0.6376	3.9655	0.3102	2.3349	0.1564	1.6583	0.0682
PDC (0.2 M ~8.2 wt.%)	5.446	4.347	2.9684	1.7875	1.8064	0.7513	1.2001	0.3184
PDC (0.4 M ~15.79 wt.%)	15.897	1.011	8.855	0.5043	4.375	0.2292	2.7626	0.1097
PDC (0.6 M ~22.53 wt.%)	5.8205	0.6372	3.7695	0.2945	2.4647	0.1313	1.7766	0.0629
PDC (0.8 M ~28.9 wt.%)	8.5015	0.7148	5.117	0.4492	2.4282	0.1663	1.7444	0.0893
PDC (1.0 M ~34.75 wt.%)	5.418	0.4376	3.1024	0.1839	2.0832	0.0962	1.5442	0.0522
PDC (1.5 M ~49.3 wt.%)	4.893	0.3433	2.6971	0.1203	1.6807	0.0597	1.1659	0.0368
PDC (2.0 M ~61.3 wt.%)	5.4215	0.3094	3.4808	0.1427	1.9565	0.0697	1.4553	0.0473

Table 3.1: Different infiltration solvents with different concentration LNF-based cathodes.

XRD and TEM

Multiple infiltration materials all provide some extent of improvement with LNF-based cathodes. Next we used PANalytical XRD (X'Pert PRO MP4) to try to prove that these materials really grained or diffused into backbones. Figure 3.10 shows spectra of bare and infiltrated LNF cathode. Ahigher-resolution morphology of electrodes was observed by transmission electron microscopy (TEM) using the FEI F20 Tecnai system at 200 kV. TEM samples were prepared by drop-casting an ethanol-based suspension of electrode powders. which were prepared by pestle grinding, upon a 3 mm Lacey carbon 400 mesh grid (Ted Pella) followed by an ambient drying. Figure 3.11 shows TEM images of bare LNF backbone, Pr_6O_{11}-infiltrated and GDC-infiltrated LNF cathodes. While the Pr_6O_{11}-infiltrated electrode does not show a distinct nanoparticle-like morphology (Figure 3.11(b)), it seems that the surface is still roughened, and thus the effective surface area becomes enlarged by infiltrated species.

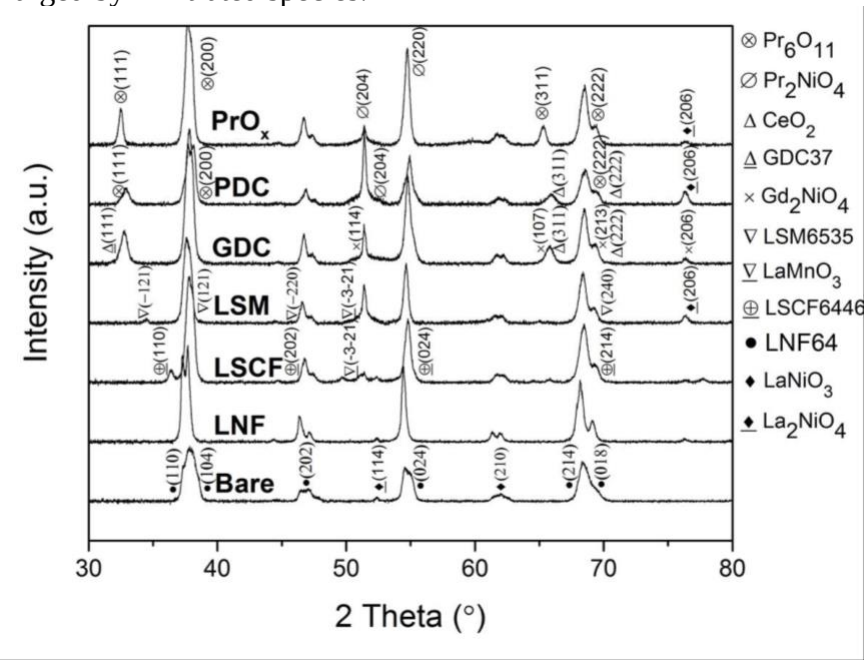

Figure 3.10: XRD spectra of bare and infiltrated LNF cathode.

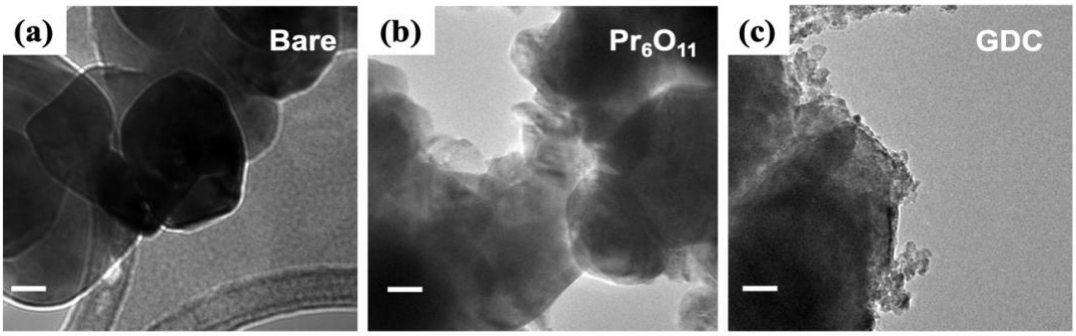

Figure 3.11: TEM images of (a) bare LNF backbone, (b) Pr_6O_{11}-infiltrated and (c) GDC-infiltrated LNF cathodes. All the scale bars correspond to 20 nm.

Activation Energy

Figure 3.12 illustrates specific activation energy corresponding to specific concentration of different infiltration solvents. The value of activation energy from ~ 1.82 eV (R_H of bare LNF-based cathode) and ~ 1.09 eV (R_L of bare LNF-based cathode) has improved to ~ 1.01 eV (R_H of PDC-infiltrated cathode) and ~ 1.02 eV (R_L of the PrO_x-infiltrated cathode) from multiple infiltration LNF-based cathodes. This result indicates that the performance of SOFC cathode was improved by infiltration treatment.

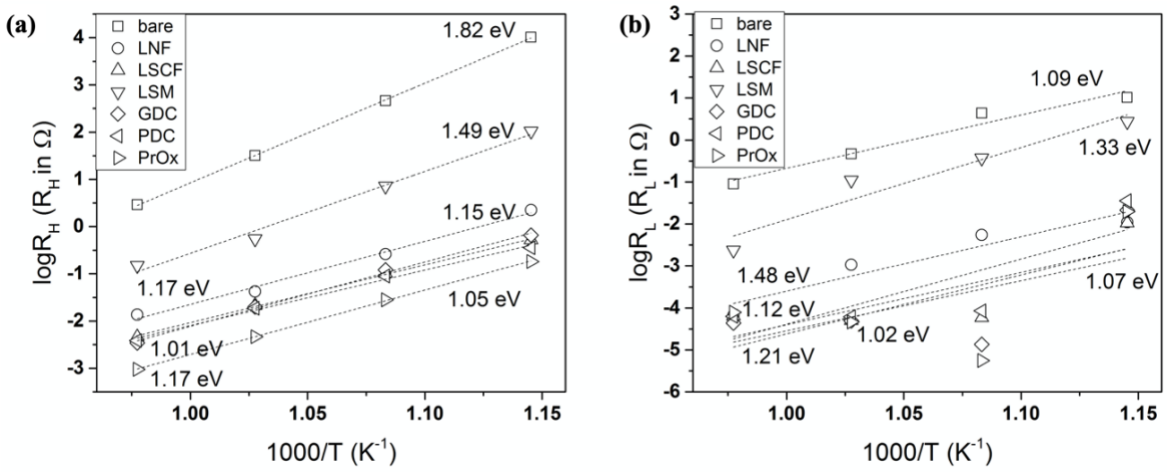

Figure 3.12: Arrhenius plots of R_H and R_L deduced from the EIS measurements of bare and infiltrated LNF cells.

	R_o [Ω cm^2]	R_H [Ω cm^2]	α_H	Q_H [F s$^{1-\alpha}$]	C_H [F cm^{-2}]	R_L [Ω cm^2]	α_L	Q_L [F s$^{1-\alpha}$]	C_L [F cm^{-2}]
Blank	1.37	4.49	0.77	2.4×10^{-4}	1.5×10^{-5}	0.72	0.75	1.3×10^{-4}	2.7×10^{-6}
LNF	1.30	0.25	0.68	1.1×10^{-3}	1.2×10^{-5}	0.05	0.57	3.5×10^{-1}	1.3×10^{-2}
LSCF	1.24	0.18	0.62	3.4×10^{-3}	2.6×10^{-5}	0.02	1.0	2.24	7.8×10^{-1}
LSM	1.53	0.77	0.89	2.1×10^{-4}	2.9×10^{-5}	0.38	0.57	3.1×10^{-3}	1.4×10^{-5}
GDC	1.43	0.18	0.63	2.2×10^{-3}	1.4×10^{-5}	0.02	0.87	2.75	7.0×10^{-1}
Pr_6O_{11}	1.25	0.11	0.54	2.8×10^{-2}	1.1×10^{-4}	0.01	0.92	3.67	1.07

Table 3.2: ohmic resistance (R_O), polarization resistances from high frequency (R_H) and low frequency (R_L) arcs, and CPE parameters (Q and α) of bare and infiltrated samples obtained at 700 °C (open circuit condition). The equivalent circuit shown in Figure 3.2 was used to fit the data. The capacitance values (C_H) and C_L) were calculated based upon Q and α.

Oxygen partial pressure dependency

To obtain a better understanding of the RDS of ORR in each sample, the dependency of ORR kinetics on the oxygen activity was also examined at the oxygen partial pressures (P_{O_2}) of 0.04 – 1.0 atm. Reaction order (m) defined in the relation $R_p \propto \left(P_{O_2}\right)^{-m}$, has been widely used to reveal the RDS of ORR processes.[185,218–222] Figure 3.13 shows the P_{O_2} dependence of polarization resistances (R_H and R_L) and characteristic

frequencies (f_c) of electrode processes in each cell. In the bare LNF cell, R_H is dominantly larger than R_L (especially at pO2 > 0.1 atm), and the high-frequency process exhibits a very high $E_{a,H}$ of 1.82 eV. This can be readily ascribed to the aforementioned extremely low concentration of oxygen vacancies in the LNF lattice under high P_{O_2}, which would make the activation barrier of dissociative adsorption or oxygen exchange extremely high. Bevilacqua *et al.* also asserted that the rate of ORR in their bare LNF cathode-based cell is limited by dissociative adsorption of O_2 with electron transfer (they called it "activation of O_2") and transport of O_2-ions, mainly based upon the high E_a of the cathodic process (133 kJ mol^{-1}).[63] Murray *et al.*'s report further supports this. They reported that E_a = 1.61 eV and m = 1/6 for a porous LSM, similar values to those of our bare LNF, and concluded that the ORR is rate-limited by oxygen dissociation and adsorption.[223] The analogy between LSM and LNF is justified by their similar characteristics including extremely low oxygen vacancy concentration under a high oxygen activity (e.g. $P_{O_2} > 10^{-3}$ atm),[224,225] high activation energy for O_2 dissociation,[63,223] and high electronic conductivity with negligible ionic conductivity.[63,226] Based upon these, it is concluded that the ORR kinetics of our bare LNF cell is rate-limited by dissociative adsorption of O_2 with electron transfer for partial reduction of oxygen. In addition, the small high-frequency capacitance ($C_H = 1.5 \times 10^{-5}$ F cm^{-2}) indicates that the ORR of our LNF cell follows a "surface process" rather than a "bulk process".[18] Here, the surface process refers to an ORR process where oxygen intermediates transport along the surface of electrode until reaching the electrode/electrolyte interface, whereas the bulk process involves oxygen transport through the bulk of electrode. Budiman *et al.* reported that a bulk process through a dense LNF film entails a much larger capacitance of $\sim 10^{-2}$ F cm^{-2} at 973 K and 1 bar of P_{O_2};[227] in a highly dense electrode, a bulk process is unavoidable because there is little route of surface transport of oxygen (except the very outer edge of the electrode). After an LNF infiltration onto the LNF backbone, the amplitude of R_H became much smaller (from 2.60 cm^2 to 0.15 cm^2 at 700 °C) but the corresponding m_H stayed the same value of 0.13. This can be interpreted that the effective reaction site was enlarged significantly by the infiltration, but the overall ORR kinetics is still limited by the surface process. However, the significant difference in the activation energy of high-frequency processes shown in Figure 3.10 ($E_{a,H}$ = 1.82 eV for bare LNF; $E_{a,H}$ = 1.15 eV for LNF-infiltrated) suggests that surface specific chemical properties affecting the dissociative adsorption and surface electron transfer process are likely different between the two samples. The aforementioned XRD (Figure 3.10) analysis showing slightly different secondary phases and crystallinity between the bare and LNF-infiltrated cells may be partially related to the difference in the electrochemical behavior. Alternatively (or additionally), it may be because of a possible difference in the vacancy concentration caused by the difference in the fabrication/synthesis process between the backbone and infiltrated LNF.

Regarding the LSM-infiltrated cell, the high-frequency process is also ascribed to the dissociative adsorption with electron transfer. The reaction order (m_H = 0.16) and capacitance ($C_H = 2.9 \times 10^{-5}$ F cm^{-2}) are similar to the values from LNF-infiltrated cell (m_H =0.13, $C_H = 1.2 \times 10^{-5}$ F cm^{-2}), but the resistance (R_H = 0.77 Ωcm^2) and its activation energy ($E_{a,H}$ = 1.49 eV) are somewhat larger than those of LNF-infiltrated cell (R_H = 0.25 Ωcm^2; $E_{a,H}$ = 1.15 eV). This is in agreement with Bevilacqua *et al.*'s report

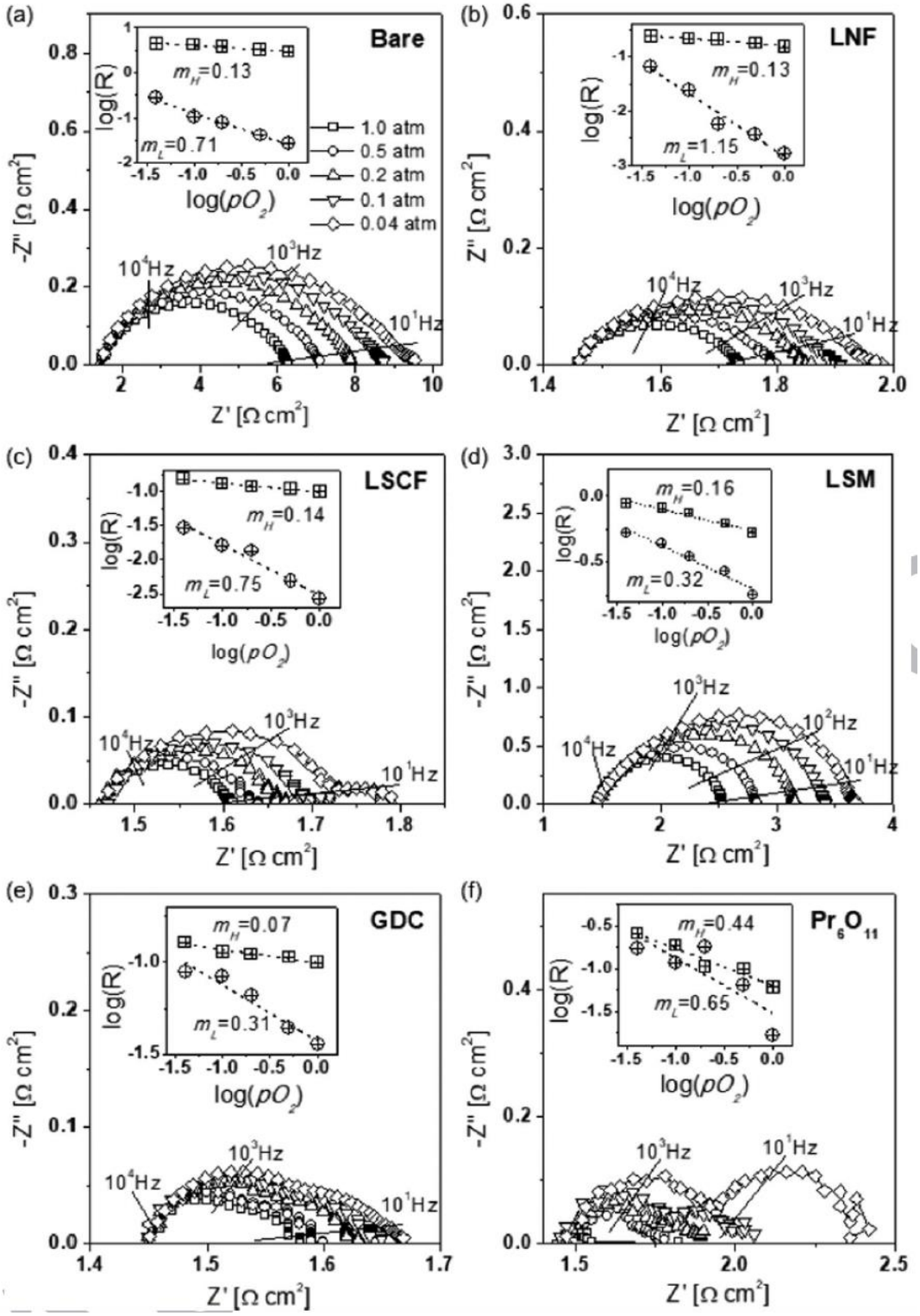

Figure 3.13: Nyquist plots of (a) bare LNF and (b)-(f) infiltrated LNF obtained under the open circuit condition at 700 °C. The nitrate concentration was optimized for lowest polarization resistances; for LNF and LSM, 0.8 M and for others, 1.0 M. The insets show the (P_{O_2}) dependency of R_H and R_L and the corresponding reaction order (m) values.

showing that the activation energy of dissociative adsorption measured in LSM (165 kJ mol^{-1}) is larger than the value obtained from LNF (133 kJ mol^{-1}).[63] Both of our LSCF- and GDC-infiltrated cells exhibit similar electrochemical behavior as the LNF-infiltrated cell in terms of R_H (LSCF: 0.18, GDC: 0.18, LNF: 0.25 cm^2 at P_{O_2} = 1 atm, 700 °C), m_H (LSCF: 0.14, GDC: 0.07, LNF: 0.16) and C_H values (LSCF: 2.6×10^{-5}, GDC: 1.4×10^{-5}, LNF: 1.2×10^{-5} F cm^{-2}), indicating that they are also likely rate-limited by dissociative adsorption with electron transfer. In the case of the GDC-infiltrated cell, R_L becomes comparable to R_H at low P_{O_2} (< ~ 0.1 atm); i.e., the low-frequency process affects the overall ORR rate significantly at low P_{O_2}. The very high C_L value (0.7 F cm^{-2} at 700 °C) indicates that the low-frequency process is likely to involve diffusion of electroactive oxygen species (e.g. O or O^-) along the electrode surface. As discussed above, the ORR of bare LNF is a "surface process", as opposed to a "bulk process". Since the infiltrations made in this study are expected to incur only surface modifications of the LNF backbone without forming a separate bulk network (due to the small amount of infiltrates), the ORR of all the infiltrated electrodes also should follow a surface process. For a bulk process, a high capacitance can be ascribed to a so-called "chemical capacitance", which is known to be related to the change of oxygen non-stoichiometry in the electrode.[18,227]

The Pr_6O_{11}-infiltrated sample exhibits a distinct electrochemical behavior. Since m_H = 0.44 and m_L = 0.65 (both close to 0.5), both high- and low-frequency processes are likely a non-electrochemical process. This is further supported by the high capacitance value of C_L = 1.07 F cm^{-2}. The high-frequency capacitance (C_H = 1.1×10^{-4} F cm^{-2}) also is higher than the other infiltrated cells by an order of magnitude, supporting that the RDS in this sample is different from the others. The polarization resistances are the smallest among the studied samples at all P_{O_2}, and a charge transfer process-related arc is not visible. This is probably due to the excellent electrochemical property of Pr_6O_{11} and Pr_2NiO_4 formed by the infiltration process. Pr is multivalent between Pr^{3+} and Pr^{4+} rendering active redox property of Pr-including oxides.[78] From the fact that the $f_{c,L}$ is several Hz only; the low-frequency arc likely originated from the diffusion of electroactive oxygen species. The high frequency arc with $f_{c,H}$ = ~ 103 Hz, on the other hand, can be ascribed to the oxygen dissociation process.

3.3.2 Durability

It is worthwhile to examine if an infiltration of Cr poisoning resistant materials on a LNF backbone preserves the chemical stability against Cr poisoning of the backbone. Here, a short-term durability test (~ 100 hours) is presented for three infiltrated electrodes: LSCF, GDC and LNF-infiltrated electrodes. A much longer-term test is necessary to evaluate true durability of a SOFC electrode, but this short-term study is still meaningful considering most degradation of infiltrated electrodes occurs during the first 100 – 200 hours of operation.[228,229] In Figure 3.14(a), the LSCF-infiltrated sample shows an additional low-frequency arc that is increasingly more pronounced with time under a Cr-containing environment at 700 °C. For the other two samples, there is not a discernible additional low-frequency arc (Figures 3.14(b) and (c)). This can be interpreted that the surface of the LSCF-infiltrated electrode is gradually blocked by Cr-containing phase (e.g.

$SrCrO_4$),[230] limiting the O_2 access to the electrode surface while the other two samples do not develop a surface passivation. However, the time evolution of R_p (values (Figure 3.14(d)) reveals that the LSCF-infiltrated sample exhibits substantially better stability than the LNF-infiltrated one. This is surprising in the context of Cr poisoning effect because LNF is known to be significantly more resistant to Cr poisoning than LSCF.[231] LNF has been consistently repor[218]ted to be stable against Cr poisoning unless it is polarized significantly.[230,232] Since the measurements here were performed at the open circuit condition, the LNF-infiltrated electrode is not expected to have Cr deposition.

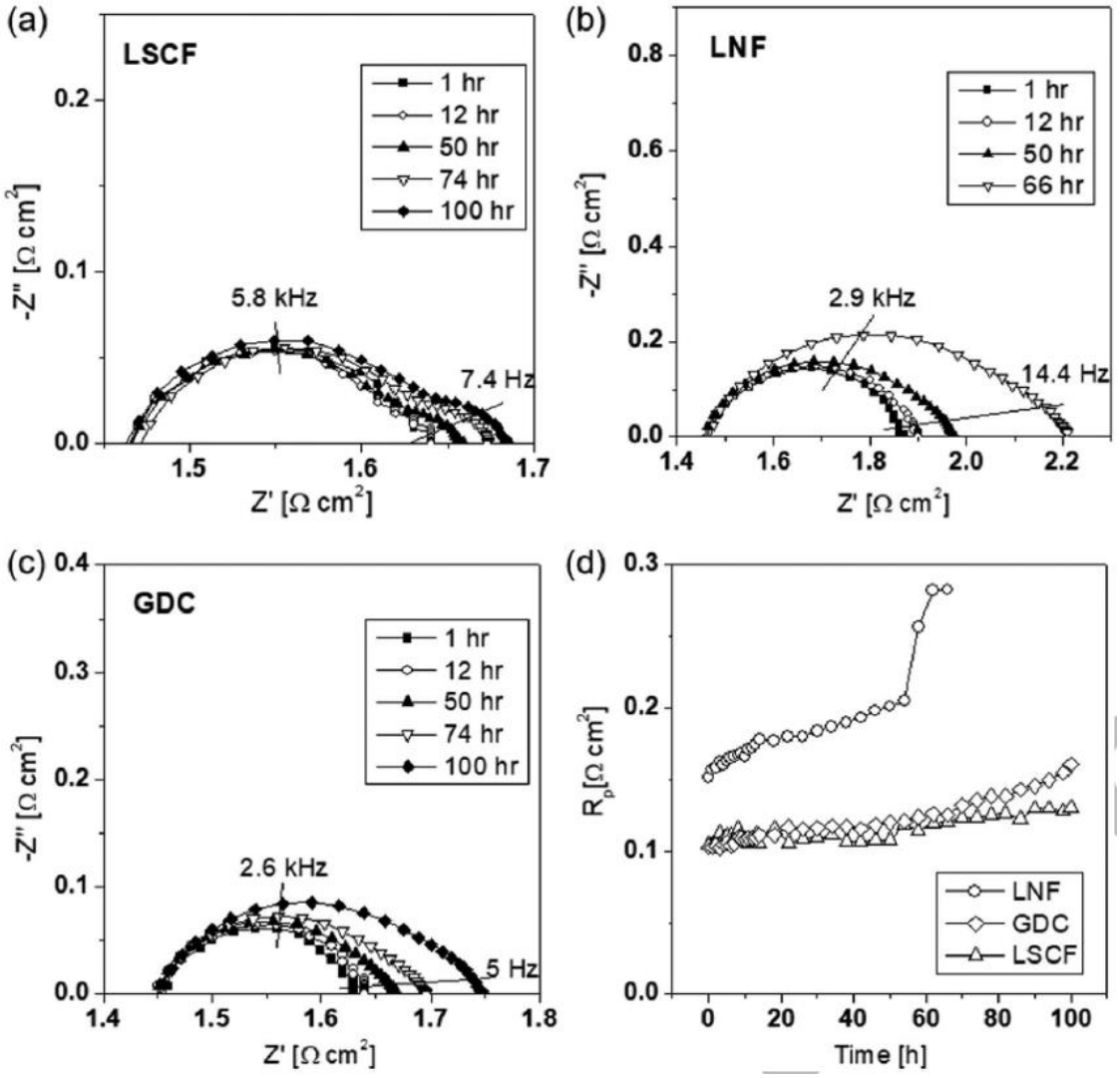

Figure 3.14: (a)-(c) Nyquist plots of LNF, LSCF and GDC-infiltrated symmetric cells obtained at the open circuit condition as a function of time in Cr-containing environment at 700 °C. 100 sccm of dry O_2 was fed to both electrodes of each cell for the measurement. (d) Evolution of area specific electrode polarization resistances from LNF, LSCF and GDC-infiltrated samples. The durability test of the LNF-infiltrated cell was stopped at 65 h due to a power outage.

The presented R_p evolution becomes understandable by considering other degradation mechanisms: change of electrode morphology by sintering. In the case of LNF-infiltrated sample, the dramatic degradation (R_p from 0.15 to 0.28 Ωcm^2 in 66 hours) is ascribed to an excessive sintering of an infiltrated electrode during high-temperature operation. As shown in the SEM images (Figures 3.15(a) and (b)), the interparticle necks grew significantly after 66 hours (see the arrows in Figures 3.15(b)), resulting in a decreased active surface area for ORR. Since the backbone and infiltrated materials are both LNF, the infiltrated overcoat could not deter the kinetics of backbone agglomeration. Given the temperature for the test was only 700 °C, the degree of sintering (e.g. neck widening) is surprisingly high. The accelerated sintering may be due to the high surface energy of the initially tiny particles that were infiltrated. In addition, an overcoat of LSCF by infiltration preserved the overall backbone microstructure without decreasing the active surface area (Figures 3.15(c) and (d)). Analogous effect has been reported in many recent reports where an ultrathin coating of an oxide is found to provide an excellent resistance against thermal agglomeration of high-surface-area backbones.[218,233,234]

On the other hand, a considerable increase in R_p from 0.10 to 0.16 Ωcm^2 was observed from the GDC-infiltrated electrode after 100 hours of operation. The degradation is also ascribed to a geometric effect. The GDC-infiltrated sample shows distinct nanoparticles of infiltrated phase on the surface of backbone (Figures 3.15(e) and (f)) unlike the other two electrodes, and the particles grew from several nanometers to tens of nanometers in size during the operation.[235] In summary, it is tentatively concluded that the mechanism of ORR performance degradation are different for each sample. The LNF-infiltrated cell decreased rapidly by a substantial sintering of the backbone structure itself while the GDC-infiltrated cell was degraded by the sintering of the infiltrated nanoparticles. The degradation of LSCF-infiltrated cells is ascribed mostly to the Cr poisoning.

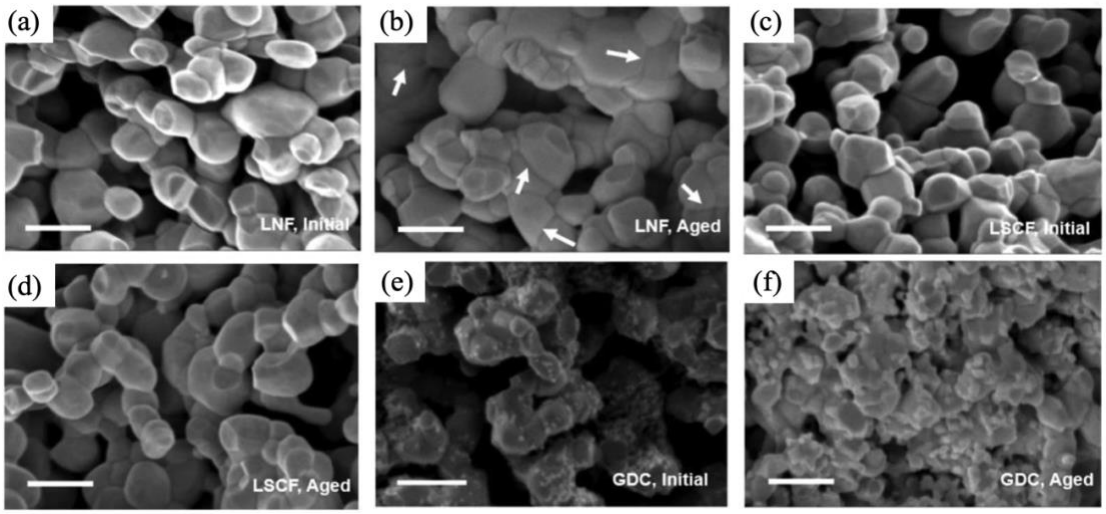

Figure 3.15: SEM images of LNF backbones infiltrated with (a, b) 0.8 M LNF, (c, d) 1.0 M LSCF and (e, f) 1.0 M GDC, before and after exposing the cell under a Cr-containing gas environment at 700 °C (65 h for LNF, 100 h for LSCF and GDC). The red arrow in (b) indicates highly sintered inter-particle necks. The scale bars correspond to 200 nm.

3.4 Conclusions

In this study, we demonstrated a dramatic impact of surface-specific treatment by a one-step infiltration on the overall kinetics and RDS of ORR for LNF-based cells. In addition, thermal stability of three infiltrated cells of choice was studied in a Cr-containing environment. Regardless of the infiltrated material, a lower electrode polarization resistance was achieved with a higher concentration of precursor solution up to ~ 1.0 M. The XRD results showed that the precursor infiltration followed by a 850 °C sintering process successfully crystallized the infiltrates for all the materials of choice. In particular, LSM, GDC and Pr_6O_{11}-infiltated samples include Ruddlesden-Popper phases such as La_2NiO_4 and Pr_2NiO_4, which are favorable for high electronic and ionic transport. The ORR kinetics of bare LNF are limited by surface process, most likely dissociative adsorption and partial reduction of oxygen, due to the extremely low concentration of oxygen vacancy. A significant reduction in electrode polarization resistance by a single step infiltration is ascribed to a facilitation of the surface process. The surface morphology (and surface area) is another major factor of ORR activity, which is supported by the fact that an infiltration of LNF (the same material as the backbone) decreased the polarization resistance by 17 times at 700 °C. Among the samples of study, Pr_6O_{11}-infiltrated cell showed the lowest polarization resistance of R_p = 0.06 Ω cm^2 at 700 °C in open circuit condition, much smaller than the value from the bare LNF cell (R_p = 2.60 Ω cm^2). This is ascribed to the excellent ORR performance of Pr_6O_{11} and Pr_2NiO_4, the two main phases of the Pr_6O_{11}-infiltrate. Unlike other infiltrated cells, the ORR kinetics of Pr_6O_{11}-infiltrated one seems limited by non-electrochemical processes only such as the diffusion of oxygen intermediates and dissociative adsorption. All others, including the bare LNF cell, exhibit an electron transfer-limited process in addition to dissociative adsorption.

Finally, the thermal durability of three infiltrated cells (LNF, LSCF and GDC-infiltrated cells) were studied in a Cr-containing gas environment. While the LSCF-infiltrated cell suffers from Cr poisoning, the overall microstructure of the nanoporous electrode was well preserved by the infiltration. On the other hand, the LNF-infiltrated electrode showed a significant sintering of the backbone, whereas the GDC infiltrated electrode exhibited an agglomeration of infiltrated particles during operation. Both of the morphological changes are believed to have degraded the overall ORR performance by decreasing active surface area. This study provides a useful guideline for a rational choice of infiltrating phase to achieve high performance and durability of nanostructured cathodes.

Chapter 4

Topic II: Effects of mechanical and electrical applications on AFM

4.1 Introduction

Conductive atomic force microscopy (CAFM) has been widely employed to study the localized electrical properties of a wide range of substrates in non-vacuum conditions by the use of noble metal-coated tips. This is the second topic of this study, I am going to briefly talk about what I have done in the first year and talk more about what I am planning to do in the future. Based on CAFM, it is important to understand the relationship between its mechanism and conductivity. In addition to this work, I also contributed to another AFM-based study on resistive switching memory. Both AFM and memory devices were luckily familiar to me from my prior exposure to those. An innovative mechanism study was performed by leveraging the unique capability of AFM, the quantification of nano-Newton-level adhesion force, leading to a publication in Scientific Reports early this year. I contributed as the third author.[236] In this first part of the next Section, we will talk more about how we connect mechanism and conductivity. It was a fundamental study on the evolution of interfacial properties under coupled mechanical and electrical stresses. In the work, we revealed that a nano-thin oxide formed on the surface of gold-coated tip during a cleaning process limits a fluent electronic transport, and its evolution in electrical properties during CAFM was analyzed with the aid of high resolution transmission electron microscopy (TEM) and modeling for tunneling current. A manuscript on this work is currently under review by the Journal of Applied Physics with favorable initial reviews.[237] I contributed to this work as a leading author (a co-first author). In the second part of the next Section, we will cover another project that was supposed to be one of my studies. I work on a nanoscale fuel cell study by AFM in collaboration with Dr. Chee Seng Ng, a visiting scholar from Nanyang Technological University in Singapore. A new advanced setup with a micro-scale heating stage enabled in-situ high temperature electrochemical measurements.

4.2 Experimental

This Section will be separated into two main experiments. The first one is based on what I have done in my first year, it is also published on Journal of Applied Physics.[237] The setup and sample preparation of this experiment would be presented in the whole Section of 4.2.1 and the measurement, analyses, discussion and conclusion would be presented in the first parts of Section 4.2.3, 4.3, and 4.4, respectively. The second experiment is based on what I am doing right now. It is still in progress and there are still some problems needed

to fix. The fabrication of Pt-Ir AFM tips will be in Section 4.2.2 and some of its microstructure characterization will be presented in the last part of Section 4.2.3. Also some discussion and conclusion will be in the last parts of Sections 4.3 and 4.4.

4.2.1 Preliminary Steps

i. Au-coated tip cleaning

Plasma cleaning of tips was performed in dry air on a cleaning system from Harrick Plasma (PDC-002). The chamber was pumped down to < 200 m Torr and fed with dry air for 60 seconds. Then, the tip was cleaned with a plasma power of 30W for 60 seconds. Ultraviolet ozone (UVO) cleaning was performed for 30 min in a commercial UVO cleaning system (model no. 42, Jelight Company) with 253.7 nm wavelength at the Hg lamp intensity of 30 mW/cm^2. The tips were carefully placed on a glass petri dish. Ethanol etching was done by submerging the AFM tips in ethyl alcohol (200 proof, anhydrous, 99.5%, Sigma-Aldrich) for 20 min at 65 °C.

ii. Force and resistance measurement

The nanoscale Au-HOPG interface was implemented by bringing a gold-coated AFM tip in contact with the surface of a high crystal quality HOPG (highly oriented pyrolytic graphite, ZYA quality; Mosaic spread of ~ 0.4°) in a commercial AFM setup (5500 AFM, Agilent Technologies). In an AFM setup, the exerted force is approximated to be proportional to the cantilever deflection, which is detected by a laser beam-assisted amplification scheme. The amount of cantilever deflection (and thus the force exerted on the tip apex) is controlled to match a set value through a feedback control scheme. For this work, a commercially available gold-coated tip (HQ: NSC36/Cr-Au, Mikromasch) with a flexible cantilever (~ 0.6 N/m) was used. The tip was fabricated by depositing a 20 nm thick adhesion layer (Cr) followed by a 30 nm thick gold film on a conventional silicon-based framework. Few layers of HOPG were peeled off using a sticky tape to expose the new graphite surface before each measurement. The basal planes of the HOPG routinely showed a surface roughness of < 0.2 nm by contact mode AFM imaging (with a usual scan area of 500×500 nm^2), which is expected to ensure a consistent contact area with a given tip and normal load. The tip-sample system was put in either ambient condition or under a continuous dry N_2 flowing environment at 0.4 lpm. An electrical measurement system, either a semiconductor analyzer or an impedance spectroscopy, was integrated with the AFM system in a two-probe setup. The reference electrode tied with the counter electrode was connected to the tip while the working electrode was attached to the HOPG. A Faraday cage enclosing the AFM setup was connected to the reference electrode to minimize ambient radio frequency electromagnetic noise.

4.2.2 Fabrication of Pt-Ir AFM tips

The fabrication of Pt-Ir AFM tip/probe was our plan for the purpose of CAFM. I was planning to use CAFM to do an electrical characterization scheme for the material of

fuel cells while leveraging my skillset on AFM. To measure electrical characteristics of YSZ (an usual material for electrolytes of fuel cells), the AFM should have high conductivity to measure the finest data. This is the main reason why we chose Pt-Ir as our AFM tips to measure electrical characterization scheme for YSZ. Unfortunately, for some realistic reasons like the tips/probes we made could not be clipped on the AFM probe nose well and it had some angle issues. However, I have spent so much time working on this and I was able to fabricate really decent size Pt-Ir AFM tips/probes so I want to keep it in this section.

First, a part of Pt-Ir was cut from a Pt-Ir wire with diameter of 0.25 mm ($Pt_{0.8}Ir_{0.2}$, Platinum STM Tip wire, nanoscience instruments). Then pressed under smooth metal block (thickness < 100 μm), the flat part is cantilever and it would be installed on the AFM tip holder when the fabrication is done. After washing by acetone it would be immersed 1.15 mm to 1.2 mm into electrolyte solution ($CaCl_2$, 1.5 M) and start the step of "rough etching". The AC current of 35 V for 90 seconds, 30 V for 45 seconds, and 28 V until done, the shape of tip should be like the top right photo of Figure 4.1(b). There is a "thin neck" (shown in the middle photo of Figure 4.1(b)) with diameter ~ 37 nm would be formed during rough etching. Next, AC pulse (±5 V) with frequency of 1 Hz (20 ms) would be provided for "fine etching". This step will stop when the thin neck breaks. Then this tip is going to the next step, "post fine etching". There are three steps in post fine etching. The first one is flame annealing, the tip is burnt by Busan flame until red. This is for the purpose of reducing dislocation and increasing the size of microcrystal. Then using 15 V, 4 Hz (16 μs) DC current to micro-polish the tip via dilute H_2SO_4 (1.0 M) as the electrolyte. The last step is electrochemical reduction, by using the current with -1.1 V for 1 to 2 minutes (Bio-Logic SP-240) to reduce the oxide film on the tip that was formed from the last step. From the publication of L. Libioulle *et al*.,[238] it is easy to tell the difference after the tip has been through the step of post fine etching. Those steps above are most referred from previous publications[238,239] and re-designed by Dr. Chee Seng Ng, including all chemical solution preparation, AC current programing and circuit modeling. Setup apparatuses for electrochemical etching are: power supply, linear micro-manipulator, microscope, switch, clip (tip holder), solution vial, counter electrode for rough etching; rough etching setup with Arduino microcontroller controlling switch for fine etching; pulsing circuit, DC power supply for micro-polishing, and Potentiostat-Biologic(EC-lab) for reduction. Figure 4.1(a) illustrates the fabrication process of Pt-Ir AFM. Figure 4.1(b) from left to right are continuous steps before, after rough etching and after fine etching. It is obvious to see there is a "thin neck" showing up after rough etching in the middle photo. Then we break the thin neck by doing fine etching. Figure 4.1(c)-(e) show the SEM images of Pt-Ir AFM tips we fabricated by different time and voltage on rough etching and rough etching. Figure 4.1(c) happens when the higher voltage is applied on rough etching, the thin neck is too narrow and tends to be a pillar shape. In this case, it is difficult to break the thin neck by fine etching. The radius of this tip is < ~ 26 nm and angle is < ~ 64º. However, this tip shape is easy to break and damage when the pressing force is applied during the experiment. Figure 4.1(d) happens when it takes too long on fine etching (after the decent thin neck fabricated by rough etching), From zoom-in SEM images we can see the tip surface is pretty rough, which means it is over-etching. The radius of this tip is < ~ 62 nm and angle is < ~ 40º, which is much larger than the tip in Figure 4.1(d). The best fabrication

Pt-Ir AFM tip we have so far shows in Figure 4.1(e), from the SEM image we can see the tip surface is smooth and its radius is < ~ 35.5 nm and angle is < ~ 20º.

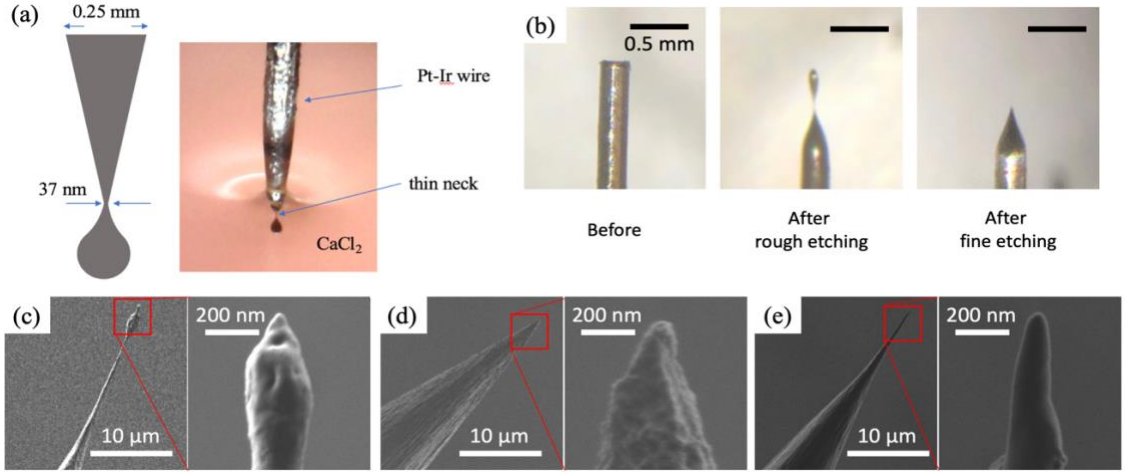

Figure 4.1: (a)This illustrates the fabrication process of Pt-Ir AFM. (b) From left to right are continuous steps before, after rough etching and after fine etching and (c)-(e) show the SEM images of Pt-Ir AFM tips fabricated by different time and voltage on rough etching and rough etching.

Figure 4.2 shows different deformed situations of the AFM tips, if the tip is under the flame annealing for too long. It is highly possible that the tip would be damaged (Figure 4.2(a)). The device we used for flame annealing was the Butane light torch, which can get the highest temperature ~ 1970 °C. Also, under the step of micro-polishing. Low-voltage pulse (3.5 – 5 V) would make the film layer crack (Figure 4.2(b)), and intermedia-voltage pulse (~ 7 V) can clean the film layer from Pt-Ir AFM tip uniformly (Figure 4.2(c)). High voltage pulse (~ 12 V) can help remove the film layer from the Pt-Ir AFM tip as well, but it may reduce the radius of the tip.

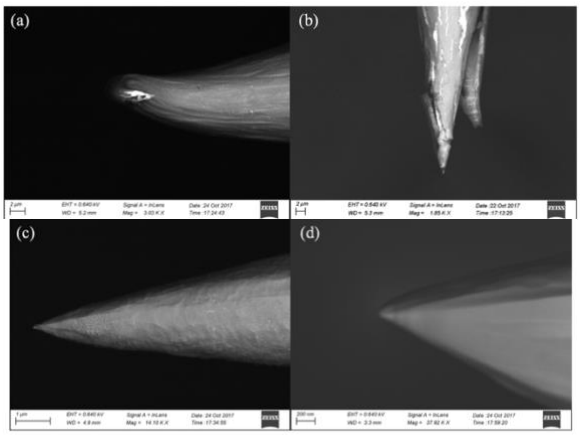

Figure 4.2: SEM images of Pt-Ir AFM tips made from different procedures: (a) flame annealing for too long, (b) after low-voltage pulse micro-polishing, (c) after intermediate-voltage pulse micro-polishing, and (d) after high-voltage pulse micro-polishing.

4.2.3 Conductive AFM measurement and Microstructure Characterization

For a well-defined quantification of parameters at the tip-sample interface, first, it is necessary to avoid the tip deformation during tip-sample engagements and subsequent measurements under a finite mechanical force between the tip and substrate surface. A tip-substrate pressing force (f_p) of 100 nN or larger resulted in a significant tip deformation as shown in Figure 4.3(a)-(c), and the deformation became more severe as f_p increases as expected. When the load was kept below ~ 50 nN, the spherical tip apex shape is preserved while a $\lesssim$ 15% increase in the tip radius can be seen in Figure 4.3(d) and (e). However, even this minimized change in the tip size was possible only when the tip made its initial contact with the substrate at a slow approach speed of 0.2 μm/s. When the approach speed was high (i.e., 2 μm/s), even a small targeted f_p < 10 nN resulted in significant tip deformation as shown in Figure 4.3(f) and (g). This is ascribed to an unintended application of excessive force during the initial tip-substrate engagement due to the force-feedback response of AFM, likely too slow to properly respond to the instantaneous pressing force.

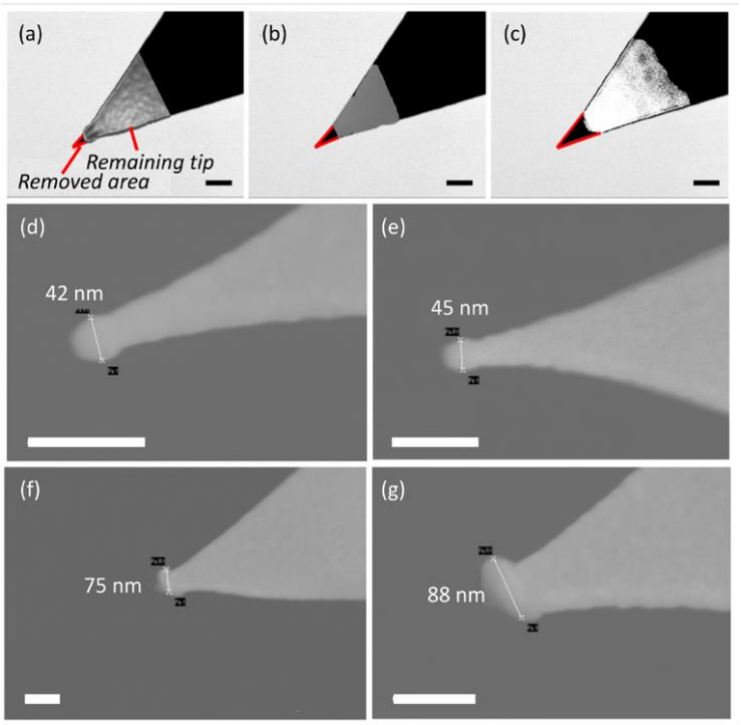

Figure 4.3: (a)-(c) SEM images of mechanically-degraded, Au-coated tips superimposed on another image of an as-cleaned tip. The images were taken after being exposed to a pressing force of 100 nN (a), 150 nN (b), and 440 nN (c) on an HOPG surface. Scale bar: 500 nm. (d)-(g) SEM images of tips after compressed on an HOPG surface with different pressing forces (f_p) at the approaching speed of (d) and (e) 0.2 μm/s and (f) and (g) 2 μm/s. Scale bar: 100 nm. Even with a small intended f_p of < 10 nN, the tips were deformed significantly when engaged at 2 μm/s. Note that the as-purchased tip apex diameter quantified from SEM images is 43 nm on average with a standard deviation of ~ 2 nm; the dimension from TEM images is somewhat different and the reason is yet to be clarified.[237]

Therefore, the tips were subjected to an f_p of < 50 nN and an approach speed of 0.2 µm/s to avoid a significant tip deformation for the subsequent study. As the geometry and mechanical properties of conventional metal-coated AFM probes are similar to each other, the aforementioned observation should be applicable to the majority of metal-coated tips. The metal-coated tips are usually covered by a bi-layered metal (a noble metal deposited on an adhesive layer) of 50 – 70 nm with the resulting apex radii of 20 – 30 nm, and noble metals have similar maximum elastic limits of 200 – 300 MPa.

Force spectroscopy (acquisition of force–distance curves)[240] has been a widely used approach to study changes in interfacial nature under different conditions.[241–243] Figure 4.4(a) shows typical force–distance curves (both approaching and retracting) with a plasma-cleaned Au-coated tip, from which the adhesion force between the tip and substrate was measured. During the retraction process after making a mechanical tip–sample contact, the tip will not be detached from the substrate at the same point where the tip was initially engaged with the surface due to a finite amount of tip substrate adhesion. A negative (tensile) force is needed before the so-called snap-off, i.e., the abrupt detachment from the substrate. The amplitude of the tensile force needed to free the tip from the substrate surface corresponds to the adhesion force. Figure 4.4(c) and (d) present the adhesion force (f_a) measured with this approach after an as purchased and an as-cleaned (i.e., plasma-treated) Au coated tips make a contact with an HOPG surface with various f_p. The as-purchased tip showed a wide variation in f_a, whereas the as-cleaned tip showed a consistent fa in the vicinity of ~ 20 nN. This justifies the critical necessity of a tip cleaning process for a reliable characterization of a contact. It is also noted that fa is independent of f_p suggesting that there was not a mechanical pressure-induced bonding formation or chemical reaction.

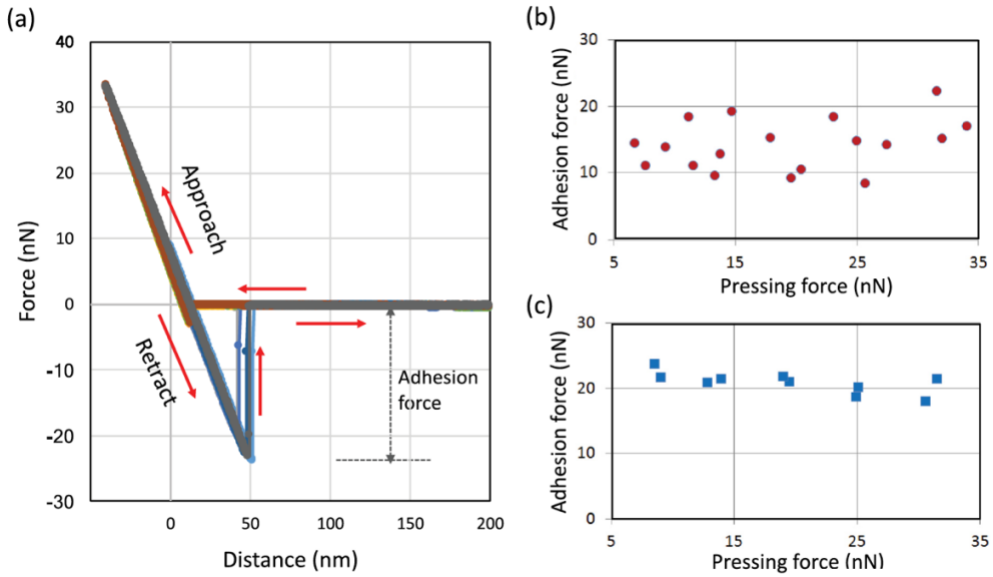

Figure 4.4: (a) Force-distance graph of the Au-HOPG interface, showing little hysteresis between approaching and retreating processes, and little difference in their trajectories with repeated cycles. (b) and (c) Adhesion forces measured after applying a range of pressing forces using an as-purchased (b) and an as plasma- cleaned tip (c). For all the measurements, the Au-coated tip was pressed on and detached from an HOPG surface.[237]

Figure 4.5(a) shows the change of R with f_p. Before performing these sweeps, the nano-cell, in which a new plasma cleaned tip is in contact with an HOPG surface, reached an LRS by a continuous 5 mV bias application. Then, the tip was retracted from and re-attached to the HOPG surface repeatedly, and R was quantified during the retracting processes by impedance measurements. As shown in Figure 4.5(a), during the initial two retracting processes (sweeps 1 and 2), R did not show a clear dependency on f_p. However, R became inversely proportional to f_p with a much higher amplitude in the subsequent sweeps (3 and 4). These behaviors, which were routinely observed, can be interpreted as follows. First, the little dependency of R on f_p shown in Sweeps 1 and 2 can be understood if the formation of a few-nm-sized conducting filaments (CFs) was responsible for the LRS. As electronic conduction is mostly governed by the tiny CFs, the interfacial force (f_p) and the resulting increase in the tip-substrate contact area has little impact on the measured R. The so-called filamentary resistive switching behavior is universally observed in metal/insulator/metal cells, in which the insulator can be virtually any metal oxide including SiO_2,[244] TiO_2,[245] and TaO_x.[246] A continuous positive bias on the oxide would extract oxygen from the oxide layer and thus make the oxide layer (Au_2O_3) partially reduced to Au_2O decreasing the electronic band gap significantly.[247] The reduction of the gold oxide layer may form CF(s), and the size of CFs is often reported to be few–several nm only.[244,248–250] As the thickness of gold oxide in our system is just few nm, the size of CFs is likely smaller than the reported values. The assertion of CF mediated electronic transport behavior is also in line with our recent observation in another metal/oxide/metal (Pt/ TiO_2/Pt) system,[236] in which the electronic transport behavior is found highly coupled with the chemical bonding status of the metal/oxide interface. As shown in Figure 4.4(a), the LRS in the first two sweeps (curves 1 and 2) is maintained until a tensile force of ~ 10 nN is reached during retraction, whereas curves 3 and 4 exhibit very high noise-level resistances even before reaching a tensile regime (negative f_p). In an LRS contact, it is conjectured that there is a chemical bonding formed between a CF and Au surface, making the contact more adhesive. We will discuss sweeps 3 and 4 more in Section 4.4 and provide an explanation for this phenomenon.

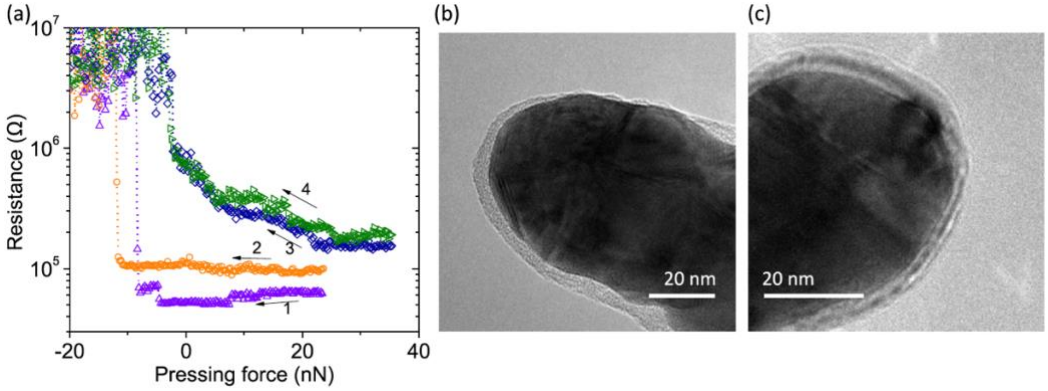

Figure 4.5: (a) The change of measured resistance with pressing force. The sweeps were quantified by impedance measurement with 2 mV of ac bias. [(b) and (c)] TEM images of a new plasma-cleaned tip (b) and another plasma-cleaned tip that experienced an LRS (c).[237]

4.3 Results and Discussion

When the tip is detached from the HOPG surface and an end of CF is exposed to an oxygen-containing environment, the CF may be readily disconnected due to the unstable nature of the reduced gold oxide (Au_2O).[247,251] As the direct channels for fluent electronic transport are not available anymore, R is now hypothetically dictated by tunneling the current flowing through the insulating Au_2O_3 layer. To check if the f_p-R curves (Sweeps 3 and 4) are aligned with the hypothesis, Equation 4.1 for field-assisted tunneling (Fowler-Nordheim current) is introduced:[252]

$$i = \gamma\alpha \frac{q^2}{8\pi h}\frac{m_0}{m^*}\frac{1}{t^2(E)}\frac{\beta^2 V^2}{\phi {s_0}^2} exp\left(-\frac{8\pi}{3}\frac{\sqrt{2m^* q}}{h} v(E)\frac{s}{\beta V}\phi^{\frac{3}{2}}\right) \qquad \text{(Equation 4.1)}$$

where i_{FN} is the current, s is the thickness of the oxide (s_0 is the zero-load oxide thickness), q is the electron charge, h is the Planck's constant, m_0 is the free-space electron mass, and m^* is the effective mass of the electron in the oxide (m_0/m^* = 0.45). $v(E)$ and $t(E)$ account for image charge lowering of the barrier ($v(E) \sim 2.2 \times 10^{-6}$; $t(E) \sim 10^{-3}$). $v(E)$ was quantified by $v(E) = \Delta\phi_B/\phi$ where $\Delta\phi_B = 2\sqrt{\frac{qE}{16\pi\varepsilon_0\varepsilon_s}}$.[253] Here, E is the electric field (when s = 5 nm), and ε_s is the relative permittivity of golden oxide film. It is calculated that $\Delta\phi_B \sim 1.16 \times 10^{-5}$ V, and thus $v(E) \sim 2.2 \times 10^{-6}$. The quantified $v(E)$ was considered a constant for the fitting. On the other hand, *t(E)*, a parameter for image charge at the breakdown fields of interest, was considered as a variable. The *t*(E) value from the fitting shown in Figure 4.6 is 9.88×10^{-4}. The fitted value is reasonable because the breakdown field strength of oxide is about 1 kV/mm, about 3 orders of magnitude smaller than that of SiO_2;[254] $t(E)$ for SiO_2 is about 1.013.[252] β is a field enhancement factor (β = 1 representing parallel plane plates), V is the applied voltage (5 mV), ϕ is the barrier height at the emitting interface (5.24 eV),[252] and γ is a parameter to reflect the change in the tip-surface interfacial area for electronic emission with the change of f_p. Assuming that the tip is spherical and elastically deformed on contact, γ is expressed as Equation 4.2:

$$\alpha \approx \pi\left[\frac{r_0(f_p+16f_a)\epsilon}{E}\right]^{\frac{2}{3}} = \pi\left[\frac{r_0(f_p+16f_a)}{E}\frac{f_p}{AE}\right]^{\frac{2}{3}} \qquad \text{(Equation 4.2)}$$

where f_p is the pressing force (spanning from -5 to 15 nN), fa is the force required to separate the AFM tip from the substrate surface (adhesive force), E is the Young's modulus of the oxide, ϵ is the strain of the oxide formed by the applied pressure, and A is the emissive interface area. In accordance with TEM observations, the zero-load oxide thickness (s_0) of 5 nm and the AFM tip radius (r_0) of 25 nm were used for the fitting. Changes in s were quantified as a function of f_p via a two-dimensional continuum analysis. If the Au_2O_3 layer is approximated as a cylinder between Au and HOPG, the change in oxide thickness by pressing force can be modeled in 2D. The relationship, E (Young's modulus) = stress/strain = $(F \times s_0)\ )/A(s - s_0)$, was used to calculate the change in oxide

thickness. Here, s is thickness, s_0 is the original thickness of Au_2O_3, and F is the pulling force. E was chosen to be ~ 250 GPa for Au_2O_3 as those for metal oxides roughly ranges from 200 – 300 GPa.[255] The interface area for electronic emission ($A = \pi a^2$) was quantified by using the generalized equation (Equation 4.3) for contact radius (a) proposed by Carpick *et al.*[199]

$$\frac{a}{a_0} = \left(\frac{a + \sqrt{1 - \frac{f_p}{f_a}}}{1 + \varphi} \right)^{\frac{2}{3}} \qquad \text{(Equation 4.3)}$$

where φ is a parameter to gauge a relative amplitude of surface force with respect to elastic deformation (see the supplementary material). Among all the parameters, the i and f_p are given variables obtained from Sweep 3, and s and $t(E)$ are the parameters fitted to Equation 4.1. All other parameters including ϕ, β, f_a, s_0, and $v(E)$ are constants obtained from relevant references or experimental observations as shown above. Based upon these constants, $v(E)$, A, s, and c were calculated using the equations provided. Within the given range of f_p, the corresponding A and s values were quantified. During the retraction from f_p =15 nN, A decreases from 103.5 nm^2 to 83.4 nm^2 while s increases from 5.0 nm to 5.3 nm as shown in Figure 4.6(a). With these parameters, the fitted line is well matched with the experimental f_p-R relationship (where $R = V/i$), supporting the field-assisted tunneling process (Figure 4.6(b)).

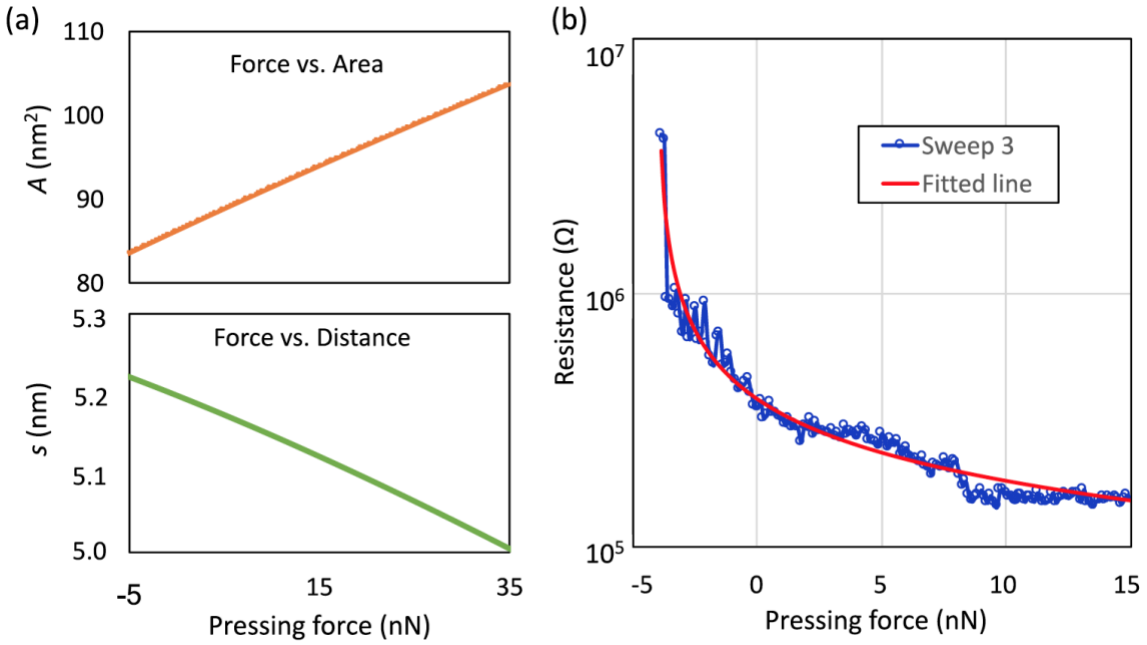

Figure 4.6: (a) The change of calculated area and distance with pressing force. (b) A fitting of an f_p-R curve [Sweep 3 shown in Figure 4.5(a)] to an equation of field-assisted tunneling.[237]

4.4 Conclusions

Experimental work was focused on the Au-HOPG interface formed with Au-coated tips and HOPG substrates. A tip surface cleaning process to remove the organic contaminant is indispensable for a consistent contact but forms a thin oxide layer screening a metallic surface. The impact of pressing force and approaching speed on the tip deformation was studied after a proper tip cleaning process was chosen. To conserve the overall tip geometry within an elastic regime, the pressing force and approaching speed needed to be limited to 50 nN and 0.2 μm/s. A prolonged electrical biasing with 5 mV decreased electrical resistance significantly and doubled the adhesion force of the interface. It is suggested that a low resistance state was realized by forming a narrow conducting channel by local electrochemical reduction of gold oxide. The reduced gold oxide is conjectured to propagate from the tip-substrate interface through the oxide film. The LRS is readily lost when the tip is detached from the HOPG surface, which is ascribed to a disconnection of the CF due to the unstable nature of the reduced gold oxide (Au_2O). When the LRS is lost, the electronic transport at the tip-substrate interface is likely governed by a tunneling behavior through the insulating oxide nano-film.

The fine etching step produces a low angle tip with diameter less than 1 μm, suspended mass for Pt neck determines the breakage radius of tip. Short AC voltage pulse (3.5 V, 20 ms) does not produce even etching after neck breaking, but it improves the radius of Pt-Ir AFM tips. In the step of micro-polishing, low micro-polishing voltage causes cracking of Pt-Ir layer. Higher micro-polishing voltage produces better surface finish for the tips. Voltage of 7 V, 16 μs (890 Hz) for 10 seconds produces the best tip radius (~ 9.5 nm) among other parameters. There are still a lot of uncertain factors we need to find out, it is necessary to understand how to make the good quality tips for the purpose of a new advanced setup with micro-scale heating stage enabled in-situ high temperature electrochemical measurements.

Chapter 5

Ionic Transport and Electrochemical Reaction on Air Electrodes of Solid Oxide Fuel Cell Study via AFM

5.1 Introduction

Ionic transport in solid oxides lays out the foundation of solid-state electrochemical energy and sensor devices. It is widely known that oxygen vacancy transport in solid oxide fuel cells (SOFCs) is temperature-dependent. At high temperatures of ~ 400 ℃ or higher, oxygen vacancies are activated and start to move fast through the oxide surface and interface(bulk). Although studies of heterogeneous ionic transport in polycrystalline oxides, a complete understanding of have been investigated over the past several decades, we are not yet able to fully understand the full picture and reasoning behind it.

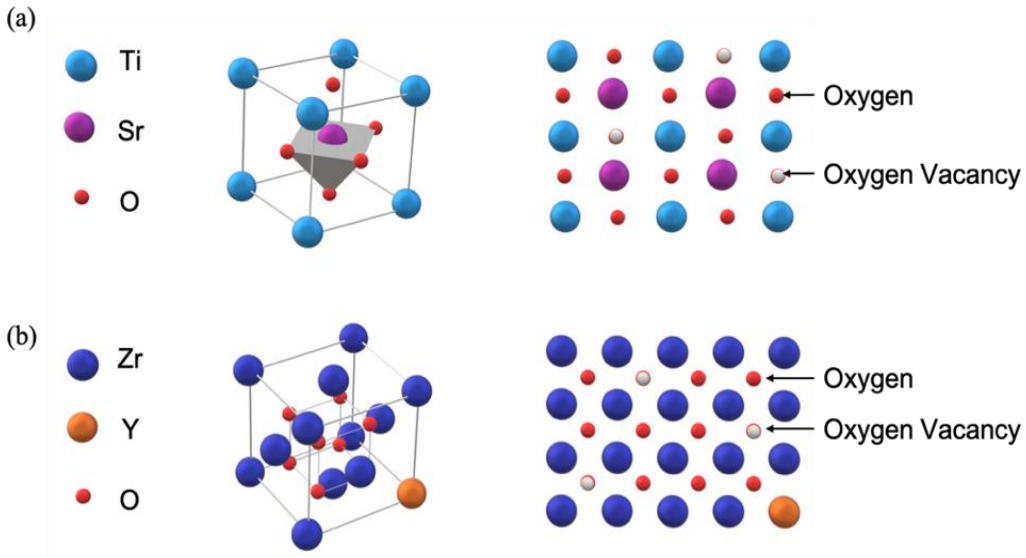

Figure 5.1: The cubic unit cell and schematic diagrams depicting the oxygen vacancy configurations (isolated state) of (a) $SrTiO_{3-\delta}$ and (b) Y_2O_3-stabilized ZrO_2.

We chose $SrTiO_3$ (STO) and Y_2O_3-stabilized ZrO_2 (YSZ) as our samples because they are both common materials for intermediate temperature SOFCs and frequently used in devices such as oxygen-ion-conducting solid electrodes, solid oxide fuel cells (SOFC), electro-chemical oxygen pumps (EOP), and catalytic membrane reactors–including partial oxidation of methane (POM) to syngas.[256–267] STO has a Perovskite structure (Figure

5.1(a)) and has a better mixed ionic and electronic conductivity (MIEC) compared to YSZ. YSZ is a face-centered cubic structured ceramic (Figure 5.1(b)), and is and commonly used as a solid oxide electrolyte, meaning it is an excellent ionic conductor.[268,269] Since they both have different characteristics and structures, we are interested in doing more research to better understand how ionic (oxygen vacancy) transports on both of them respectively. This topic is always interesting and a lot of research groups have been done before.[270,271] However, it is a novel method to observe and measure diffusivity and electrical characteristics of oxygen vacancy by AFM. In our study, we used CAFM and KPFM on AFM and tried to obtain an understanding of oxygen vacancy's mechanical and electrical characterization.

5.2 Experimental

5.2.1 Experiment setup and sample preparation

In our study, we applied a positive bias (+10 V) to the AFM probe when it was in contact with the samples for 5 to 10 seconds at room temperature (25 ℃). We then increased the temperature to 100 ℃ and 200 ℃ through ceramic heating (Shown in Figure 5.2(b)) after detaching the AFM probe. Afterwards, we used KPFM to measure the surface potential for every specific time period. The experiment setup is shown in Figure 5.2(a). Here we chose STO ($SrTiO_3$) and YSZ (8 mol% Y_2O_3 stabilized ZrO_2) crystal substrates as our samples (Crystal orientation <100> by MSE Supplies™). The entire experiment was conducted under nitrogen inflow to prohibit water in the air from influencing the generation and derogation of oxygen vacancy.

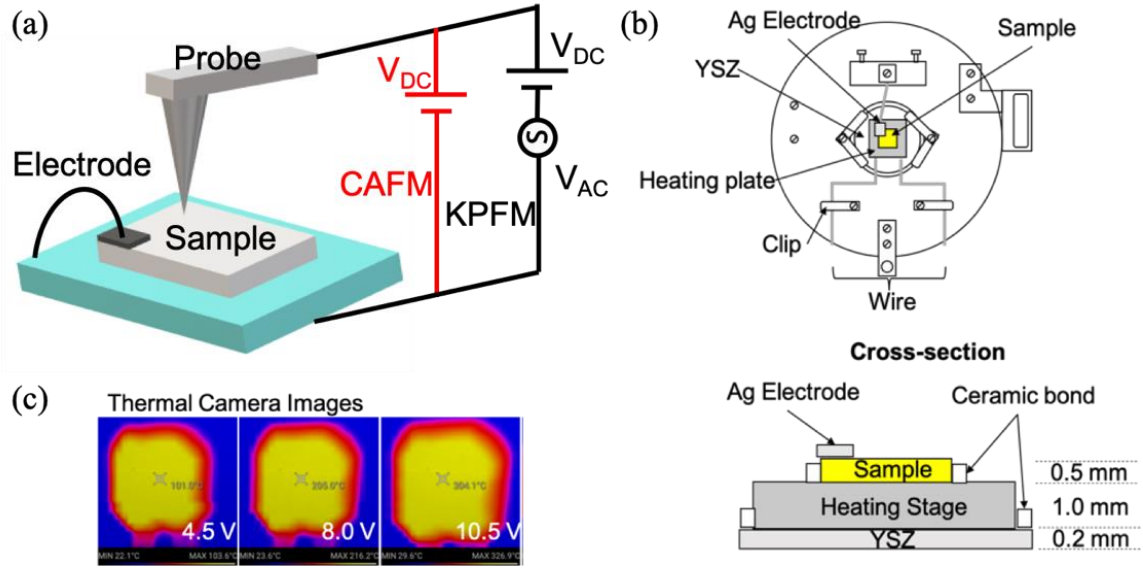

Figure 5.2: (a) Experiment setup with conductive atomic force microscopy method (CAFM, path in red) and Kelvin probe force microscopy (KCFM) on the AFM device, (b) AFM sample heating stage setup, and (c) thermal imaging of the heating stage using different voltages.

5.2.2 Oxygen vacancy generation

Positive bias was applied to the tip with respect to the electrode on the side of the sample, making electron injection into the sample surface and forming local oxygen vacancies via an oxygen evolution reaction (Shown in Figure 5.3(a) to Figure 5.3(b)). Stopping the application of positive bias after a short period of time may have caused the accumulation of oxygen vacancies to rearrange and diffuse. There are two paths of diffusion of oxygen vacancies as shown in Figure 5.3(c); Path I, surface diffusion; and Path II, diffusion into the bulk.

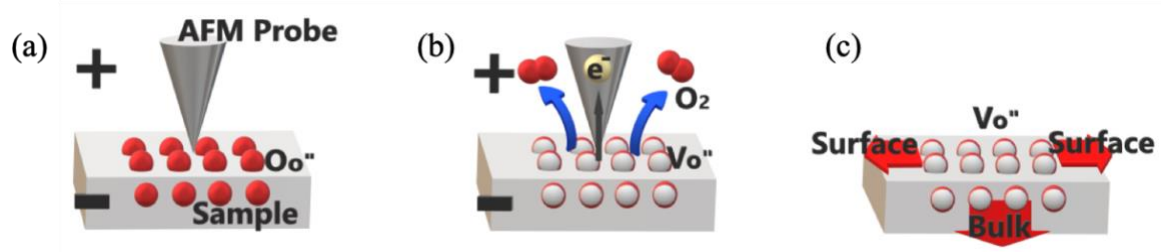

Figure 5.3: The continuous steps of oxygen vacancy generation: (a) provide a positive bias on the AFM probe; (b) vicinity oxygen ions have an oxidation reaction to generate oxygen vacancies and release oxygen; and (c) those oxygen vacancies move through the surface and bulk.

We needed to find a method of observing and measuring the ion/oxygen vacancy transport among surfaces and interfaces of STO and YSZ. In our study, the method we found was to use Kelvin probe force microscopy (KPFM) and conductive atomic force microscopy (CAFM) by atomic force microscope (AFM) after oxygen vacancies were generated by providing a positive bias to the probe-sample contact under CAFM mode. CAFM is a common method which has been widely used by AFM set-up on different measurement purposes, such as resistive random access memory.[272,236] KPFM is a method that can be used to measure the local contact potential difference (CPD) between the probe and the sample.[273]

5.2.3 Removal implementation

One group previously studying U. Celano *et al.*[274] built a 3D interpolation conductive filament image by over imposition of the collected 2D CAFM slices. They used the diamond probe as a scalpel to remove material from the sample surface by the precise force-control of AFM in order to collect data based on a slice-and view approach. In our study, we chose a similar method of collecting surface potential of the sample by KPFM as every slice was removed by a diamond-coated probe. The process and result are shown in Figure 5.4(a). We used a diamond-coated probe (DCP) (HQ:DMD-XSC11, Force constant: 10 – 30 N/m by MikroMasch SPM Probes&Test Structures) to remove the sample surface layer by layer by scanning AFM's contact mode (shown in Figure 5.4(b)). Similar

to what we did on the sample's surface, we measured the potential by KPFM after removing each layer. In order to accurately calculate the oxygen vacancy distribution on each layer we must first understand how deep the oxygen vacancy goes beneath the surface under different temperatures. The probes were cleaned thoroughly before the experiment to best eliminate contamination and mechanism issues.[237]

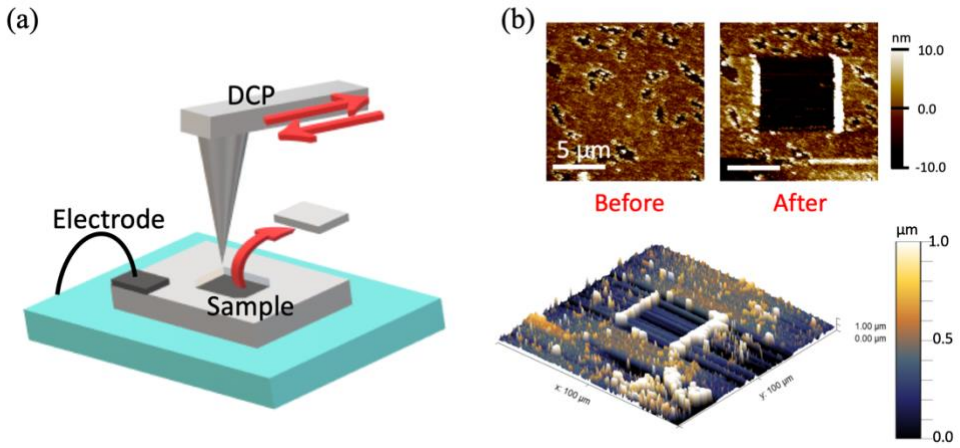

Figure 5.4: (a)The demonstration of the process of sample surface removal by diamond coated probe on the AFM. (b)Topography AFM images of before and after sample surface removal work. In the after image there is an about 3μm×3μm size of squared removal area. The lower graph is the 3D topography image on AFM.

5.2.4 Data analysis

In order to calculate diffusivity (D) and activation energy (E_a), we needed to formulate a mathematical expression. First, Poisson's equation (Equation 5.1) was applied to convert surface potential to charge density (ρ) from the resulting KPFM maps of the sample. Then, we utilized the solution of Fick's second law, which can be expressed as a Gaussian distribution (Equation 5.2) to fit the charge density distribution at different time frames.

$$\left(\frac{\partial}{\partial x^2}+\frac{\partial}{\partial y^2}\right)V(x,y)=-\frac{\rho(x,y)}{\varepsilon} \qquad \text{(Equation 5.1)}$$

$$c(x,t)=\frac{Q}{\sqrt{4\pi Dt}}exp\left(-\frac{x^2}{4Dt}\right) \qquad \text{(Equation 5.2)}$$

To quantify the distribution and diffusion of oxygen vacancy, the ionic diffusivity and its activation energy were calculated for both surface and bulk diffusion at various temperatures. To do so, we first calculated the conductivity coefficient σ and compared it to previous publications.[275,276] Because the dimensions of AFM probes are much smaller than that of typical scenarios, we chose the spreading resistance to calculate.[277] The spreading resistance (Equation 5.3) is associated with a small area of material around the

contact point of the tip and sample. To find r, a circular radius of point of contact, for calculating spreading resistance we need to know the contact area ($A = 4\pi r^2$, and $\tilde{\rho}$ is resistivity of the sample, which $\tilde{\rho} = \sigma^{-1}$). From previous publications of Carpick RW *et al.*[199] (in section 2.4.3) help us calculate it.

$$R_{SR} = \frac{\tilde{\rho}}{4r} \qquad \text{(Equation 5.3)}$$

Moreover, there are different amounts of induced charge on the sample's surface and subsurface (bulk) after charging. According to the definition of current and ohmic law, we are able to quantify the amount of induced charge at specific times from the surface potential and distance data we got from KPFM measurements (Equation 5.4-1 and Equation 5.4-2,). Here, we assume the resistance is a constant during the CAFM charging process. Figure 5.5(a) demonstrates the amount of induced charge on the surface and in the bulk of the sample after charging. To analyze the experiment data, we used the Dirac distribution to fit raw KPFM data. Then, we used the 2D Poisson equation (Equation 5.1) to obtain the charge density distribution (ρ). The value of permittivity (ε) here we used values from publications.[278–280]

$$\int dQ = \frac{1}{R}\int_0^{t_n} V_n\, dt = \frac{1}{R}\left(\frac{dt}{dx}\right)\int_{-x_n}^{x_n} V_n(x)\, dx \qquad \text{(Equation 5.4-1)}$$

$$Q_n = 4r\sigma_i\left(\frac{t_n - t_{n-1}}{x_n - x_{n-1}}\right)\int_{-x_n}^{x_n} V dx \qquad \text{(Equation 5.4-2)}$$

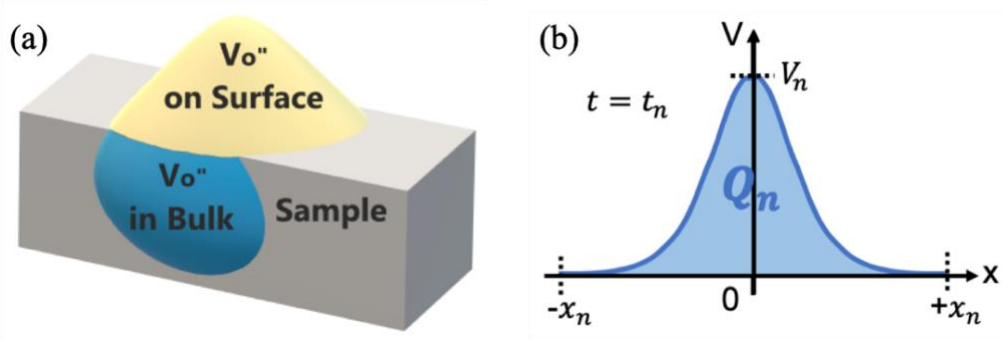

Figure 5.5: (a) A drawing demonstrating induced charge on the surface and in the bulk after charging ; and (b) the method quantifying the amount of induced charge by integral.

To calculate the diffusivity of the sample's bulk, we used solutions from Fick's first and second laws (Equation 5.5).[281–283] Calculating with Gaussian integral and error function, we got Equation 5.6, where Q_n is the amount of induced charge at the depth of d_n and time of t_n. From Equation 5.6, we have to quantify the value of induced charge to continue calculating.

$$\frac{dc(x,t)}{dt} = D\frac{d^2c}{d^2x} \qquad \text{(Equation 5.5)}$$

$$Q_n = Q(d_n, t_n) = \frac{Q_{n-1}}{2} erfc\left(\frac{|d_{n-1}-d_n|}{2\sqrt{D(t_{n-1}-t_n)}}\right) \qquad \text{(Equation 5.6)}$$

To quantify diffusivity of oxygen vacancy from our KPFM data, we used Gaussian distribution (Equation 5.2) for the surface and the solution from Fick's first and second laws (Equation 5.5) for bulk. First, we used the Dirac distribution equation to fit data we got from KPFM (Shown in Figure 5.6(a) and (b)). There are a few assumptions in place to calculate the diffusivity on the sample surface: (1) After ending bias application, the vacancy profile is a Dirac function at the center of the tip-sample contact area; (2) The amount of the induced charge, Q, is quantified by the methods mentioned in Figure 5.5; and (3) before bias application, the sample is neutral and the effective charge density is zero. Using all values of the induced charge (C), we put those in Equation 5.2 and Equation 5.6. We are able to derive the diffusivity of the sample surface and bulk at different temperatures by Arrhenius equation.[287]

When analyzing the data on MATLAB, we did some mathematical method on Gaussian distribution and the solution from Fick's first and second laws. By power series expansion for exponentials (Equation 5.7), Gaussian distribution will be converted to Equation 5.8.

$$e^x = \sum_{n=0}^{\infty} \frac{x^n}{n!} \qquad \text{(Equation 5.7)}$$

$$c(x,t) = \frac{Q}{\sqrt{4\pi Dt}}\left[(1)x^0 - \left(\frac{1}{4Dt}\right)x^2 + \left(\frac{1}{32D^2t^2}\right)x^4 - \left(\frac{1}{384D^3t^3}\right)x^6 + \left(\frac{1}{6144D^4t^4}\right)x^4 + \cdots\right] \qquad \text{(Equation 5.8)}$$

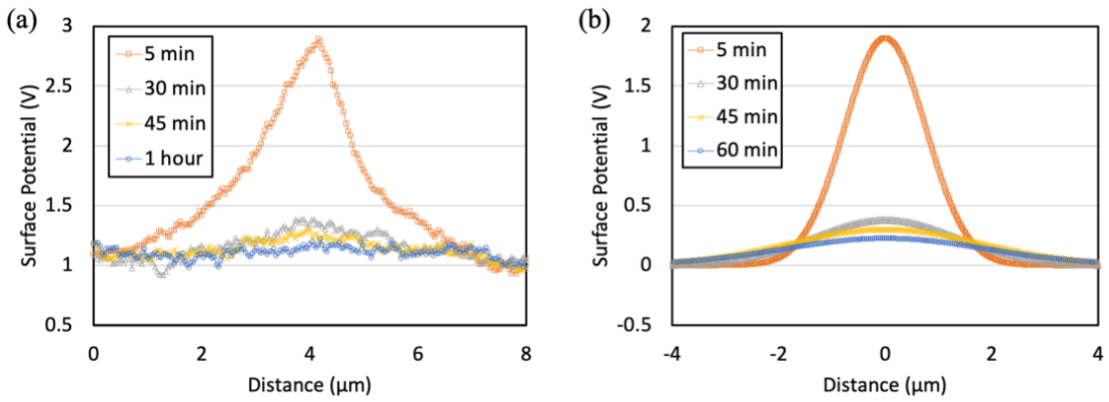

Figure 5.6: (a) The raw KPFM data of YSZ surface after charging 10 V for 10 seconds, then measuring the surface potential by time; and (b) the fine data fitted from the raw data by the Dirac distribution equation.

At the same time, the solution from Fick's first and second laws (Equation 5.9, M is total amount of diffusing substance) can be rewritten as Equation 5.10 by Consider the diffusing substance in an element of width $\delta\xi$ to be a line source of strength $c_0\delta\xi$, Shown in Figure 5.7. After integrating and converting by Gaussian integral and complementary error function.[281] To calculate diffusivity in sample's bulk, Equation 5.10 can be

understood as Equation 5.6. For the same purpose of calculating on MATLAB, we did power series expansion for exponential again in a complementary error function. We got Equation 5.11 eventually. Where $\Delta z = |z_{n-1} - z_n|$ and $\Delta t = t_{n-1} - t_n$ (z is thickness/depth and t is time).

$$c(x,t) = \frac{M}{2\sqrt{Dt\pi}} e^{-\frac{x^2}{4Dt}} \qquad \text{(Equation 5.9)}$$

$$c(x,t) = \frac{c_0}{2} erfc\left(\frac{x}{2\sqrt{Dt}}\right) \text{ (Equation 5.10)}$$

$$Q_n = \frac{Q_{n-1}}{\sqrt{\pi}}\left\{\frac{1}{2}\left(\frac{\Delta z}{\sqrt{D\Delta t}}\right) - \frac{1}{24}\left(\frac{\Delta z}{\sqrt{D\Delta t}}\right)^3 + \frac{1}{320}\left(\frac{\Delta z}{\sqrt{D\Delta t}}\right)^5 - \frac{1}{5376}\left(\frac{\Delta z}{\sqrt{D\Delta t}}\right)^7 + \cdots\right\} \qquad \text{(Equation 5.11)}$$

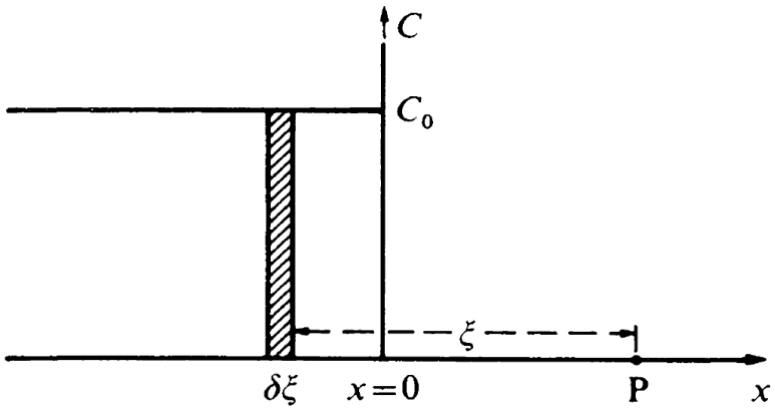

Figure 5.7: Extended initial distribution. [281]

During the time periods of increase to the high temperature we needed and decrease of the room temperature, we needed to quantify and calculate the relative time period under different temperature environments. For example, when we consider the situation of a 200 ℃ environment for oxygen vacancy diffusivity, the time is relatively faster under the temperature of 25 ℃. To achieve this purpose, we used a sort of mathematical induction method and set time is inversely proportional to exponential to the power of negative activation energy: $t^{-1} \propto \exp(-E_a/kT)$; more details are shown in the supplementary file. We assume the different activation energy first, then compare the result of activation energy value from this assumed activation energy value if they are close to each other. We started by analyzing the temperature increase and decrease speed of the ceramic heating plate while STO and YSZ were attached to it. Figure 5.8(a) and (b) show the temperature increase and decrease speed of STO/YSZ on the heating plates, respectively. Figure 5.9(a)-(h) shows the different ratios between temperature and time from different activation energy assumptions for STO/YSZ surface and bulk at temperatures of 100 ℃ and 200 ℃. For example, the blue line in Figure 5.9(a) is from the assumption activation energy of 0.5 eV.

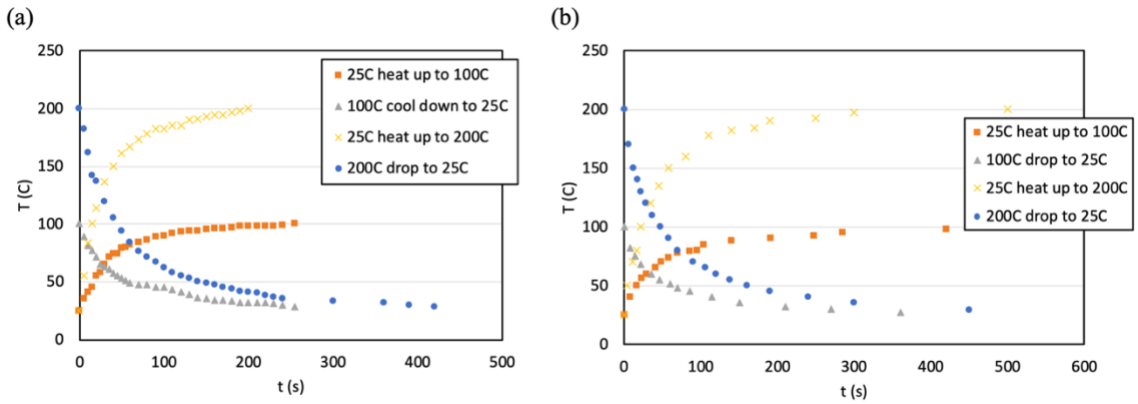

Figure 5.8: The temperature increase and decrease speed of (a) STO and (b) YSZ on the heating plates from room temperature (25 ℃) to the temperatures we need (100 ℃ and 200 ℃).

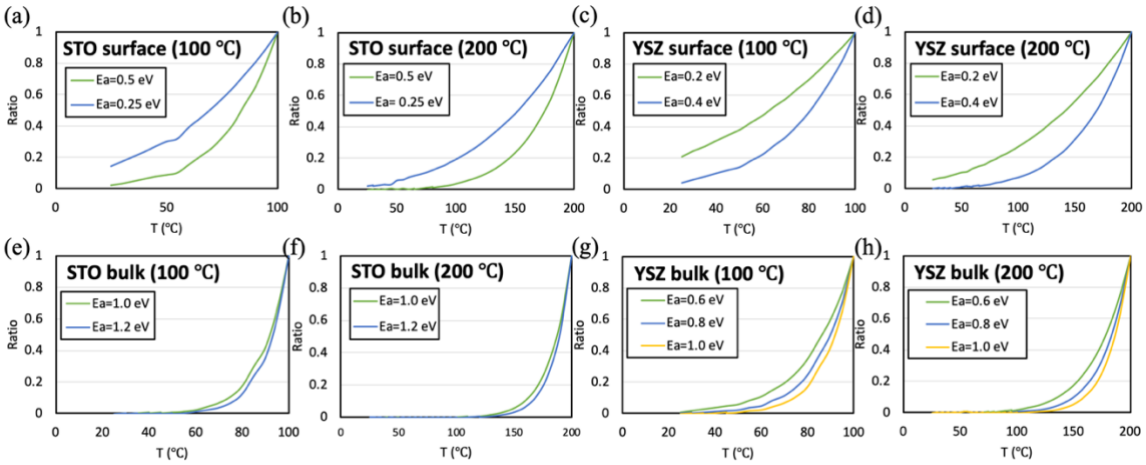

Figure 5.9: The different ratios between temperature and time from different activation energy assumption for (a) STO surface at 100 ℃, (b) STO surface at 200 ℃, (c) YSZ surface at 100 ℃, (d) YSZ surface at 200 ℃, (e) STO bulk at 100 ℃,(f) STO bulk at 200 ℃,(g) YSZ bulk at 100 ℃, and (h) YSZ bulk at 200 ℃.

Figure 5.10 to Figure 5.17 show the timeline for the oxygen vacancy diffusivity experiment for STO/YSZ surface/bulk, samples were on the heating plate from 25 ℃ to 100 ℃/200 ℃ and dropped back to 25 ℃. From these timeline data profiles we were able to quantify the relative time by mathematical induction method and calculate the most accurate activation energy of samples as well.

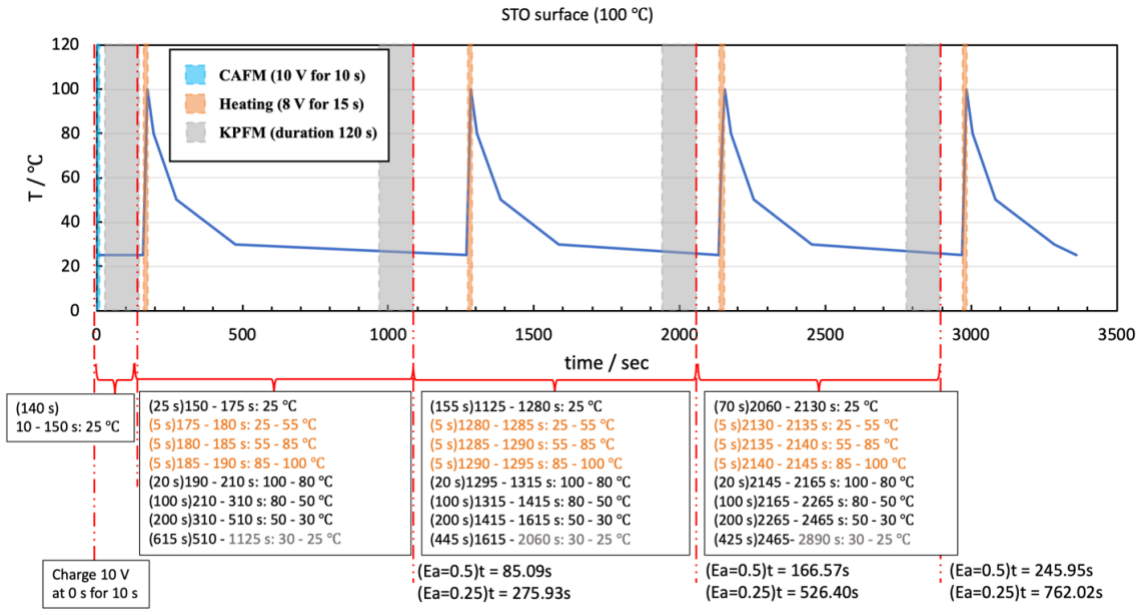

Figure 5.10: The timeline for the oxygen vacancy diffusivity experiment for STO surface. STO was on the heating plate from 25 ℃ to 100 ℃ and dropped back to 25 ℃.

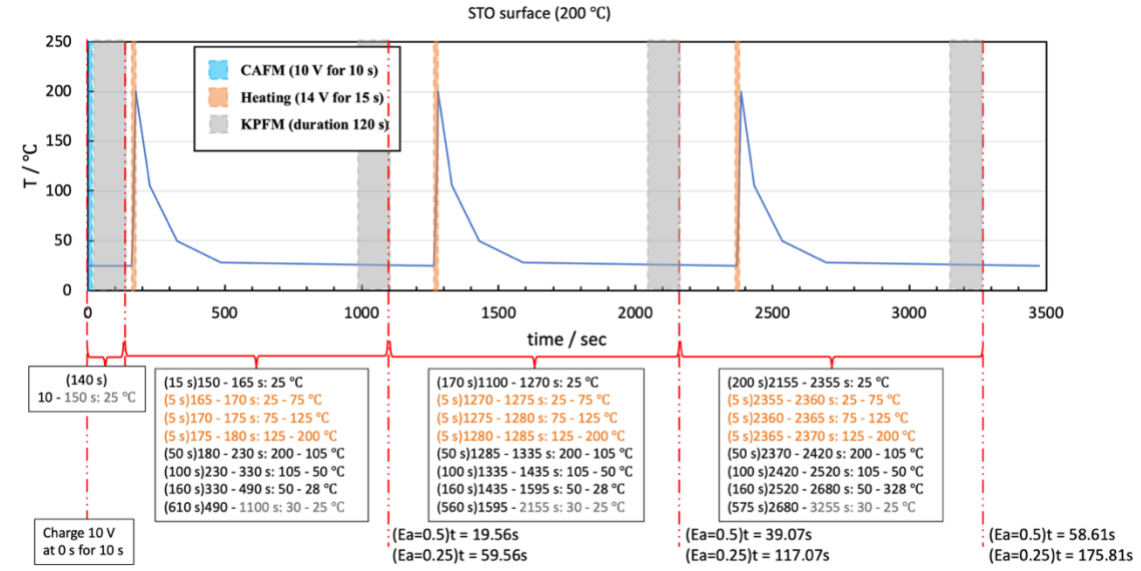

Figure 5.11: The timeline for the oxygen vacancy diffusivity experiment for the STO surface. STO was on the heating plate from 25 ℃ to 200 ℃ and dropped back to 25 ℃.

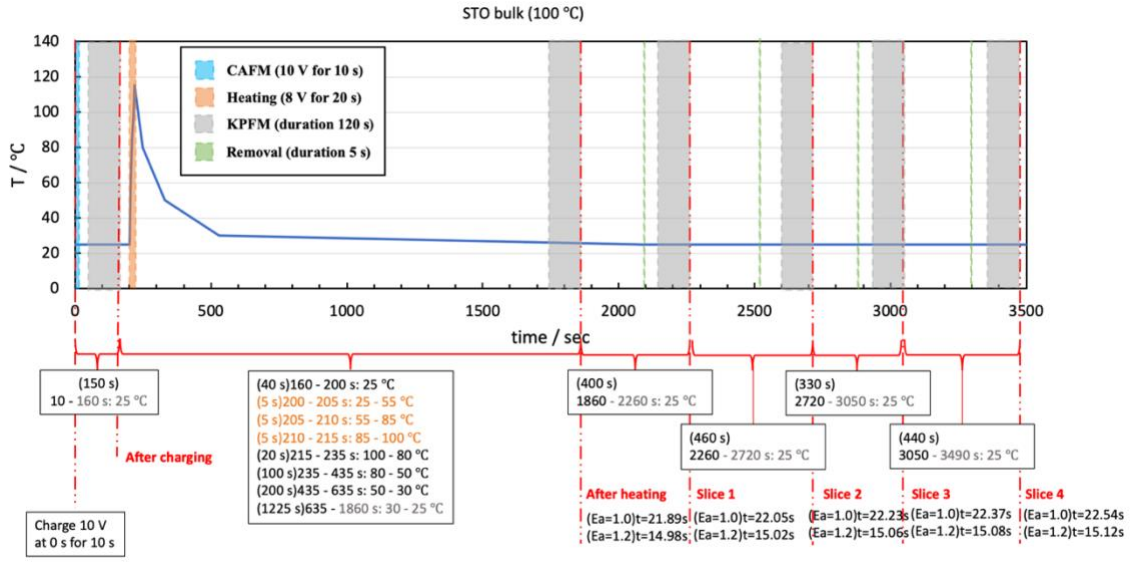

Figure 5.12: The timeline for the oxygen vacancy diffusivity experiment for STO bulk. STO was on the heating plate from 25 ℃ to 100 ℃ and dropped back down to 25 ℃.

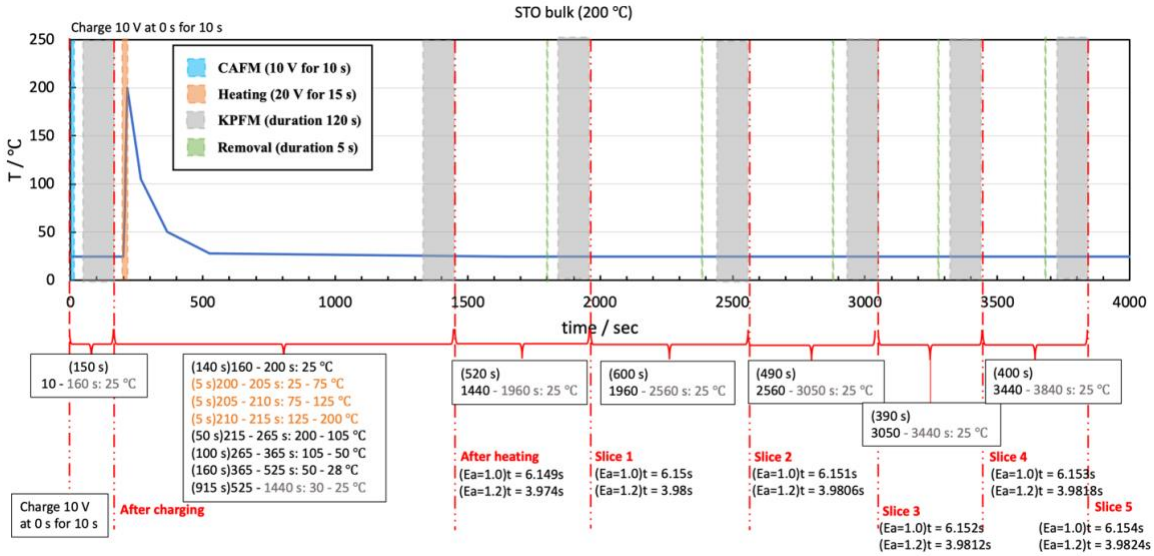

Figure 5.13: The timeline for the oxygen vacancy diffusivity experiment for STO bulk. STO was on the heating plate from 25 ℃ to 200 ℃ and dropped back down to 25 ℃.

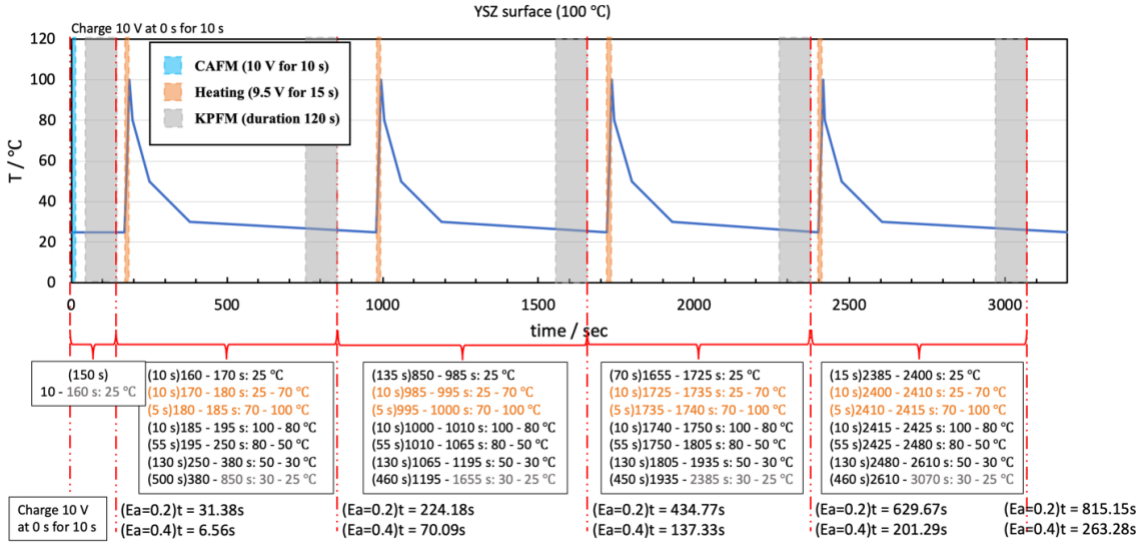

Figure 5.14: The timeline for oxygen vacancy diffusivity experiment for YSZ surface, YSZ was on the heating plate from 25 ℃ to 100 ℃ and dropped back down to 25 ℃.

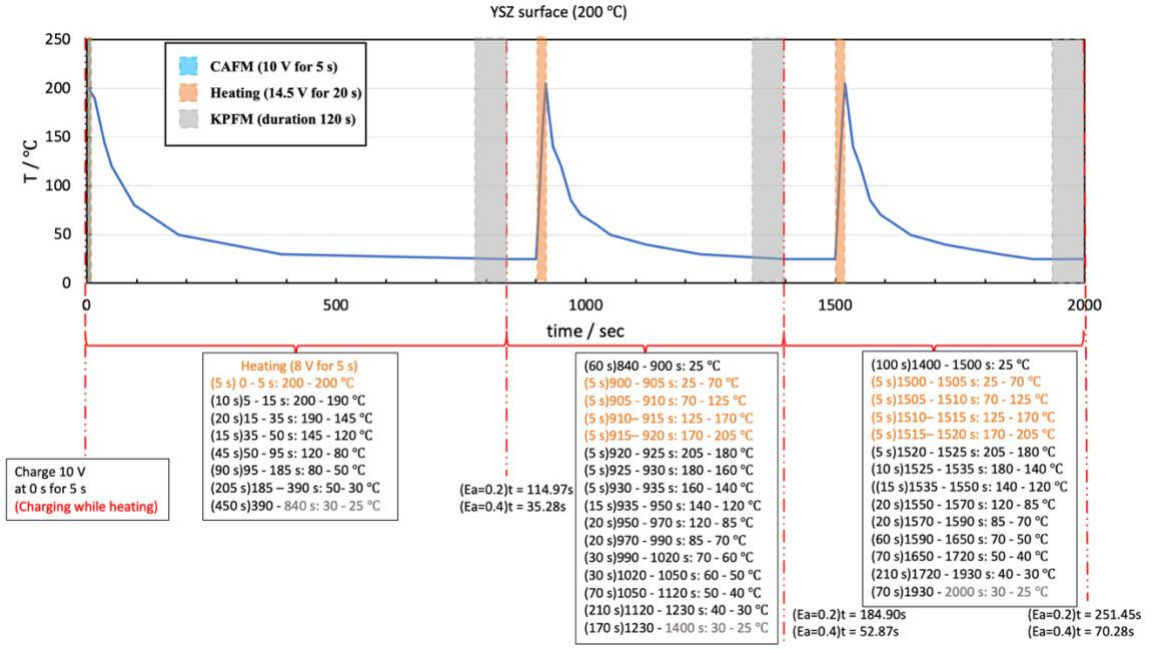

Figure 5.15: The timeline for the oxygen vacancy diffusivity experiment for the YSZ surface. YSZ was on the heating plate from 25 ℃ to 200 ℃ and dropped back down to 25 ℃.

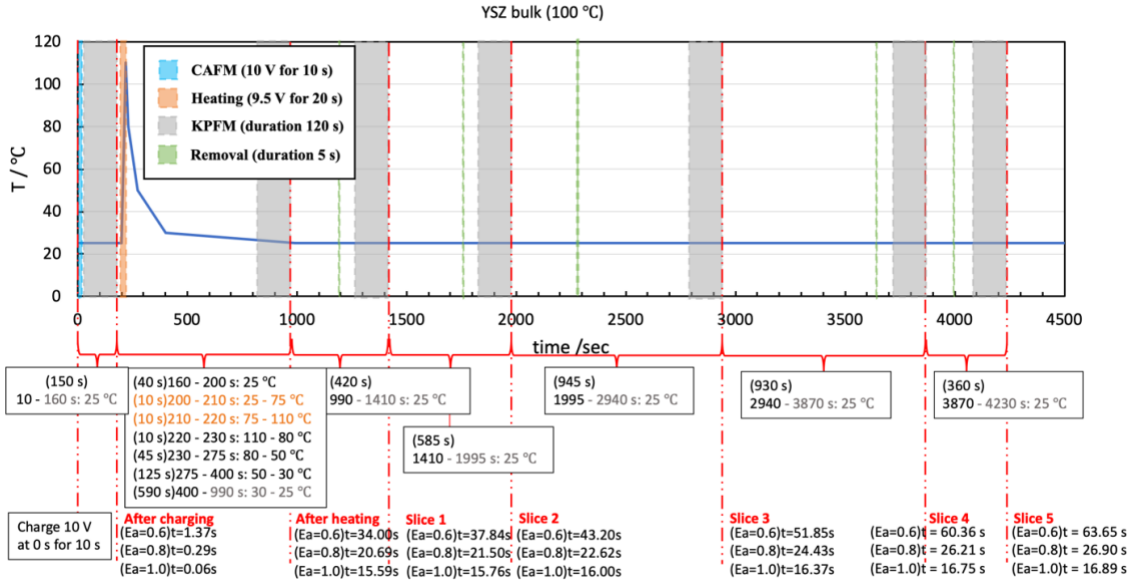

Figure 5.16: The timeline for the oxygen vacancy diffusivity experiment for YSZ bulk, YSZ was on the heating plate from 25 ℃ to 100 ℃ and dropped back down to 25 ℃.

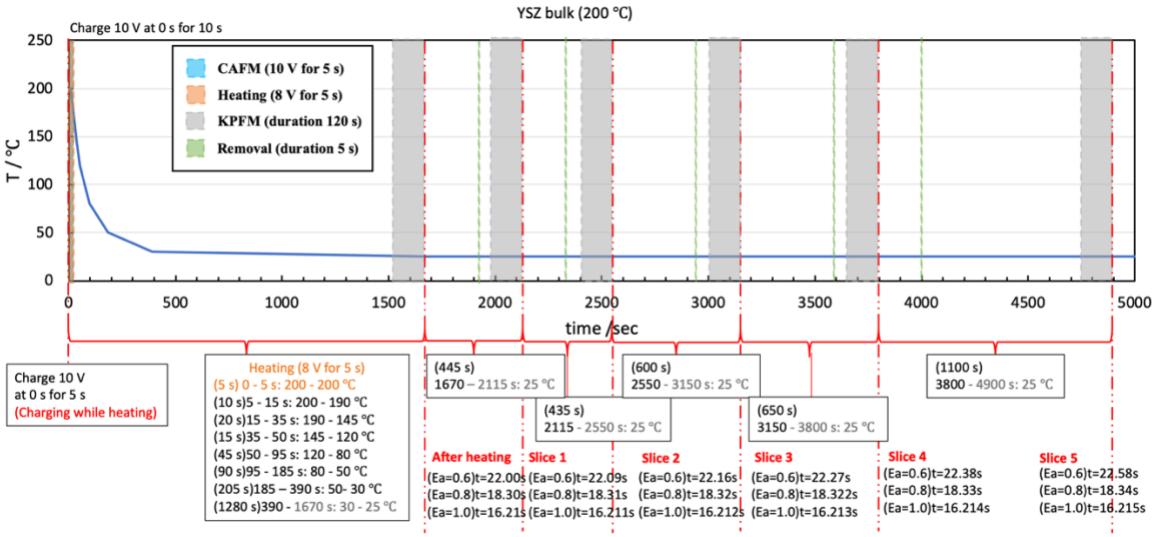

Figure 5.17: The timeline for the oxygen vacancy diffusivity experiment for YSZ bulk, YSZ was on the heating plate from 25 ℃ to 200 ℃ and dropped back down to 25 ℃.

5.3 Results and Discussion

5.3.1 Induced charge on STO/YSZ

The amount of induced charge by charging varies as a dependence of the sample's conductivity (resistance), which is different from temperature as well. Figure 5.18(a), shows the percentage of induced charge (unit is in coulomb, Q) on STO and YSZ under temperatures of 25 ℃, 100 ℃, and 200 ℃. The table in Figure 5.18(a) shows the ideal induced charge values charged on STO and YSZ. Here we used the definition of current ($q = i \times t$) and Ohm's law ($i = V/R$) to calculate those values. R is spreading resistance (Equation 5.3), V is 10 V and t is 10 seconds since we applied a bias of positive 10 V for 10 seconds. Around 50 – 60% of the total charge stays on the surface at 25 ℃ according to the calculation from Equation 5.4-2. The rest of the charge is either diffused to the bulk or otherwise dissipated. Therefore, less induced charge remains on the surface as the temperature increases. The same calculation was done for oxygen environments. Compared to STO, oxygen vacancy on the surface of YSZ has higher oxidation sensitivity because of less induced charge remaining on the surface (Shown in Figure 5.18(b)).

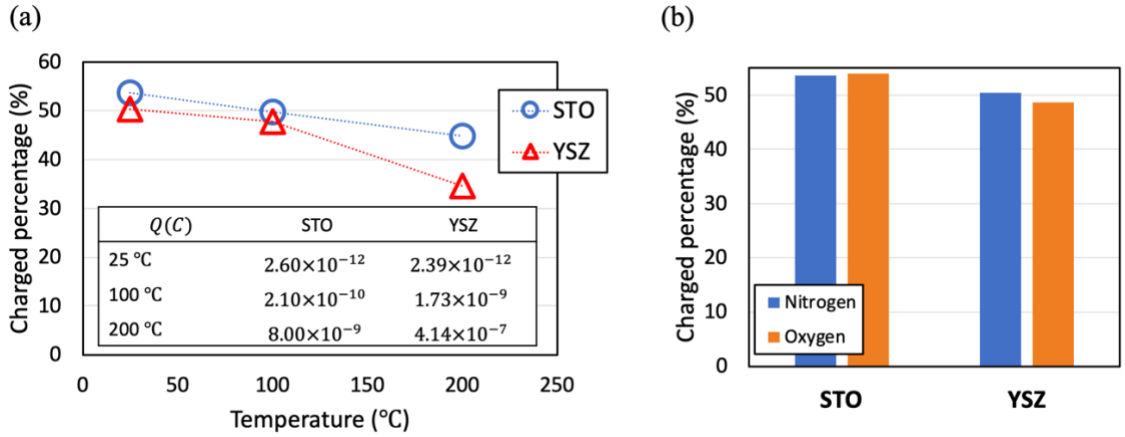

Figure 5.18: (a) Graph plotting percentage of induced charge according to temperature; and (b) The percentage of induced charge on STO and YSZ at the temperature of 25 ℃ in an environment of pure oxygen.

5.3.2 Oxygen vacancy mobility on STO/YSZ surface

Figure 5.19(a)-(c) and Figure 5.20(a)-(c) map the sequential surface potential after a positive bias application (+10 V) under temperatures of 25 ℃, 100 ℃, and 200 ℃. They show features remaining for different time periods on the STO and YSZ surfaces. We found that oxygen vacancy moves quickly even under room temperature. For STO, the oxygen vacancy was nearly entirely dissipated after 4 hours. Oxygen vacancy diffuses even faster on a YSZ surface, dissipating completely in less than two hours. Figure 5.21 indicates that under pure-oxygen environments, oxygen vacancy on STO surfaces have a similar mobility

to under pure-nitrogen environments at 25 ℃. Oxygen vacancy on YSZ surfaces has faster mobility in pure-oxygen environments. As previously mentioned, YSZ has a higher sensitivity to oxygen when oxygen vacancies on its surface.

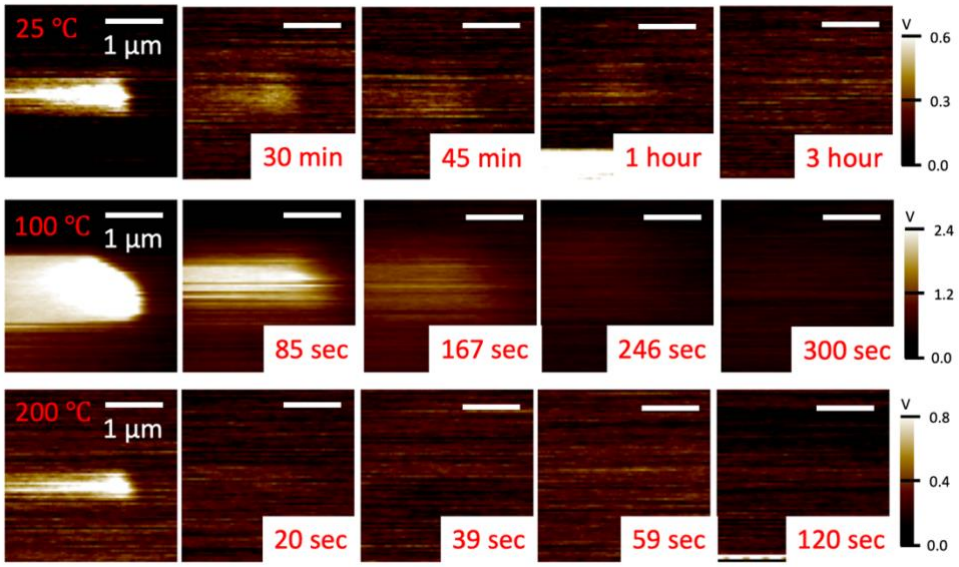

Figure 5.19: KPFM images of an STO surface at 25℃, 100℃, and 200℃ after charging with 10 V for 10 seconds each time. This was conducted and measured under a pure nitrogen environment.

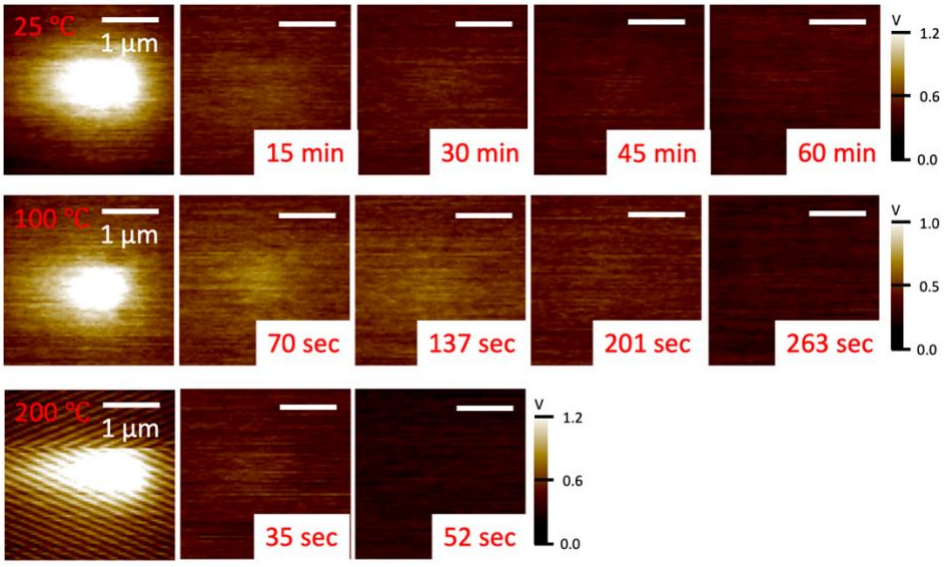

Figure 5.20: KPFM images of a YSZ surface at 25℃, 100℃, and 200℃ after charging with 10 V for 10 seconds each time. This was conducted and measured under a pure nitrogen environment.

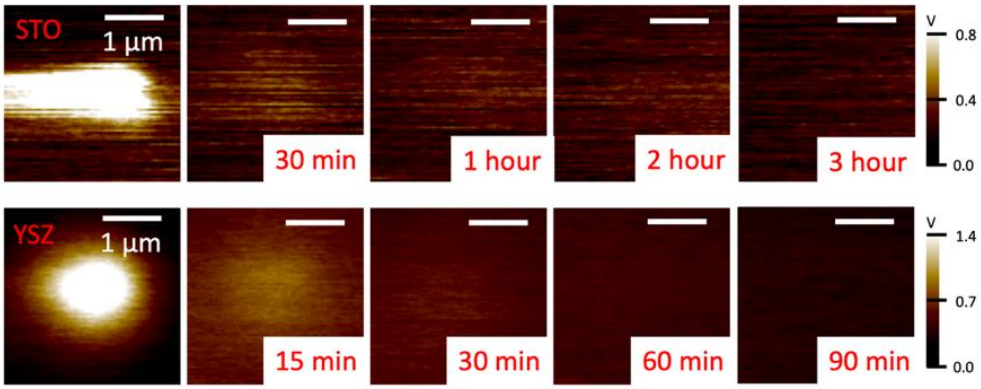

Figure 5.21: KPFM images of STO and YSZ surfaces at 25℃ after charging with 10 V for 10 seconds each time. This was conducted and measured under a pure oxygen environment.

5.3.3 Oxygen vacancy mobility in the bulk of STO/YSZ

Figure 5.22(a) and Figure 5.23(a) show AFM topology maps before and after removing STO and YSZ surfaces 30 times (the setpoint of AFM was set at 0.8 V). They show removal depths of approximately 0.15 nm and 0.10 nm per scan on STO and YSZ, respectively. Which is reasonable since Mohs hardness of YSZ is higher than STO (8 and 6). Figure 5.22(b) and Figure 5.23(b) show KPFM maps of the stages of surface removal performed on STO and YSZ under temperatures of 25 ℃, 100 ℃, and 200 ℃ after +10 V bias was applied for 10 seconds. Oxygen vacancies diffused slightly deeper at 200 ℃ compared to 25 ℃ and 100 ℃ in bulk STO. However, it shows that oxygen vacancy diffusivity has no specific difference between 100 ℃ and 200 ℃ in bulk YSZ. The diffusion depth of oxygen vacancy is less than 2.0 nm on STO and less than 1.5 nm on YSZ from our study. Obviously, temperature of 200 ℃ is not high enough to stimulate fast mobility of oxygen vacancy because STO and YSZ are materials of low-temperature SOFCs which operate ≤ 650 ℃.[284–286] When we analyzed KPFM data from this oxygen vacancy diffusivity study by removal application, we chose the layer after the first removal (slice 1) to analyze. To make sure what we were analyzing was the z-direction movement of oxygen vacancy and not the movement in the sample surface.

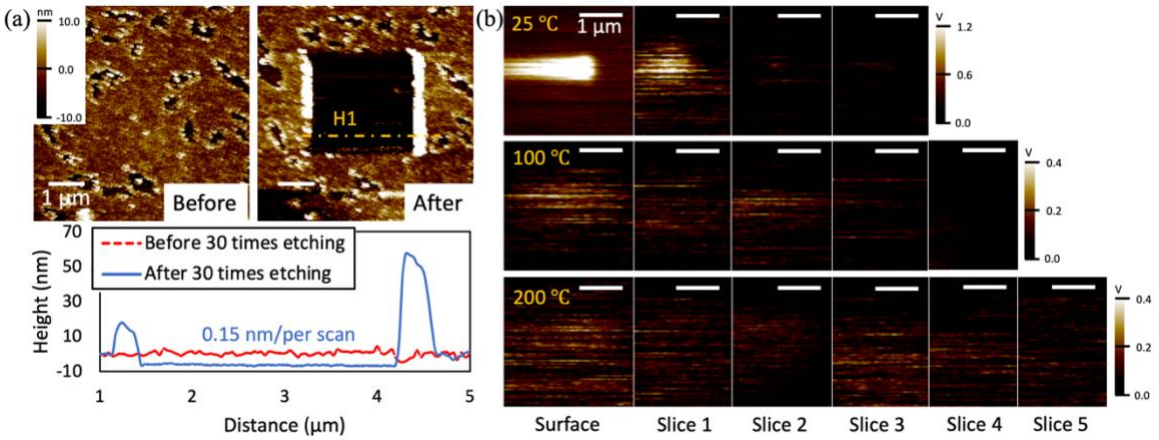

Figure 5.22: (a) AFM topography images detailing the before and after of removal work (30 times) on an STO surface; and (b) KPFM images of each slice that was removed layer by layer at 25℃, 100℃, and 200℃ after charging with 10V for 10 seconds on an etched STO bulk surface. This was conducted and measured under a pure nitrogen environment.

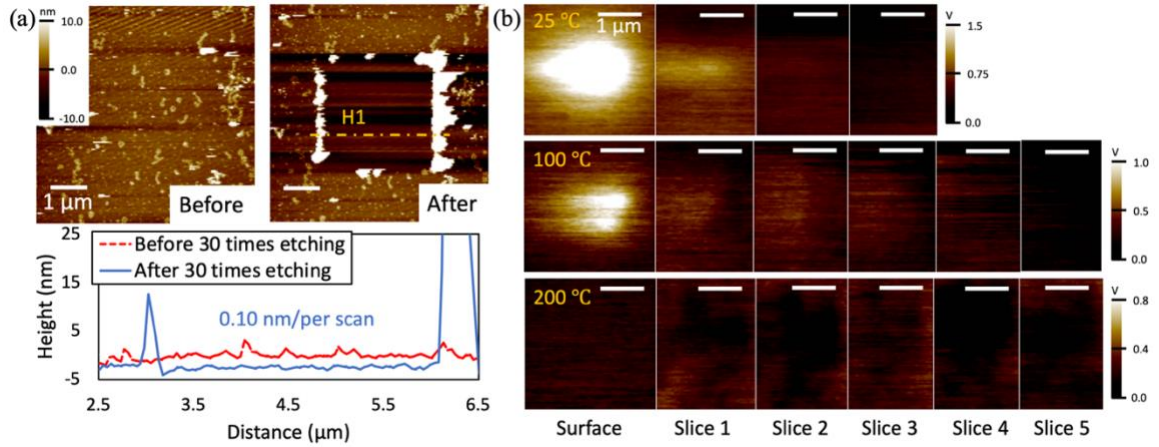

Figure 5.23: (a) AFM topography images detailing the before and after of removal work (30 times) on a YSZ surface; and (b) KPFM images of each slice that was removed layer by layer at 25℃, 100℃, and 200℃ after charging with 10V for 10 seconds on an etched YSZ bulk surface. This was conducted and measured under a pure nitrogen environment.

5.3.4 Diffusivity

Table 5.1 shows the diffusivity values of STO and YSZ surfaces and bulk that we calculated at different temperatures of 25 ℃, 100 ℃, and 200 ℃. The diffusivity of STO[287], STO bulk[288] and YSZ[289] from references is listed in the table as well. Take note that the values of STO bulk from our calculation and reference are really close to each other (besides the one from 100 ℃), making our mathematical induction method more reasonable.

Diffusivity (cm^2/s)	25 ℃	100 ℃	200 ℃
STO surface	3.16×10^{-15}	2.81×10^{-14}	4.85×10^{-12}
STO bulk	7.66×10^{-27}	2.12×10^{-20}	7.60×10^{-19}
STO Reference[287]	4.78×10^{-25}	1.42×10^{-21}	4.25×10^{-18}
STO bulk Reference[288]	8.77×10^{-27}	1.93×10^{-22}	5.75×10^{-19}
YSZ surface	9.43×10^{-12}	7.29×10^{-11}	1.78×10^{-8}
YSZ bulk	3.80×10^{-17}	8.80×10^{-14}	6.87×10^{-12}
YSZ Reference[289]	1.27×10^{-14}	8.45×10^{-13}	6.22×10^{-11}

Table 5.1 : The diffusivity values of STO and YSZ surfaces and bulk that we calculated at different temperatures of 25 ℃, 100 ℃, and 200 ℃.

5.3.5 Activation energy

By analyzing the slope from diffusivity of different temperatures we got and Arrhenius equation, we were able to get the activation energy. Figure 5.24 shows the diffusivity of STO surface and bulk (blue hollow and filled circles), and YSZ surface and bulk (orange hollow and filled triangles), compared to the reference value we obtained through interpolation calculation from R. Krishnamurthy *et al.*,[289] Lucia Iglesias *et al.*[290] and Christoph Slouka's research groups.[288] As we can see by looking at the green, purple (Figure 2.24(a)) and red (Figure 2.24(b))solid lines on the graph, the diffusivity of the surface is higher than the references for both STO and YSZ. Contrary to what happens on the surface, the diffusivity of the bulk is lower than the references. Besides STO bulk at 100 ℃, it is higher than reference likely due to measurement errors. Using this data obtained, we can further calculate that the activation energy of STO surfaces is approximately 0.40 eV, and is similar to the activation energy of YSZ surfaces, which is 0.43 eV. For STO and YSZ bulk, activation energy values are 1.33 eV and 1.10 eV, respectively. The activation energy of STO bulk is much higher than YSZ bulk. The values of activation energy for the surface and bulk of STO/YSZ are reasonable because the activation energy values from references are 1.12 eV and 0.60 eV. The fact that our resulting data points land between the values we took from references further supports our certainty in the values we obtained.

Moreover, Figure 5.24(a) displays the diffusivity values of STO bulk from the reference.[288] Surprisingly, diffusivity values for temperatures of 25 ℃ and 200 ℃ are almost overlapping the diffusivity values from our calculation (in Table. 1, 8.77×10^{-27} and 7.66×10^{-27} at 200 ℃, and 5.75×10^{-19} and 7.60×10^{-19} at 25 ℃). We think for some reason, the heating plate was not able to be heated uniformly, and the temperature around the charged position is higher than we expected. It caused oxygen vacancies to move faster than they should in 100 ℃. Figure 5.25(a) shows the diffusivity of STO and YSZ surfaces under pure nitrogen and oxygen environments at 25 ℃, respectively. The bar graph indicates that the diffusivity of STO surfaces does not change much when under pure-oxygen environments. However, the YSZ surface diffusivity increases slightly under pure-oxygen environments. YSZ surfaces are therefore more sensitive to oxygen compared

to STO. From Figure 5.7, Figure 5.8, Figure 5.10 and Figure 5.11. In Figure 5.25(b), we can see oxygen vacancy diffusion is limited under pure oxygen environments from KPFM maps. We assumed that when applying the same amount of induced charge on the surface and bulk (removed surface) of STO and YSZ, oxygen vacancies in STO tend to diffuse into the sub-layer (bulk) by showing a much smaller bright area compared to YSZ. This behavior can be readily understood with mechanistic interpretations of perovskite structure, providing a better way for oxygen vacancy's diffusion.

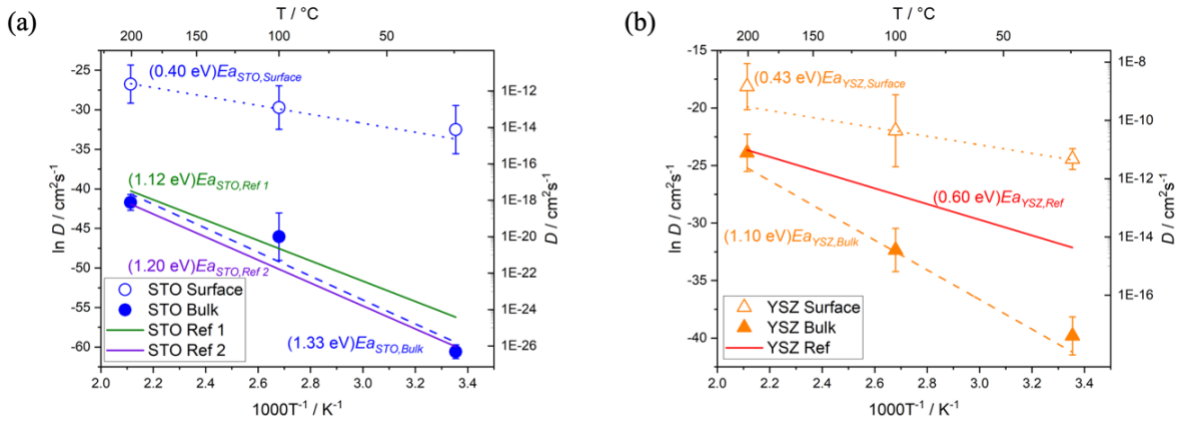

Figure 5.24: Plot of diffusivity (*D*) vs temperature, with activation energy of (a) STO and (b) YSZ surface and bulk.

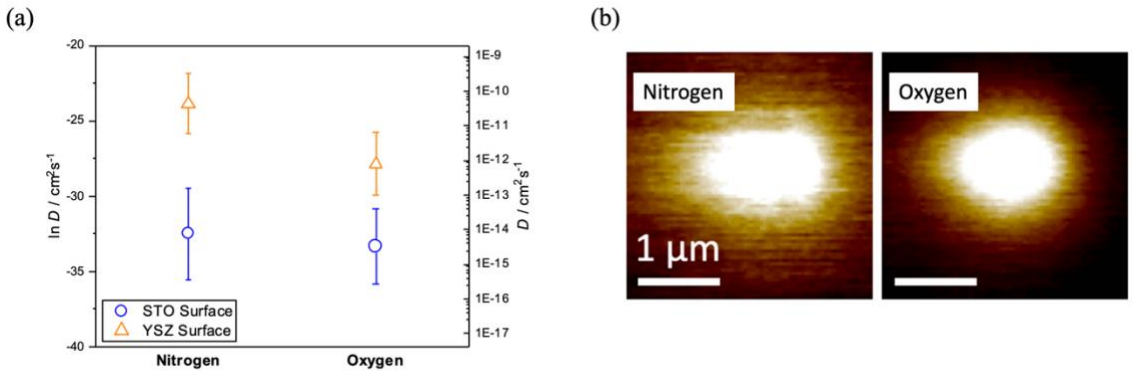

Figure 5.25: (a) The graph shows diffusivity values of STO and YSZ surface at the temperature of 25 ℃ and in the environment of pure oxygen (in orange) and pure nitrogen (blue) and (b) KPFM images.

5.4 Conclusions

Movement of oxygen vacancies was observed through KPFM in this study. The following lists a brief summary of the observations made in this study: (1) The conclusion of the mobility within sample surfaces of oxide material being much greater than that of the bulk can be safely drawn. However, 200 ℃ is still too low of a temperature to initiate the mobility of the oxygen vacancy below the surface level. Below the surface, we barely saw any definitive mobility and diffusivity of oxygen vacancy when increasing the temperature from room temperature to 200 ℃. (2) Overall, there are less restrictions for oxygen vacancy on the surface when compared to being in the bulk. Observations and calculations of the diffusivity on the surface were not affected. On the surface, oxygen vacancy on YSZ has a slightly higher diffusivity than it has on STO. The mobility of oxygen vacancy in the bulk area is much lower due to more restrictions. (3) Compared to STO, YSZ is more sensitive to oxygen. It is therefore easier to charge and generate oxygen vacancies on the surface of YSZ. (4) Oxygen vacancies in STO tend to diffuse into the sub-layer (z-direction) more compared to YSZ. This characteristic is supported by the findings of our experiments under pure-nitrogen and pure-oxygen environments. STO has a lattice structure of cubic perovskite and a good Goldschmidt tolerance factor of 0.9-1.0, making the oxygen vacancy move slightly easier than in bulk YSZ. We utilized KPFM and CAFM on AFM to help us better understand the mobility and diffusivity of oxygen vacancy on two different kinds of sample surfaces and bulk. It is challenging to accurately calculate the diffusivity of oxygen vacancy under different temperatures by AFM. Although more supporting research would help expand the use of and apply this knowledge, these findings still provide us with a better understanding of how ion/oxygen vacancy transport works.

Chapter 6

Summary

In Chapter 1, the need for clean and sustainable energy was described and the basics of SOFCs as a promising alternative to the fossil fuel-based devices was provided. In Chapter 2, an overview of SOFC operation and components (Section 2.1), an introduction to nanoscale treatments of SOFCs (Section 2.2) and the characterization methods used in this study (Section 2.3) were outlined. An overview of AFM, the instrument of choice used for high resolution *in situ* ORR study, was also provided in the chapter. In the subsequent chapters, three research topics I have worked on – nanoscale engineering of cathode surfaces by infiltration (Chapter 3), scanning probe-based instrumentation and preliminary CAFM study (Chapter 4), and ionic diffusivity and mobility study of oxygen reduction/evolution reaction by nanoscale *in situ* characterization via AFM (Chapter 5) – were detailed.

In Chapter 3, topic I, through the nanoscale engineering of cathodes by so-called infiltration (i.e. solvent impregnation) process, I found that: (1) The nanoparticle-like infiltrates boost the overall ORR activity by a significant margin (up to two orders of magnitudes) and that (2) the degree of performance enhancement and the shift in rate-limiting step of ORR varies depending upon the nature of infiltrates in terms of ionic/electronic conductivity, catalytic activity and other parameters. I analyzed the factors of performance and rate-determining step through additional electrochemical characterization (e.g. dependency of performance on partial pressure, temperature and overpotential), XRD, SEM, and TEM analyses by focusing on any change in microstructure (e.g. porosity, particle size), lattice constant and phase and possible inter diffusion of atomic/ionic species by the infiltrates.

In Chapter 4, topic II, a scanning probe-based instrumentation and preliminary CAFM studies were presented with the eventual goal of *in situ* nanoscale ORR study on SOFC electrolytes. In this topic we found that: (1) Thin oxide film/layer is formed on the metallic probe(tip). (2) Low resistance state (LRS) was realized by forming a narrow conducting channel by local electrochemical reduction of gold oxide, (3) and in high resistance state (HRS), the electron transport at the probe-sample interface is likely governed by a tunneling behavior through the insulating oxide nano-film.

In Chapter 5, topic III, we generated oxygen ions (or oxygen vacancy) on the samples by CAFM, and did removal implementations on sample surfaces to build 3-D surface potential maps via AFM diamond coated probes (DCP) and KPFM. In addition, we got the diffusivity and activation energy of the samples by nanoscale *in situ* characterization via AFM. In conclusion of this topic, we found that: (1) The surface(subsurface), we barely saw any definitive mobility and diffusivity of oxygen vacancy when increasing the temperature from 100 ℃ to 200 ℃. (2) there are less restrictions for oxygen vacancy on the surface when compared to being in the bulk. Lastly,

(3) oxygen vacancies in STO tend to diffuse into the sub-layer (z-direction) more compared to YSZ. This characteristic is supported by lattice structure differences.

As an overall summary of my dissertation composed with these three topics. From topic I, we improved the performance of SOFCs by using ALD and infiltration. Establishing basic knowledge of ORR/OER was key. Establishing a fundamental understanding of the mechanisms of AFM was also paramount to using AFM to study ORR/OER from topic II. Finally, measuring surface potential of oxygen vacancy in the samples using CAFM and KPFM allowed us to better understand ORR/OER in topic III. In summary, operating electrical measurements/experiments by manipulating CAFM and KPFM is challenging due to unexpected contaminations and oxide films forming from humidity, yet achievable.

REFERRENCES

1. Zini, G. Z. & Tartarini, P. *Solar Hydrogen Energy Systems: Science and Technology for the Hydrogen Economy*. (Springer Science & Business Media, 2012).
2. Ball, M. & Wietschel, M. *The Hydrogen Economy: Opportunities and Challenges*. (Cambridge University Press, 2009).
3. Kemp, W. H. *The renewable energy handbook : the updated comprehensive guide to renewable energy and independent living*. (New York : Aztext Press, 2012).
4. Geller, H. *Energy Revolution: Policies For A Sustainable Future*. (Island Press, 2002).
5. Aleklett, K. *Peeking at Peak Oil*. (Springer Science & Business Media, 2012).
6. Pagliaro, M. & Konstandopoulos, A. G. *Solar Hydrogen: Fuel of the Future*. (Royal Society of Chemistry, 2012).
7. Johnson, R. W., Hultqvist, A. & Bent, S. F. A brief review of atomic layer deposition: From fundamentals to applications. *Mater. Today* **17,** 236–246 (2014).
8. Vohs, B. J. M. & Gorte, R. J. High-Performance SOFC Cathodes Prepared by Infiltration. 943–956 (2009). doi:10.1002/adma.200802428
9. Garrison, E. in (2014).
10. Singhal, S. C. & Kevin, K. *High-temperature Solid Oxide Fuel Cells*. (Elsevier, 2003).
11. O'Hayre, R., Cha, S.-W., Prinz, F. B. & Colella, W. *Fuel Cell Fundamentals*. (John Wiley & Sons, 2009).
12. Ni, M. & Zhao, T. S. *Solid Oxide Fuel Cells: From Materials to System Modeling*. (Royal Society of Chemistry, 2013).
13. Chen, D. *et al.* New $Ba_{0.5}Sr_{0.5}Co_{0.8}Fe_{0.2}O_{3-\delta}$+$Co_3O_4$ composite electrode for IT-SOFCs with improved electrical conductivity and catalytic activity. *Electrochem. commun.* **13,** 197–199 (2011).
14. Mai, A., Haanappel, V. A. C., Tietz, F. & Stöver, D. Ferrite-based perovskites as cathode materials for anode-supported solid oxide fuel cells. Part II. Influence of the CGO interlayer. *Solid State Ionics* **177,** 2103–2107 (2006).
15. Mai, A., Haanappel, V. A. C., Uhlenbruck, S., Tietz, F. & Stöver, D. Ferrite-based perovskites as cathode materials for anode-supported solid oxide fuel cells: Part I. Variation of composition. *Solid State Ionics* **176,** 1341–1350 (2005).
16. Minh, N. Q. Ceramic Fuel Cells. *J. Am. Ceram. Soc.* **76,** 563–588 (1993).
17. Matsuzaki, Y. & Yasuda, I. Electrochemical properties of reduced-temperature SOFCs with mixed ionic-electronic conductors in electrodes and/or interlayers. *Solid State Ionics* **152–153,** 463–468 (2002).
18. Adler, S. B. Factors Governing Oxygen Reduction in Solid Oxide Fuel Cell Cathodes †. *Chem. Rev.* **104,** 4791–4844 (2004).
19. Mobius, H.-H. On the history of solid electrolyte fuel cells. *J. Solid State Electrochem.* **1,** 2–16 (1997).
20. Horita, T. *et al.* Active Sites Imaging for Oxygen Reduction at the $La_{0.9}Sr_{0.1}MnO_{3-\delta}$ /Yttria-Sta bilized Zirconia Interface by Secondary-Ion Mass Spectrometry. *J. Electrochem. Soc.* **145,** (1998).
21. Yang, Z., Weil, K. S., Paxton, D. M. & Stevenson, J. W. Selection and Evaluation of Heat-Resistant Alloys for SOFC Interconnect Applications. *J. Electrochem. Soc.* **150,** A1188 (2003).
22. Huang, K., Hou, P. Y. & Goodenough, J. B. Characterization of iron-based alloy interconnects for reduced temperature solid oxide fuel cells. *Solid State Ionics* **129,** 237–250 (2000).
23. Alcock, C. B. Solid state sensors and process control. *Solid State Ionics* **53–56,** 3–17 (1992).
24. Kilner, J., Benson, S., Lane, J. & David, W. Ceramic ion conducting membranes for oxygen separation. *Chem. Ind.* **907,** (1997).
25. Mazanec, T. J. Prospects for ceramic electrochemical reactors in industry. *Solid State Ionics* **70–71,** 11–19 (1994).
26. Ormerod, R. M. Solid oxide fuel cells. *Chem. Soc. Rev.* **32,** 17–28 (2003).
27. Carrette, L., Friedrich, K. A. & Stimming, U. Fuel Cells - Fundamentals and Applications. *Fuel Cells* **1,** 5–39 (2001).
28. Kim, J., Virkar, A. V, Fung, K., Mehta, K. & Singhal, S. C. Polarization Effects in Intermediate Temperature , Anode-Supported Solid Oxide Fuel Cells. *J. Electrochem. Soc.* **146,** 69–78 (1999).

29. Badwal, S. P. S. Materials for solid oxide fuel cells. *Mater. Forum* **21,** (1997).
30. Yamamoto, O. Solid oxide fuel cells: fundamental aspects and prospects. *Electrochim. Acta* **45,** 2423–2435 (2000).
31. Steele, B. C. H. Materials for IT-SOFC stacks - 35 years R&D: The inevitability of gradualness? *Solid State Ionics* **134,** 3–20 (2000).
32. Skinner, S. J. Recent advances in Perovskite-type materials for solid oxide fuel cell cathodes. *Int. J. Inorg. Mater.* **3,** 113–121 (2001).
33. Will, J., Mitterdorfer, A., Kleinlogel, C., Perednis, D. & Gauckler, L. J. Fabrication of thin electrolytes for second-generation solid oxide fuel cells. *Solid State Ionics* **131,** 79–96 (2000).
34. Polytechnique, E., Lausanne, D. & Publishers, K. A. Materials for high-temperature oxygen reduction in solid oxide fuel cells. *J. Mater. Sci.* **6,** 1087–1091 (2001).
35. Adler, S. B., Henderson, B. T., Wilson, M. A., Taylor, D. M. & Richards, R. E. Reference electrode placement and seals in electrochemical oxygen generators. *Solid State Ionics* **134,** 35–42 (2000).
36. Steele, B. C. H. Interfacial reactions associated with ceramic ion transport membranes. *Solid State Ionics* **75,** 157–165 (1995).
37. Steele, B. C. H. Survey of materials selection for ceramic fuel cells: II. Cathodes and anodes. *Solid State Ionics* **86–88,** 1223–1234 (1996).
38. Doshi, R. Development of Solid-Oxide Fuel Cells That Operate at 500°C. *J. Electrochem. Soc.* **146,** 1273 (1999).
39. Bossel, U. G. *Facts & Figures: Final Report on SOFC Data*. (1992).
40. Lenser, C. *et al.* Interaction of a ceria-based anode functional layer with a stabilized zirconia electrolyte: Considerations from a materials perspective. *J. Am. Ceram. Soc.* **101,** 739–748 (2018).
41. Chang, I., Ji, S., Park, J., Lee, M. H. & Cha, S. W. Ultrathin YSZ coating on Pt cathode for high thermal stability and enhanced oxygen reduction reaction activity. *Adv. Energy Mater.* **5,** 1–7 (2015).
42. Park, J. *et al.* Atomic layer deposition of yttria-stabilized zirconia thin films for enhanced reactivity and stability of solid oxide fuel cells. *Energy* **116,** 170–176 (2016).
43. Dyer, P. N., Richards, R. E., Russek, S. L. & Taylor, D. M. Ion transport membrane technology for oxygen separation and syngas production. *Solid State Ionics* **134,** 21–33 (2000).
44. Huijsmans, J. P. ., van Berkel, F. P. . & Christie, G. . Intermediate temperature SOFC – a promise for the 21st century. *J. Power Sources* **71,** 107–110 (1998).
45. Steele, B. C. H., Hori, K. M. & Uchino, S. Kinetic parameters influencing the performance of IT-SOFC composite electrodes. *Solid State Ionics* **135,** 445–450 (2000).
46. Zhou, W. *et al.* $Ba_{0.5}Sr_{0.5}Co_{0.8}Fe_{0.2}O_{3-\delta}$ + LaCoO3composite cathode for $Sm_{0.2}Ce_{0.8}O_{1.9}$-electrolyte based intermediate-temperature solid-oxide fuel cells. *J. Power Sources* **168,** 330–337 (2007).
47. Hui, S. (Rob) *et al.* A brief review of the ionic conductivity enhancement for selected oxide electrolytes. *J. Power Sources* **172,** 493–502 (2007).
48. Chiba, R., Yoshimura, F. & Sakurai, Y. Properties of $La_{1-y}Sr_yNi_{1-x}Fe_xO_3$ as a cathode material for a low-temperature operating SOFC. *Solid State Ionics* **152–153,** 575–582 (2002).
49. Lau, G. Y. *et al.* Chromium transport by solid state diffusion on solid oxide fuel cell cathode. *J. Power Sources* **195,** 7540–7547 (2010).
50. Li, S., Sun, J., Sun, X. & Zhu, B. A High Functional Cathode Material $LaNi_{0.4}Fe_{0.6}O_3$ for Low-Temperature Solid Oxide Fuel Cells. *Electrochem. Solid-State Lett.* **9,** A86–A87 (2006).
51. Hashimoto, S. I., Kammer, K., Larsen, P. H., Poulsen, F. W. & Mogensen, M. A study of $Pr_{0.7}Sr_{0.3}Fe_{1-x}Ni_xO_{3-\delta}$ as a cathode material for SOFCs with intermediate operating temperature. *Solid State Ionics* **176,** 1013–1020 (2005).
52. Bevilacqua, M. *et al.* Influence of synthesis route on morphology and electrical properties of LaNi0.6Fe0.4O3. *Solid State Ionics* **177,** 2957–2965 (2006).
53. Lee, S., Bevilacqua, M., Fornasiero, P., Vohs, J. M. & Gorte, R. J. Solid oxide fuel cell cathodes prepared by infiltration of $LaNi_{0.6}Fe_{0.4}O_3$ and $La_{0.91}Sr_{0.09}Ni_{0.6}Fe_{0.4}O_3$ in porous yttria-stabilized zirconia. *J. Power Sources* **193,** 747–753 (2009).
54. Jiang, S. . A comparison of O2 reduction reactions on porous (La,Sr)MnO_3 and (La,Sr)(Co,Fe)O_3 electrodes. *Solid State Ionics* **146,** 1–22 (2002).
55. Chiba, R., Yoshimura, F. & Sakurai, Y. An investigation of $LaNi_{1-x}Fe_xO_3$ as a cathode material for

solid oxide fuel cells. *Solid State Ionics* **124,** 281–288 (1999).
56. Basu, R. N. *et al.* $LaNi_{0.6}Fe_{0.4}O_3$ as a cathode contact material for solid oxide fuel cells. *J. Solid State Electrochem.* **7,** 416–420 (2003).
57. Rapagná, S., Provendier, H., Petit, C., Kiennemann, A. & Foscolo, P. U. Development of catalysts suitable for hydrogen or syn-gas production from biomass gasification. *Biomass and Bioenergy* **22,** 377–388 (2002).
58. Provendier, H., Petit, C. & Kiennemann, A. Steam reforming of methane on $LaNi_xFe_{1-x}O_3$ $(0 \leq x \leq 1)$ perovskites. Reactivity and characterisation after test. *Comptes Rendus l'Académie des Sci. - Ser. IIC - Chem.* **4,** 57–66 (2001).
59. Provendier, H., Petit, C., Estournès, C., Libs, S. & Kiennemann, a. Stabilisation of active nickel catalysts in partial oxidation of methane to synthesis gas by iron addition. *Appl. Catal. A Gen.* **180,** 163–173 (1999).
60. Orui, H. *et al.* Development of Practical Size Anode-Supported Solid Oxide Fuel Cells with Multilayer Anode Structures. *J. Electrochem. Soc.* **155,** B1110 (2008).
61. Tsipis, E. V. *et al.* Transport properties and thermal expansion of Ti-substituted $La_{1-x}Sr_xFeO_{3-\delta}$(x = 0.5-0.7). *Solid State Sci.* **7,** 355–365 (2005).
62. Chiba, R. *et al.* SOFC Cathodes Composed of $LaNi_{0.6}Fe_{0.4}O_3$ and Pr-Doped CeO_2. *Electrochem. Solid-State Lett.* **12,** B69 (2009).
63. Bevilacqua, M. *et al.* Preparation, characterization, and electrochemical properties of pure and composite $LaNi_{0.6}Fe_{0.4}O_3$-Based cathodes for IT-SOFC. *Chem. Mater.* **19,** 5926–5936 (2007).
64. Huang, B. *et al.* Comparison of the electrochemical properties of impregnated and functionally gradient $LaNi_{0.6}Fe_{0.4}O_3$–$Gd_{0.2}Ce_{0.8}O_2$ composite cathodes for Solid Oxide Fuel Cell. *J. Power Sources* **235,** 20–28 (2013).
65. Taguchi, H. *et al.* LNF SOFC cathodes with active layer using Pr_6O_{11} or Pr-doped CeO_2. *J. Power Sources* **241,** 768–775 (2013).
66. Mori, T., Drennan, J., Lee, J. H., Li, J. G. & Ikegami, T. Oxide ionic conductivity and microstructures of Sm- or La-doped CeO_2-based systems. *Solid State Ionics* **154–155,** 461–466 (2002).
67. Orui, H., Watanabe, K., Chiba, R. & Arakawa, M. Application of $LaNi(Fe)O_3$ as SOFC cathode. *J. Electrochem. Soc.* **151,** A1412–A1417 (2004).
68. Basu, R. N., Tietz, F., Wessel, E., Buchkremer, H. P. & Stöver, D. Microstructure and electrical conductivity of $LaNi_{0.6}Fe_{0.4}O_3$ prepared by combustion synthesis routes. *Mater. Res. Bull.* **39,** 1335–1345 (2004).
69. Zhen, Y. D., Tok, A. I. Y., Jiang, S. P. & Boey, F. Y. C. $La(Ni,Fe)O_3$ as a cathode material with high tolerance to chromium poisoning for solid oxide fuel cells. *J. Power Sources* **170,** 61–66 (2007).
70. Kiselev, E. A., Proskurnina, N. V, Voronin, V. I. & Cherepanov, V. A. Phase Equilibria and Crystal Structures of Phases in the La – Fe – Ni – O System at 1370 K in Air. **43,** 209–217 (2007).
71. Świerczek, K., Marzec, J., Pałubiak, D., Zajac, W. & Molenda, J. LFN and LSCFN perovskites - structure and transport properties. *Solid State Ionics* **177,** 1811–1817 (2006).
72. Tantayanon, S., Yeyongchaiwat, J., Lou, J. & Ma, Y. H. Synthesis and characterization of Sr and Fe substituted $LaGaO_3$ perovskites and membranes. *Sep. Purif. Technol.* **32,** 319–326 (2003).
73. Yuenyongchaiwat, J., Tantayanon, S., Lou, J. & Ma, Y. H. Synthesis of Sr- and Fe-doped $LaGaO_3$perovskites by the modified citrate method. *J. Mater. Sci.* **39,** 7067–7074 (2004).
74. Bontempi, E., Garzella, C., Valetti, S. & Depero, L. E. Structural study of $LaNi_xFe_{1-x}O_3$ prepared from precursor salts. *J. Eur. Ceram. Soc.* **23,** 2135–2142 (2003).
75. Basu, R. N., Tietz, F., Wessel, E. & Stöver, D. Interface reactions during co-firing of solid oxide fuel cell components. *J. Mater. Process. Technol.* **147,** 85–89 (2004).
76. Sukpirom, N., Iamsaard, S., Charojrochkul, S. & Yeyongchaiwat, J. Synthesis and properties of $LaNi_{1-x}Fe_xO_{3-\delta}$ as cathode materials in SOFC. *J. Mater. Sci.* **46,** 6500–6507 (2011).
77. Barros, B. S., Kulesza, J., De Arajo Melo, D. M. & Kiennemand, A. Nickel-based catalyst precursor prepared via microwave-induced combustion method: Thermodynamics of synthesis and performance in dry reforming of CH_4. *Mater. Res.* **18,** 732–739 (2015).
78. Ding, X., Zhu, W., Hua, G., Li, J. & Wu, Z. Enhanced oxygen reduction activity on surface-

decorated perovskite $La_{0.6}Ni_{0.4}FeO_3$ cathode for solid oxide fuel cells. *Electrochim. Acta* **163,** 204–212 (2015).
79. Ding, X. *et al.* Improved electrochemical activity and stability of $LaNi_{0.6}Fe_{0.4}O_{3-\delta}$ cathodes achieved by an in-situ reaction. *Electrochim. Acta* **236,** 378–383 (2017).
80. Nicollet, C. *et al.* An innovative efficient oxygen electrode for SOFC: Pr_6O_{11} infiltrated into Gd-doped ceria backbone. *Int. J. Hydrogen Energy* **41,** 15538–15544 (2016).
81. Jiang, S. P. A review of wet impregnation - An alternative method for the fabrication of high performance and nano-structured electrodes of solid oxide fuel cells. *Mater. Sci. Eng. A* **418,** 199–210 (2006).
82. Park, S. Direct Oxidation of Hydrocarbons in a Solid Oxide Fuel Cell: I. Methane Oxidation. *J. Electrochem. Soc.* **146,** 3603 (1999).
83. Park, S., Vohs, J. M. & Gorte, R. J. Direct oxidation of hydrocarbons in a solid-oxide fuel cell. *Nature* **404,** 265–267 (2000).
84. Kim, H., Park, S., Vohs, J. M. & Gorte, R. J. Direct Oxidation of Liquid Fuels in a Solid Oxide Fuel Cell. *J. Electrochem. Soc.* **148,** A693 (2001).
85. Kim, T. *et al.* A study of carbon formation and prevention in hydrocarbon-fueled SOFC. *J. Power Sources* **155,** 231–238 (2006).
86. Fleig, J. & Maier, J. The polarization of mixed conducting SOFC cathodes: Effects of surface reaction coefficient, ionic conductivity and geometry. *J. Eur. Ceram. Soc.* **24,** 1343–1347 (2004).
87. Tanner, C. W., Fung, K.-Z. & Virkar, A. V. The Effect of Porous Composite Electrode Structure on Solid Oxide Fuel Cell Performance I. Theoretical Analysis. *J. Electrochem. Soc.* **144,** 21 (1997).
88. Radhakrishnan, R., Virkar, A. V. & Singhal, S. C. Estimation of Charge-Transfer Resistivity of $La_{0.8}Sr_{0.2}MnO_3$ Cathode on $Y_{0.16}Zr_{0.84}O_2$ Electrolyte Using Patterned Electrodes. *J. Electrochem. Soc.* **152,** A210 (2005).
89. Zhao, F. & Virkar, A. V. Dependence of polarization in anode-supported solid oxide fuel cells on various cell parameters. *J. Power Sources* **141,** 79–95 (2005).
90. Virkar, A. The role of electrode microstructure on activation and concentration polarizations in solid oxide fuel cells. *Solid State Ionics* **131,** 189–198 (2000).
91. MINH, N. Solid oxide fuel cell technology?features and applications. *Solid State Ionics* **174,** 271–277 (2004).
92. Mertens, J., Haanappel, V. A. C., Wedershoven, C. & Buchkremer, H.-P. Sintering Behavior of (La,Sr)MnO_3 Type Cathodes for Planar Anode-Supported SOFCs. *J. Fuel Cell Sci. Technol.* **3,** 415 (2006).
93. Stöver, D., Buchkremer, H. P. & Uhlenbruck, S. Processing and properties of the ceramic conductive multilayer device solid oxide fuel cell (SOFC). *Ceram. Int.* **30,** 1107–1113 (2004).
94. Yokokawa, H., Tu, H., Iwanschitz, B. & Mai, A. Fundamental mechanisms limiting solid oxide fuel cell durability. *J. Power Sources* **182,** 400–412 (2008).
95. Kleveland, K. *et al.* Reactions between Strontium-Substituted Lanthanum Manganite and Yttria-Stabilized Zirconia: II, Diffusion Couples. *J. Am. Ceram. Soc.* **82,** 729–734 (2004).
96. Craciun, R. *et al.* A Novel Method for Preparing Anode Cermets for Solid Oxide Fuel Cells. **146,** 4019–4022 (1999).
97. Kim, H., Lu, C., Worrell, W. L., Vohs, J. M. & Gorte, R. J. Cu-Ni Cermet Anodes for Direct Oxidation of Methane in Solid-Oxide Fuel Cells. *J. Electrochem. Soc.* **149,** A247 (2002).
98. Gorte, R. J., Park, S., Vohs, J. M. & Wang, C. Anodes for direct oxidation of dry hydrocarbons in a solid-oxide fuel cell. *Adv. Mater.* **12,** 1465–1469 (2000).
99. He, H. *et al.* Low-Temperature Fabrication of Oxide Composites for Solid-Oxide Fuel Cells. *J. Am. Ceram. Soc.* **87,** 331–336 (2004).
100. Gross, M. D., Vohs, J. M. & Gorte, R. J. Recent progress in SOFC anodes for direct utilization of hydrocarbons. *J. Mater. Chem.* **17,** 3071 (2007).
101. Ahn, K., Jung, S., Vohs, J. M. & Gorte, R. J. A support layer for solid oxide fuel cells. *Ceram. Int.* **33,** 1065–1070 (2007).
102. Zhao, F., Armstrong, T. J. & Virkar, A. V. Measurement of O_2-N_2 Effective Diffusivity in Porous Media at High Temperatures Using an Electrochemical Cell. *J. Electrochem. Soc.* **150,** A249 (2003).

103. Jung, S. *et al.* Influence of composition and Cu impregnation method on the performance of Cu/CeO_2/YSZ SOFC anodes. *J. Power Sources* **154,** 42–50 (2006).
104. Huang, Y., Vohs, J. M. & Gorte, R. J. SOFC Cathodes Prepared by Infiltration with Various LSM Precursors. *Electrochem. Solid-State Lett.* **9,** A237 (2006).
105. Sholklapper, T. Z., Lu, C., Jacobson, C. P., Visco, S. J. & De Jonghe, L. C. LSM-Infiltrated Solid Oxide Fuel Cell Cathodes. *Electrochem. Solid-State Lett.* **9,** A376 (2006).
106. Tucker, M. C., Lau, G. Y., Jacobson, C. P., DeJonghe, L. C. & Visco, S. J. Performance of metal-supported SOFCs with infiltrated electrodes. *J. Power Sources* **171,** 477–482 (2007).
107. Sholklapper, T. Z., Radmilovic, V., Jacobson, C. P., Visco, S. J. & De Jonghe, L. C. Synthesis and Stability of a Nanoparticle-Infiltrated Solid Oxide Fuel Cell Electrode. *Electrochem. Solid-State Lett.* **10,** B74 (2007).
108. Sholklapper, T. Z., Kurokawa, H., Jacobson, C. P., Visco, S. J. & De Jonghe, L. C. Nanostructured solid oxide fuel cell electrodes. *Nano Lett.* **7,** 2136–2141 (2007).
109. Huang, Y., Ahn, K., Vohs, J. M. & Gorte, R. J. Characterization of Sr-Doped $LaCoO_3$-YSZ Composites Prepared by Impregnation Methods. *J. Electrochem. Soc.* **151,** A1592 (2004).
110. Mineshige, A., Kobune, M., Fujii, S., Ogumi, Z. & Inaba, M. Metal–Insulator Transition and Crystal Structure of La1-xSrxCoO3 as Functions of Sr-Content , Temperature , and Oxygen Partial Pressure. *J. Solid State Chem.* **142,** 374–381 (1999).
111. Uchida, H., Arisaka, S. & Watanabe, M. High performance electrodes for medium-temperature solid oxide fuel cells: Activation of $La(Sr)CoO_3$ cathode with highly dispersed Pt metal electrocatalysts. *Solid State Ionics* **135,** 347–351 (2000).
112. Horita, T. *et al.* Oxygen reduction mechanism at porous $La_{1-x}Sr_xCoO_{3-d}$ cathodes/ $La_{0.8}Sr_{0.2}Ga_{0.8}Mg_{0.2}O_{2.8}$ electrolyte interface for solid oxide fuel cells. *Electrochim. Acta* **46,** 1837–1845 (2001).
113. Adler, S. B., Chen, X. Y. & Wilson, J. R. Mechanisms and rate laws for oxygen exchange on mixed-conducting oxide surfaces. *J. Catal.* **245,** 91–109 (2007).
114. Giidickemeier, M., Sasaki, K., Gauckler, L. J. & Riessb, I. Perovskite cathodes for solid oxide fuel cells based on ceria electrolytes. *Solid State Ionics* **86–88,** 691–701 (1996).
115. Shiono, M. *et al.* Effect of CeO_2 interlayer on ZrO_2 electrolyte/$La(Sr)CoO_3$ cathode for low-temperature SOFCs. *Solid State Ionics* **170,** 1–7 (2004).
116. Rossignol, C., Ralph, J. M., Bae, J. M. & Vaughey, J. T. $Ln_{1-x}Sr_xCoO_3$ (Ln=Gd, Pr) as a cathode for intermediate-temperature solid oxide fuel cells. *Solid State Ionics* **175,** 59–61 (2004).
117. Sakai, N. *et al.* Interface Stability of Perovskite Cathodes and Rare-Earth Doped Ceria Interlayer in SOFCs. *J. Electrochem. Soc.* **154,** B1331 (2007).
118. Armstrong, T. J. & Rich, J. G. Anode-Supported Solid Oxide Fuel Cells with $La_{0.6}Sr_{0.4}CoO_{3-\lambda}$-$Zr_{0.84}Y_{0.16}O_{2-\delta}$ Composite Cathodes Fabricated by an Infiltration Method. *J. Electrochem. Soc.* **153,** A515 (2006).
119. Huang, Y., Vohs, J. M. & Gorte, R. J. An Examination of LSM-LSCo Mixtures for Use in SOFC Cathodes. *J. Electrochem. Soc.* **153,** A951 (2006).
120. Sase, M. *et al.* Interfacial reaction and electrochemical properties of dense (La,Sr) $CoO_{3-\delta}$ cathode on YSZ (1 0 0). *J. Phys. Chem. Solids* **66,** 343–348 (2005).
121. Wang, W., Gross, M. D., Vohs, J. M. & Gorte, R. J. The Stability of LSF-YSZ Electrodes Prepared by Infiltration. *J. Electrochem. Soc.* **154,** B439 (2007).
122. Patrakeev, M. V. *et al.* Electron/hole and ion transport in $La_{1-x}Sr_xFeO_{3-\delta}$. *J. Solid State Chem.* **172,** 219–231 (2003).
123. Yoo, J., Park, C. Y. & Jacobson, A. J. Determination of the equilibrium oxygen non-stoichiometry and the electrical conductivity of $La_{0.5}Sr_{0.5}FeO_{3-x}$. *Solid State Ionics* **175,** 55–58 (2004).
124. Bidrawn, F., Lee, S., Vohs, J. M. & Gorte, R. J. The Effect of Ca, Sr, and Ba Doping on the Ionic Conductivity and Cathode Performance of $LaFeO_3$. *J. Electrochem. Soc.* **155,** B660 (2008).
125. Ralph, J. M., Rossignol, C. & Kumar, R. Cathode Materials for Reduced-Temperature SOFCs. *J. Electrochem. Soc.* **150,** A1518 (2003).
126. Simner, S. P., Shelton, J. P., Anderson, M. D. & Stevenson, J. W. Interaction between $La(Sr)FeO_3$SOFC cathode and YSZ electrolyte. *Solid State Ionics* **161,** 11–18 (2003).
127. Huang, Y., Vohs, J. M. & Gorte, R. J. Fabrication of Sr-Doped $LaFeO_3$ YSZ Composite Cathodes.

J. Electrochem. Soc. **151,** A646 (2004).
128. Sasaki, K. & Maier, J. Re-analysis of defect equilibria and transport parameters in Y_2O_3-stabilized ZrO_2 using EPR and optical relaxation. *Solid State Ionics* **134,** 303–321 (2000).
129. Simner, S. P., Anderson, M. D., Engelhard, M. H. & Stevenson, J. W. Degradation Mechanisms of La–Sr–Co–Fe–O_3 SOFC Cathodes. *Electrochem. Solid-State Lett.* **9,** A478 (2006).
130. Li, S. *et al.* Comparison of Oxygen Permeability and Stability of Perovskite Type $La_{0.2}A_{0.8}Co_{0.2}Fe_{0.8}O_{3-\delta}$ (A = Sr, Ba, Ca) Membranes. *Ind. Eng. Chem. Res.* **38,** 2963–2972 (1999).
131. Lee, S. *et al.* Oxygen-permeating property of $LaSrBFeO_3$(B=Co, Ga) perovskite membrane surface-modified by $LaSrCoO_3$. *Solid State Ionics* **158,** 287–296 (2003).
132. Wang, W. G. & Mogensen, M. High-performance lanthanum-ferrite-based cathode for SOFC. *Solid State Ionics* **176,** 457–462 (2005).
133. Mai, A. *et al.* Time-dependent performance of mixed-conducting SOFC cathodes. *Solid State Ionics* **177,** 1965–1968 (2006).
134. Jin, C., Liu, J., Guo, W. & Zhang, Y. Electrochemical characteristics of an $La_{0.6}Sr_{0.4}Co_{0.2}Fe_{0.8}O_3$-$La_{0.8}Sr_{0.2}MnO_3$ multi-layer composite cathode for intermediate-temperature solid oxide fuel cells. *J. Power Sources* **183,** 506–511 (2008).
135. Chen, J. *et al.* Nano-structured (La, Sr)(Co, Fe)O_3+ YSZ composite cathodes for intermediate temperature solid oxide fuel cells. *J. Power Sources* **183,** 586–589 (2008).
136. Huang, Y., Vohs, J. M. & Gorte, R. J. Characterization of LSM-YSZ Composites Prepared by Impregnation Methods. *J. Electrochem. Soc.* **152,** A1347 (2005).
137. McIntosh, S., Adler, S. B., Vohs, J. M. & Gorte, R. J. Effect of Polarization on and Implications for Characterization of LSM-YSZ Composite Cathodes. *Electrochem. Solid-State Lett.* **7,** A111 (2004).
138. McIntosh, S., Vohs, J. M. & Gorte, R. J. Impedance Spectroscopy for the Characterization of Cu-Ceria-YSZ Anodes for SOFCs. *J. Electrochem. Soc.* **150,** A1305 (2003).
139. Chen, X. J., Khor, K. A. & Chan, S. H. Identification of O_2 reduction processes at yttria stabilized zirconia|doped lanthanum manganite interface. *J. Power Sources* **123,** 17–25 (2003).
140. Mitterdorfer, A. $La_2Zr_2O_7$ formation and oxygen reduction kinetics of the $La_{0.85}Sr_{0.15}Mn_yO_3$, O_2(g)|YSZ system. *Solid State Ionics* **111,** 185–218 (1998).
141. Horita, T. *et al.* Oxygen transport at the interface of $La_{0.92}MnO_{3-x}$ film $Y_{0.15}Zr_{0.85}O_{1.925}$ single crystal. *Solid State Ionics* **136–137,** 897–904 (2000).
142. Jiang, S. P. & Love, J. G. Origin of the initial polarization behavior of Sr-doped $LaMnO_3$ for O_2 reduction in solid oxide fuel cells. *Solid State Ionics* **138,** 183–190 (2001).
143. Jiang, S. The electrochemical performance of LSM/zirconia–yttria interface as a function of a-site non-stoichiometry and cathodic current treatment. *Solid State Ionics* **121,** 1–10 (1999).
144. Kuznecov, M., Otschik, P., Obenaus, P., Eichler, K. & Schaffrath, W. Diffusion controlled oxygen transport and stability at the perovskite/electrolyte interface. *Solid State Ionics* **157,** 371–378 (2003).
145. Vance, A. A. & McIntosh, S. Performance and Activation Behavior of Surface-Doped Thin-Film $La_{0.8}Sr_{0.2}MnO_{3-\delta}$ Cathodes. *J. Electrochem. Soc.* **155,** B1 (2008).
146. Mizusaki, J. *et al.* Oxygen nonstoichiometry and defect equilibrium in the perovskite-type oxides $La_{1-x}Sr_xMnO_{3+d}$. *Solid State Ionics* **129,** 163–177 (2000).
147. Chiba, R. *et al.* $LaNi_{0.6}Fe_{0.4}O_3$–Ceria Composite Cathode for SOFCs Operating at Intermediate Temperatures. *J. Electrochem. Soc.* **155,** B575 (2008).
148. Huang, B., Zhu, X. J., Lv, Y. & Liu, H. High-performance $Gd_{0.2}Ce_{0.8}O_2$-impregnated $LaNi_{0.6}Fe_{0.4}O_{3-\delta}$ cathodes for intermediate temperature solid oxide fuel cell. *J. Power Sources* **209,** 209–219 (2012).
149. Jain, S. R., Adiga, K. C. & Pai Verneker, V. R. A new approach to thermochemical calculations of condensed fuel-oxidizer mixtures. *Combust. Flame* **40,** 71–79 (1981).
150. Hwang, H. J., Moon, J. W., Moon, J. & Awano, M. Removal of Nitric Oxide (NO) by perovskite-type composite catalytic thick film, $La_{0.6}Sr_{0.4}Co_{0.2}Fe_{0.8}O_{3-\delta}$ and gadolinia-doped ceria electrolyte, $Gd_{0.2}Ce_{0.8}O_{2-\delta}$. *J. Am. Ceram. Soc.* **88,** 79–84 (2005).
151. Hwang, H. J., Moon, J. W., Lee, S. & Lee, E. A. Electrochemical performance of LSCF-based composite cathodes for intermediate temperature SOFCs. *J. Power Sources* **145,** 243–248 (2005).
152. Liu, J., Co, A. C., Paulson, S. & Birss, V. I. Oxygen reduction at sol–gel derived

$La_{0.8}Sr_{0.2}Co_{0.8}Fe_{0.2}O_3$ cathodes. *Solid State Ionics* **177,** 377–387 (2006).
153. Dong, F., Chen, Y., Chen, D. & Shao, Z. Surprisingly high activity for oxygen reduction reaction of selected oxides lacking long oxygen-ion diffusion paths at intermediate temperatures: A case study of cobalt-free $BaFeO_{3-\delta}$. *ACS Appl. Mater. Interfaces* **6,** 11180–11189 (2014).
154. Zhi, M., Lee, S., Miller, N., Menzler, N. H. & Wu, N. An intermediate-temperature solid oxide fuel cell with electrospun nanofiber cathode. *Energy Environ. Sci.* **5,** 7066 (2012).
155. Elam, J. W., Dasgupta, N. P. & Prinz, F. B. ALD for clean energy conversion, utilization, and storage. *MRS Bull.* **36,** 899–906 (2011).
156. George, S. M. Atomic Layer Deposition: An Overview. *Chem. Rev.* **110,** 111–131 (2009).
157. Knez, M., Nielsch, K. & Niinistö, L. Synthesis and surface engineering of complex nanostructures by atomic layer deposition. *Adv. Mater.* **19,** 3425–3438 (2007).
158. Leskelä, M. & Ritala, M. Atomic Layer Deposition Chemistry: Recent Developments and Future Challenges. *Angew. Chemie - Int. Ed.* **42,** 5548–5554 (2003).
159. Sik Son, K., Bae, K., Woo Kim, J., Suk Ha, J. & Hyung Shim, J. Ion conduction in nanoscale yttria-stabilized zirconia fabricated by atomic layer deposition with various doping rates. *J. Vac. Sci. Technol. A Vacuum, Surfaces, Film.* **31,** 01A107 (2013).
160. Hultqvist, A., Edoff, M. & Törndahl, T. Evaluation of Zn-Sn-O buffer layers for $CuIn_{0.5}Ga_{0.5}Se_2$ solar cells. *Prog. Photovoltaics Res. Appl.* **19,** 478–481 (2011).
161. Kosola, A., Putkonen, M., Johansson, L. S. & Niinistö, L. Effect of annealing in processing of strontium titanate thin films by ALD. *Appl. Surf. Sci.* **211,** 102–112 (2003).
162. Vehkamäki, M. Growth of $SrTiO_3$ and $BaTiO_3$ Thin Films by Atomic Layer Deposition. *Electrochem. Solid-State Lett.* **2,** 504 (1999).
163. Elliott, S. D. & Nilsen, O. Reaction Mechanisms in ALD of Ternary Oxides. in **41,** 175–183 (2011).
164. Wang, H. *et al.* Atomic Layer Deposition of Lanthanum-Based Ternary Oxides. *Electrochem. Solid-State Lett.* **12,** G13 (2009).
165. Pore, V., Hatanpa, T., Ritala, M. & Leskela, M. Atomic Layer Deposition of Metal Tellurides and Selenides Using Alkylsilyl Compounds of Tellurium and Selenium Atomic Layer Deposition of Metal Tellurides and Selenides Using Alkylsilyl Compounds of Tellurium and Selenium. 3478–3480 (2009). doi:10.1021/ja8090388
166. Miikkulainen, V., Leskelä, M., Ritala, M. & Puurunen, R. L. Crystallinity of inorganic films grown by atomic layer deposition: Overview and general trends. *J. Appl. Phys.* **113,** (2013).
167. Hämäläinen, J. *Atomic Layer Deposition of Noble Metal Oxide and Noble Metal Thin Films*. (2013).
168. Yum, J. H. *et al.* Atomic layer deposited beryllium oxide: Effective passivation layer for III-V metal/oxide/semiconductor devices. *J. Appl. Phys.* **109,** 1–5 (2011).
169. Uusi-Esko, K. & Karppinen, M. Extensive series of hexagonal and orthorhombic $RMnO_3$ (R = Y, La, Sm, Tb, Yb, Lu) thin films by atomic layer deposition. *Chem. Mater.* **23,** 1835–1840 (2011).
170. Povey, I. M. *et al.* Photonic crystal thin films of GaAs prepared by atomic layer deposition. *Appl. Phys. Lett.* **89,** (2006).
171. Park, H. B. *et al.* Comparison of HfO_2 films grown by atomic layer deposition using $HfCl_4$ and H_2O or O_3 as the oxidant. *J. Appl. Phys.* **94,** 3641–3647 (2003).
172. Steele, B. C. H. & Heinzel, A. in *Materials for Sustainable Energy* 224–231 (Co-Published with Macmillan Publishers Ltd, UK, 2010). doi:10.1142/9789814317665_0031
173. Akikusa, J., Adachi, K., Hoshino, K., Ishihara, T. & Takita, Y. Development of a Low Temperature Operation Solid Oxide Fuel Cell. *J. Electrochem. Soc.* **148,** A1275 (2001).
174. Chan, S. H., Chen, X. J. & Khor, K. A. Cathode Micromodel of Solid Oxide Fuel Cell. *J. Electrochem. Soc.* **151,** A164 (2004).
175. Dokiya, M., Yamamoto, O., Tagawa, H. & Singhal, S. C. *Proceedings of the Fourth International Symposium on Solid Oxide Fuel Cells*. (Electrochemical Society, 1995).
176. Noren, D. A. & Hoffman, M. A. Clarifying the Butler-Volmer equation and related approximations for calculating activation losses in solid oxide fuel cell models. *J. Power Sources* **152,** 175–181 (2005).
177. Bidrawn, F. *et al.* Efficient Reduction of CO_2 in a Solid Oxide Electrolyzer. *Electrochem. Solid-*

State Lett. **11,** B167 (2008).
178. O'Brien, J. E. *et al.* Performance Measurements of Solid-Oxide Electrolysis Cells for Hydrogen Production. *J. Fuel Cell Sci. Technol.* **2,** 156 (2005).
179. Wang, W., Huang, Y., Jung, S., Vohs, J. M. & Gorte, R. J. A Comparison of LSM, LSF, and LSCo for Solid Oxide Electrolyzer Anodes. *J. Electrochem. Soc.* **153,** A2066 (2006).
180. Winkler, J. Geometric Requirements of Solid Electrolyte Cells with a Reference Electrode. *J. Electrochem. Soc.* **145,** 1184 (1998).
181. Chan, S. H., Chen, X. J. & Khor, K. A. Reliability and accuracy of measured overpotential in a three-electrode fuel cell system. *J. Appl. Electrochem.* **31,** 1163–1170 (2001).
182. Kato, T. Influence of cell configuration on measuring interfacial impedances between a solid electrolyte and an electrode. *Solid State Ionics* **132,** 287–295 (2000).
183. Nagata, M., Itoh, Y. & Iwahara, H. Dependence of observed overvoltages on the positioning of the reference electrode on the solid electrolyte. *Solid State Ionics* **67,** 215–224 (1994).
184. Singhal, S. C. & Dokiya, M. *Proceedings of the Eighth International Symposium on Solid Oxide Fuel Cells*. (Electrochemical Society, 2003).
185. Pizzini, S., Bianchi, M., Colombo, P. & Torchio, S. On the influence of the annealing temperature and heavy current treatments on the porous structure of platinum electrodes and on the kinetics of the oxygen reaction at high temperatures. *J. Appl. Electrochem.* **3,** 153–159 (1973).
186. Soc, S. N. F. J. E. Overpotential Behavior of Stabilized Zirconia Solid Electrolyte Fuel Cells Overpotential Behavior of Stabilized Zirconia Solid Electrolyte Fuel Cells. (1971).
187. Society, T. E. Platinum Electrodes and Calcia-Stabilized Zirconia: The Relation between Electrode Processes and Electrode Structure. (1971).
188. Steady, E. I., Overpotential, S., Yu, D. & Soc, A. S. N. J. E. Cathodic and Anodic Polarization Phenomena at Platinum Electrodes Cathodic and Anodic Polarization Phenomena at Platinum Electrodes with Doped CeO as Electrolyte. (1979).
189. Williamson, S. S., Cassani, P. A., Lukic, S. & Blunier, B. *Energy Storage*. *Power Electronics Handbook* (2011). doi:10.1016/B978-0-12-382036-5.00046-X
190. Friedrich, W., Knipping, P. & Laue, M. von. *nterferenz-Erscheinungen bei Röntgenstrahlen*. (München : Verlag der Königlich-Bayerischen Akademie der Wissenschaften, 1912).
191. Laue, M. Von. Concerning the detection of X-ray interferences. *Nobel Lect.* 347–355 (1915). doi:10.1038/090410b0
192. Dana, Salisbury, E. & Ford, W. E. *A Textbook of Mineralogy*. (John Wiley & Sons, 1932).
193. Binnig, G. & Quate, C. F. Atomic Force Microscope. *Phys. Rev. Lett.* **56,** 930–933 (1986).
194. Cappella, B. & Dietler, G. Force-distance curves by atomic force microscopy. *Surf. Sci. Rep.* **34,** 1–104 (1999).
195. Carpick, R. W., Ogletree, D. F. & Salmeron, M. A General Equation for Fitting Contact Area and Friction vs Load Measurements. **400,** 395–400 (1999).
196. Hertz, H. Ueber die Berührung fester elastischer Körper. *J. fur die Reine und Angew. Math.* **1882,** 156–171 (1882).
197. Israelachvili, J. N. & Tabor, D. The Measurement of Van Der Waals Dispersion Forces in the Range 1.5 to 130 nm. *Proc. R. Soc. A Math. Phys. Eng. Sci.* **331,** 19–38 (1972).
198. Tabor, D. & Winterton, R. H. S. The Direct Measurement of Normal and Retarded van der Waals Forces. *Proc. R. Soc. A Math. Phys. Eng. Sci.* **312,** 435–450 (1969).
199. Carpick, R. W., Agrait, N., Ogletree, D. F. & Salmeron, M. Measurement of interfacial shear (friction) with an ultrahigh vacuum atomic force microscope. *J. Vac. Sci. Technol. B Microelectron. Nanom. Struct.* **14,** 1289 (1996).
200. Langstreth, J. K. *Contact Mechanics*. (Cambridge University Press, 1987).
201. Johnson, K. L., Kendall, K. & Roberts, A. D. Surface Energy and the Contact of Elastic Solids. *Proc. R. Soc. A Math. Phys. Eng. Sci.* **324,** 301–313 (1971).
202. Derjaguin, B. V, Muller, V. M. & Toporov, Y. U. P. Effect of contact deformation on the adhesion of particles. *J. Colloid Interface Sci.* **52,** 105–108 (1975).
203. Maugis, D. Adhesion of spheres: The JKR-DMT transition using a dugdale model. *J. Colloid Interface Sci.* **150,** 243–269 (1992).
204. Greenwood, J. A. Adhesion of elastic spheres. *Proc. R. Soc. A Math. Phys. Eng. Sci.* **453,** 1277–

1297 (1997).
205. Lantz, M. A., O'Shea, S. J., Welland, M. E. & Johnson, K. L. Atomic-force-microscope study of contact area and friction on NbSe2. *Phys. Rev. B* **55,** 10776–10785 (1997).
206. Bietsch, A., Schneider, M. A., Welland, M. E. & Michel, B. Electrical testing of gold nanostructures by conducting atomic force microscopy. *J. Vac. Sci. Technol. B Microelectron. Nanom. Struct.* **18,** 1160 (2000).
207. Houzé, F., Meyer, R., Schneegans, O. & Boyer, L. Imaging the local electrical properties of metal surfaces by atomic force microscopy with conducting probes. *Appl. Phys. Lett.* **69,** 1975–1977 (1996).
208. Agraït, N., Rodrigo, J. G. & Vieira, S. Conductance steps and quantization in atomic-size contacts. *Phys. Rev. B* **47,** 12345–12348 (1993).
209. Muller, C. J., van Ruitenbeek, J. M. & de Jongh, L. J. Conductance and supercurrent discontinuities in atomic-scale metallic constrictions of variable width. *Phys. Rev. Lett.* **69,** 140–143 (1992).
210. Holweg, P. A. M., Caro, J., Verbruggen, A. H. & Radelaar, S. Ballistic electron transport and two-level resistance fluctuations in noble-metal nanobridges. *Phys. Rev. B* **45,** 9311–9319 (1992).
211. Ralls, K. S., Ralph, D. C. & Buhrman, R. A. Individual-defect electromigration in metal nanobridges. *Phys. Rev. B* **40,** 11561–11570 (1989).
212. Guo, D.-Z., Hou, S.-M., Zhang, G.-M. & Xue, Z.-Q. Conductance fluctuation and degeneracy in nanocontact between a conductive AFM tip and a granular surface under small-load conditions. *Appl. Surf. Sci.* **252,** 5149–5157 (2006).
213. Kogut, L. & Komvopoulos, K. Electrical contact resistance theory for conductive rough surfaces. *J. Appl. Phys.* **94,** 3153–3162 (2003).
214. Sharvin, Y. V. A Possible Method for Studying Fermi Surfaces. *Sov. Phys. JETP* **21,** 655 (196AD).
215. Holm, R. *Electric Contacts: Theory and Application*. (Springer Science & Business Media, 1967).
216. O'Hayre, R., Feng, G., Nix, W. D. & Prinz, F. B. Quantitative Impedance measurement using atomic force microscopy. *J. Appl. Phys.* **96,** 3540–3549 (2004).
217. Melitz, W., Shen, J., Kummel, A. C. & Lee, S. Kelvin probe force microscopy and its application. *Surf. Sci. Rep.* **66,** 1–27 (2011).
218. Karimaghaloo, A., Andrade, A. M., Grewal, S., Shim, J. H. & Lee, M. H. Mechanism of Cathodic Performance Enhancement by a Few-Nanometer-Thick Oxide Overcoat on Porous Pt Cathodes of Solid Oxide Fuel Cells. *ACS Omega* **2,** 806–813 (2017).
219. Takeda, Y. Cathodic Polarization Phenomena of Perovskite Oxide Electrodes with Stabilized Zirconia. *J. Electrochem. Soc.* **134,** 2656 (1987).
220. Etsell, T. H. & Flengas, S. N. Overpotential Behavior of Stabilized Zirconia Solid Electrolyte Fuel Cells. *J. Electrochem. Soc.* **118,** 1890 (1971).
221. Brook, R. J., Pelzmann, W. L. & Kröger, F. A. Platinum Electrodes and Calcia-Stabilized Zirconia. *J. Electrochem. Soc.* **118,** 185 (1971).
222. Wang, D. Y. & Nowick, A. S. Cathodic and Anodic Polarization Phenomena at Platinum Electrodes with Doped CeO_2 as Electrolyte: I. Steady-State Overpotential. *J. Electrochem. Soc.* **126,** 1155–1165 (1979).
223. Murray, E. P., Tsai, T. & Barnett, S. A. Oxygen transfer processes in (La , Sr) MnO_3/Y_2O_3-stabilized ZrO_2 cathodes : an impedance spectroscopy study. *Solid State Ionics* **110,** 235–243 (1998).
224. Chen, J. Y. *et al.* Thermal stability, oxygen non-stoichiometry and transport properties of LaNi0.6Fe0.4O3. *Solid State Ionics* **192,** 424–430 (2011).
225. Tofield, B. C. & Scott, W. R. Oxidative Nonstoichiometry in Perovskites, an Experimental Survey; the Defect Structure of an Oxidized Lanthanum Manganite by Powder Neutron Diffraction. *J. Solid State Chem.* **10,** 183–194 (1974).
226. Chiba, R. An investigation of $LaNi_{1-x}Fe_xO_3$ as a cathode material for solid oxide fuel cells. *Solid State Ionics* **124,** 281–288 (1999).
227. Budiman, R. A. *et al.* Electrochemical Study of $LaNi_{0.6}Fe_{0.4}O_{3-\delta}$ Film Electrode. *J. Electrochem. Soc.* **162,** F1445 (2015).
228. Lee, S., Miller, N. & Gerdes, K. Long-Term Stability of SOFC Composite Cathode Activated by Electrocatalyst Infiltration. *J. Electrochem. Soc.* **159,** F301–F308 (2012).

229. Jiang, Z., Xia, C., Zhao, F. & Chen, F. $La_{0.85}Sr_{0.15}MnO_{3-x}$ Infiltrated $Y_{0.5}Bi_{1.5}O_3$ Cathodes for Intermediate-Temperature Solid Oxide Fuel Cells. *Electrochem. Solid-State Lett.* **12,** B91–B94 (2009).
230. Ping, S. & Chen, X. ScienceDirect Chromium deposition and poisoning of cathodes of solid oxide fuel cells e A review. *Int. J. Hydrogen Energy* **39,** 505–531 (2014).
231. Yokokawa, H. *et al.* Thermodynamic considerations on Cr poisoning in SOFC cathodes. *Solid State Ionics* **177,** 3193–3198 (2006).
232. Komatsu, T. *et al.* Degradation behavior of anode-supported solid oxide fuel cell using LNF cathode as function of current load. *J. Power Sources* **195,** 5601–5605 (2010).
233. Gong, Y. *et al.* Stabilizing Nanostructured Solid Oxide Fuel Cell Cathode with Atomic Layer Deposition. *Nano Lett.* **13,** 4340–4345 (2013).
234. Gong, Y. *et al.* Atomic Layer Deposition Functionalized Composite SOFC Cathode $La_{0.6}Sr_{0.4}Fe_{0.8}Co_{0.2}O_{3-\delta}$-$Gd_{0.2}Ce_{0.8}O_{1.9}$: Enhanced Long-Term Stability. *Chem. Mater.* **25,** 4224–4231 (2013).
235. Hansen, T. W., Delariva, A. T., Challa, S. R. & Datye, A. K. Sintering of Catalytic Nanoparticles : Particle Migration or Ostwald Ripening? *Acc. Chem. Res.* **46,** 1720–1730 (2013).
236. Moon, H. *et al.* Interfacial chemical bonding-mediated ionic resistive switching. *Sci. Rep.* **7,** 1264 (2017).
237. Zade, V., Kang, H. Sen & Lee, M. H. Effect of mechanical and electrical stimuli in conductive atomic force microscopy with noble metal-coated tips. *J. Appl. Phys.* **123,** (2018).
238. Libioulle, L., Houbion, Y. & Gilles, J. M. Very sharp platinum tips for scanning tunneling microscopy. *Rev. Sci. Instrum.* **66,** 97–100 (1995).
239. Sørensen, A. H., Hvid, U., Mortensen, M. W. & Mo/rch, K. A. Preparation of platinum/iridium scanning probe microscopy tips. *Rev. Sci. Instrum.* **70,** 3059–3067 (1999).
240. Schaefer, D. M. & Gomez, J. Atomic Force Microscope Techniques for Adhesion Measurements. *J. Adhes.* **74,** 341–359 (2000).
241. Leite, F. L. & Herrmann, P. S. P. Application of atomic force spectroscopy (AFS) to studies of adhesion phenomena: A review. *J. Adhes. Sci. Technol.* **19,** 365–405 (2005).
242. Feng, X., Kieviet, B. D., Song, J., Schön, P. M. & Vancso, G. J. Adhesion forces in AFM of redox responsive polymer grafts: Effects of tip hydrophilicity. *Appl. Surf. Sci.* **292,** 107–110 (2014).
243. Neuman, K. C. & Nagy, A. Single-molecule force spectroscopy: Optical tweezers, magnetic tweezers and atomic force microscopy. *Nat. Methods* **5,** 491–505 (2008).
244. Yang, Y. *et al.* Observation of conducting filament growth in nanoscale resistive memories. *Nat. Commun.* **3,** 732–738 (2012).
245. Kwon, D.-H. *et al.* Atomic structure of conducting nanofilaments in TiO_2 resistive switching memory. *Nat. Nanotechnol.* **5,** 148–153 (2010).
246. Prakash, A., Jana, D. & Maikap, S. TaOx-based resistive switching memories: Prospective and challenges. *Nanoscale Res. Lett.* **8,** 1–17 (2013).
247. Shi, H., Asahi, R. & Stampfl, C. Properties of the gold oxides Au_2O_3 and Au_2O: First-principles investigation. doi:10.1103/PhysRevB.75.205125
248. Jeong, D. S. *et al.* Emerging memories: Resistive switching mechanisms and current status. *Reports Prog. Phys.* **75,** (2012).
249. Waser, R., Dittmann, R., Staikov, C. & Szot, K. Redox-based resistive switching memories nanoionic mechanisms, prospects, and challenges. *Adv. Mater.* **21,** 2632–2663 (2009).
250. Chen, J. Y. *et al.* Dynamic evolution of conducting nanofilament in resistive switching memories. *Nano Lett.* **13,** 3671–3677 (2013).
251. Szlachetko, J. *et al.* Real time determination of the electronic structure of unstable reaction intermediates during Au_2O_3 reduction. *J. Phys. Chem. Lett.* **5,** 80–84 (2014).
252. O'Shea, S. J. Conducting atomic force microscopy study of silicon dioxide breakdown. *J. Vac. Sci. Technol. B Microelectron. Nanom. Struct.* **13,** 1945 (1995).
253. Zeng, L. *et al.* Gate-induced image force barrier lowering in Schottky barrier FETs. *IEEE Trans. Nanotechnol.* **8,** 10–15 (2009).
254. Budenstein, P. P. *In Digest of Literature on Dielectrics*. (National Academy of Sciences, 1971).
255. Filipovic, L. & Selberherr, S. Performance and Stress Analysis of Metal Oxide Films for CMOS-

Integrated Gas Sensors. *Sensors* **15,** 7206–7227 (2015).
256. Kolodiazhnyi, T. & Petric, A. The Applicability of Sr-deficient n-type $SrTiO_3$ for SOFC Anodes. *J. Electroceramics* 5–11 (2005).
257. Savaniu, C. D. & Irvine, J. T. S. La-doped $SrTiO_3$ as anode material for IT-SOFC. *Solid State Ionics* **192,** 491–493 (2011).
258. Hemminger, J. C., Carr, R. & Somorjai, G. A. The Photoassisted Reaction of Gaseous water and Carbon Dioxide Adsorbed on the $SrTiO_3$ (111) Crystal Face to form methane. *Chem. Phys. Lett.* **57,** 100–104 (1978).
259. Sanna, B. S. *et al.* Fabrication and Electrochemical Properties of Epitaxial Samarium-Doped Ceria Films on $SrTiO_3$-Buffered MgO Substrates. *Adv. Funct. Mater.* **19,** 1713–1719 (2009).
260. Yoon, J. S. *et al.* Catalytic Activity of Y and Fe Co-Doped SrTio 3 Perovskites for Methane Oxidation. **7,** 209–213 (2011).
261. Tian, T., Wang, W., Zhan, M. & Chen, C. Catalytic partial oxidation of methane over $SrTiO_3$ with oxygen-permeable membrane reactor. *Catal. Commun.* **11,** 624–628 (2010).
262. Liu, S. *et al.* METHANE COUPLING USING CATALYTIC MEMBRANE REACTORS. *Catal. Rev.* **43,** 147–198 (2001).
263. Ye, Y., Soc, J. E., Ye, Y., Rihko-struckmann, L. & Munder, B. Partial Oxidation of n-Butane in a Solid Electrolyte Membrane Reactor : Influence of Electrochemical Oxygen Pumping. *J. Electrochem. Soc.* **153,** D21–D29 (2006).
264. Ma, Q. *et al.* Short communication A high-performance ammonia-fueled SOFC based on a YSZ thin-film electrolyte. **164,** 86–89 (2007).
265. Han, M., Tang, X., Yin, H. & Peng, S. Fabrication , microstructure and properties of a YSZ electrolyte for SOFCs. **165,** 757–763 (2007).
266. Gu, X., Jin, W., Chen, C., Xu, N. & Shi, J. Oxidation of Methane to Syngas. *AIChE J.* **48,** 2051–2060 (2002).
267. Transactions, E. C. S. Methane Partial Oxidation-Assisted H_2O/CO_2 Co-Electrolysis for Syngas Production in Both Electrodes. *ECS Trans.* **78,** 3159–3166 (2017).
268. Maier, R. A., Johnston-peck, A. C. & Donohue, M. P. (Magic Dopant) Amphoteric Behavior of a Redox-Active Transition Metal Ion in a Perovskite Lattice : New Insights on the Lattice Site Occupation of Manganese in $SrTiO_3$. *Adv. Funct. Mater.* **26,** 8325–8333 (2016).
269. Okazaki, H., Suzuki, H. & Ihata, K. A possibility of the oxygen diffusion enhancement in YSZ: a molecular dynamics study. *Phys. Lett. A* **188,** 291–295 (1994).
270. Tan, H. *et al.* Oxygen Vacancy Enhanced Photocatalytic Activity of Pervoskite $SrTiO_3$. *ACS Appl. Mater. Interfaces* **6,** 19184–19190 (2014).
271. Dow, W., Wang, Y. & Huang, T. Yttria-Stabilized Zirconia Supported Copper Oxide Catalyst. *J. Catal.* **160,** 155–170 (1996).
272. Hong, S. S., Cha, J. J. & Cui, Y. via Atomic Metal Filament Formation. 231–235 (2011). doi:10.1021/nl103603v
273. Nonnenmacher, M., O'Boyle, M. P. & IH. K. Wickramasinghe. Kelvin probe force microscopy. *Appl. Phys. Lett.* **2921,** 2921–2923 (1991).
274. Celano, U. *et al.* Three-Dimensional Observation of the Conductive Filament in Nanoscaled Resistive Memory Devices. *Nano Lett.* **14,** 2401–2406 (2014).
275. Maier, R. A. & Randall, C. A. Low-Temperature Ionic Conductivity of an Acceptor-Doped Perovskite: I. Impedance of Single-Crystal $SrTiO_3$. *J. Am. Ceram. Soc.* **99,** 3350–3359 (2016).
276. Jiang, J. & Hertz, J. L. On the variability of reported ionic conductivity in nanoscale YSZ thin films. *J Electroceram* **32,** 37–46 (2014).
277. O'Hayre, R., Lee, M. & Prinz, F. B. Ionic and electronic impedance imaging using atomic force microscopy. *J. Appl. Phys.* **95,** 8382–8392 (2004).
278. Kawayama, I., Misra, M. C. & Tonouchi, M. Dielectric properties of $(Ba,Sr)TiO_3$ thin films in MHz and THz frequency regions : Quantitative evaluation of the orientational polarization Dielectric properties of $(Ba,Sr)TiO_3$ thin films in MHz and THz frequency regions : Quantitative. *Jpn. J. Appl. Phys.* **53,** 09PD06 (2014).
279. MINAMI, H. *et al.* Rapid Synthesis and Scanning Probe Analysis of $Ba_xSr_{1-x}TiO_3$ Composition Spread Films on a Temperature Gradient Si (100) Substrate. *Jpn. J. Appl. Phys.* **41,** L149–L151

(2002).
280. Perry, N. H., Kim, S. & Mason, T. O. Local electrical and dielectric properties of nanocrystalline yttria-stabilized zirconia. *J Mater Sci* **43,** 4684–4692 (2008).
281. Crank, J. *THE MATHEMATICS OF DIFFUSION*. (1975).
282. Poirier, D. R. & Geiger, G. H. *Transport Phenomena in Materials Processing*. (Springer Nature, 2016). doi:10.1007/978-3-319-48090-
283. Knoche, K. L. *et al.* On the applicability of Fick ' s law to diffusion in inhomogeneous systems On the applicability of Fick ' s law to diffusion in inhomogeneous systems and R S anchez. *Eur. J. Phys.* **26,** 913–925 (2005).
284. Kang, H., Grewal, S., Li, H. & Lee, M. H. Effect of Various Wet Impregnations into $LaNi_6Fe_4O_{3-\delta}$ Cathodic Backbone for Solid Oxide Fuel Cells. **166,** 1–9 (2019).
285. Karimaghaloo, A. *et al.* Nanoscale Surface and Interface Engineering of Solid Oxide Fuel Cells by Atomic Layer Deposition. *Int. J. Precis. Eng. Manuf. Technol.* (2019). doi:10.1007/s40684-019-00090-9
286. Li, H. *et al.* durability and activity of nanoparticle-decorated. 15927–15935 (2020). doi:10.1039/d0ta02915g
287. Korablev, G. A. CALCULATION OF ACTIVATION ENERGY OF DIFFUSION AND SELF-DIFFUSION. *Eur. Chem. Bull.* **7,** 23–29 (2018).
288. Slouka, C. *et al.* The Effect of Acceptor and Donor Doping on Oxygen Vacancy Concentrations in Lead Zirconate. *Materials (Basel).* **9,** (2016).
289. Krishnamurthy, R., Yoon, Y.-G., Srolovitz, D. J. & Car, R. Oxygen Diffusion in Yttria-Stabilized Zirconia: A New Simulation Model. *J. Am. Ceram. Soc.* **87,** 1821–1830 (2004).
290. Iglesias, L., AndrésGómez, Gich, M. & Rivadulla, F. Tuning Oxygen Vacancy Di ff usion through Strain in $SrTiO_3$ Thin Films ´ Go m. *ACS Appl. Mater. Interfaces* **10,** 35367–35373 (2018).